# Signal Processing Techniques for Ultrasonic Tissue Doppler and Real-time B-mode Imaging in Cardiology

*Michael J. Bennett*

A thesis submitted for the degree of Doctor of Philosophy.
**The University of Edinburgh.**
March 2005

# Abstract

Coronary heart disease is the most common cause of death in the UK affecting more then one in five men and one in six women. The cause is generally a constriction of the coronary arteries which supply the heart muscle, or myocardium, with blood. In around 95% of cases, the constriction is caused by the process of arteriosclerosis which results in the development of a plaque on the vessel wall. Even though these plaques tend to develop quite slowly, they are sometimes liable to sudden rupture, which causes clotting of the blood in the vessel and hence a sudden reduction in the supply of blood to the myocardium.

This sudden loss of blood supply to a portion of the myocardium will result in the death, or infarction, of some of the muscle tissue in that area. There will be a region of tissue around the edge of damaged area which will recover because the body is able to form a new collateral blood supply and a central region which will become infarcted.

Of the many medical imaging modalities available today, such as Magnetic Resonance Imaging (MRI), X-Ray or Computer Tomography (CT), ultrasound, in the form of echocardiography, forms the most commonly used technique for performing cardiac diagnosis, the principle reasons being that it is relatively cheap, safe and instantaneous compared to the others.

This thesis is concerned with the signal processing techniques which are used in the form of Doppler Tissue Imaging (DTI) and real-time B-Mode imaging to study the motion of cardiac structures. Although these techniques are well suited to this task, improvements in B-mode contrast resolution and DTI velocity resolution are required if image quality and quantitative measurements are to reach a more acceptable level.

Results are presented which demonstrate that the accuracy of the velocity estimations made using DTI can be improved with the use of model based signal processing techniques. The use of the fractional Fourier transform is explored in the context of coded excitation, which is a technique to allow improvements in imaging depth and axial resolution and results are shown which show that this technique is able to offer improvements similar to matched filtering. The combined techniques of empirical mode decomposition and the Hilbert spectrum are used to demonstrate a new interpretation of the physical process underlying non-linear acoustic wave propagation and the existing technique of tissue harmonic imaging.

# Acknowledgements

There are so many people who have helped me along the way during the last 3 years that I am sure I will forget to mention at least some of them! So, to be sure that I cover everyone, I'd like to take this opportunity to thank everyone who has known me and been my friend while I've been here in Edinburgh.

However, there are, of course, some who deserve particular attention. Firstly, I'd like to thank my supervisors Steve and Norman for their continuous supply of help and advice when I needed it. I'd also like to thank them for allowing me to have the academic freedom that I have enjoyed during my PhD and for making sure that I didn't wonder too far off track!

I must also thank Tom for his endless patience and efforts, particularly right at the start when I was a complete new-comer to the field of medical ultrasound! Without his help, the single crystal ultrasound system, on which this project hinged, would probably have not come into being.

Thanks must also go to Douglas Carmichael for his help and advice when I was trying to design a suitable rotating phantom device. He should also be congratulated for managing to understand my somewhat woolly explanations of what I wanted!

I would also like to thank Kate for proof reading.

Obviously, credit must also go to my Mum, for all the support she has given me when I was low. And, of course, to my various friends. I feel I should make particular mention of Katherine, Mairéad and Jude, who aided in many good nights out which provided an important distraction! Also, I should give credit to Mika, Nedko, Moti, Ken, Stam and Tamie, who have all at one time or another provided me with useful advice to keep me on the right path.

# Contents

# List of figures

# List of tables

# Acronyms and abbreviations

| | |
|---|---|
| A-mode | Amplitude Mode |
| ADC | Analog to Digital Converter |
| ASCII | American Standard Code for Information Interchange |
| B-mode | Brightness Mode |
| C3M | Complex Cross Correlation Model |
| CCM | Cross Correlation Model |
| CHI | Contrast Harmonic Imaging |
| CW | Continuous Wave |
| DLC | Delay Line Canceller |
| DTI | Doppler Tissue Imaging |
| ECG | Electrocardiogram |
| EMD | Empirical Mode Decomposition |
| FET | Field Effect Transistor |
| FFT | Fast Fourier Transform |
| FIR | Finite Impulse Response |
| FM | Frequency Modulation |
| IMF | Intrinsic Mode Function |
| IVS | Inter Ventricular Septum |
| LED | Light Emitting Diode |
| M-mode | Motion Mode |
| PC | Personal Computer |
| PRF | Pulse Repetition Frequency |
| PSD | Power Spectral Density |

| | |
|---|---|
| PW | Pulse Wave |
| RAM | Random Access Memory |
| RF | Radio Frequency |
| SNR | Signal to Noise Ratio |
| SONAR | Sound Navigation and Ranging |
| THI | Tissue Harmonic Imaging |
| RADAR | Radio Detection and Ranging |
| WFUMB | World Federation for Ultrasound in Medicine and Biology |

# Nomenclature

| | |
|---|---|
| $x_i$ | some definition |
| $a$ | Chirp rate [Hz/s] |
| $c$ | Speed of sound in specified medium [m/s] |
| $E$ | Average energy of range gated echo |
| $f_c$ | Carrier frequency / center frequency / spatial frequency [Hz] |
| $\bar{f}_c$ | Spatial mean frequency [Hz] |
| $\bar{f}_{nc}$ | Normalised spatial mean frequency |
| $\bar{f}_{nt}$ | Normalised temporal mean frequency |
| $f_{prf}$ | Pulse repetition frequency [Hz] |
| $f_s$ | Sampling frequency [Hz] |
| $f_{s-rf}$ | Radio frequency sampling frequency / spatial sampling frequency [Hz] |
| $\bar{f}_t$ | Temporal mean freqeucny |
| $f$ | Frequency [Hz] |
| $G(x)$ | Spatial power spectral distribution |
| $H()$ | Heavyside step function |
| $h$ | Periodicity factor |
| $I(x)$ | In-phase signal |
| $I_d$ | Distance from transducer at which acoustic shock phenomenon will occur [m] |
| $j$ | $\sqrt{-1}$ Imaginary number |
| $N$ | Noise power [W] |
| $N_i$ | Noise power. $N_{i=0} = N$ and $N_{i\neq 0} = 0$ [W] |
| $N_0$ | Noise PSD |
| $N_{\text{sig}}$ | Number of samples in a signal |
| $N_{\text{TB}}$ | Time-bandwidth product |
| $p$ | Acoustic pressure [Pa] |
| $p_0$ | Acoustic pressure at source [Pa] |
| $P\int$ | Integrate taking Cauchy principle value |

| | |
|---|---|
| $Q$ | Spatial quality factor (spatial mean frequency divided by bandwidth) |
| $Q(x)$ | Quadrature phase signal |
| $r$ | Distance from center of curvature [m] |
| $r_0$ | Effective radious of spherical source [m] |
| $S$ | Signal power [W] |
| $T$ | Sampling interval ($\frac{1}{f_s}$ or $\frac{1}{f_{prf}}$) [s] |
| $v$ | Velocity [m/s] |
| $w_{rf}(k,i)$ | Sampled radio frequency signal |
| $z$ | Displacement from transducer [m] |
| | |
| $\alpha$ | [Chapter 4] Doppler angle |
| $\alpha$ | [Chapter 5] Fractional Fourier transform order |
| $\beta$ | [Chapter 4] RMS bandwidth [Hz] |
| $\beta$ | [Chapter 6] Coefficient of non-linearity |
| $\rho$ | [Chapter 4] Maximum correlation coefficient of received signals without noise |
| $\rho$ | [Chapter 6] Density of medium [kg/m$^3$] |
| $\sigma$ | Degree of non-linear distortion |
| $\phi$ | [Chapter 4] Phase |
| $\phi$ | [Chapter 5] Fractional Fourier transform order $\phi = \frac{\alpha\pi}{2}$ |
| $\phi'(x)$ | Instantaneous rate of change of phase |
| $\varphi$ | Normalised mean velocity |
| $\omega$ | Angular frequency [rad/s] |

# Chapter 1
# Introduction

## 1.1 Motivation

A heart attack, technically known as "myocardial infarction", occurs when the supply of blood to the heart muscle, the myocardium, is disrupted. This is usually caused by a blockage of one of the coronary arteries which supply the myocardium with blood. Without this blood, the muscle is starved of oxygen and nutrients and will eventually die. In around 95 % of cases this occurs because of the process of arteriosclerosis in the coronary vessels. This process leads to the development of a plaque on the vessel wall, which may rupture suddenly leading to clotting of the blood in the vessel and a sudden reduction in the blood supply to the myocardium.

This sudden change results in two things, a reduction in cardiac output (the heart is unable to pump as strongly) and a damming of blood in the veins leading to increased systemic venous pressure. Immediately after suffering damage, the output of the heart will fall rapidly and within a few seconds can fall to as little as two-fifths of normal. This level of cardiac output is still sufficient to keep a person alive, but will probably result in fainting. This stage only lasts for a few seconds before sympathetic reflexes in other parts of the body occur to compensate. This increases the strength with which the remaining heart muscle operates, thus increasing the cardiac output back toward a normal level. The sympathetic reflexes also lead to an increase in the ability of the blood to flow back to the heart because of a resulting increase in the tone of the vessels. This makes it easier for the heart to pump the blood and so also helps to return the cardiac output to normal. This condition is adequate to sustain a person who remains quiet, although chest pain may persist.

The sudden loss of supply to a portion of the myocardium will result in the death, or infarction of that region. However, the body implements immediate corrective action and a new collateral blood supply will begin to penetrate the peripheral regions of the infarcted area, which often allows much of the muscle in the fringe areas to regain functionality. Under normal circumstances, the heart will recover rapidly during the first few days after a heart attack and will have achieved most of its final state of recovery within 5 to 7 weeks [3].

It is therefore important to be able to assess the extent of myocardial damage which has occurred during the initial stages of this process and to be able to monitor the degree of recovery. Knowledge of these factors can be used to decide what forms of treatment would be best suited to the particular patient. Currently, the majority of cardiac diagnoses' are made using ultrasound based techniques of one form or another, which come under the broad umbrella term 'echocardiography'. Such techniques are relatively cheap, safe and instantaneous when compared to the other possibilities such as Magnetic Resonance Imaging (MRI), X-Ray, Positron Emission Tomography (PET), etc. More importantly though is the fact that over the years echocardiography has been proven to be effective and has earned the trust of clinicians.

This thesis is primarily concerned with increasing the degree of quantification which is available to the clinician. Until recently, echocardiography has developed as a predominantly qualitative tool, which provides information to the user in a visual form which can be interpreted based on operator experience. More recently, there has been a drive towards more quantitative systems, which would provide the user with accurate measurements of specific quantities. The aim of this is to improve the accuracy and repeatability of diagnoses made and to a lesser extent, to reduce the level of operator experience required. In order for such an improvement in quantification to take place it will be necessary to increase our understanding of the optimum signal processing techniques, such that the maximum amount of information can be extracted from the returned signals.

Much has been published recently describing the results of using a new form of quantitative Doppler tissue imaging, called strain, strain-rate or velocity gradient imaging. Strain imaging is based on measuring the velocity gradient between two points and using this value to derive a value for the strain. The original velocity estimates on which this technique is based are made using the existing Doppler tissue imaging technology, however it appears that very little attention has been paid to the accuracy of this underlying technique. As with any method which is derived from the result of another, there is a danger that initially small errors may become more significant through compounding.

## 1.2 Aims and Objectives

The aims of this thesis are therefore two fold, firstly to investigate how accurate the underlying technique of Doppler tissue imaging is and secondly to investigate whether more modern signal processing techniques could be used to improve the processing of the returned signals, with a view to improving overall quantification. The second of these two objectives incorporated a wider investigation into the possible application of two modern signal processing techniques, namely the fractional Fourier transform and empirical mode decomposition, which prior to this work have not been applied to the field of medical ultrasound.

The accuracy with which velocity estimations could be made using the conventional techniques of Doppler tissue imaging was investigated using a combination of a simple rotating phantom arrangement with a custom developed, single crystal ultrasound system and a series of computer simulations generated using the Field II ultrasound simulation engine.

These two arrangements were also used to investigate the possibility of implementing a more advanced velocity estimator of the form of a correlation model based technique, which had the potential to offer greater spatial resolution coupled with greater accuracy of the estimated velocities.

The fractional Fourier transform represents a generalisation of the conventional Fourier transform which offers significant benefits when combined with linear frequency-modulated signals. Such signals have been shown in the literature to offer benefits in terms of maximising the available imaging depth without having to increase the peak transmitted power, which has significant safety implications.

Empirical mode decomposition is a technique for breaking a signal down into a series of intrinsic mode functions which have well defined instantaneous frequencies at each point. This technique was used to demonstrate a new interpretation of the process of non-linear acoustic wave propagation.

## 1.3 Contributions

The original contributions made within this thesis can be summarised as follows:

- The development of a simple, open, single crystal ultrasound system for the analysis of ultrasound signal processing techniques, including the use of approximately linear, frequency modulated chirped signals.
- A thorough analysis of the accuracy of time-domain correlation based Doppler tissue

imaging, including analysis of the sensitivity to noise based on a combination of results from the single crystal ultrasound system and the Field II ultrasound simulation engine.

- Demonstration that the use of correlation model based techniques for velocity estimation can provide an order of magnitude improvement in velocity estimation accuracy along with a significant improvement in spatial resolution, compared to a correlation search based method.
- Demonstration that the requirements for producing 2-D images limit the accuracy of Doppler tissue imaging to such an extent as to put into question the quantification of the results obtained and therefore argue that truly quantitative analysis should be performed using colour M-mode only.
- Application of the fractional Fourier transform as an effective method for processing the received echo signals resulting from the transmission of approximately linear, frequency modulated chirp signals.
- Demonstration that the fractional Fourier technique is able to offer spatial resolutions equivalent to those obtained with matched filtering without the need for a-priori knowledge of the transmitted signal or the transducer.
- Derivation of a method for directly relating the position of features in the fractional Fourier transform domain to the corresponding position in the time domain.
- Demonstration that using this method allows the fractional Fourier transform based technique to give results which are equivalent to matched filtering in terms of axial resolution, but which offer significantly reduced range side-lobes for the same transmit signal apodization.
- A new interpretation of the phenomenon of non-linear propagation of acoustic waves based on the combined techniques of empirical mode decomposition and the Hilbert spectrum.

The investigation into the accuracy of Doppler Tissue Imaging (DTI) demonstrated that the accuracy of the velocity estimations is currently limited by the desire to have 2D images. Obviously, 2D images are preferable because they enable easy understanding of the geometry being inspected, however this limitation has been shown to be of clinical significance because it reduces the reproducibility of the results obtained from secondary measurements such as strain or strain rate. The complex cross-correlation model based velocity estimator is shown to offer an order of magnitude improvement in accuracy, but at the cost of requiring more temporal domain samples to produce the velocity estimates. It would not be possible to use this method for producing 2D images of the velocities, unless the segment size width was very small, but it would work very well for interrogating a single spatial line. It is argued that in order to improve the reproducibility of the results, it would be worth sacrificing the 2D images in favour of this more accurate approach.

The use of the fractional Fourier transform, combined with the technique of coded excitation was investigated and it was shown that this technique could be successfully used to gain a significant improvement in the spatial resolution. The problem of measuring velocity is intimately related to measuring position, since velocity is simply the rate of change of position. Therefore, a more accurate measurement of position could lead to more accurate velocity estimations. Also, the use of coded excitation allows longer signals to be used without sacrificing spatial resolution. This allows for imaging at greater depths because it is possible to transmit with a higher average energy. Simply increasing the amplitude of the transmitted signal increases the peak power, which has been shown to have possible health and safety implications. Therefore, being able to increase the imaging depth by only increasing the average power has obvious advantages. The fractional Fourier transform is shown to be able to offer the same degree of pulse compression as the more conventional matched filtering approach, but without the need for a-priori knowledge of the transmitted signal and with significantly lower range side-lobes.

The combined techniques of empirical mode decomposition and the Hilbert spectrum were used to demonstrate an alternative interpretation of the process of non-linear wave propagation. It has been shown that the propagation of acoustic waves with pressures and intensities of those used in the field of medical ultrasound and echocardiography is highly non-linear. In the past, Fourier based methods have been used to analyse these signals and this has led to the notion that the distortion caused by the non-linear propagation causes signal energy to be transferred into the frequency bands which correspond to the harmonics of the fundamental, transmitted frequency. The new results presented in this thesis clearly show that that spreading of energy into the harmonic frequencies is a result of the use of Fourier based methods of analysis and is not related to a physical phenomenon. The new interpretation offered is that the effect of the non-linear distortion is to introduce an intra-wave frequency modulation. Currently, ultrasound scanners produce images based on the amplitude modulation of the wave cause by the medium through which is has passed. The new results clearly show that this amplitude modulation is only half of the picture and in reality, the medium through which the wave is passing is also modulating its frequency.

## 1.4 Organisation of Thesis

The organisation of the remainder of this thesis is as follows: Chapter 2 provides a basic insight into echocardiography and the use of Doppler ultrasound. Chapter 3 describes the methods used for collecting data, including the development of the single crystal ultrasound system. Chapter 4 describes the experiments for determining the accuracy of the current techniques for Doppler tissue imaging and presents results obtained using these and correlation model based techniques. Chapter 5 introduces the fractional Fourier transform and presents results obtained, while Chapter 6 introduces the technique of empirical mode decomposition and presents results obtained. Finally, Chapter 7 contains the overall conclusions. It should be noted that throughout the thesis various symbols have been chosen to be consistent with the literature. In some cases, this means that a particular symbol will have multiple definitions. Reference to the nomenclature section should clarify the meaning of a particular symbol with respect to any of the chapters.

# Chapter 2
# Introduction to Echocardiography

## 2.1 The Heart and the Myocardium

The heart is a hollow muscular organ whose purpose is to pump blood around the body. Generally, it is about 10 cm long and its overall size is roughly the same as the owners fist. The heart is slightly heavier in men than in woman, but generally weighs about 225 g. The position of the heart in the body relative to the other organs may be seen in Figure 2.1, which clearly shows that the heart is situated in the middle of the chest, slightly to the left of centre.

The heart itself consists of four chambers; the left and right atria and the left and right ventricles. When the heart is beating, blood passes from the superior and inferia vena cava into the right atrium. From here, it passes into the right ventricle, from which it is pumped into the pulmonary artery. It then passes through the lungs, absorbing oxygen before ending up in the left atrium. From here, it passes into the left ventricle from which it is pumped into the aorta and on to the rest of the body. Both sides of the heart operate simultaneously so that blood is continuously moved from the right side to the left side via the lungs. Figure 2.2 shows the exterior anatomy of the heart and the location of the ventricles.

The heart itself is constructed from three distinct layers, the epicardium which forms the outer layer, the myocardium which is the muscle which actually makes the heart beat and the endocardium, which lines the inside of the ventricles and atria. The myocardium is constructed from smooth muscle, which is different from the muscle used to construct normal muscles in that the muscle fibres are smaller and more tightly packed. Also unlike other muscles in the body, the myocardium is not under control of the will, but is part of a closed, self-regulating system. It constitutes most of the heart and is thickest at the apex and thinest at the base. Since it is a muscle, it needs to be supplied with oxygen via the blood as any other muscle. This is achieved via the coronary arteries, which mostly lie on the surface of the heart, but perfuse into the myocardium at key points. The heart muscle is actually unable to absorb any significant amount of oxygen from the blood within the heart, so it is entirely dependent on these arteries for it's supply of oxygen.

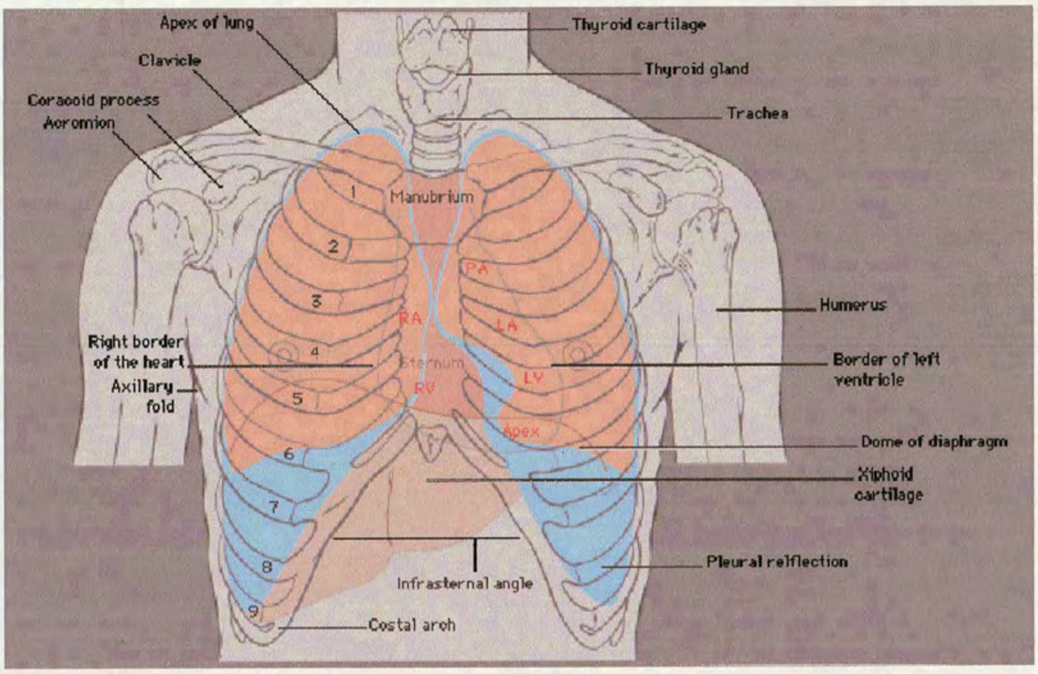

**Figure 2.1:** *Illustration of the location of the heart within the body [1].*

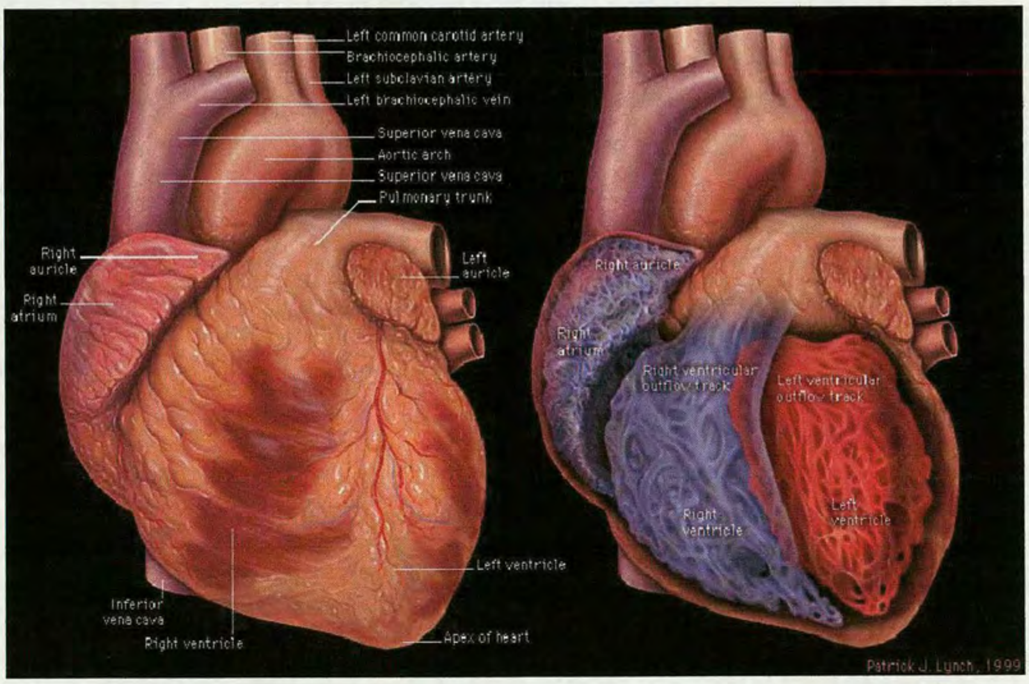

**Figure 2.2:** *Illustration of the exterior anatomy of the heart [1].*

## 2.2 Echocardiography

Despite ultrasound having been used as early as the first world war, the development of the technique as a diagnostic tool in medicine is a relatively recent one. As early as 1929, ultrasound was used as a method for detecting flaws in metals, however, further developments did not occur until after the second world war. During the war, ultrasound was used extensively in the form of SONAR for the detection of underwater objects, mostly submarines. Because of the situation at the time, information about these techniques was classified and the engineering skills and parts were not available. However, by the late 1940's and early 1950's, numerous investigators were applying ultrasound to investigate almost every organ in the body [4].

In 1950, W.D.Keidel attempted to use ultrasound to measure the volume of the heart. His method involved using a separate transmitter and receiver, positioned on opposite sides of the body, but was ultimately unsuccessful. In 1953, Inge Edler (a physician) and C. Hellmuth Hertz (an engineer) performed the first echocardiogram, which they termed *ultrasound cardiography.* They achieved this using a borrowed SONAR machine which was designed for identifying flaws in the hulls of ships. This technique differed from the approach used by Keidel in that the ultrasound equipment detected sound reflected from structures within the body, rather than detecting the sound which had passed through. This work formed the basis of echocardiography as it is used today.

The field of echocardiography has advanced significantly since then. Today, it is established as one of the principal medical imaging modalities used in cardiology, although its use is not exclusively limited to this field of medicine. The original work described above used a system based on a single element transducer, which would produce a trace on an oscilloscope which a well trained clinician would be able to interpret. This form of ultrasound is called 'A-Mode', or Amplitude-Mode, because it displays the amplitude of the received signal against time. This was later extended to 'M-Mode' or Motion-Mode, which records multiple 'A-Mode' lines together giving information about the position of structures in the body with time.

Figure 2.3 shows an example of an A-Mode scan, which is simply a plot of the envelope of a signal against time, as would be observed on the screen of an oscilloscope. In this form, it is obviously quite hard to determine the anatomy that is being looked at and it would take a great deal of experience to be able to understand and interpret this form of display. Figures 2.4 and 2.5 show examples of M-Mode scans which are formed by plotting a series of A-

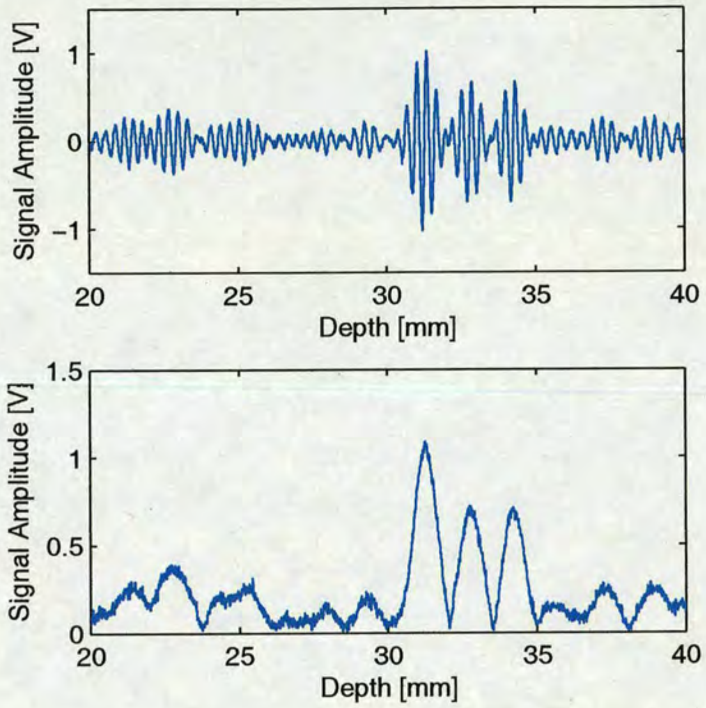

**Figure 2.3:** *Example of an A-Mode scan. The top portion shows the original signal, as would be seen on an oscilloscope, while the lower part shows a plot of the envelope of this signal, as would be seen on an A-Mode ultrasound machine.*

Mode lines together such that it is possible to observe how they change over time. In this case, the horizontal axis is time and the vertical axis is depth. The grey-level is determined by the magnitude of the signal envelope. Figure 2.4 shows how an original M-Mode scan would look, whereas Figure 2.5 is representative of how an M-Mode scan would look on a modern scanner. The main difference is the addition of a two dimensional B-Mode image from which the user can define the particular line from which the M-Mode display is generated.

'M-Mode' ultrasound persisted in echocardiography for some time since it was relatively easy to make quantitative measurements from the results obtained, which is important for making the correct diagnosis. However, although 'M-Mode' is still used today it is gradually being surpassed by real-time 2D imaging, although it is likely that it will persist in some form because it has a couple of advantages. Firstly, it allows changes of position with time to be observed very clearly and secondly it allows the ultrasound information to be easily combined with other physiological data, such as ECG traces. This makes it relatively easy to understand what the heart was doing at each particular stage of the M-mode recording.

The first attempts to produce 2D ultrasound images of the heart were done using a 1D sys-

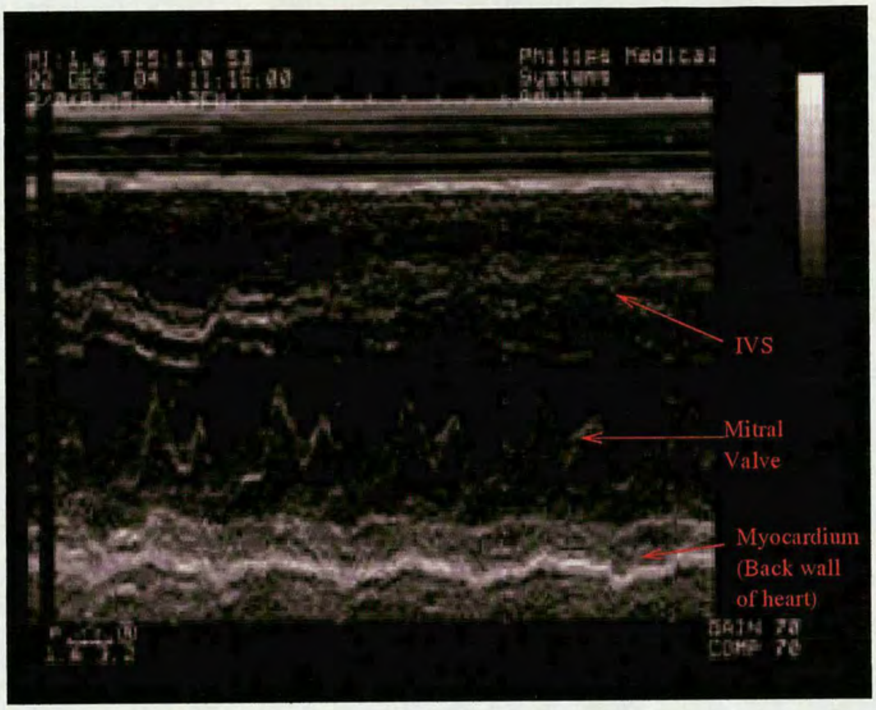

**Figure 2.4:** *Example M-Mode image*

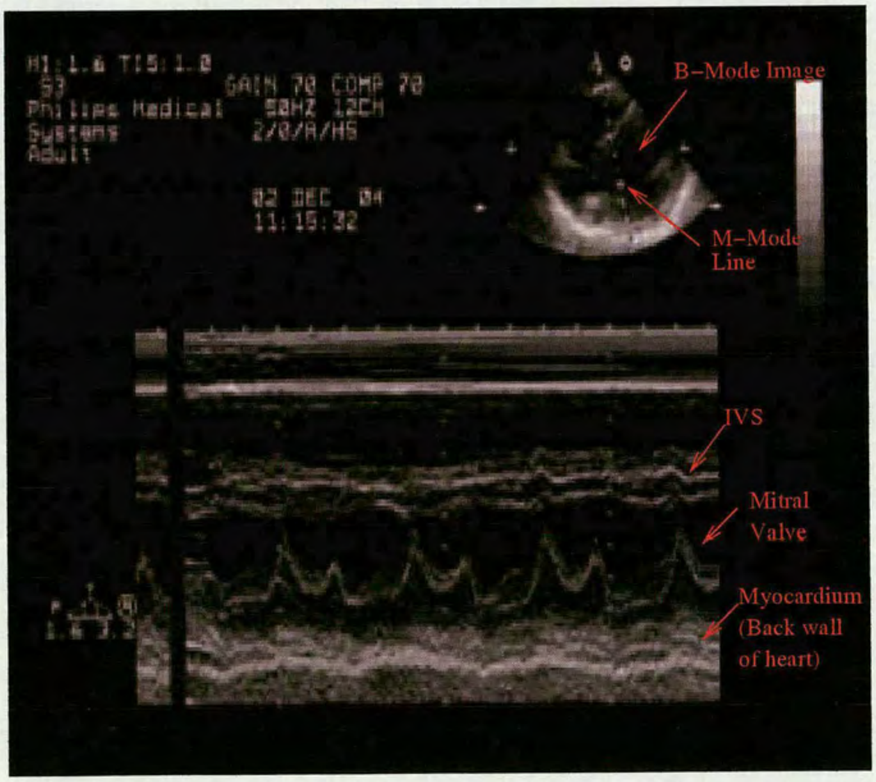

**Figure 2.5:** *Example of M-Mode on a modern clinical scanner*

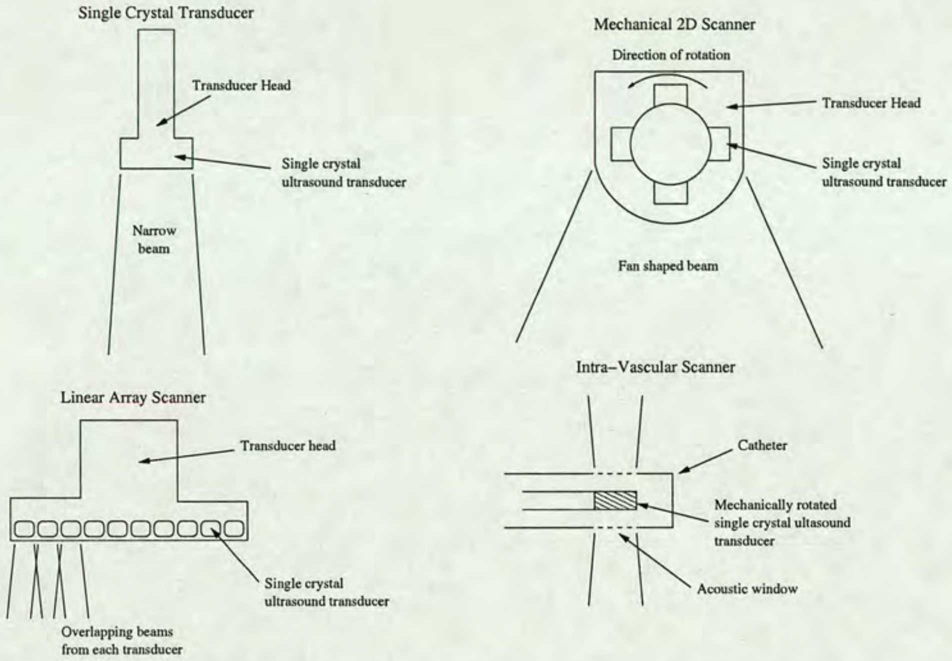

**Figure 2.6:** *Illustration of the four main types of medical ultrasound transducers*

tem, as described above, but with cardiac gating and position sensing such that as the operator moved the transducer around the lines were stored in the correct orientation such that a 2D image was eventually built up. However, the technique really became useful with the advent of real-time 2D imaging. Originally, this worked with a mechanically rotated transducer designed to sweep a beam across the region being imaged, thus allowing a 2D image to be built up. Today, mechanical scanners are hardly ever used, although they still do find applications in intra-vascular ultrasound where the transducer is required to be of very high frequency and as small as possible. Modern ultrasound machines used phased-array transducers, which may typically have 128 or so elements arranged in a linear array. Such an arrangement coupled with modern signal processing techniques make it possible to electronically steer the beam over a range of angles, thus forming a 2D image. Linear array transducers are also used without the phased-array technology and as such operate essentially as a collection of single-crystal ultrasound scanners arranged next to each other. These transducers do not require as much signal processing to operate as the phased-array type, which means they are capable of achieving higher frame rates. The differences between the four main types of transducer described above are illustrated in Figure 2.6, while an example echocardiogram showing the main anatomical features of the heart may be seen in Figure 2.7.

More recently, these techniques for forming two-dimensional images from ultrasound signals

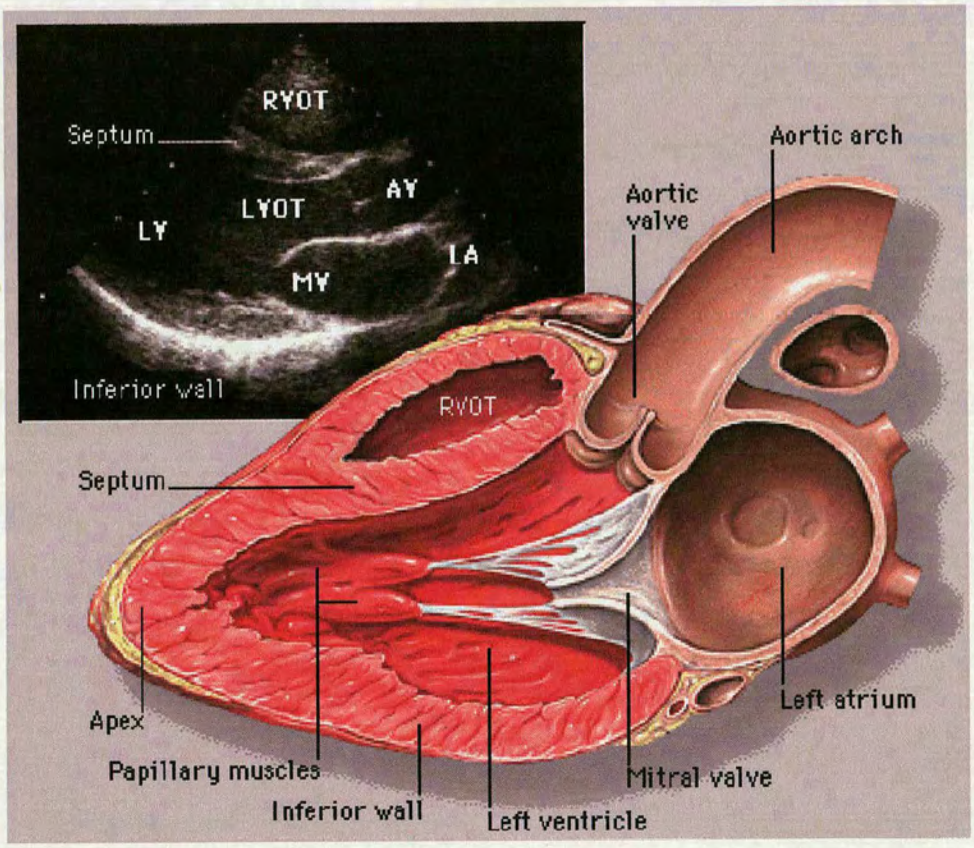

**Figure 2.7:** *Example echocardiogram showing left parasternal, long-axis view [1].*

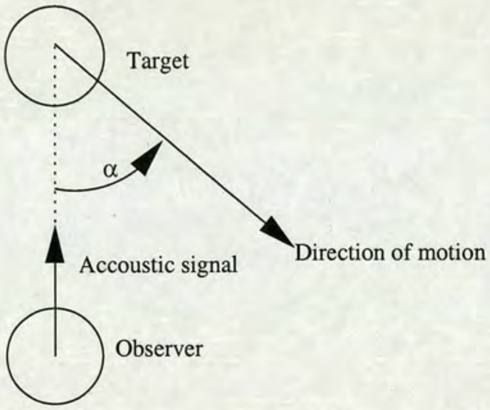

**Figure 2.8:** *Illustration of the Doppler angle, $\alpha$.*

have been extended into three dimensions and some modern ultrasound scanners now support this feature which allows them to produce three- dimensional 'models' of various anatomical features.

## 2.3 Doppler Ultrasound

The Doppler effect, first described by Christian Andreas Doppler (1803 - 1853), [5], describes how the observed frequency of sound from a moving source depends on the speed and direction of the movement relative to the observer. In the field of medical ultrasound, the Doppler effect cannot be used exactly as described because the elements being observed do not spontaneously emit ultrasound. Rather, the sound is transmitted into the body and the frequency of the returned echoes may be analysed to determine information about the Doppler shift incurred due to motion of the reflecting and / or scattering elements. The velocity is related to the Doppler shift by the Doppler equation 2.1:

$$v = \frac{c}{2\cos\alpha}\frac{f_s}{f_c} \tag{2.1}$$

Where $c$ is the speed of sound in the medium, $\alpha$ is the angle of motion with respect to the sound beam, $f_s$ is the Doppler shift which was measured and $f_c$ is the carrier, or centre frequency of the original signal. The meaning of the angle $\alpha$ is illustrated in Figure 2.8.

The first use of Doppler ultrasound for medical applications was described by Satomura [6] and Franklin et al. [7]. The latter of these works describes a system whereby separate transmitting and receiving transducers are used, arranged such that some of the scattered signal will be received at the receiving transducer. Franklin et al. demonstrated the ability of this setup to measure the speed of flowing blood by observing the change in frequency of the received signal compared to the transmitted signal.

Since the system described by Franklin et al. [7] transmits and receives continuously, it is an example of a continuous wave (CW) Doppler system. Modern Doppler systems may be broadly categorised into two types, continuous wave and pulsed wave (PW). The latter is more recent, but both have their own advantages and as such it is common to find that modern scanners still support both types. The PW systems operate by transmitting a short pulse in the same manner as for ultrasound imaging systems and in this way allow the use of time-of-flight principles to determine depth. In this manner it is possible to use the PW Doppler system to examine signals from a specified depth within the body, by gating the received signal at the appropriate time. The time between the transmission of the pulse and the receive signal gating determines the depth at which the signal will be analysed, while the time the gate is left 'open' for combined with the beam width and the transmit pulse length determines the size of the sample volume. In general, there will be more than one moving scatterer within the sample volume and these will usually be moving with a range of velocities. Therefore, the received signal will contain a spectrum of frequencies, the bandwidth of which depends on the velocities being measured and the sample volume size.

As well as the distribution of the velocities within the sample volume, the bandwidth of the returned signal will also be affected by intrinsic spectral broadening, which will result in an increased bandwidth even if there were only one scatterer in the sample volume. Initially, this was thought to be down to two different effects, one caused by the change of angle between the direction of motion and the ultrasound beam as the scatterer traverses the sample volume, which was termed geometrical broadening. The other effect was thought to be caused by the amplitude modulation caused by the finite transit time of the scatterer through the sample volume, which was termed transit time broadening. Griffith et al. [8] and Newhouse et al. [9] studied the effects of transit time broadening while Newhouse et al. [10] studied the effects of geometrical broadening. However, Newhouse et al. [11] later showed that these two effects were actually the same.

One method for displaying this information is in the form of a 'sonogram', which is essentially nothing more than a spectrogram of the Doppler signals. When presented in this manner, the display shows not only the peak and mean velocity within a sample volume, but also the bandwidth of the signals gives some information about the distribution of velocities in the sample

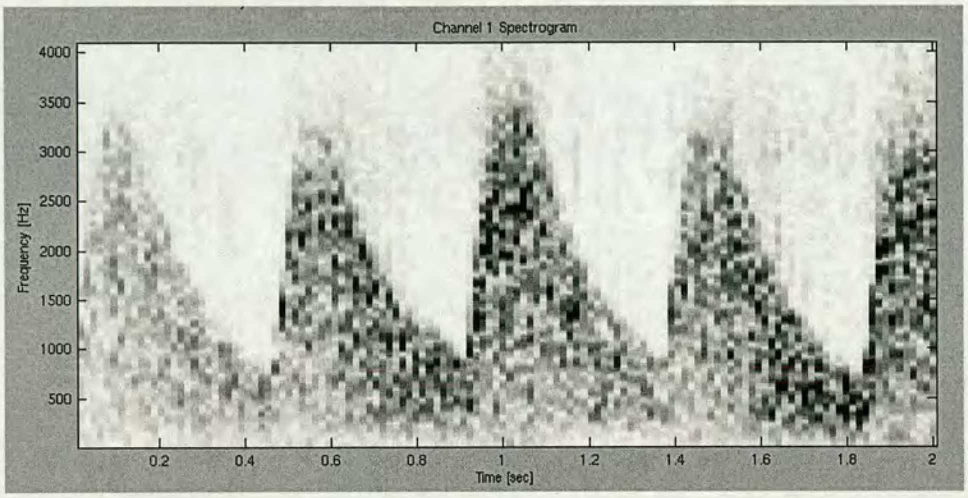

**Figure 2.9:** *Example sonogram, generated from the signal received from blood flowing through the umbilical cord.*

volume, although this will be corrupted to some extent by the intrinsic spectral broadening effects described above. Figure 2.9 shows an example of such a sonogram.

Alternatively, by gating the signal over a number of different depths and combining this with beams from a number of different directions, it becomes possible to estimate the velocities over a 2D area. These velocities can then be put together to form a 2D image, which forms a technique called Colour Flow Imaging. This technique allows many complex flow situations to be visualised, such as the motion of blood around the carotid bifurcation and the movement of blood through the heart. In general, this image would be colour coded, with one set of colours showing motion towards the transducer and another showing motion away from it. Clinical scanners will usually overlay the colour flow information onto the grey scale image and usually allow the user to define a region of interest in which the velocity estimations will be made.

Figure 2.10 shows a colour M-Mode image which was generated using Doppler ultrasound. Here, areas which are coloured red are moving towards the transducer, while those which are coloured blue are moving away. The precise shade of the colour gives information about the magnitude of the velocity. This image demonstrates how it is possible to observe the movement of the various anatomical features of the heart and to determine the magnitude of the velocity with which they are moving. It is not possible with the Doppler ultrasound technique to be able to determine the angle of the motion with respect to the transducer and this can cause problems because the velocity measured by the Doppler method is highly angle dependent due to the $\alpha$ term in equation 2.1.

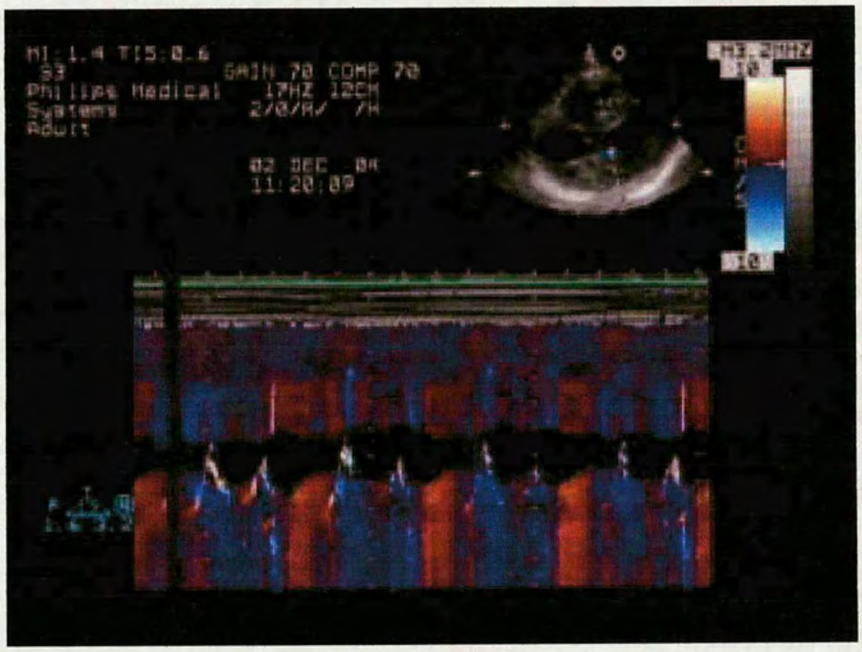

**Figure 2.10:** *Example of colour M-Mode*

# Chapter 3
# Data Collection

## 3.1 Introduction

It would appear the the only previous work done on the assessment of the accuracy of tissue Doppler imaging, Fleming et al. [12], has been done using velocity information derived from the colour images produced by the scanner and captured using a digital frame-grabber to transfer the images onto a computer. This form of off-line analysis has been described and verified by Zuna et al. [13] and Criton et al. [14]. The technique is based on comparing the colour of the pixels in the image with the colour scale produced by the scanner to determine the velocity. According to the manufacturers of the scanner used in each case, this colour bar gives a linear relationship to the velocity. Although such a technique is undoubtably of value for the assessment of the performance of a particular scanner it does not offer an overall picture of the performance of the technique of Doppler tissue imaging in general. The reason for this is that it does not allow the effects of factors such as the sample volume size, pulse length or pulse repetition frequency to be determined easily.

In this light, it was decided that it would be better to take a lower level approach and use raw, unfiltered, radio-frequency signals. The thinking behind this was that these signals would not have been subject to any unspecified signal processing and it would therefore be possible to use them to assess the actual signal processing techniques rather than a manufacturers specific implementation. Many clinical scanners provide outputs of the in-phase and quadrature-phase Doppler signals, which result from a pulse-wave Doppler scan. However, these signals have been demodulated within the scanner and have therefore been subject to a fair degree of signal processing. Owing to commercial constraints, the manufacturers of the clinical scanners are generally reluctant to reveal the exact nature of the signal processing they use, since perceived image quality is one of the main areas in which they compete. Therefore, it was concluded that these signals would not be suitable.

Some scanners also allow access to the radio-frequency signals, either in digital or analogue form. These have obviously been subjected to less signal processing and therefore are more suitable than the demodulated signals. For this thesis, a Philips SONOS 5500 clinical scanner was available which had been modified to allow access to the 'raw' RF signals in digital form. The use of this equipment will be described in more detail in the next section, but there were two limitations to the use of these signals. Firstly, they had still been subject to a degree of 'black-box' signal processing and secondly it was still not possible to have complete control over factors such as the pulse length, pulse repetition frequency or the packet size.

It was therefore decided that for a complete, low-level approach to this problem it would be necessary to develop a custom ultrasound system which allowed complete control over all stages of the signal path and performed no signal processing prior to digitisation of the signals. This system is described in more detail in the next but one section. Since it allowed complete control over every part of the system, it proved invaluable for the assessment of more advanced ultrasound techniques such as chirp coded excitation.

## 3.2 Clinical Scanner Data

Data were collected from an Philips Sonos 5500 clinical scanner, which was modified to allow the extraction of raw RF signals. All of the data presented here were collected using an S3 probe, which is a 128 element phased array transducer. A phased array transducer was chosen over a linear array transducer because the fan shaped image allows more of the heart to be examined through the space between the ribs.

The modification allowed the raw RF signals to be captured digitally to a dedicated PC. This was significantly superior to obtaining an analogue output from the scanner and re-capturing this using a data capture board, since the latter method would introduce more noise into the signal. A set of Matlab software was supplied by Philips to allow the resulting data files to be read and analysed. The capture process was controlled by the supplied software running on the PC and this allowed the user to specify how many frames of data would be captured and when the capture should be initiated. The rate at which the frames were produced was the same as the frame rate of the scanner, which was highly dependent on the scanner settings in use at the time.

Once the resulting data was read into Matlab [Version 6.5, The MathWorks, Inc], it was of the form of a structured array, which could be broken down into a series of 2D arrays, each containing all of the lines from a particular frame. Example images produced directly from the 2D

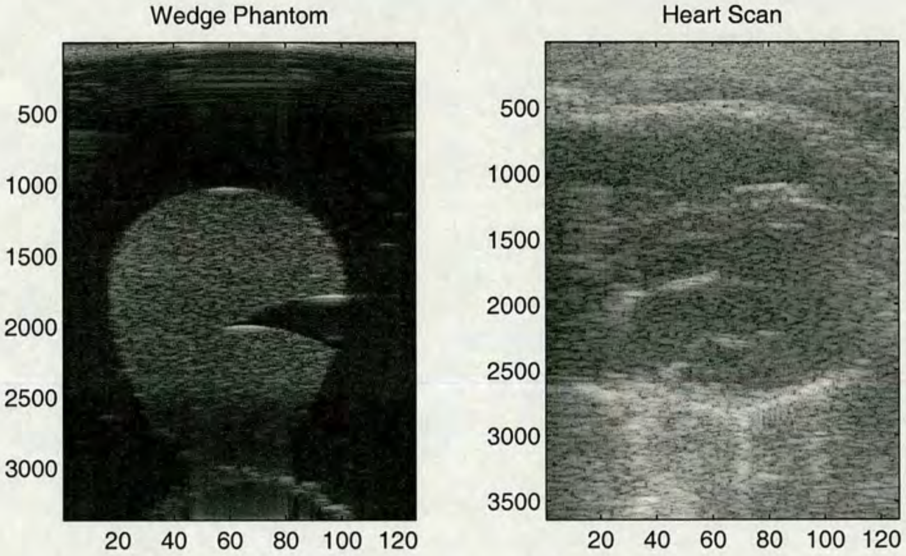

**Figure 3.1:** *Example images produced from raw RF signals captured directly from the clinical scanner. Left: Image of a phantom in a tank of water. Right: Image taken from an actual heart scan.*

arrays may be seen in Figure 3.1, where the image on the left shows a simple wedge phantom, which was made of tissue-mimicking material and immersed in a tank of water, while the right hand image is from an actual heart scan. These images were produced without performing any additional signal processing on the RF signals, which is the cause of the poor quality of the image from the heart scan. Usually, clinical scanners use advanced signal processing techniques, such as tissue harmonic imaging (described in detail in Chapter 6) which produce much clearer images for display during a scan. The raw RF signals may be extracted by simply taking single lines from the 2D array, an example of which may be seen in Figure 3.2 which shows a portion of the 80th line from the wedge phantom data. The apparent level of quantisation in these signals was taken to indicate that the scanner was only using an 8-bit ADC, which would limit the dynamic range of the signals.

As already mentioned, the transducer used for this work was of the phased array variety, which had a fan-shaped beam, as illustrated in Figure 2.6. Therefore simply displaying the 2D data in the form of a rectangular image will result in a distortion. To overcome this, Matlab software was written to transform the 2D data array into the correct, fan shaped viewing geometry. Applying this code to the images shown in Figure 3.1 gave the results shown in Figure 3.3, from which it may be observed that after correcting the geometry, the edges of the wedge in the phantom image are straight, which reflects the nature of the phantom.

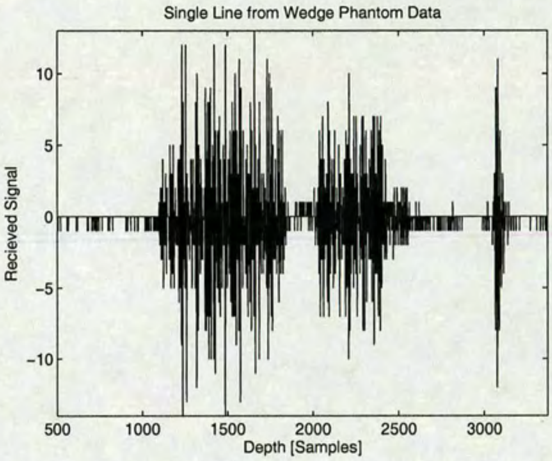

**Figure 3.2:** *Single line from the wedge phantom data set.*

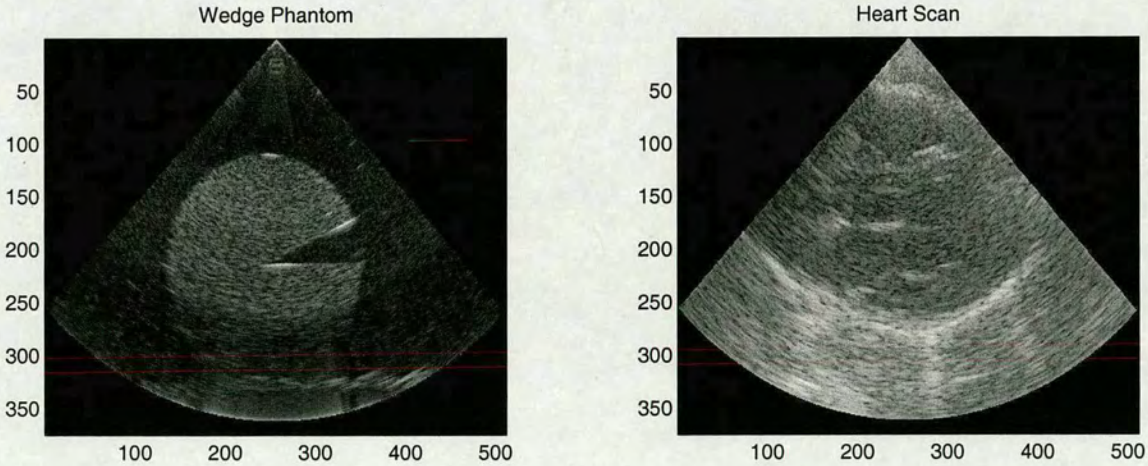

**Figure 3.3:** *Viewing geometry corrected images.*

## 3.3 Development of Single Crystal Ultrasound System

As it was not possible to know exactly what signal processing the clinical scanner was performing prior to the signals being available, it was decided that it would be necessary to have a more open system which would allow more complete control over the signals at every stage of the process. To this end, a single crystal [1] ultrasound system was developed. The use of a single crystal transducer eliminated the need for complex beam-forming hardware, although the disadvantage of this approach was that it was not possible to produce images in the manner that was possible with the clinical scanner.

### 3.3.1 Hardware

The system was mostly based on readily available off-the-shelf hardware and was arranged as illustrated in Figure 3.4. The signals which were transmitted were produced using a TTi TG1334 programmable function generator. These signals were amplified with a EIN 240L RF power amplifier with a 50 dB gain and a maximum frequency of 10 MHz. The programmable function generator was capable of producing signals of higher frequency than 10 MHz, but the bandwidth of the RF power amplifier limited what could be achieved. The connection between the RF power amplifier and the transducer / receiver amplifier was made using the circuit shown in Figure 3.5. This was necessary to protect the input of the receiver amplifier and to block low level noise from the source. D1, D2, D3 and D4 were all 1N4148 high conductance fast

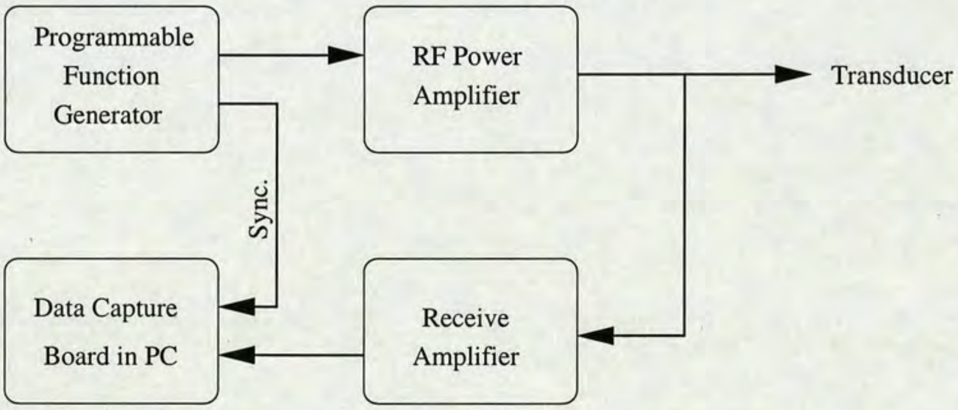

**Figure 3.4:** *Schematic of single crystal system hardware.*

---

[1] In this case, and for the remainder of this document, the term 'single crystal' is used to refer to a transducer which contains only one ultrasound producing / receiving element which need not be manufactured from a single piezo electric crystal.

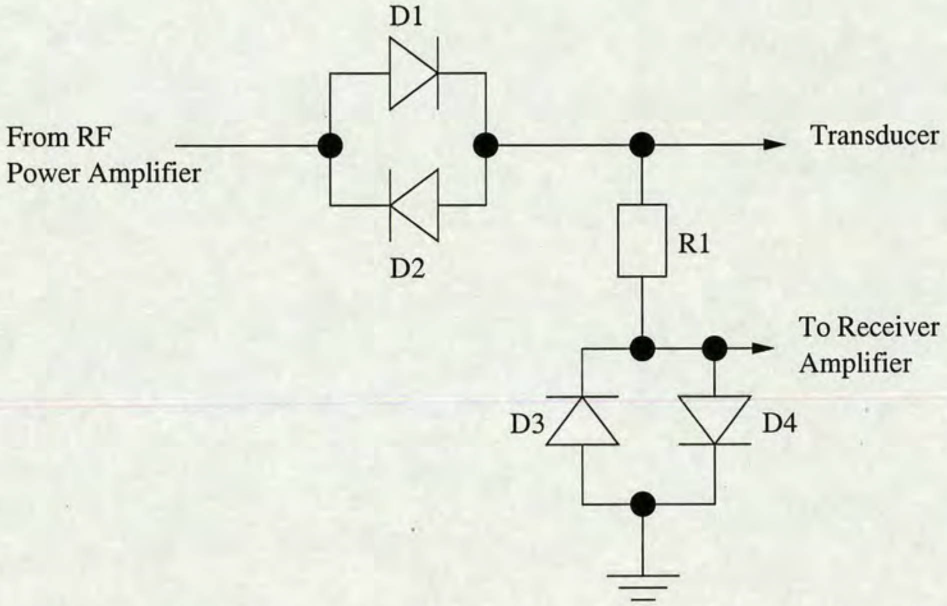

**Figure 3.5:** *Circuit for input level protection of the receive amplifier*

switching diodes, which were rated for an average forward current, $I_f = 200\ \mathbf{mA}$. R1 was chosen to limit the current through D3 and D4, but as this system was designed to operate with very short transmitted signals, it was possible to exceed the average forward current rating of the diodes. The value of R1 used was 68 Ω.

Initially, the receiver amplifier design was based on the Analog Devices AD605 wide-band amplifier chip, which is specifically designed for ultrasound applications. This device contained two separate amplifiers, each with a maximum gain of 48 dB, which could be cascaded together to achieve a total maximum gain of 96 dB. The quoted bandwidth of the device was 40 MHz, well above the maximum bandwidth achievable with the rest of the system. The AD605EB evaluation board was used to test the suitability of this device, however it was found that although the performance of the AD605 device itself was probably suitable for this application, the evaluation board failed to be adequate due mainly to noise susceptibility. It was felt that this was due to the design of the evaluation board since it was made to be as general purpose as possible and therefore had many features which were unnecessary for this application. Unfortunately, there was insufficient time to develop a custom board for the AD605 device, so an alternative amplifier was found in the form of a custom made, field-effect transistor (FET) based design. The gain of this amplifier was tested by using the programmable function generator to provide a 2.5 MHz, 10 mVp-p sine wave to the input. Under these conditions, the output was 17.5 Vp-p, which gave a figure for the gain of 65 dB. The noise floor was observed

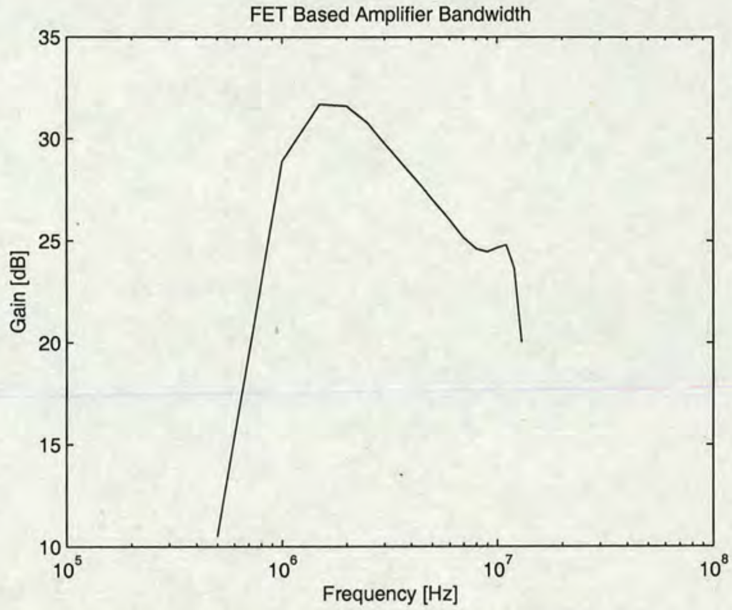

**Figure 3.6:** *Plot of the frequency response of the FET based amplifier*

to be around 1 mVp-p, which with the maximum output signal of 17.5 Vp-p, gave a dynamic range of 85 dB. Using the same method, the dynamic range of the AD605 based amplifier was observed to be only 47 dB, indicating the superiority of the FET based design. The bandwidth of the amplifier was measured by using the programmable function generator to supply a 10 mVp-p signal over a range of frequencies. The resulting frequency response of the amplifier may be seen in Figure 3.6. Inspection of these results revealed that the 3 dB bandwidth of the amplifer was approximately 2.5 MHz, which was not as high as would be ideal, but it was the best that was available at the time.

The signals were captured using a Signatec PDA12 capture board, which was of the form of a PCI card which could be inserted into a standard PC. This device allowed sampling rates of up to 50 MSamples/sec on two channels with 12 bit accuracy. The board was configured with 1.5 MBytes of RAM, which allowed 1048576 samples to be captured. This equated to 524288 samples per channel, which at a sampling rate of 50 MHz, gave a maximum recording time of 10.5 ms. Assuming the sound was travelling through water with a velocity of 1480 m/s, this gave a maximum depth of 7.75 m, which was well above anything that would be required in the medical ultrasound context. For most of the work presented here, only 8192 samples were captured from each channel, giving a maximum depth of 121 mm, which was more than adequate. An example signal from this system may be seen in Figure 3.7. This signal was captured from the same wedge phantom seen in the left hand image of Figure 3.1 and the

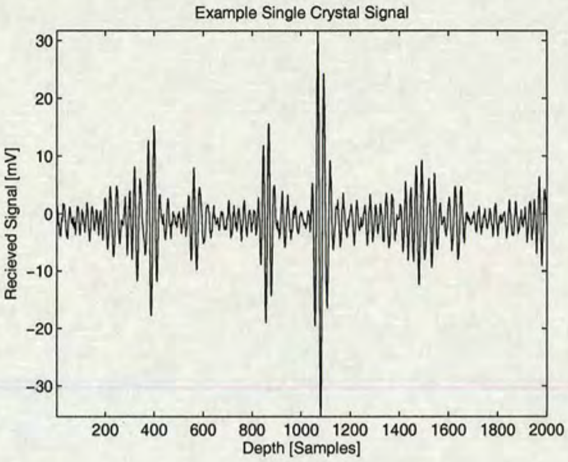

**Figure 3.7:** *Example signal from the single crystal system.*

cut-out of the wedge may be seen after a depth of 800 samples, extending to 1100 samples. The decrease in signal quantisation brought about through the use of a 12 bit ADC in the data capture card is immediately obvious in comparison with the signal from the clinical scanner shown in Figure 3.2.

### 3.3.2 Transducers

The inherent flexibility of the system developed allowed it to be used with more or less any single crystal ultrasound transducer. All of the work presented was performed using one of a selection of three different transducers. Two of these were custom manufactured by GE Panametrics, with centre frequencies of 3.5 MHz and 6 MHz respectively and a diameter of 1 inch. The third was a 2.25 MHz centre frequency, pencil probe with a diameter of 13 mm. The two Panametrics transducers both had a focal depth of 50 mm, whereas the pencil probe had an unknown focal depth. The two Panametrics transducers had a bandwidth of 100 %.

### 3.3.3 Software

For most of the work presented, the software supplied with the data capture card was sufficient. This was of the form of a sample application, which gave a number of oscilloscope like features. Once captured, the data were stored in ASCII format which could be easily read into Matlab for further analysis.

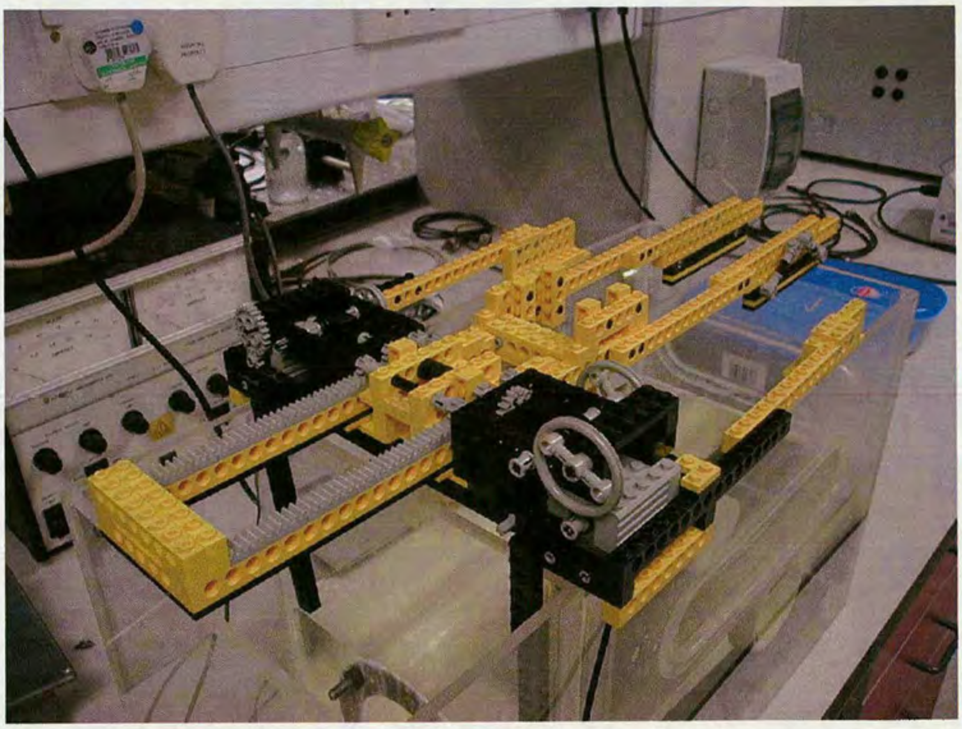

**Figure 3.8:** *Photo of the mechanical scanner used to allow the single crystal ultrasound system to capture 2D images.*

### 3.3.4 Mechanical Scanner

Since the standard single crystal system was only capable of capturing signals from a single line, a mechanical 'scanner' was constructed from Technic Lego [Lego UK Limited. Captial Point, 33 Bath Road, Slough, Berks. SL1 3UF, UK] which would allow the transducer to be scanned over a phantom such that a series of lines could be captured to form a 2D image. The 'scanner' was designed to fit over the phantom tank, as illustrated in Figure 3.8. Ideally, the transducer drive mechanism should have been made using a stepper motor, which would have made it possible to move the transducer along in discrete steps. This was not possible within the time constraints of this project, so a continuous motion design was used instead. The disadvantage of this was that it meant that the transducer would be moving while it was receiving the echo signal. To counter this, the scan speed was kept low so as to minimise the resulting distortion. The number of lines captured during the scan was controlled by varying the pulse repetition frequency of the transmitting system. Despite these rather rough approximations to the ideal system, it was still possible to obtain good results, an example of which is illustrated in Figure 3.9.

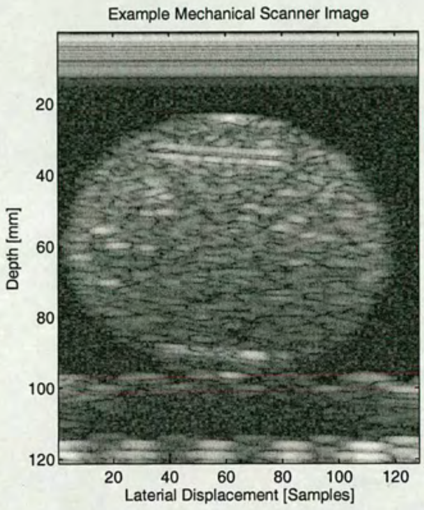

**Figure 3.9:** *Example image created using the mechanical scanner with a simple phantom.*

## 3.4 Summary

The issues surrounding the type of signals used and the method of their capture have been discussed. Ultimately, raw RF signals, captured from both a Philips SONOS 5500 clincal scanner and from a custom developed single crystal ultrasound system, were chosen to be used. The development of the latter has been described and example signals from both systems have been presented. A mechanical scanner was also constructed to allow the single crystal system to capture two-dimensional images.

# Chapter 4
# Doppler Tissue Imaging

## 4.1 Introduction

The concept of Doppler ultrasound has already been introduced in the form of colour flow imaging which allows the flow of blood within the body to be visualised. This technique requires a high-pass filter be used to remove the high amplitude, low velocity signals which result from the tissue, otherwise these would over-power the low amplitude, high velocity signals from the blood. Doppler Tissue Imaging (DTI) is a technique which allows the motion of tissue structures within the body to be visualised and this can be implemented by simply removing the high-pass filter stage from a colour flow imaging system and reducing the gain.

As for colour flow imaging, the velocity information may be displayed either as a 2D image overlaid onto the normal grey scale image, or in colour coded M-Mode format. Either way, velocities towards the transducer are normally coloured in shades of red and those away from the transducer in shades of blue. The shade of the colour usually gives information about the magnitude of the velocity while the intensity can be used to give information about the signal power.

The technique was first described by McDicken et al. [15], who demonstrated that colour velocity imaging had the potential to provide information about the velocities within the myocardium and speculated that this might give insight into myocardial viability. They also showed that the velocity estimator used for colour flow imaging, as described by Kasai et al. [16], was able to provide meaningful results when used to measure the relatively slow velocities which result from the motion of myocardial tissue.

DTI offers the possibility for evaluation of regional and global myocardial function using real-time 2-D and M-Mode imaging. This also allows for improved border definition in technically difficult patients and quantification of myocardial contractility. [17]

The technique was originally intended as a qualitative aid for the study of left ventricular wall motion [17] and it has been shown that it is possible to observe differences between the velocities of normal and infarcted myocardium [18], [19], [20].

The remainder of this chapter is organised as follows: The next section describes the current status of the technique of DTI, describing the current trends in research as well as the type of performance available. The next section describes the experiment setup which was used in conjunction with the single crystal ultrasound system described earlier to measure the accuracy of the velocity estimation algorithms. Following this, the next section describes the basis of the techniques used for velocity estimation, giving reasons for the current trend toward all digital solutions. This is followed by an analysis of the performance of three different velocity estimation techniques; time-domain cross correlation, cross correlation model or correlation interpolation and the complex cross correlation model based technique.

## 4.2 Current Status

In general, all modern clinical ultrasound scanners for cardiology offer DTI facilities, although it may be under a slightly different name on different machines. Despite being widely available, up-take of the technique in the clinical environment has been slow. This is probably due to a number of reasons, but the most likely seem to be the qualitative nature of the results produced and the degree of experience required to interpret them correctly. Much research has been published detailing possible clinical applications of the technology, some of which may be summarised through the following references; Kapusta et al. [21], [22], Frommelt et al. [23], Fyfe et al. [24] and Lange et al. [25], although this is only a very brief representation.

Currently, the technique is able to offer spatial resolutions adequate for detecting anatomical features of the order of 3 × 3 mm, with frame rates of between 20 and 40 Hz [17], [20]. The temporal resolution, determined by the frame rate, is very important for being able to visualise the fast moving parts of the heart, such as the valves. These features are within the capabilities of B-Mode imaging, where the frame rates are of the order 100 frames/sec or more, but the temporal resolution of DTI is often too low to reflect the motion accurately. It is possible to achieve significantly higher frame rates and hence higher temporal resolutions by using colour-coded M-Mode since it is the requirements of forming a 2D image which are the main limiting factor.

Quantification of the results is often achieved using on-line or off-line analysis of the colour encoded Doppler images. This works by determining the colour of each pixel in a user defined region of interest and then comparing this with a colour scale to derive the velocity. This technique has been verified *in-vitro* by Fleming et al. [12] and *in-vivo* by Fraser et al. [26].

One of the problems with quantification of myocardial velocities from the Doppler tissue images is that the motion represented is not only due to the movement of the heart. As the person breaths, the heart moves around within the chest cavity, which causes a global motion of the myocardial tissue. Using conventional techniques it is not possible to subtract this global motion from the local motion which is of interest. One method for achieving this is to measure the *velocity gradient* rather than the absolute velocity. This is achieved by taking the estimated velocity at two points and using the measured distance between them to determine the gradient. Since each of the two points will be similarly affected by the global motion, it will effectively be cancelled out. The method of measuring myocardial velocity gradients was first described by Fleming et al. [27], who used colour Doppler M-Mode scans to estimate the Doppler velocity gradient and compared this with the rate of change of wall thickness calculated from conventional pulse-echo M-Mode scans. They observed statistically significant velocity gradients in all cases and verified that the velocity gradients were consistent with the wall thickness changes, suggesting that the technique had the potential for assessment of myocardial contractility. The usefulness of the velocity gradient technique for assessing myocardial contractility independently of global translational motion of the heart was demonstrated by Uematsu et al. [28]. It was also shown to be an indicator of regional left ventricular contraction by Miyatake et al. [29].

There have been a significant number of publications in recent years on the subject of myocardial velocity gradient estimation, which has become known as *strain-rate* imaging. Many of these focus on the potential clinical applications of the technique, for example: detecting ischemic myocardium by Dobutamine challenge [30]; improved assessment of myocardial viability in patients with depressed left ventricular function [31]; characterising acutely ischemic myocardium through the observation of higher strain rates during isovolumic relaxation phase than during ejection [32] and assessment of left ventricular myocardial function in congenital valvular aortic stenosis [33], to name a few.

It would appear that the velocity gradient method forms the bulk of current attempts at quantifying the technique of DTI. Nearly all of the published papers appear to use strain and strain-rate values derived from the velocity estimations made using tissue Doppler imaging, however in nearly all cases this appears to have been done with little regard for the accuracy of the underlying velocity estimations. Obviously, there is a danger that errors in these initial estimates will be propagated through to the strain estimations and may even become exaggerated through this process. As has been stated in Chapter 2, the myocardium is a complex structure consisting of multiple muscle layers which contract in different directions and are perfused by blood vessels. All of these artifacts are likely to be able to introduce error into the initial velocity estimations, for example, if the sample volume for one velocity estimation includes a perfusing blood vessel, how does this affect the estimation for that region? This is currently unknown and therefore cannot be simply dismissed as insignificant.

To this end, it was decided that it would be useful to investigate the accuracy of the underlying DTI technique. A number of techniques have been reported for the assessment of colour Doppler imaging accuracy, including string phantoms as described by for example, Philips et al. [34] or Russell et al. [35] which consist of a thin string which is driven by a stepper motor in such a way that its speed can be precisely controlled. The string is partly immersed in water, such that it intersects with the ultrasound beam at a known depth and angle. Stewart [36] however points out that string phantoms are not particularly suitable for the assessment of 2-D colour imaging systems because the moving string forms a stationary, narrow colour image that cannot be easily interpreted.

Fleming et al. [12] describe the use of two different types of phantom for investigating the efficacy of DTI. Firstly, they used a rotating phantom consisting of a metal cylinder with an attached cylinder of tissue mimicking material. The speed of rotation could be measured using an optical encoder allowing the accuracy of the velocity estimations made using DTI to be investigated. Secondly, they used a phantom consisting of two grooved sections of tissue mimicking material which could slide over each other. The purpose of this phantom was to investigate the spatial resolution which could be obtained with DTI. For the analysis of the velocity estimation accuracy of DTI, they recorded the colour images resulting from a scan of the rotating phantom and used a computer program to analyse the colour of each pixel. The actual velocities were derived by comparing these colours to the colour bar produced by the scanner as shown in Figure 2.10.

Generally, these works seem to indicate accuracies of the order of 10 %. The work in [36] demonstrates clear statistical significance of the effects due to type of transducer, Doppler angle and instrument settings. This last point may be the most important since these will vary the most from one scan to another. These figures are backed-up by Embree et al. [37] who quote the precision of the time domain correlation technique, working on raw, unfiltered signals as being around 5% to 10%.

All of this work has generally focused on the assessment of particular clinical scanners. It was felt that a study into the performance of the fundamental techniques used for velocity estimation would be more useful as this would give a more detailed overview of the issues which may affect quantification of myocardial velocities using DTI and derivative techniques. This study was performed using the single crystal ultrasound system described earlier, along with simulations, to enable complete control over the signal processing at every stage. It was decided to focus on time-domain based techniques, rather than covering all of the possible phase-domain approaches. The reasons for the slow uptake of the time-domain techniques in the clinical scanner arena is that they are more computationally expensive and it would appear that, so far at least, the equipment manufacturers have decided that there is little to be gained by switching from a phase-domain approach. However, it was felt that the time-domain techniques are able to offer certain advantages, such as being able to work beyond the Nyquist limit for example and that as digital signal processing hardware becomes cheaper, this option will become increasingly viable.

## 4.3 Experiment Setup

The experiment setup used for this study was of the form of a rotating phantom, similar to that described by Fleming et al. [12] and Miyatake et al. [19]. The phantom itself consisted of a cylinder constructed from tissue mimicking material which was attached to a plastic cylinder of the same diameter. This setup was driven, via a gear box, by a DC motor. The gear box was necessary because the motor would be unable to rotate smoothly at the low rotational speeds required to mimic the motion of the myocardium. The drive shaft of the motor was also connected to an optical encoder consisting of a disk with 360 slits which allowed light from and infra-red L.E.D. to pass through. This device produced two signals, one $90^o$ out of phase with the other, which would enable the direction of rotation to be determined. For this study, it was not necessary to detect the direction of motion, so only one of the outputs was used. This signal was used to drive an off-the-shelf frequency counter, which gave a measure of the speed of rotation of the motor and hence the phantom itself. The rotating phantom was designed to fit into a hole molded into an additional block of tissue mimicking material, which formed the

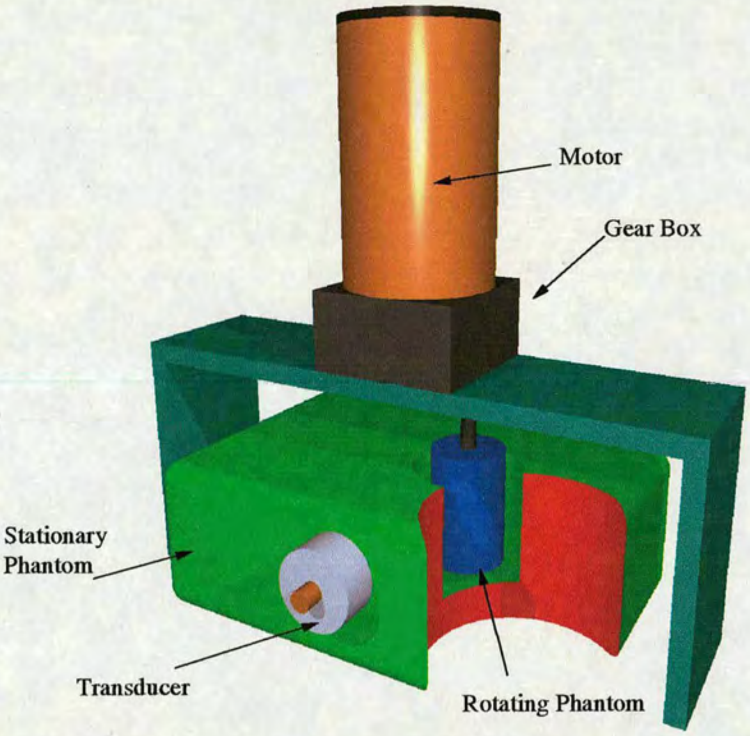

**Figure 4.1:** *Illustration of the rotating phantom setup used for this study.*

stationary part of the phantom. The whole experiment setup is illustrated in Figure 4.1, while the dimensions of the entire setup are shown in Figure 4.2.

The nature of the rotating phantom arrangement is such that the component of the velocity parallel to the ultrasound beam will be constant with depth. This is a simple result of the geometry of the situation, as illustrated in Figure 4.3.

A standard clamp and stand combined with a micro-manipulator was used to enable the transducer to be moved around the edge of the stationary phantom accurately. Although it was possible to have 3 degrees of freedom with this setup, only lateral motion across the width of the phantom was used. In this manner it was possible to use the single crystal system to obtain a single line signal from any lateral displacement across the phantom, allowing the whole width of the rotating portion to be used. The transducer could be aligned with the centre of the rotating phantom by adjusting the position until the echoes from the edges of the phantom were of the maximum strength. At this position, the edges would be perpendicular to the beam from the transducer, which causes them to give the strongest reflection. This method was verified by estimating the dimensions of the phantom from the received signal, which may be seen in Fig-

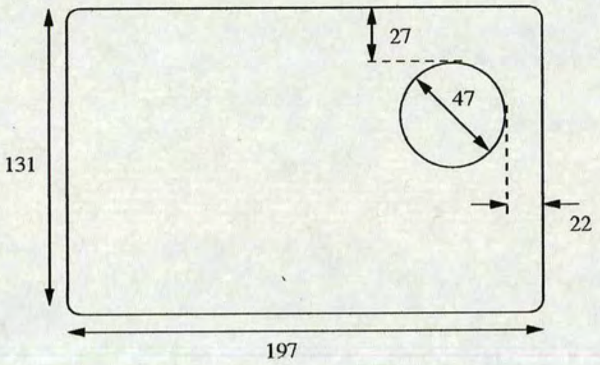

**Figure 4.2:** *Overall dimensions of the phantom setup used. Dimensions are shown in mm, diagram is not drawn to scale.*

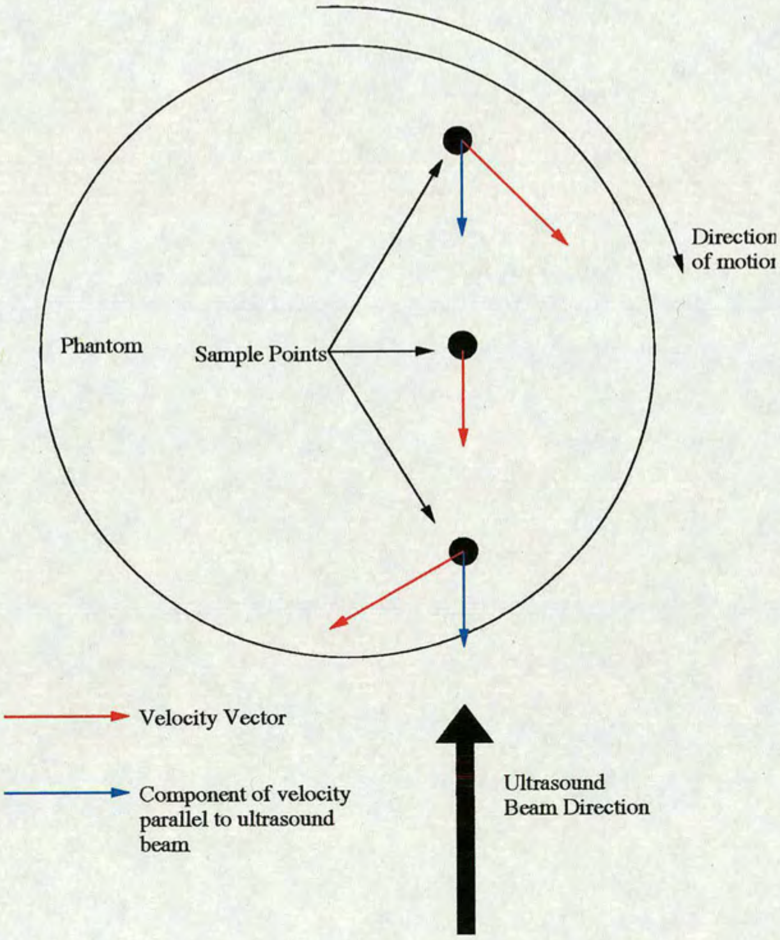

**Figure 4.3:** *Illustration of the rotating phantom geometry showing how the component of the velocity parallel to the ultrasound beam will be constant with depth.*

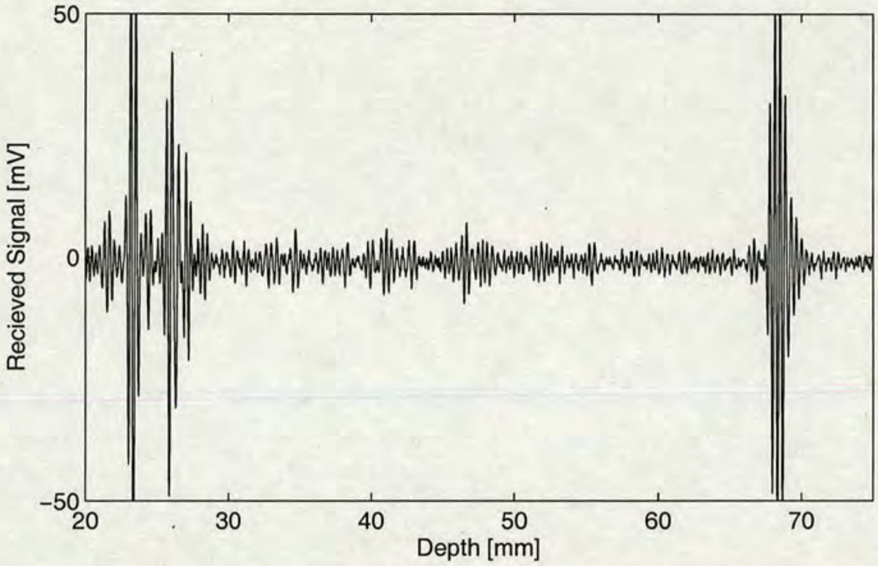

**Figure 4.4:** *Received echo signal demonstrating the technique for locating the centre of the rotating phantom.*

ure 4.4, where the distances were calculated assuming a velocity of sound of 1480 m/sec. The first large peak occurs at a depth of 23 mm, which was suitably close to the measured phantom dimensions. The location of the second peak, which corresponds to the water/tmm interface with the rotating part of the phantom indicated a distance of 3 mm between the rotating and stationary parts. The last peak occurred at a depth of 68 mm, which again correlated well with the measured dimensions. In this case, the rotating part of the phantom was orientated such that the wedge did not intersect with the ultrasound beam.

The rotating phantom was operated such that it would provide velocities within the range of 0 mm/sec to 50.3 mm/sec. It was observed from the literature that normal myocardial velocities are within this range [21], [26], [38] and [39].

Whilst the single crystal ultrasound system allowed complete control over most of the relevant factors, it was subject to a fixed signal-to-noise ratio (SNR). Therefore, in order to investigate the performance of the various velocity estimators in terms of the SNR, it was necessary to be able to produce signals with known SNRs. This was achieved using the Field II ultrasound simulation tool, developed by Jensen et al. [40], [41], [42]. The simulation was designed to reflect the physical rotating phantom as closely as possible. A scatterer density of 10 per cubic wavelength was used, giving a total of $1 \times 10^6$ scatterers for the rotating part and $6.4 \times 10^6$ for the stationary part, for a 2.25 MHz signal. The computational requirements of these simulations

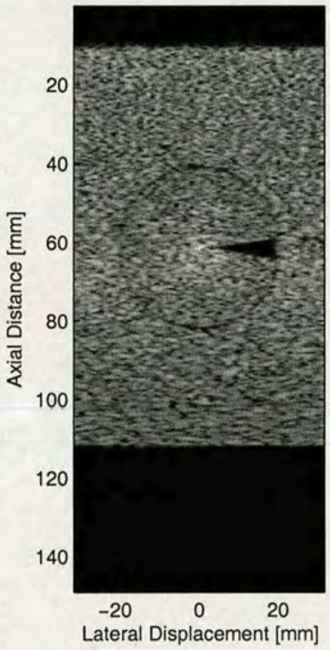

**Figure 4.5:** *Simulated phantom, produced using the Field II ultrasound simulation tool. Clearly shows how it was possible to create a simulation which closely matched the physical phantom.*

were very large, taking approximately 2 days to complete a simulation of a single line through the phantom over 64 frames, running on four 2.0 GHz Intel Xeon processors. The model was designed to have identical dimensions to the physical phantom, including an identical wedge cut-out. It was also designed to have a 1 mm gap between the rotating part of the phantom and the stationary part. A simulated overall view of the model may be seen in Figure 4.5. Note that the simulation was created using a model based on a 64 element linear array transducer, which was deemed to be suitably equivalent to a single crystal transducer being used at 64 different displacements over the width of the phantom. The centre of the simulated phantom was located at a depth of 60 mm, which was different to the dimensions of the physical phantom, however this was not felt to be significant in any way as the simulation engine used did not allow for depth dependent effects such as attenuation or spectral broadening.

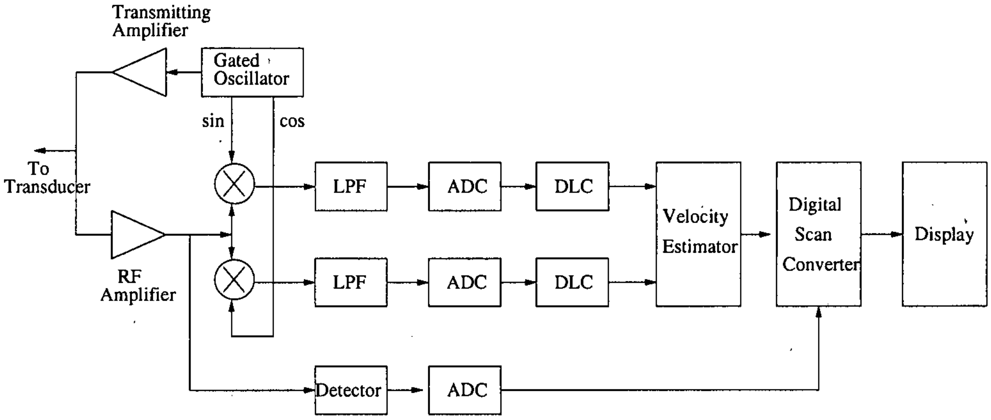

**Figure 4.6:** *Simplified schematic of a phase-domain velocity estimating system. The upper two signal paths are for the velocity estimation, which colours the image, while the lower signal path is for the grey scale, B-Mode image. LPF = Low Pass Filter, ADC = Analogue to Digital Converter, DLC = Delay Line Canceller. [43]*

## 4.4 Velocity Estimation

### 4.4.1 Phase Domain versus Time Domain Techniques

Low frequency, base-band or phase-domain velocity estimation techniques all utilise demodulation to shift the received RF signal down to the baseband, such that the remaining frequency content corresponds to the Doppler shift experienced by the signal. In general, all such systems operate in the manner illustrated in Figure 4.6 [43]. The basic principle of operation is that the received signal is split into two, forming two signal paths. Each of these is demodulated by multiplying the received signal by the transmitted signal, although one path is multiplied by a $90^o$ phase-shifted version. These are then digitised by the ADC and then they are passed through a delay line canceller (DLC), the purpose of which is to remove any stationary signals which would otherwise obstruct the blood flow estimations. These signals then pass to the velocity estimator, which will usually estimate the mean frequency of the signals which gives the velocity information.

For a pulse-wave Doppler system, some form of spectral analysis technique, such as the FFT or an autoregressive modelling approach is used to form a spectrogram of the demodulated signals. However, in order to have enough samples to get a good frequency resolution in the resulting spectrum, this technique can only operate on fairly large regions of interest.

When it is necessary to create a two dimensional image, as in the case of Doppler tissue imaging, the velocity estimator used does not perform full spectral analysis of the signals, but will use some form of spectral estimation technique. There are three main reasons for this, firstly that when colour flow imaging was first introduced, the hardware for performing real-time FFTs of signals did not exist. Secondly, the frequency resolution obtainable using the FFT is the reciprocal of the length of the data segment being analysed, so for example using a 1 ms window would limit the frequency resolution to 1 kHz. The third reason is due to the problem of displaying the vast amount of data which would result from a full spectral analysis. In practice, the user only needs to know the mean or maximum velocity within a particular sample volume and therefore much of the full spectral analysis data would be redundant. Even though a number of phase domain algorithms for estimating the frequency have been suggested, the autocorrelation technique was the first and remains the most widely used [43].

This technique was originally described by Kasai et al. [16] and is based on the principle of transmitting a number of pulses in each direction and then using the Wiener-Khinchine theorem to relate the autocorrelation of a number of these signals at a fixed depth to the power spectrum. Once an estimate of the power spectrum has been derived, this can be used to form an estimate of the mean frequency.

The basis of the autocorrelation method is that the instantaneous angular frequency of a signal is related to the instantaneous rate of change of phase:

$$\omega = \frac{\mathrm{d}\phi}{\mathrm{d}t} \approx \frac{\phi_i - \phi_{i-1}}{T} \tag{4.1}$$

Where $\phi_i$ and $\phi_{i-1}$ represent the instantaneous phase of the signal at two different samples. The tangent of the required phase difference, $\phi_i - \phi_{i-1}$ could then be written as a ratio of sine and cosine terms:

$$\begin{aligned} \tan(\phi_i - \phi_{i-1}) &= \frac{\sin(\phi_i - \phi_{i-1})}{\cos(\phi_i - \phi_{i-1})} \\ &= \frac{\sin\phi_i \cos\phi_{i-1} - \cos\phi_i \sin\phi_{i-1}}{\cos\phi_i \cos\phi_{i-1} - \sin\phi_i \sin\phi_{i-1}} \end{aligned} \tag{4.2}$$

Of course, the sine and the cosine terms relate to the in-phase ($I$) and quadrature-phase ($Q$) signal components, hence an average frequency may be calculated by summing over a number of pulse pairs:

$$\bar{\omega} = \frac{1}{T}\tan^{-1}\left[\frac{\sum_{i=1}^{n} Q(i)I(i-1) - I(i)Q(i-1)}{\sum_{i=1}^{n} I(i)I(i-1) + Q(i)Q(i-1)}\right] \tag{4.3}$$

Radio-frequency, or time-domain methods work directly with the received RF signals and do

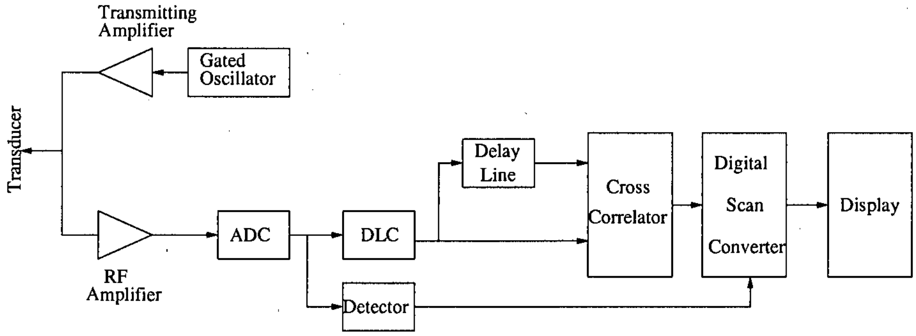

**Figure 4.7:** *Simplified schematic of an RF, or time-domain, velocity estimator. The upper signal path is for the velocity estimation, whereas the low path is for producing the grey scale, B-Mode image. ADC = Analog-to-Digital Converter, DLC = Delay Line Canceller. [43]*

not actually use the Doppler effect at all. As a result of this there has been much discussion about whether systems based on such techniques should be referred to as Doppler systems, but it is probable that the name will remain out of convention. A simplified schematic representation of a time-domain velocity estimation system may be seen in Figure 4.7. These systems work by determining the time-shift, or lag, between two signals by locating the maximum of the cross-correlation function of the two signals [43].

One of the main differences between the two systems is that the time-domain system samples the raw RF signals directly, before any other signal processing is performed. This is important because once the signals have been digitised, any further processing will not introduce more noise. Once the signal has been digitised, it is passed through a delay line canceller, which removes the components of the signal which correspond to stationary tissue structures. The signal is then split into two, one part goes directly to the cross-correlator, while the other part goes to a delay line. The purpose of the delay line is to store the entire received signal such that the cross-correlator receives both the current signal and the previous signal.

It appears that there has been a general trend towards all digital systems, with offerings from both GE [44] and Philips [45]. Although there is little information available regarding the actual velocity estimation techniques which are most common among the various clinical ultrasound scanners, it seems that the general approach is to use the Kasai autocorrelation algorithm. The reasons for this are that this technique is relatively computationally efficient when compared to the time domain cross-correlation approach. However, as the cost of the digital signal processing hardware decreases and the performance increases, this will become less of an issue.

Figures 4.6 and 4.7 illustrate that one of the potential advantages of moving to a time-domain based technique would be the significantly reduced component count. This could have potential benefits in areas such as reduced power consumption and overall device size, both of which are important for making smaller, more portable scanners.

A further advantage of the time-domain techniques is that the maximum measurable velocity is not limited by the sampling frequency in the same way as for the phase-domain techniques. As the later are based on estimating a frequency, they are limited because, according to the Nyquist sampling theorem, the maximum frequency which can be sampled reliably is half the sampling frequency. In this case, the sampling frequency is the PRF, so velocities which cause a Doppler frequency greater then half the PRF will be aliased. The time-domain techniques, on the other hand, are based on tracking the motion of a group of scatterers using some form of correlation technique, rather then estimating the Doppler frequency. They are, therefore, able to reliably measure velocities which would cause aliasing in a phase-domain system.

It must be noted that the above system illustrations are for colour flow imaging, which was the original application of Doppler ultrasound. In order to achieve good visualisation of blood velocities it is necessary to filter out the high amplitude signals from slow moving tissue, which is achieved by the delay line canceller in the above systems (and the low-pass filter in the phase-domain system). However, for Doppler tissue imaging, it is exactly this signal which is of interest, so the filtering stage is either removed or by-passed and the gain adjusted.

### 4.4.2 Sample Volumes

In the case of Doppler techniques, such as Doppler tissue imaging, the sample volume refers to the region from which a single velocity estimation is made. This volume has a finite size which is determined by the properties of the ultrasound beam, the pulse length and the range gating. The width of the ultrasound beam is largely determined by the properties of the transducer, in the single element case it is the diameter of the transducer and the shape of any lens at the coupling interface which will determine the beam width. The length of the sample volume may be determined by the convolution of the transmitted pulse length and the range gate length. The combination of these factors leads to the conclusion that a single velocity estimation will be the mean of the velocities of the scatterers which fall within the resulting three-dimensional volume.

This can lead to problems, since the velocities which are of interest may be masked by the velocities of other scatterers which happen to pass through the sample volume. This is particularly a problem where low velocities are to be measured, for example near to the wall in a blood vessel. In this situation it is extremely likely that the sample volume will include some of the flowing blood scatterers and some of the stationary vessel wall scatterers, which will lead to a false measurement of the velocity. In the same way, boundaries between stationary and moving tissue would also cause problems. It is well known that the myocardium consists of three muscle layers which contract in different directions, the effect of which is that each will give a different value for the velocity. Current spatial resolutions offered by TDI are of the order of 3 mm x 3 mm, which is due to the finite sample volume. Since the layers of the myocardium are very thin, it is likely therefore that each sample volume within the myocardium will contain scatterers belonging to at least two layers and which will thus contribute differently to the overall velocity measurement.

### 4.4.3 Time Domain Cross Correlation for Velocity Estimation

The first reference to the cross correlation method for velocity estimation was by Dotti et al. [46], who described the technique as a method for measuring blood flow. Bonnefous et al. [47] also describe the cross correlation technique and compare its performance with that of phase domain based velocity estimators. In particular, they noted that the cross correlation approach does not suffer from aliasing of velocities which are higher than the Nyquist limit.

As illustrated in Figure 4.7, the time-domain method uses the cross-correlation between the current and previous received signals. If these are termed $w_1(t)$ and $w_2(t)$ respectively, then the correlation of these two signals will be given by:

$$R(\tau) = \int_{-\infty}^{\infty} w_1(t) w_2(t+\tau) \mathrm{d}t \tag{4.4}$$

These two signals will be almost identical except for the second echo being essentially a time delayed version of the first, hence:

$$w_2(t) = w_1(t - t_s) \tag{4.5}$$

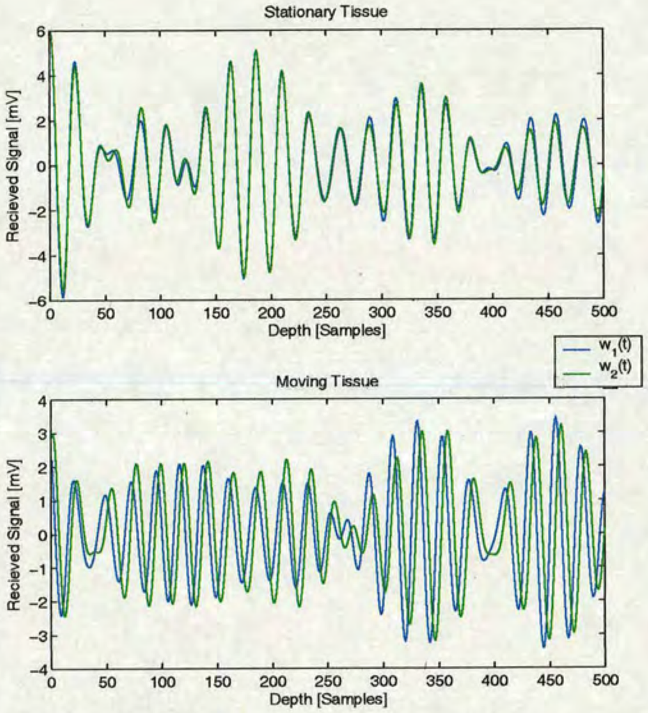

**Figure 4.8:** *Received signals after transmission of two signals, $w_1(t)$ and $w_2(t)$ separated in time by $\Delta t$, for stationary scatterers (top) and moving scatterers (bottom).*

Where $t_s$ is the time lag between them. Putting this back into equation 4.4 gives:

$$R(\tau) = \int_{-\infty}^{\infty} w_1(t) w_1(t - t_s + \tau)\mathrm{d}t = R_{11}(\tau - t_s) \tag{4.6}$$

Where $R_{11}(\tau - t_s)$ is the autocorrelation function of $w_1(t)$. This will have a maximum when $\tau = t_s$, which therefore means that the maximum of the cross-correlation of the two signals, as given by equation 4.4, may be used to determine the time shift between the two signals.

The above will work for the case when there is only one scatterer or reflector, however in the medical context at least, there will always be a large number of scatterers within any given sample volume, be it blood or tissue. Because of this and the fact that it is desirable to have information about how the velocity varies with depth, it is necessary to gate, or window, the received signals into a number of discrete sections. The cross correlation technique may then be described as:

$$\hat{\tau} = \max \int_{a}^{b} w_1(t) w_2(t + \tau)\mathrm{d}t \tag{4.7}$$

Where $a$ and $b$ are the start and finish times of the window respectively and max means to determine the value of $\tau$ for which the integral is maximised. Figure 4.8 shows an example of two received signals resulting from two transmissions separated in time by $\Delta t$. The top part of the figure shows the result for stationary scatterers, so there is no difference between the received signals. The lower part shows the result for a region of moving scatterers, which has the predicted effect of causing a lag between the two signals, which could be measured using the cross-correlation of the two signals as expressed by equation 4.7. In this case, the time between the two signals, $\Delta t$ was 6 ms, which is greater than that which would normally be used, but it provides a better illustration. The scatterer velocity was 10 mm/sec.

An analysis of the errors involved in using this method to estimate the velocity of flowing blood has already been performed by Foster et al. [48]. They derive an expression for the theoretical variance of the measured time-lag, $\tau$ about the true lag, $\tau_0$:

$$\mathrm{VAR}[\hat{\tau}] = \frac{2N_0}{\beta^2 \rho^2 E} \tag{4.8}$$

Where $N_0$ is the white noise power spectral density of each echo [W/Hz], $\beta$ is the RMS bandwidth of the received signals [rad/sec], $\rho$ is the maximum correlation coefficient of the received signals without noise and $E$ is the average energy of each range-gated echo [J]. They therefore conclude that the precision of the time-domain velocity estimate, $[\sqrt{\mathrm{VAR}(\hat{\tau})}/\tau_0]$ will be given by:

$$\mathrm{Precision}[\hat{\tau}] = \frac{\sqrt{2}}{\beta \rho \tau_0 \mathrm{SNR}} \tag{4.9}$$

Where in this case SNR is the signal-to-noise ratio defined as:

$$\mathrm{SNR} = \sqrt{\frac{N\mathrm{VAR}(s)}{\mathrm{VAR}(n)}} \tag{4.10}$$

Where $N$ is the number of samples in the range gate and $\mathrm{VAR}(s)$ and $\mathrm{VAR}(n)$ are the signal and noise variances respectively, also in the range gate.

From this, it is possible to observe that the performance, in terms of accuracy, will improve if either the bandwidth or the signal-to-noise ratio are increased.

It is likely that the implementation used in a clinical scanner will involve some form of interpolation of the cross-correlation function. The reason for this is that the velocity resolution is limited to the accuracy with which the position of the peak may be located. Since this is a discrete time system, the position can only vary by a whole number of samples, therefore, velocities which would cause the peak to shift by an amount less than this cannot be detected.

| Displacement [mm] | Actual Velocity [mm/sec] |
|---|---|
| 0 | 0 |
| 2 | 12.6 |
| 4 | 25.1 |
| 6 | 37.7 |
| 8 | 50.3 |

**Table 4.1:** *Actual velocities at the lateral displacements which were used.*

| Window Length [Samples] | Time [$\mu sec$] | Distance [mm] |
|---|---|---|
| 16 | 0.32 | 0.25 |
| 32 | 0.64 | 0.49 |
| 64 | 1.28 | 0.99 |
| 128 | 2.56 | 1.97 |
| 256 | 5.12 | 3.94 |

**Table 4.2:** *Window lengths in samples and $\mu$sec and equivalent distance at $f_s = 50 \times 10^6$ Hz and assuming velocity of sound in tissue, $v = 1540$ m/s.*

This limitation can, however, be overcome by interpolating between the samples of the cross-correlation function which allows sub-sample accuracy to be achieved.

The single crystal system was used with the rotating phantom setup described earlier to determine the actual accuracy which would be obtainable using this technique. The speed of rotation was set at 1 revolution per second, which corresponded to an encoder signal frequency of 6250 Hz. Measurements were taken at various lateral displacements from the centre, in 2 mm increments. Table 4.1 gives the actual velocities at each of the lateral displacements. The pulse repetition frequency was set to 1 kHz and the pulse length was varied between 1, 2 and 4 cycles.

Matlab code was used to emulate the action of a cross-correlation based velocity estimator, by taking windowed 'segments' of the received signals and using the cross-correlation function provided by Matlab to determine the lag between the two signals. The code used here interpolated the cross-correlation function using the Matlab 'interp' function, to interpolate the cross-correlation function by 2, 4 and 8 times. The window length used was also varied between 16, 32, 64, 128 and 256 samples, which equates to the times and distances summarised in Table 4.2. In this manner, it was possible to observe the effects that each of these independent variables had on the accuracy of the velocity estimates. The accuracy of the estimations under these varying conditions may be seen in Figures 4.9 to 4.13, where the percentage error of the estimates has been plotted against the interpolation factor, for different window lengths, pulse lengths and lateral displacements. The percentage error was calculated using the mean

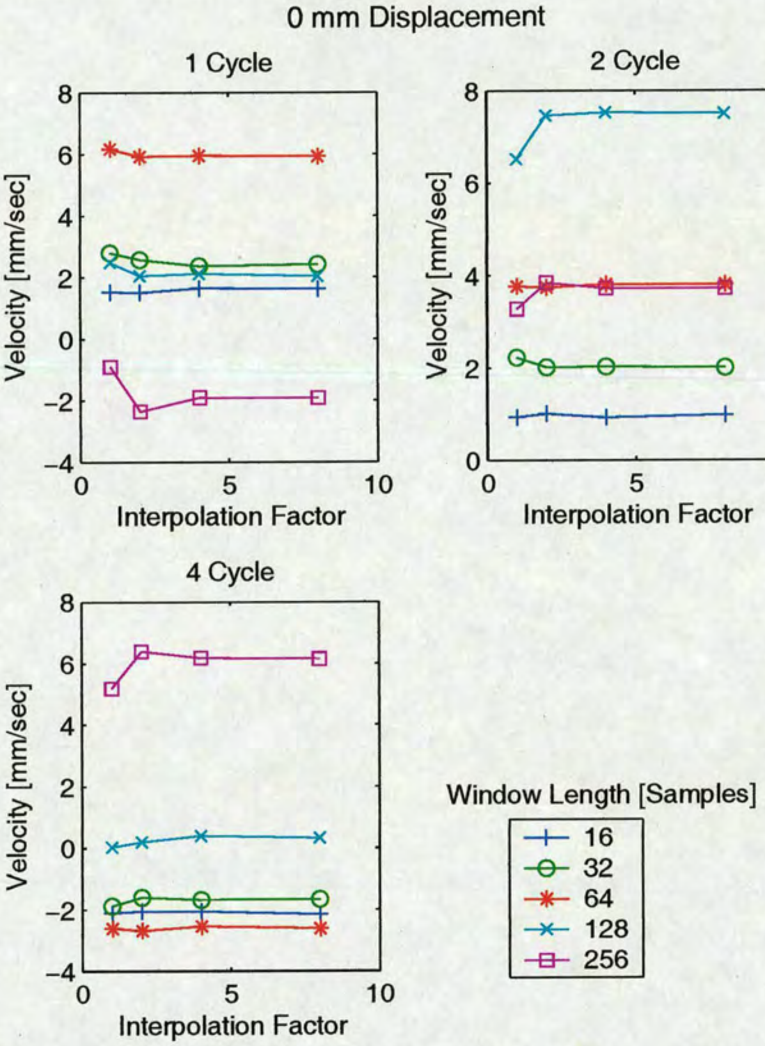

**Figure 4.9:** *Velocity estimation accuracy for 0 mm lateral displacement, showing the estimated velocity vs. the interpolation factor.*

of the estimated velocities over the region of the signal which was known to correspond to the moving part of the phantom only and was averaged over three separate tests. In the 0 mm displacement case, the percentage error would have been meaningless, so that estimated velocities were plotted instead.

From these results it was observed that the best achievable accuracy with the simple cross-correlation technique was around 10% - 15% and that the best results were, in nearly all cases, achieved with a pulse length of 2 cycles and a window length of 128 samples. Increasing the pulse length to 4 cycles or decreasing it to 1 cycle resulted in a degradation of the accuracy. This would be expected as increasing the pulse length increases the signal-to-noise ratio, but

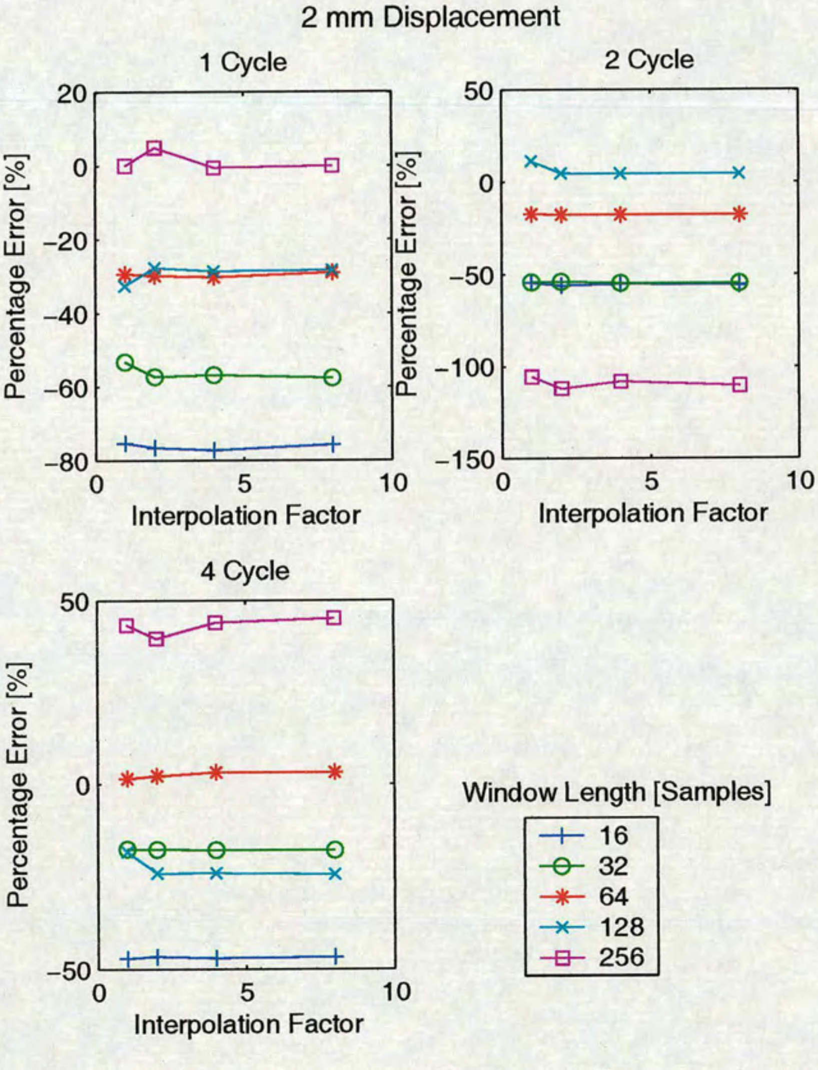

**Figure 4.10:** *Velocity estimation accuracy for 2 mm lateral displacement, showing the percentage error vs. the interpolation factor.*

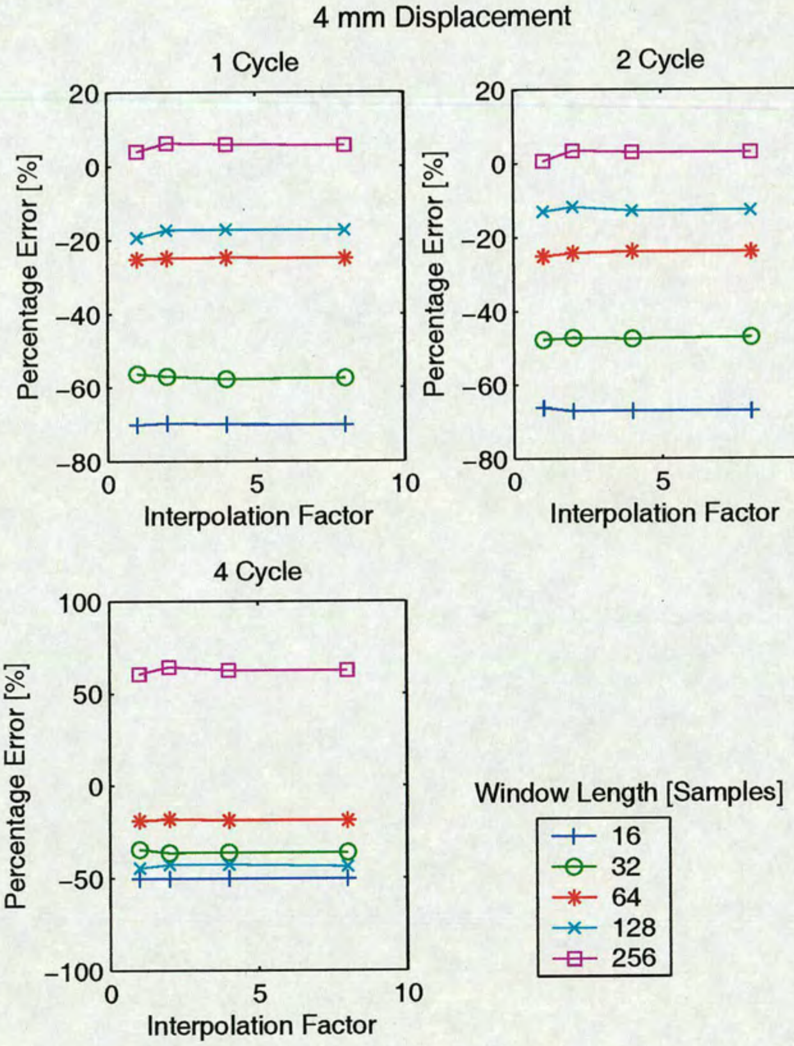

**Figure 4.11:** *Velocity estimation accuracy for 4 mm lateral displacement, showing the percentage error vs. the interpolation factor.*

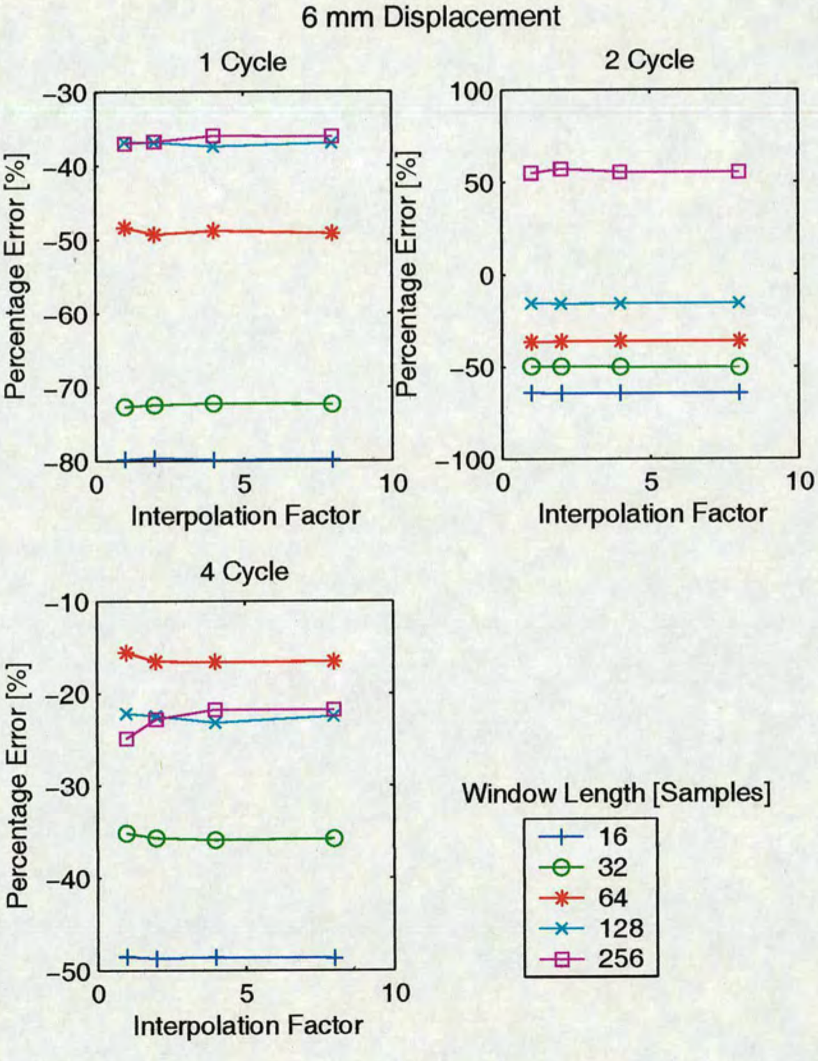

**Figure 4.12:** *Velocity estimation accuracy for 6 mm lateral displacement, showing the percentage error vs. the interpolation factor.*

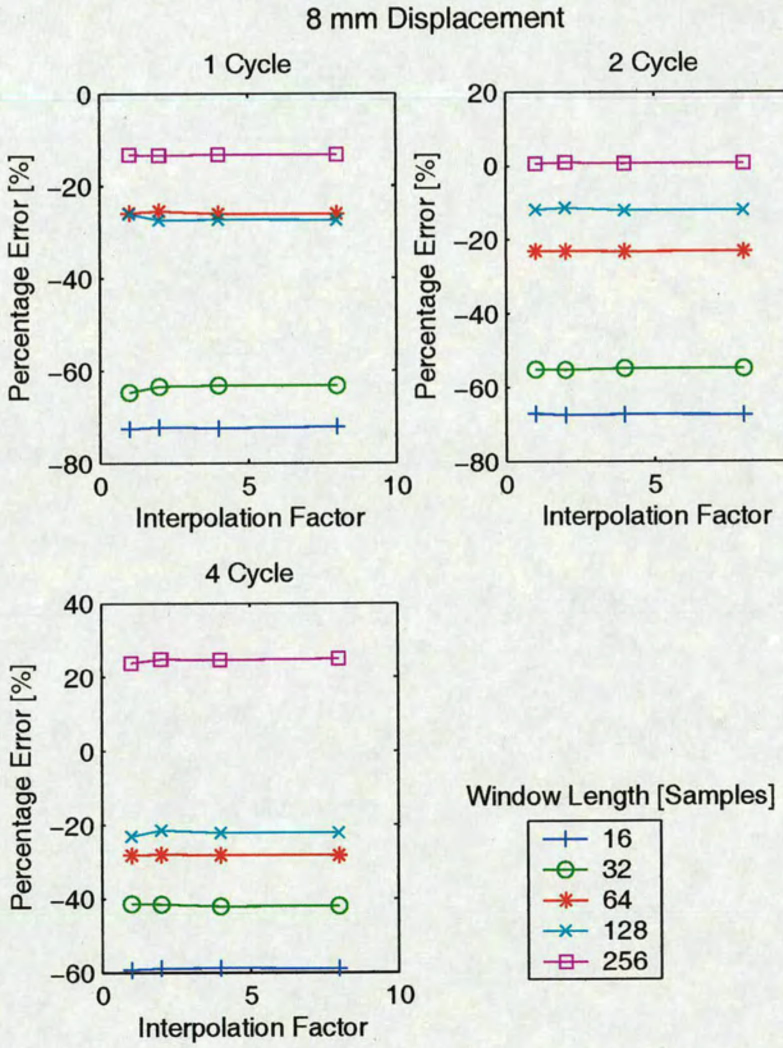

**Figure 4.13:** *Velocity estimation accuracy for 8 mm lateral displacement.*

decreases the signal bandwidth. Increasing the window length up to 128 samples improved the accuracy in nearly all cases, but a further increase to 256 samples only caused an improvement in the 4 mm and 8 mm cases with a pulse length of 2 cycles and in the 2 mm case with a pulse length of 1 cycle. As shown in Table 4.2, a window length of 128 samples equates to a distance of 1.97 mm in tissue, which effectively places a limit of 2 mm on the maximum spatial resolution which can be achieved whilst maintaining relatively accurate velocity estimates. Increasing the window length further results in an improvement in the accuracy in some cases, but this limits the spatial resolution to around 4 mm, which would be quite likely to obscure a number of anatomical features within the heart. Increasing the window length also increases the computational complexity by increasing the number of samples which need to be cross-correlated.

Using the single crystal ultrasound system alone, it was not possible to control the signal-to-noise ratio of the signals, therefore the Field II simulation engine described above was used to test this variable. The simulations were designed to match as closely as possible with the physical phantom setup and velocity profiles were obtained from lateral displacements of 0mm through to 10mm in 2mm increments, as with the physical experiments. The initial simulations results have an infinite signal-to-noise ratio, so they were corrupted with additive, white, Gaussian noise to yield SNRs in the range of 0 dB up to 100 dB in 10 dB increments. The results obtained are summarised for a range of window lengths and velocities in Figure 4.14.

As well as illustrating the significance of the window length on the resulting accuracy, these results also show that as the velocity decreases higher signal-to-noise ratios are required to maintain the same level of accuracy. In reality an ultrasound system could easily have a signal-to-noise ratio higher than 50 dB and these results show that beyond around 30 dB there is little variation. It was therefore concluded that the cross-correlation technique is relatively independent of the SNR of the signal, provided it is higher than 30 dB.

### 4.4.4 Alternative Techniques

#### 4.4.4.1 Correlation Model Based Techniques

The cross-correlation method described above used two received signals, resulting from the transmission of two separate pulses separated in time by $\Delta t$, in the same direction. This technique may be extended by increasing the number of pulses transmitted in each direction, such

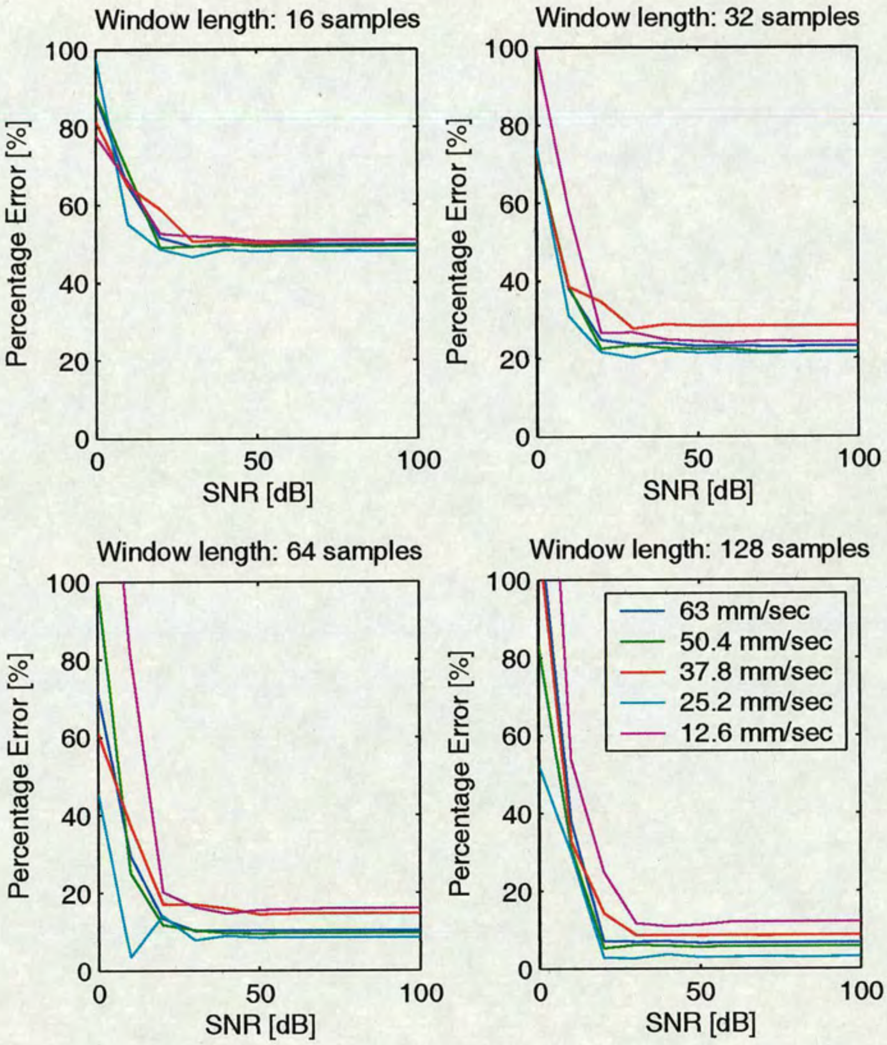

**Figure 4.14:** *Effects of signal-to-noise ratio and window length on velocity estimation accuracy. Clearly shows that lower velocities require higher SNRs.*

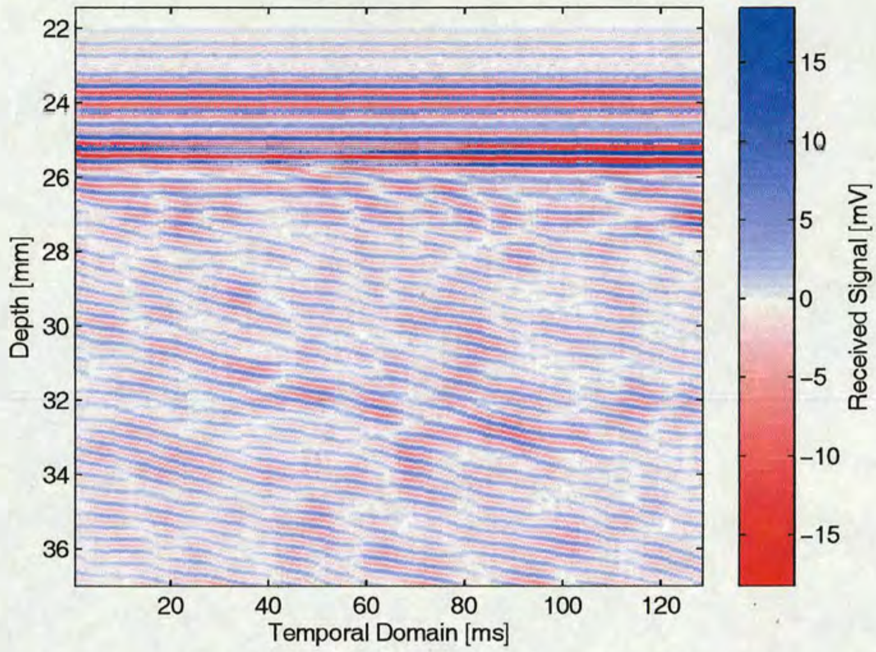

**Figure 4.15:** *Example data set illustrating temporal and spatial domains.*

that a two dimensional data set is created consisting of *temporal* and *spatial* axis which correspond to the time of the transmission, $n\Delta t$ (where $n$ is the pulse number) and depth respectively. An example of the resulting data may be seen in Figure 4.15, which was produced using the single crystal system with the rotating phantom setup. The carrier frequency was 2.25 MHz and the signals were post-processed by band-pass filtering to increase the clarity of the example. In this case, the pulse repetition frequency, $f_{\mathrm{PRF}}$ was 1 kHz and 128 transmit / receive cycles were used. Only a particular depth region of the entire data set has been shown to aid clarity, but it is possible to observe the gap between the rotating and stationary parts of the phantom at depths of 24 mm and 26 mm. The colouring has been chosen to show the peaks and troughs of the signals, blue for the peaks and red for the troughs. Therefore, signals from stationary scatterers (above a depth of 24 mm) show as horizontal lines, while the signals from moving scatterers produce diagonal lines, as would be expected. The data were collected with the transducer at a lateral displacement of 6 mm, giving a theoretical velocity of 37.7 mm/sec.

Once the data are in this format, the temporal domain signal at a particular depth will look something like either of the two examples shown in Figure 4.16, where the signals corresponding to depths of 23 mm and 28 mm have been extracted. It is clear from this that the signal from a depth of 28 mm, which corresponds to the region of moving scatterers, contains more then just noise, whereas the signal from 23 mm appears to be only noise. This was confirmed

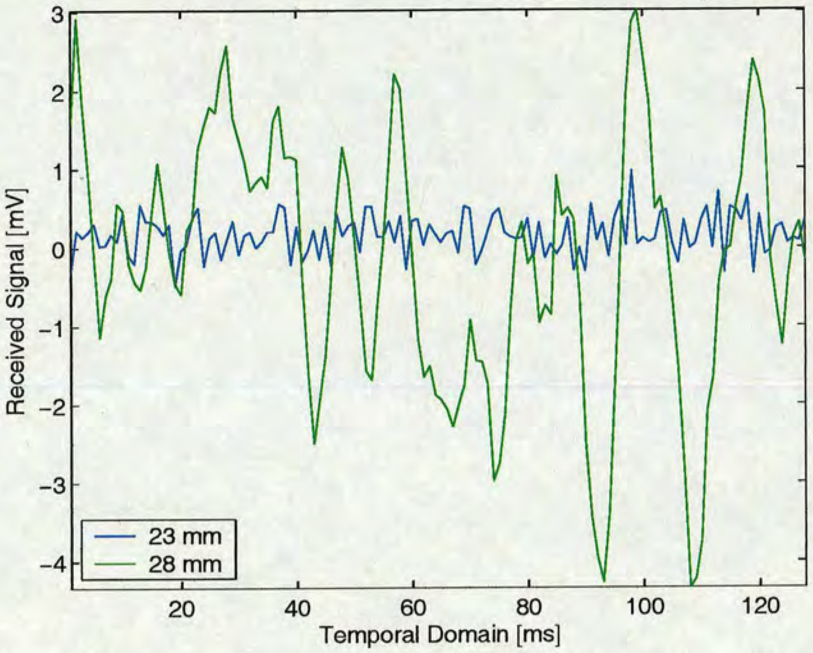

**Figure 4.16:** *Temporal domain plot from the data set shown in Figure 4.15, at a depth of 23 mm (blue) and 28 mm (green).*

by looking at the power spectral density for each of these signals, as shown in Figure 4.17. Considering the Doppler equation [2.1], the frequency shift due to a velocity of 37.7 mm/sec should be around 115 Hz. Inspection of Figure 4.17 shows a peak near to this frequency, but it is far from the only peak in the signal. Under ideal circumstances, the mean frequency of the temporal domain signal will correspond to the Doppler frequency, but with real, noisy signals, this method cannot be used to form a reliable velocity estimator. Also, this example has used 128 temporal domain samples, which with a pulse repetition frequency of 1 Khz would require 128 ms to capture. Although this is possible, using such a long time degrades the temporal resolution significantly and it would certainly be impossible to use for 2D imaging where a whole frame, consisting of tens of lines needs to be generated at least 25 times a second.

However, it is possible to estimate the frequency of the temporal domain signals and hence produce a velocity estimation, using two-dimensional cross-correlation. P.G.M. de Jong et al. [49], [50] describe a technique called "correlation interpolation", which is based on the idea that the power spectrum of a typical received signal may be modelled by a Gaussian function. The required function may be derived using signal power, noise power, spatial mean frequency and spatial bandwidth as parameters. If the displacement between observations is also taken into account, then the cross-spectrum is obtained. This can be transformed to a complex cross-

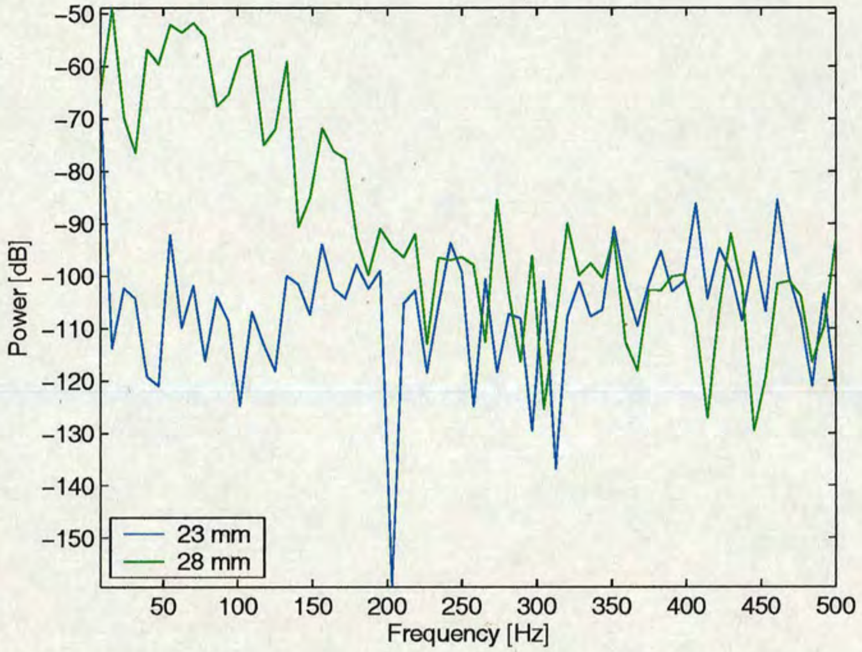

**Figure 4.17:** *Power spectra of signals shown in Figure 4.16, clearly showing that the signal from 23 mm is just noise, whereas the signal from 28 mm has a definite frequency content.*

correlation by means of the Wiener-Khinchin relation and then because only a few unknown parameters are involved, a velocity estimator may be derived using only a few depth and time lags.

The work by P.G.M. de Jong et al. was based on the assumption that the received signal would have a narrow spatial bandwidth, which simplified the derivation of an expression. However, Brands et al. [51] later extended this work into the "complex cross correlation model" technique, which was not based on such an assumption. This will be described in more detail later in the chapter, but the correlation interpolation, or "cross correlation model" technique may be described as follows.

Normalising the Doppler equation (equation 2.1) results in an expression for the normalised mean velocity derived as the ratio of the mean velocity to the ratio between the spatial sampling interval $\Delta y = c/(2\cos\alpha f_{s-rf})$ and the temporal sampling interval $\Delta t = 1/\text{PRF}$:

$$\begin{aligned}\varphi &= \frac{\bar{v}}{\Delta y/\Delta t} \\ &= \frac{\frac{c}{2\cos\alpha}\frac{\bar{f}_t}{\bar{f}_c}}{\frac{c}{2\cos\alpha}\frac{\text{PRF}}{f_{s-rf}}} \\ &= \frac{\bar{f}_t/\text{PRF}}{\bar{f}_c/f_{s-rf}} \\ &= \frac{\bar{f}_{nt}}{\bar{f}_{nc}} \qquad (4.11)\end{aligned}$$

Where $c$ is the speed of sound, $\alpha$ the angle of the velocity with respect to the ultrasound beam, $\bar{f}_t$ the temporal mean frequency, $\bar{f}_{nt}$ the normalised temporal mean frequency, PRF is the temporal sampling frequency, $\bar{f}_c$ the spatial mean frequency, $\bar{f}_{nc}$ the normalised spatial mean frequency and $f_{s-rf}$ is the spatial sampling frequency. Then, the relation between one sampled RF signal, $w_{rf}(k_0 + k, i_0 + i)$ and the next, $w_{rf}(k_0 + k, i_0 + i + 1)$, where $k_0$ denotes depth and $i_0$ time, can be defined as:

$$w_{rf}(k_0 + k, i_0 + i) \approx w_{rf}(k_0 + k - i\varphi, i_0 + i + 1) + n \qquad (4.12)$$

Where $n$ denotes the noise contribution, k denotes shift in depth and i denotes shift in time.

Then, considering a received RF signal, $w_{rf}(t)$, whose spatial power spectral density distribution $W_{rf}(f)$ can be modelled by: [51]

$$G(f) = \sum_{h=-\infty}^{h=+\infty} \frac{Q(N+S)}{\bar{f}_{nc}} \exp\left[\frac{-\pi Q^2(f - \bar{f}_{nc} - h)^2}{\bar{f}_{nc}^2}\right] \qquad (4.13)$$

Where $G$ is the spatial power spectral distribution of the model, $S$ is the signal power, $N$ the noise power, $f$ the normalised spatial frequency, $Q$ the spatial quality factor (spatial mean frequency divided by bandwidth) and $h$ is the periodicity factor. Taking into account the displacement between observations $\varphi i$, then the cross-spectrum may be modelled by:

$$G(f,i) = \sum_{h=-\infty}^{h=+\infty} \frac{Q(N + S\exp[-j2\pi f\varphi i])}{\bar{f}_{nc}^2} \exp\left[\frac{-\pi Q^2(f - \bar{f}_{nc} - h)^2}{\bar{f}_{nc}^2}\right] \qquad (4.14)$$

From which the cross-correlation function may be determined by means of the Wiener-Khinchin relation:

$$R(k,i) = \int_{-0.5}^{0.5} G(f,i)\exp(j2\pi fk)\mathrm{d}f \tag{4.15}$$

From which Peter Brands et al. [51] derive an expression for the complex cross-correlation function as:

$$R(k,i) = (S+N_i)\exp\left[\frac{-\pi \bar{f}_{nc}^2(k-\varphi i)^2}{Q^2} + j2\pi\bar{f}_{nc}(k-\varphi i)\right] \tag{4.16}$$

### 4.4.4.2 Cross-Correlation Model (CCM) Estimator

If a narrow spatial bandwidth is assumed and only the real part considered, then equation [4.16] may be simplified to:

$$R(k,i) = (S+N_i)\cos\left(2\pi\bar{f}_{nc}(k-\varphi i)\right) \tag{4.17}$$

From which it is necessary to determine the unknown model parameters, $S$, $N$, $\bar{f}_{nc}$ and $\varphi$. This can be achieved by considering the following cross-correlation lags:

$$\begin{aligned} R(0,0) &= S+N \\ R(1,0) &= (S+N)\cos(2\pi\bar{f}_{nc}) \\ R(0,1) &= S\cos(2\pi\bar{f}_{nc}\varphi) \\ R(1,1) &= S\cos(2\pi\bar{f}_{nc}(1-\varphi)) \\ R(-1,1) &= S\cos(2\pi\bar{f}_{nc}(-1-\varphi)) \end{aligned} \tag{4.18}$$

Note that the noise terms, $N$, disappear in the later three expression of equation [4.18] because the noise is uncorrelated across the different received signals. In this way, the model parameters may be estimated from a set of sampled signals using the cross-correlation defined as:

$$\hat{R}(k,i) = \frac{1}{(M-k)(N-i)}\sum_{d=0}^{M-k-1}\sum_{\tau=0}^{N-i-1} w_{rf}(k_0+d, i_0+\tau)w_{rf}(k_0+d+k, i_0+\tau+i) \tag{4.19}$$

Then:

$$\begin{aligned}
\hat{\hat{f}}_{nc} &= \frac{1}{2\pi}\cos^{-1}\left(\hat{R}(1,0)/\hat{R}(0,0)\right) \\
\hat{\hat{f}}_{nt} &= \frac{1}{2\pi}\tan^{-1}2\left[\frac{0.5(\hat{R}(1,1)-\hat{R}(-1,1))}{\hat{R}(0,1)\sin\left(\cos^{-1}(\hat{R}(1,0)/\hat{R}(0,0))\right)}\right] \\
\hat{\varphi} &= \frac{\hat{\hat{f}}_{nt}}{\hat{\hat{f}}_{nc}} \\
\frac{\hat{S}}{\hat{N}} &= \frac{\hat{R}(0,1)}{\hat{R}(0,0)\cos(2\pi\hat{\hat{f}}_{nt})-\hat{R}(0,1)}
\end{aligned} \tag{4.20}$$

From which the mean velocity, $\hat{v}$ may be calculated using:

$$\hat{v} = \frac{c}{2\cos\alpha}\frac{\text{PRF}}{f_{s-rf}}\hat{\varphi} \tag{4.21}$$

Where $\alpha$ is the Doppler angle, as defined in Figure 2.8.

Using this method with the same data which was used with the cross-correlation technique described above gave the results shown in Figures 4.18 to 4.22. In this case, the percentage error has been plotted against the number of temporal domain samples used, for each of 2, 4 and 16 spatial samples. As before, the percentage error would have been meaningless in the 0 mm displacement case shown in Figure 4.18, so the estimated velocity was plotted instead. Each figure represents a different lateral displacement of the transducer and hence a different scatterer velocity.

As was observed with the conventional cross-correlation results, the best results were achieved when the pulse length was 2 cycles. Generally, these results were felt to indicate that the kind of accuracy achievable with the cross-correlation model technique was between 10 % and 20 %, slightly worse than the results from conventional cross-correlation. However, the best results were achieved when 16 spatial samples were used, compared to a window length of 128 samples which was needed to get the best results from the conventional cross-correlation technique. From Table 4.2, this may be observed to correspond to a distance of only 0.25 mm, which represents an order of magnitude improvement in the obtainable spatial resolution. Decreasing the sample volume size by this degree would also improve the accuracy of the technique in more complex situations where the scatterers may well be moving with different velocities within the sample volume.

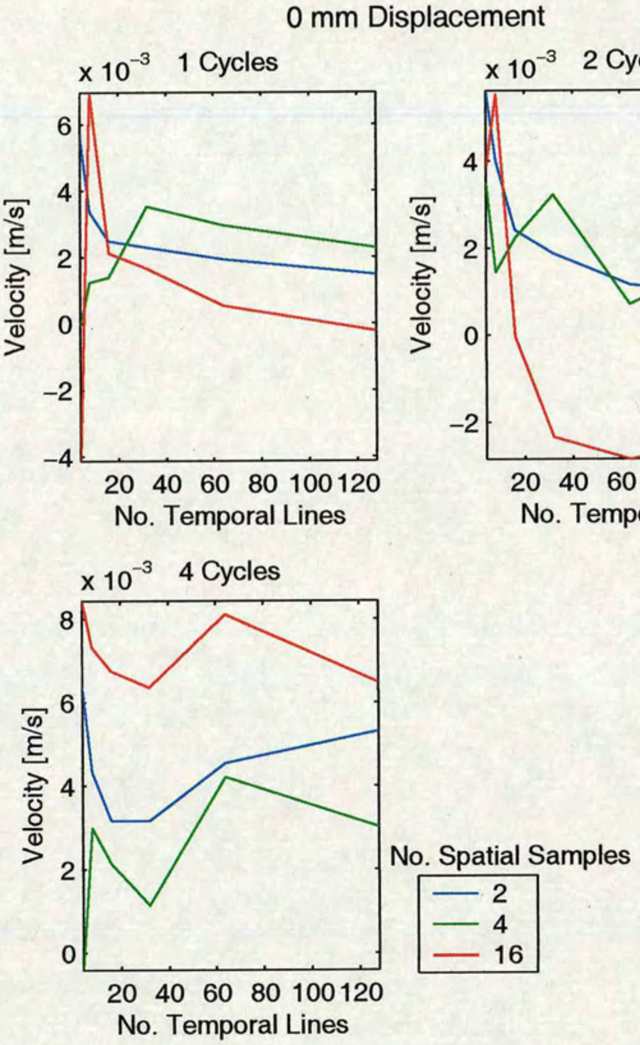

**Figure 4.18:** *Velocity estimation accuracy for 0 mm lateral displacement, showing estimated velocity vs. the number of temporal lines used.*

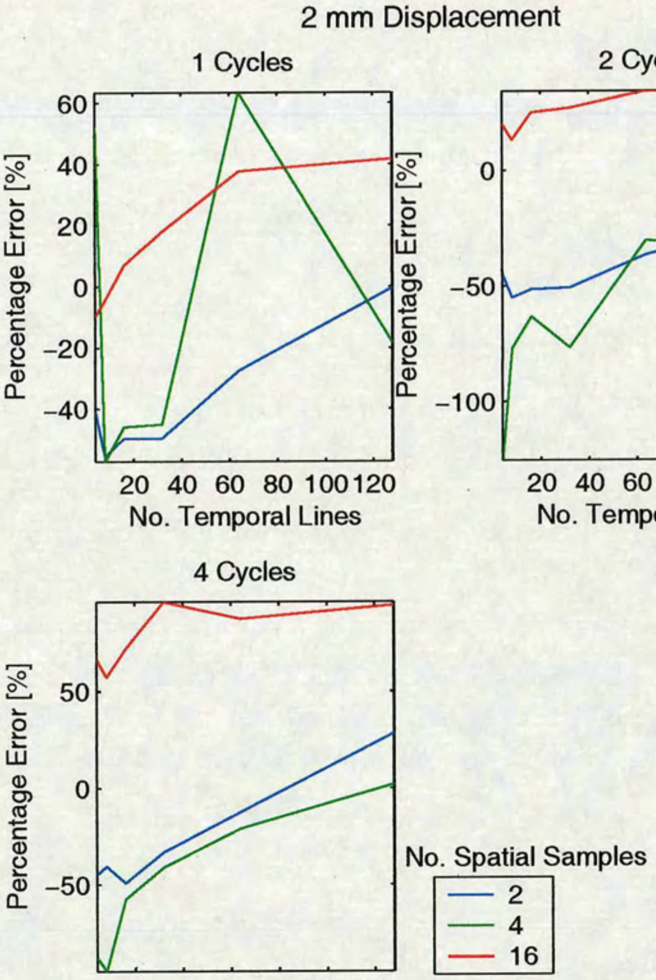

**Figure 4.19:** *Velocity estimation accuracy for 2 mm lateral displacement, showing percentage error vs. the number of temporal lines used.*

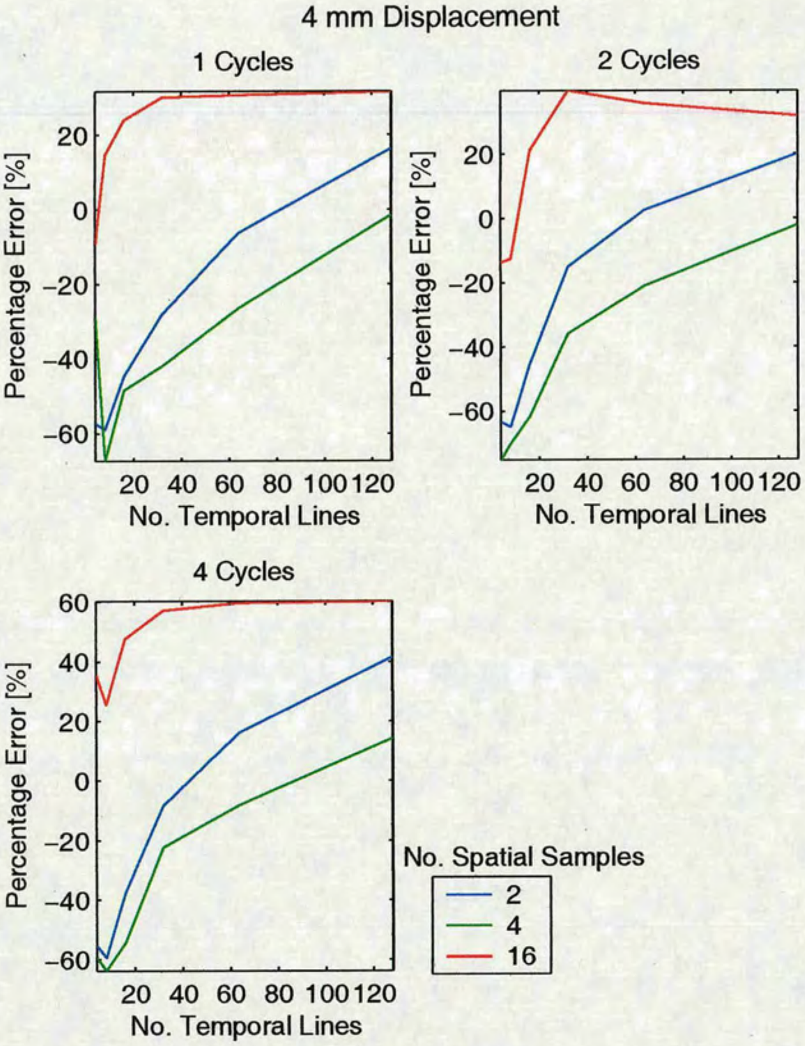

**Figure 4.20:** *Velocity estimation accuracy for 4 mm lateral displacement, showing percentage error vs. the number of temporal lines used.*

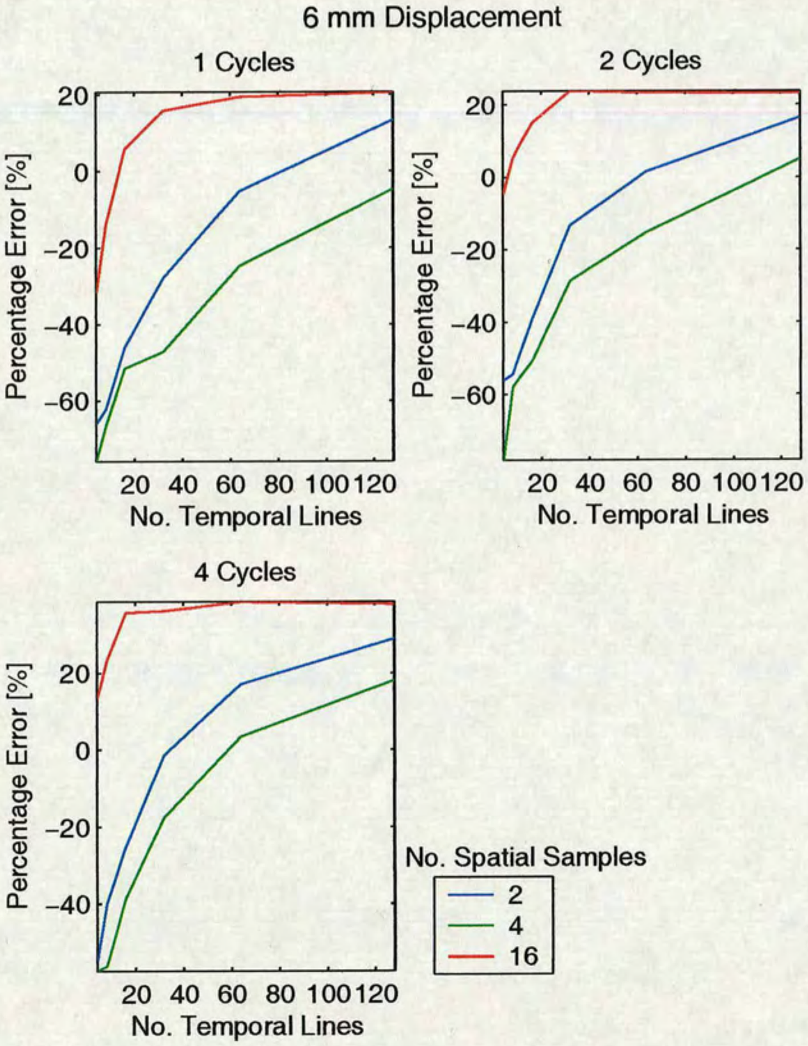

**Figure 4.21:** *Velocity estimation accuracy for 6 mm lateral displacement, showing percentage error vs. the number of temporal lines used.*

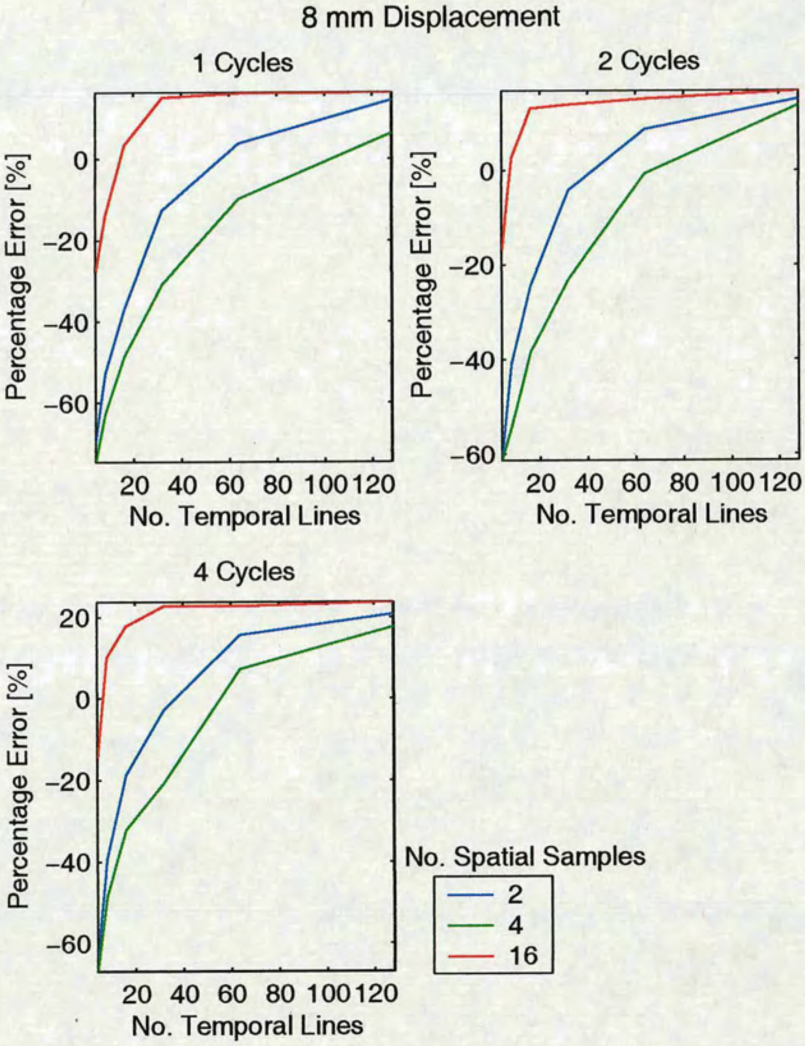

**Figure 4.22:** *Velocity estimation accuracy for 8 mm lateral displacement.*

| SNR [dB] | Mean Velocity [mm/sec] | Variance [mm/sec] |
|---|---|---|
| 100 | 59.5 | 0.03 |
| 90 | 59.5 | 0.03 |
| 50 | 59.6 | 0.03 |
| 40 | 60.8 | 0.02 |
| 30 | 2.59 | 4.02 |
| 20 | 8.45 | 0.60 |
| 10 | 4.95 | 0.13 |
| 0 | 2.95 | 0.10 |

**Table 4.3:** *Table of mean velocity and variance for the CCM estimator with 64 temporal samples and 12 spatial samples.*

The noise performance of the CCM estimator was assessed using the results from the simulations described in the previous section. As before, these were corrupted with additive, white, Gaussian noise of levels ranging from 0 dB to 100 dB in 10 dB increments. Figures 4.23 to 4.27 show the results obtained for five different lengths of spatial and temporal windows. In the vast majority of cases it was observed that the performance of the estimator improved considerably at a threshold SNR of between 30 dB and 40 dB. As would be expected given the previous results from the single crystal ultrasound system, the best performance was achieved with a temporal window length of 64 samples. However, these results appear to suggest that for this temporal window length, a spatial window length of 12 samples was optimum.

It was observed that even in the case of the 0 dB SNR, the CCM estimator gave a slightly higher mean velocity in the region corresponding to the moving part of the phantom, which resulted in the finite percentage error. Considering only the 10 mm displacement line by way of example, Table 4.3 shows the mean velocities and the variance of the velocity profile for the moving part of the phantom at various SNRs. The temporal and spatial windowing was kept constant at 64 samples and 12 samples respectively. These results clearly show that the mean velocity and the variance of the velocity estimate both change significantly in the region between SNRs of 30 dB and 40 dB and that the mean velocity does not decrease to zero even in the 0 dB SNR case.

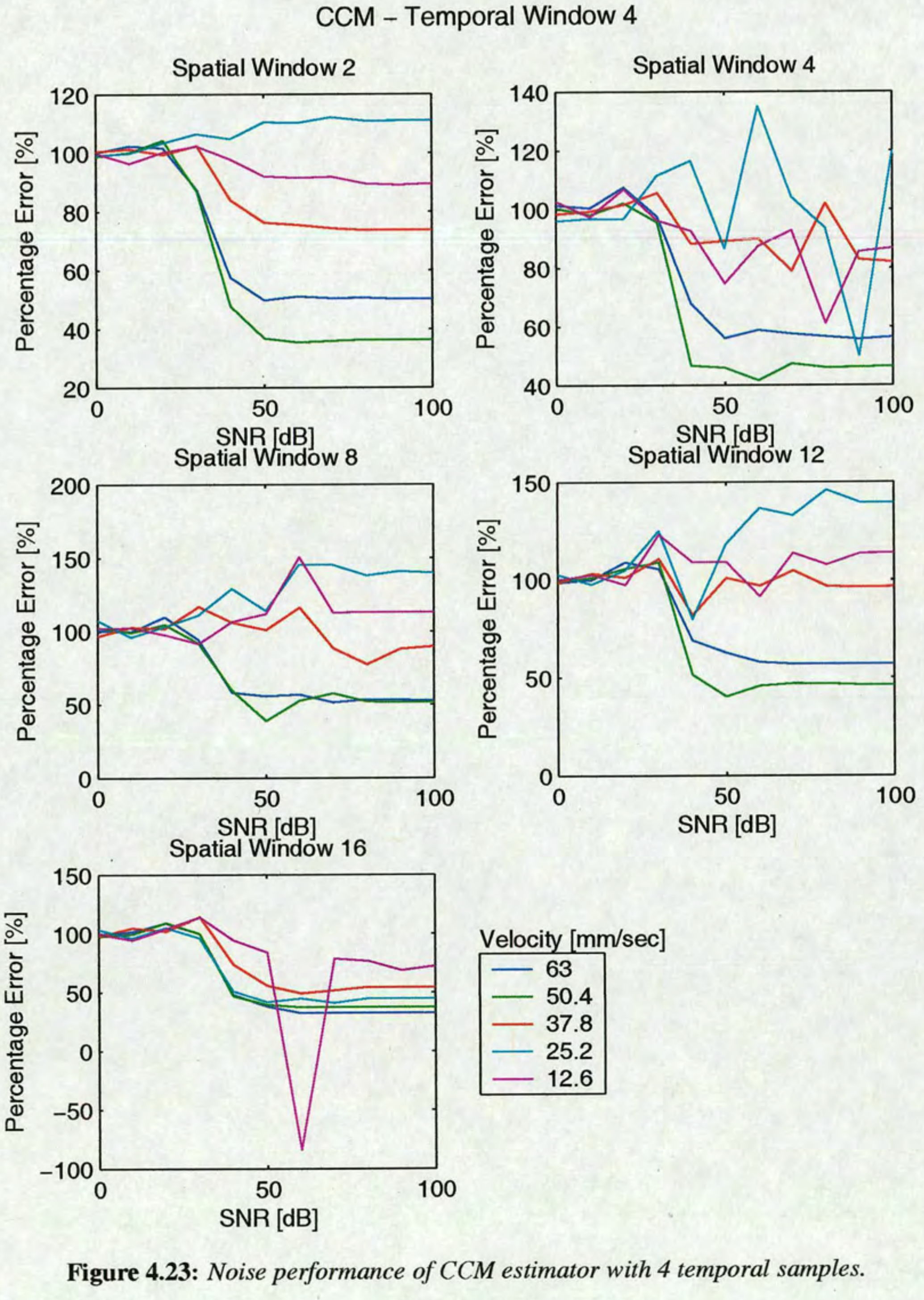

**Figure 4.23:** *Noise performance of CCM estimator with 4 temporal samples.*

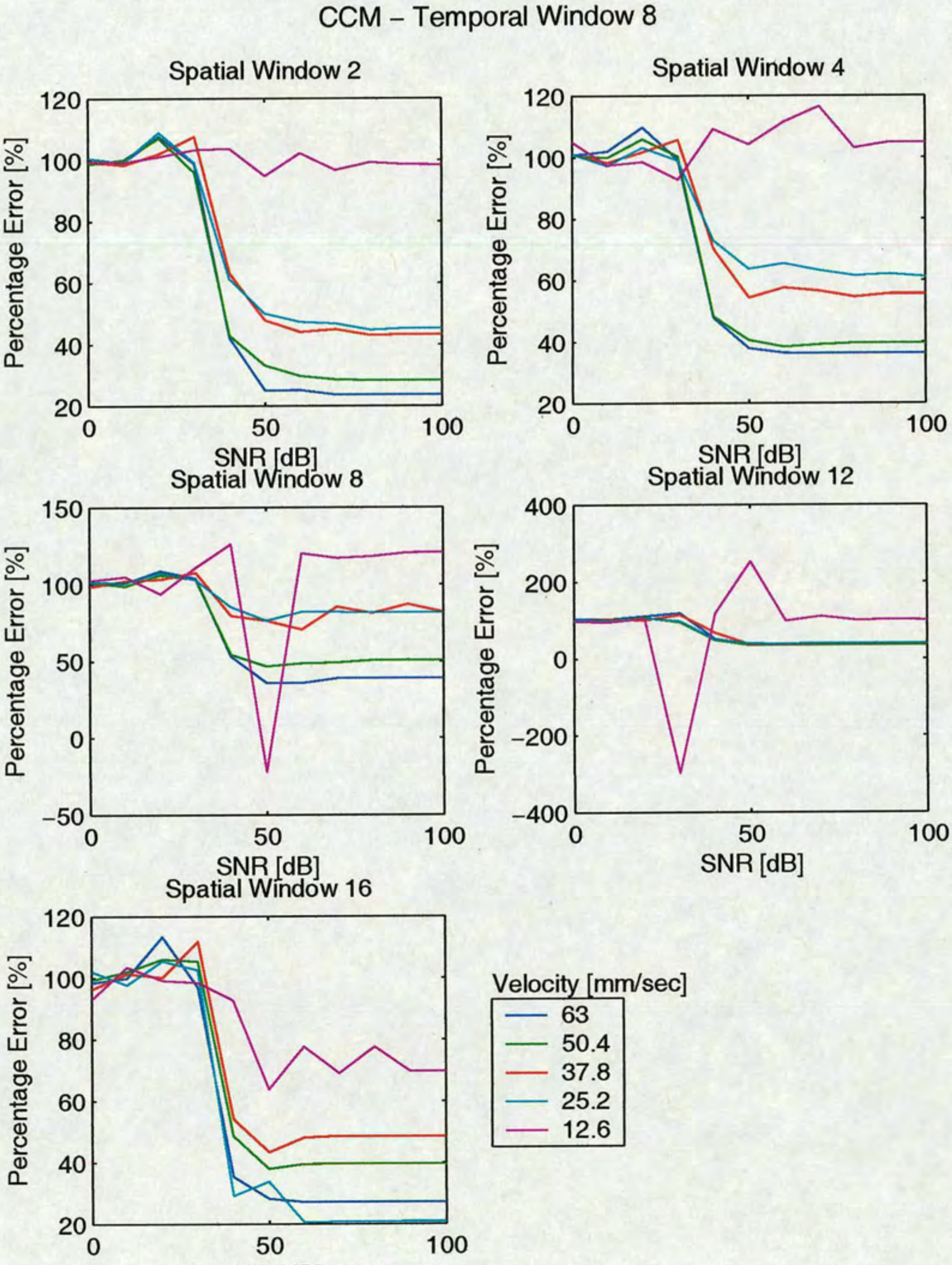

**Figure 4.24:** *Noise performance of CCM estimator with 8 temporal samples.*

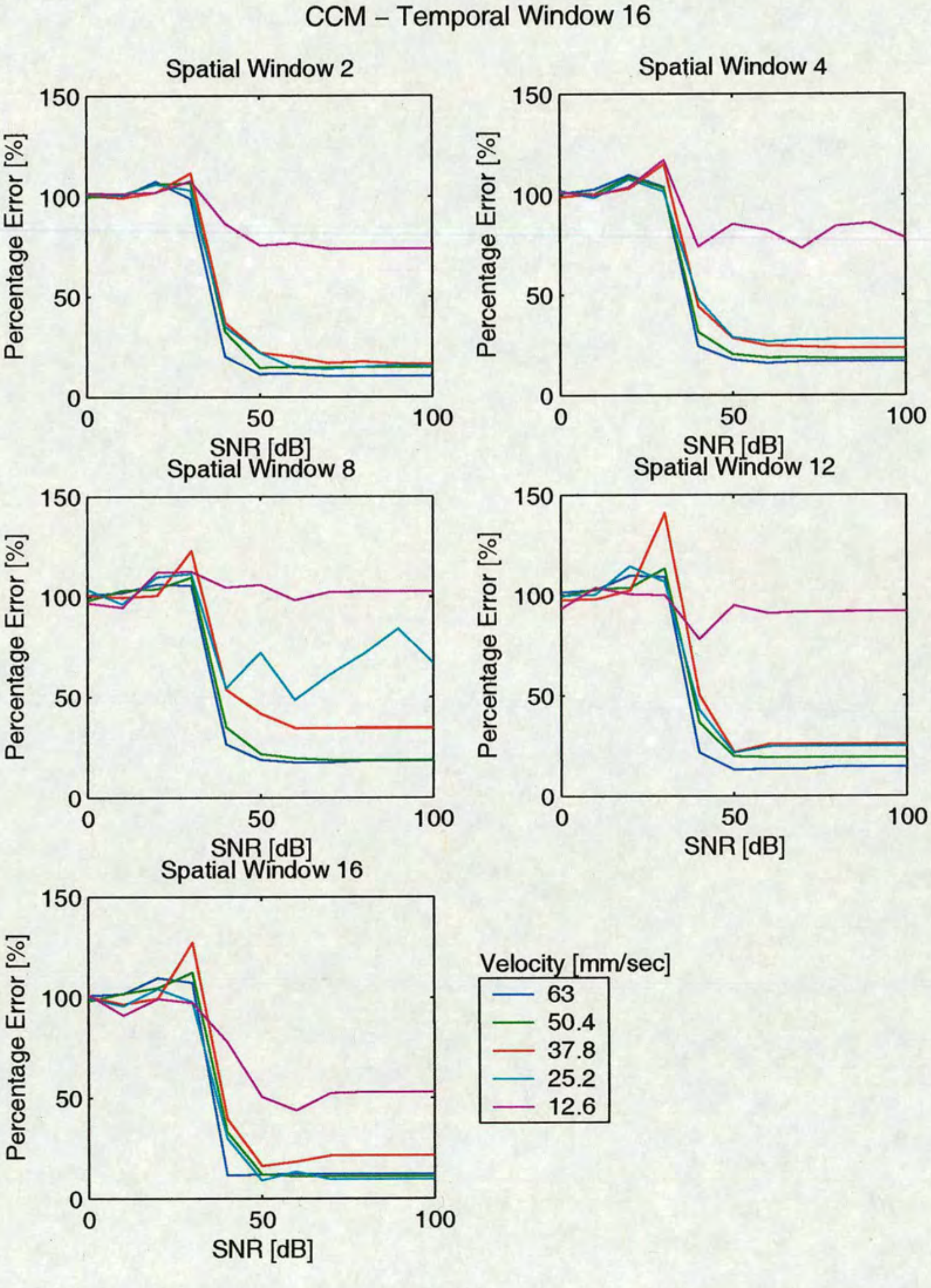

**Figure 4.25:** *Noise performance of CCM estimator with 16 temporal samples.*

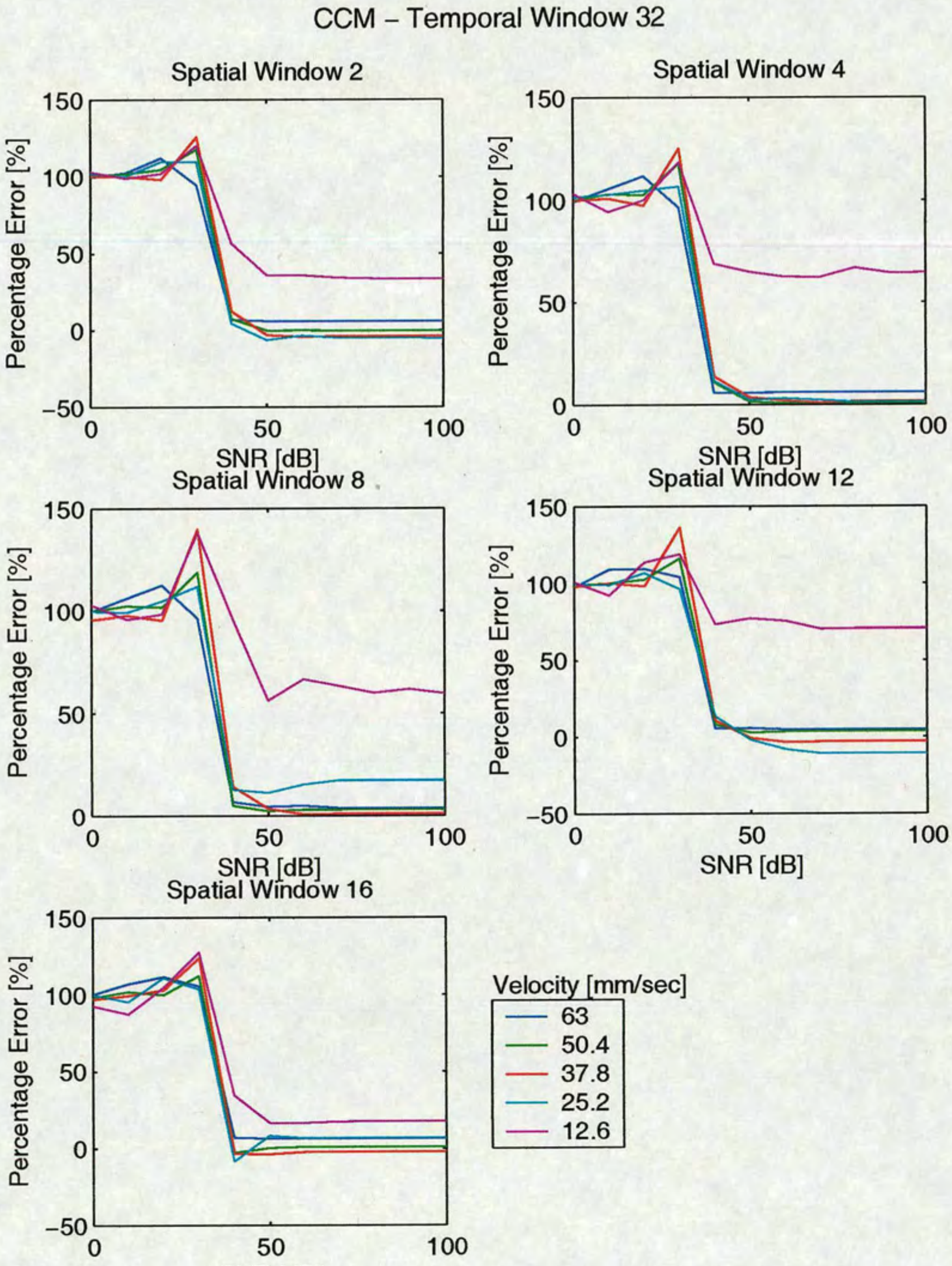

**Figure 4.26:** *Noise performance of CCM estimtor with 32 temporal samples.*

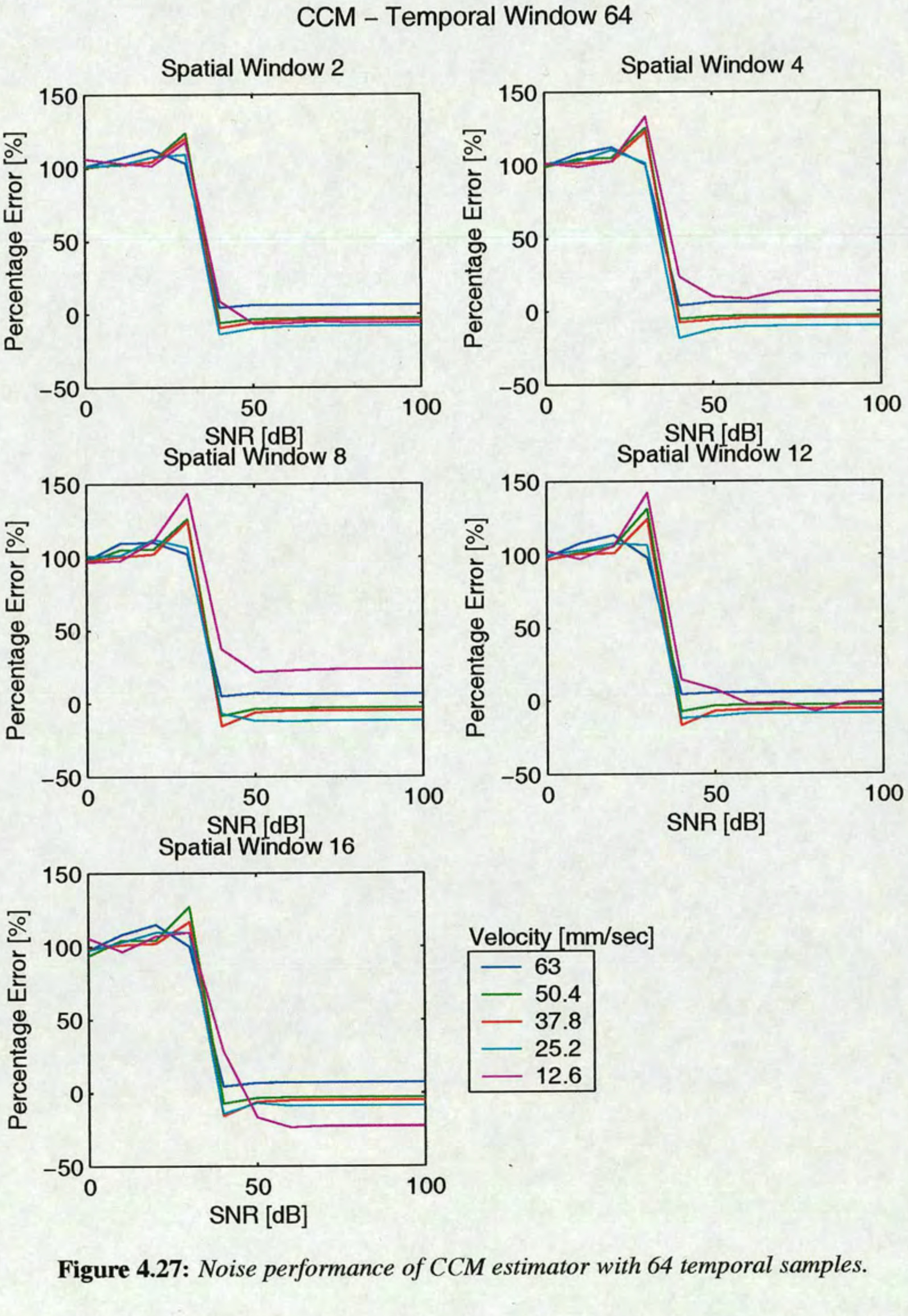

**Figure 4.27:** *Noise performance of CCM estimator with 64 temporal samples.*

#### 4.4.4.3 Complex Cross-Correlation Model (C3M) Estimator

The model parameters may be determined from the complex cross-correlation function given by equation 4.16 by considering the following lags:

$$\begin{aligned} R(0,0) &= S+N \\ R(1,0) &= (S+N)\exp\left[\frac{-\pi \bar{f}_{nc}^2}{Q^2}+j2\pi \bar{f}_{nc}\right] \\ R(0,1) &= S\exp\left[\frac{-\pi \bar{f}_{nc}^2\varphi^2}{Q^2}+j2\pi \bar{f}_{nc}\varphi\right] \end{aligned} \tag{4.22}$$

And using the cross-correlation of a set of sampled signals defined by:

$$\hat{R}(k,i)=\frac{1}{(M-k)(N-i)}\sum_{d=0}^{M-k-1}\sum_{\tau=0}^{N-i-1} w_{rf}(k_0+d,i_0+\tau)w_{rf}^*(k_0+d+k,i_0+\tau+i) \tag{4.23}$$

Then:

$$\begin{aligned} \hat{\varphi} &= \frac{\arg(\hat{R}(0,1))}{\arg(\hat{R}(1,0))} \\ \frac{\hat{S}}{\hat{N}} &= \frac{|\hat{R}(0,1)|}{\hat{R}(0,0)\exp\left[\frac{-\pi \bar{f}_{nc}^2\hat{\varphi}^2}{\hat{Q}^2}\right]-|\hat{R}(0,1)|} \end{aligned} \tag{4.24}$$

From which the velocity can be calculated using equation 4.21.

Applying this technique to the data sets used for the previous two tests gave the results shown in Figures 4.28 to 4.32. Note that the complex cross-correlation estimator requires analytic signals, whereas the cross-correlation estimator worked with purely real signals. The analytic signals were obtained using the Hilbert transform via the Matlab 'Hilbert' function.

These results clearly demonstrate the superiority of the complex cross-correlation model based technique over either the conventional cross-correlation approach or the purely real correlation model. As before, the best results were obtained when the pulse length was 2 cycles and in all but the 2 mm displacement case, the error was less than 10%. In the 8 mm displacement case, the error was actually less than 1%. These results also showed that this technique is not sensitive to the number of spatial samples used, meaning that it was possible to achieve the maximum velocity estimation accuracy with only 2 spatial domain samples. This equates to a sample volume length of only $30\mu m$.

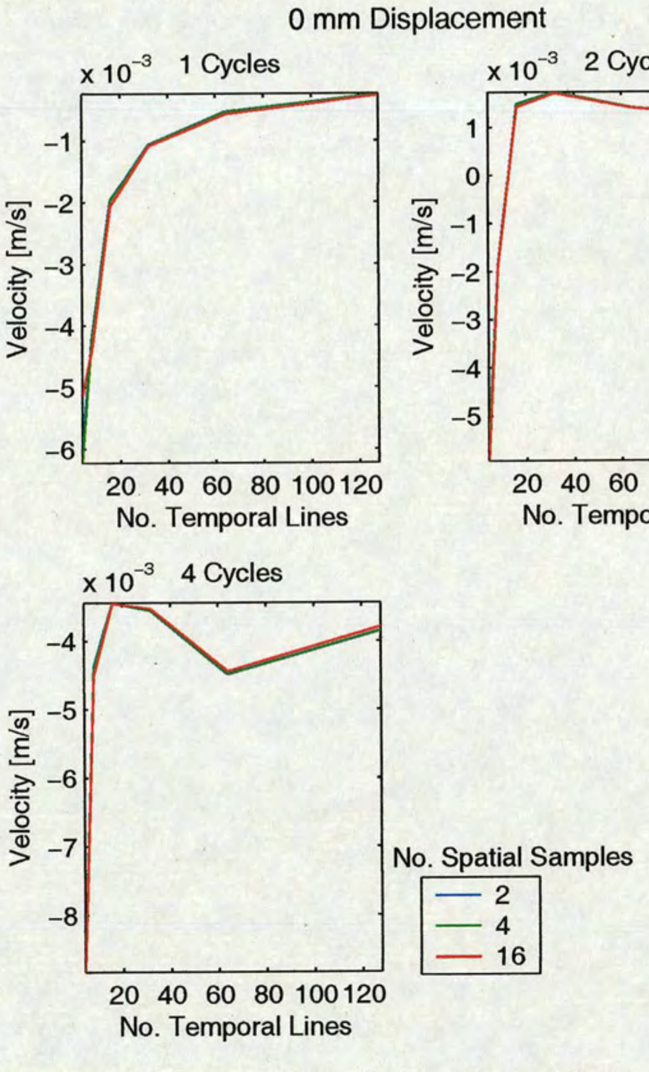

**Figure 4.28:** *Velocity estimation accuracy for 0 mm lateral displacement, showing estimated velocity vs. the number of temporal lines used.*

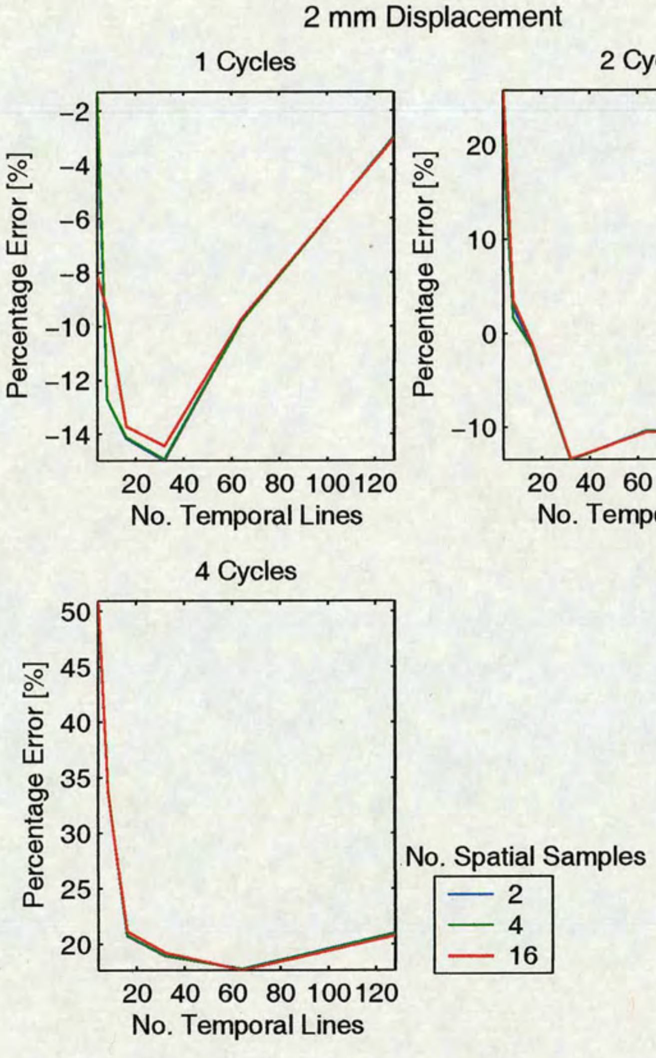

**Figure 4.29:** *Velocity estimation accuracy for 2 mm lateral displacement, showing percentage error vs. the number of temporal lines used.*

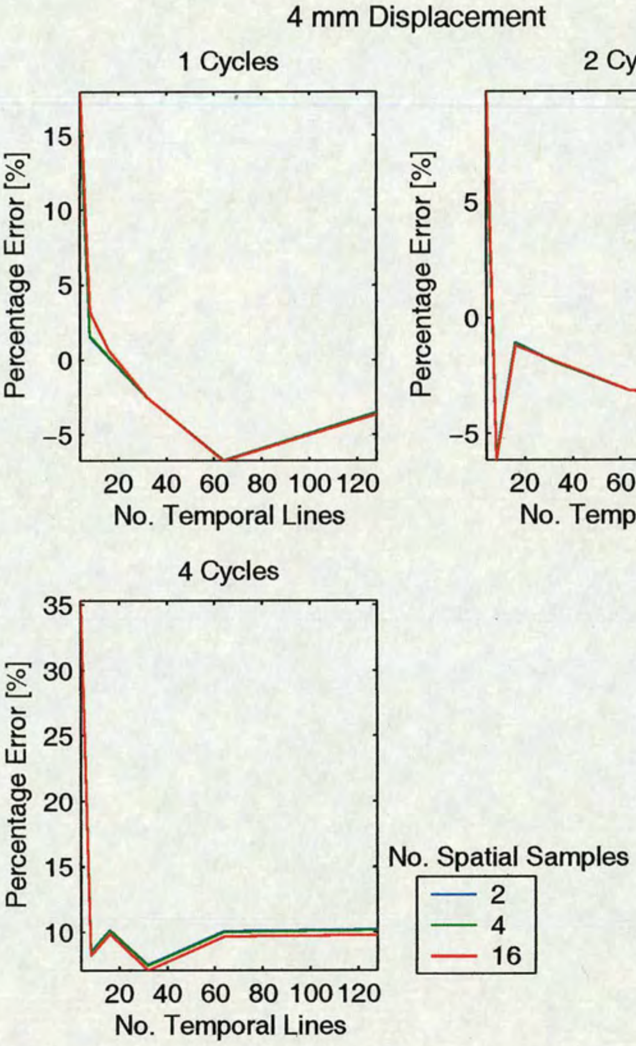

**Figure 4.30:** *Velocity estimation accuracy for 4 mm lateral displacement, showing percentage error vs. the number of temporal lines used.*

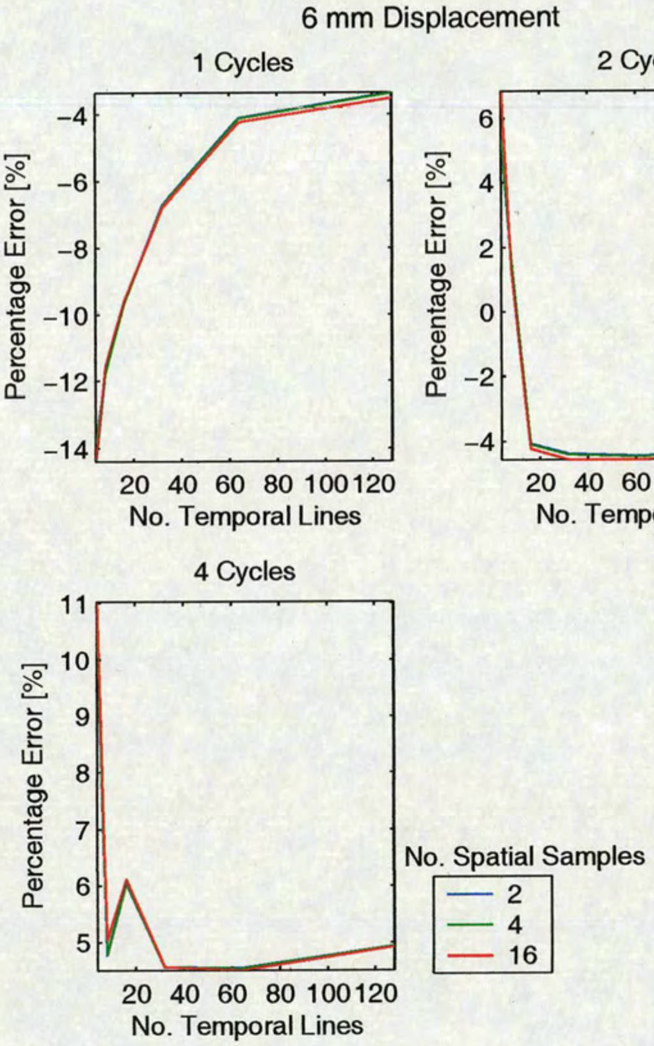

**Figure 4.31:** *Velocity estimation accuracy for 6 mm lateral displacement, showing percentage error vs. the number of temporal lines used.*

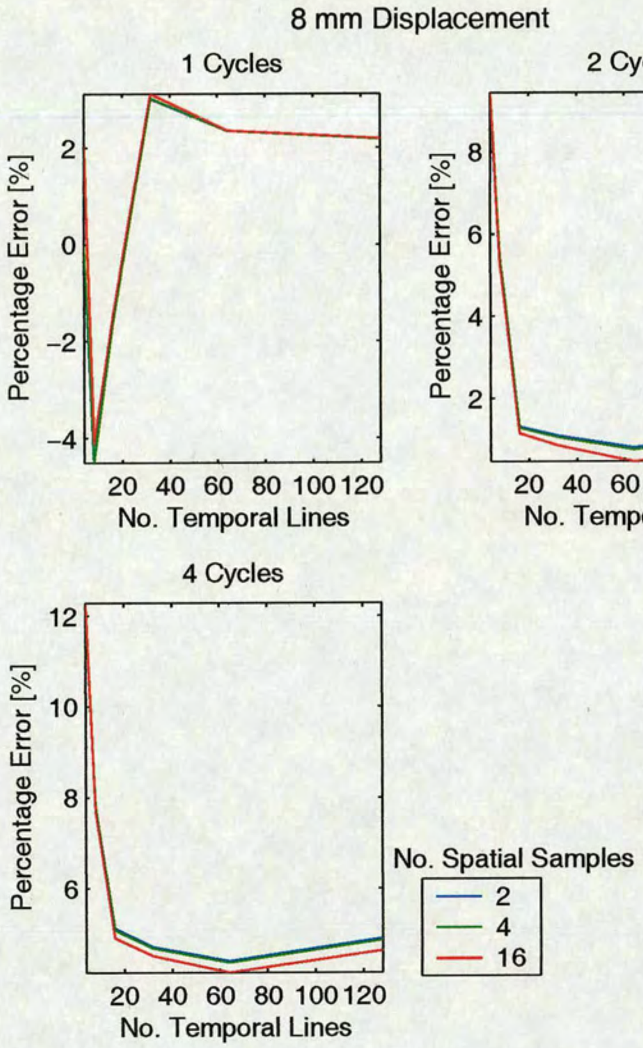

**Figure 4.32:** *Velocity estimation accuracy for 8 mm lateral displacement, showing percentage error vs. the number of temporal lines used.*

| SNR [dB] | Mean Velocity [mm/sec] | Variance [mm/sec] |
|---|---|---|
| 100 | 59.8 | 0.002 |
| 90 | 59.8 | 0.002 |
| 50 | 59.8 | 0.002 |
| 40 | 59.6 | 0.003 |
| 30 | 57.3 | 0.015 |
| 20 | 42.8 | 0.068 |
| 10 | 16.9 | 0.022 |
| 0 | 6.48 | 0.184 |

**Table 4.4:** *Table of mean velocity and variance for C3M estimator with 64 temporal samples and 12 spatial samples.*

The noise performance of the C3M estimator was assessed using the same data as the analysis of the CCM and cross-correlation estimators. The results of this may be seen in Figures 4.33 to 4.37. The analysis was performed over the same range of temporal and spatial window lengths as for the CCM case above.

As for the CCM case, these results show that at a certain threshold SNR of between 30 dB and 40 dB, the percentage error rapidly decreases and then flattens out. The shape of these curves was observed to be different to those of the CCM estimator in that the percentage error decreases more steadily as the SNR is increased as opposed to remaining level until the threshold value. It was observed that for temporal window lengths greater than 8 samples there was very little variation in the results with the spatial window length. This was as expected given the results from the single crystal ultrasound system.

Table 4.4 shows the mean velocities and variances for the 10 mm displacement line over a range of SNRs for fixed temporal and spatial window lengths of 64 and 2 samples respectively.

## 4.5 Conclusions

A phantom and simulations for the assessment of tissue Doppler imaging accuracy have been described and results from these have been used to demonstrate that the accuracy of conventional cross-correlation based velocity estimations is around 10 % - 20 %. Two newer, model based velocity estimators, the cross-correlation model (CCM) and complex cross-correlation model (C3M), and results have been given comparing these to conventional cross-correlation of two signals. It was demonstrated that the CCM estimator gave results which were similar to those obtained using conventional cross-correlation, but the C3M estimator was able to give

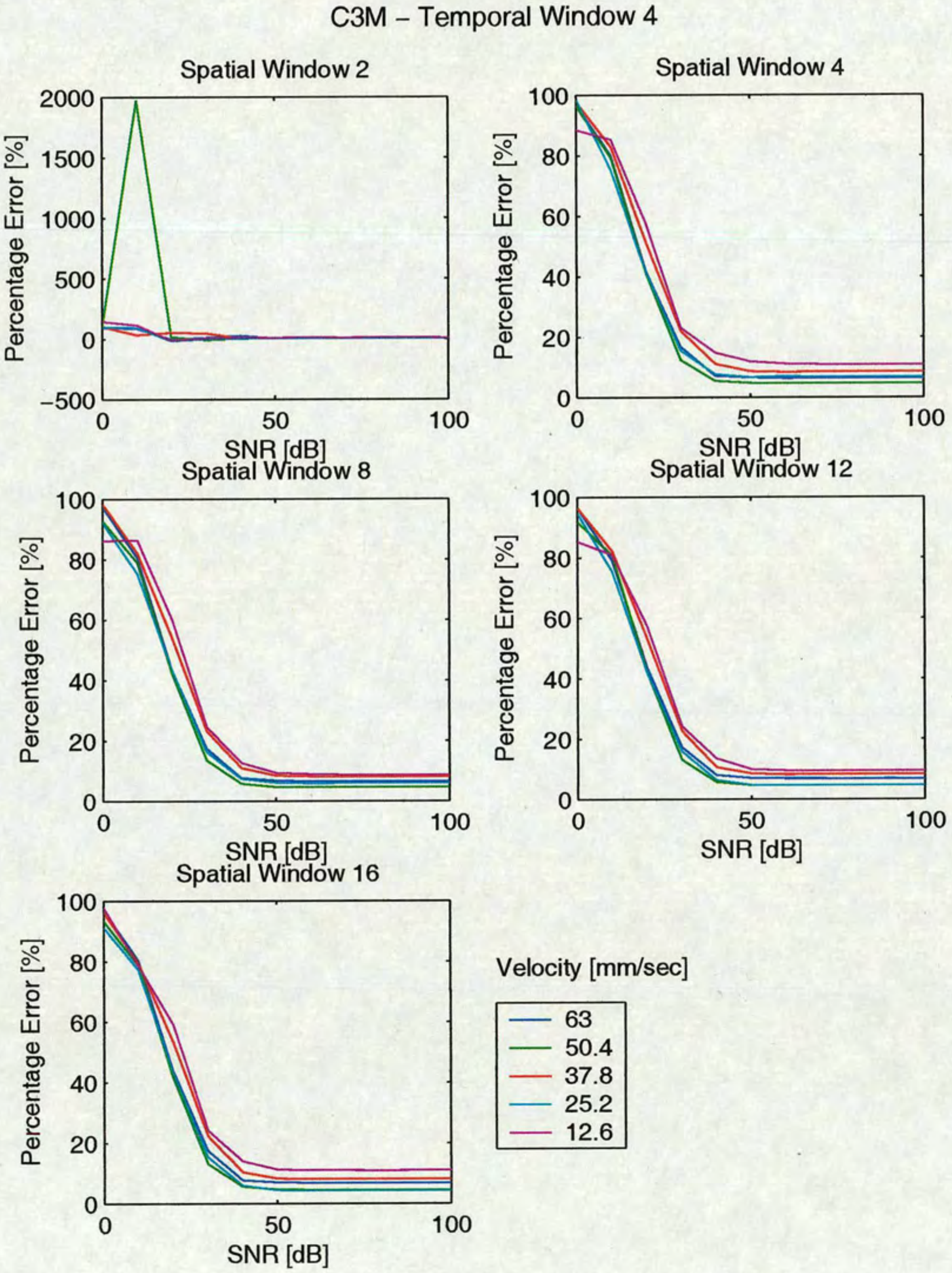

**Figure 4.33:** *Noise performance of C3M estimator with 4 temporal samples.*

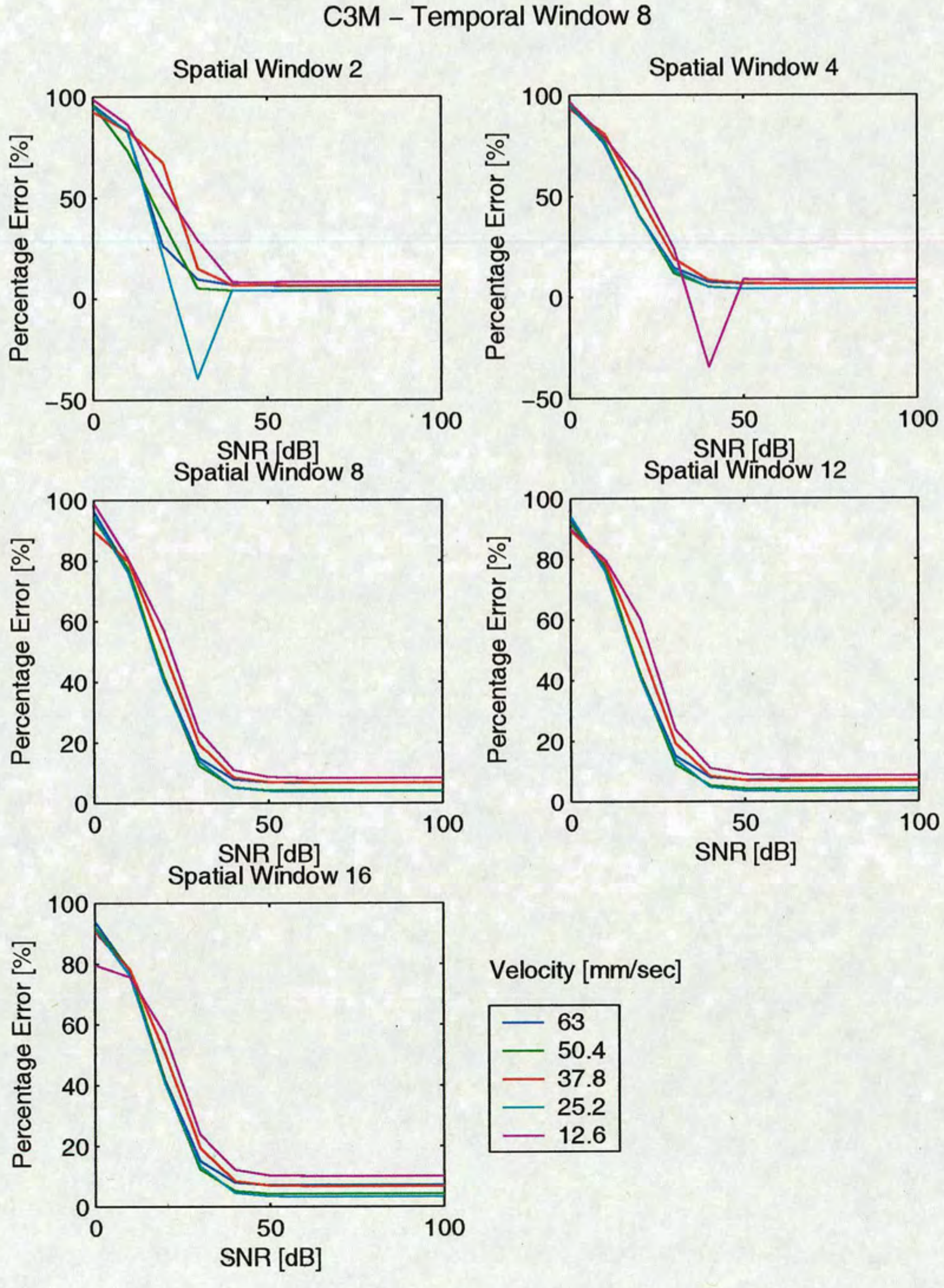

**Figure 4.34:** *Noise performance of C3M estimator with 8 temporal samples.*

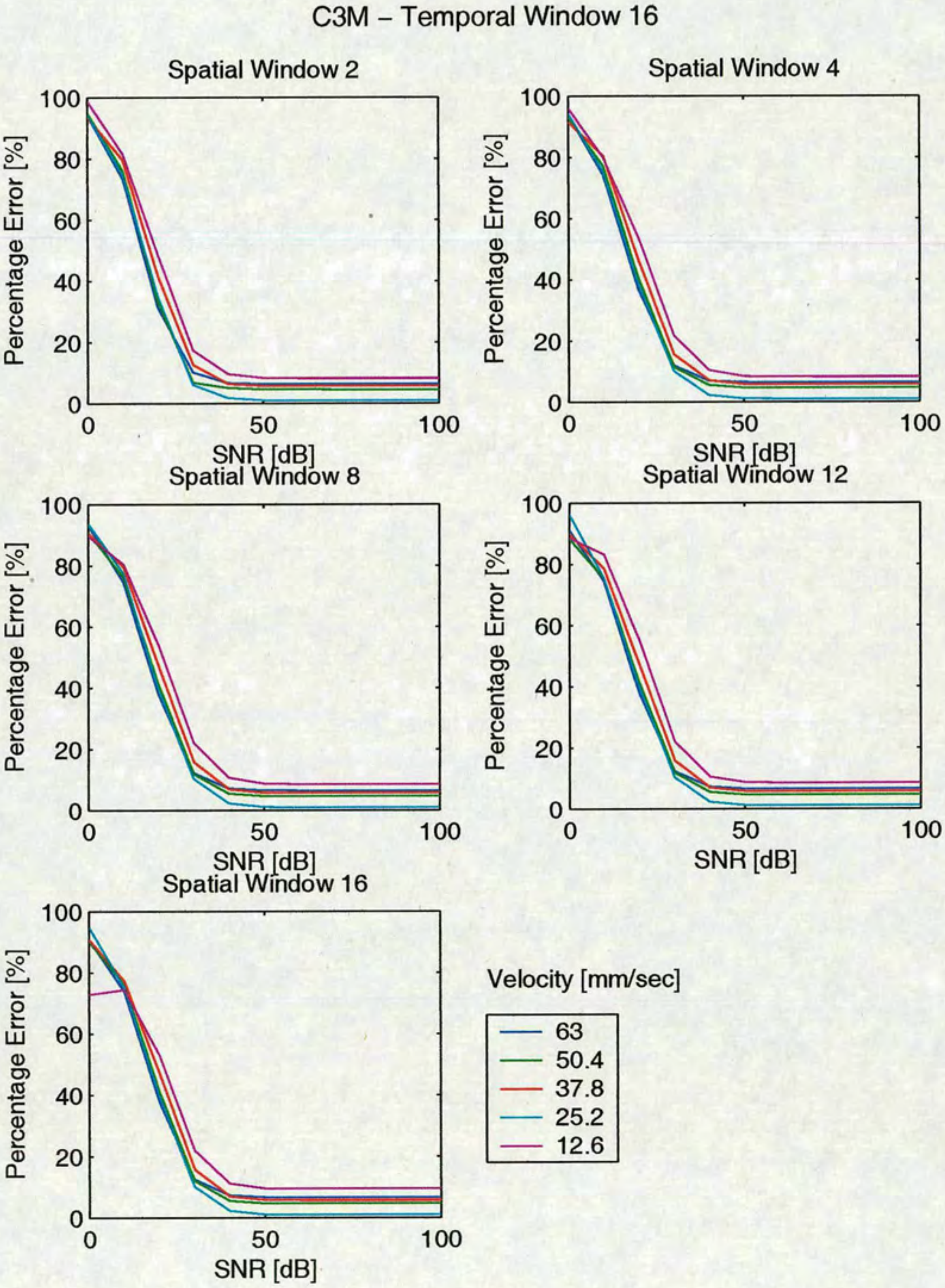

**Figure 4.35:** *Noise performance of C3M estimator with 16 temporal samples.*

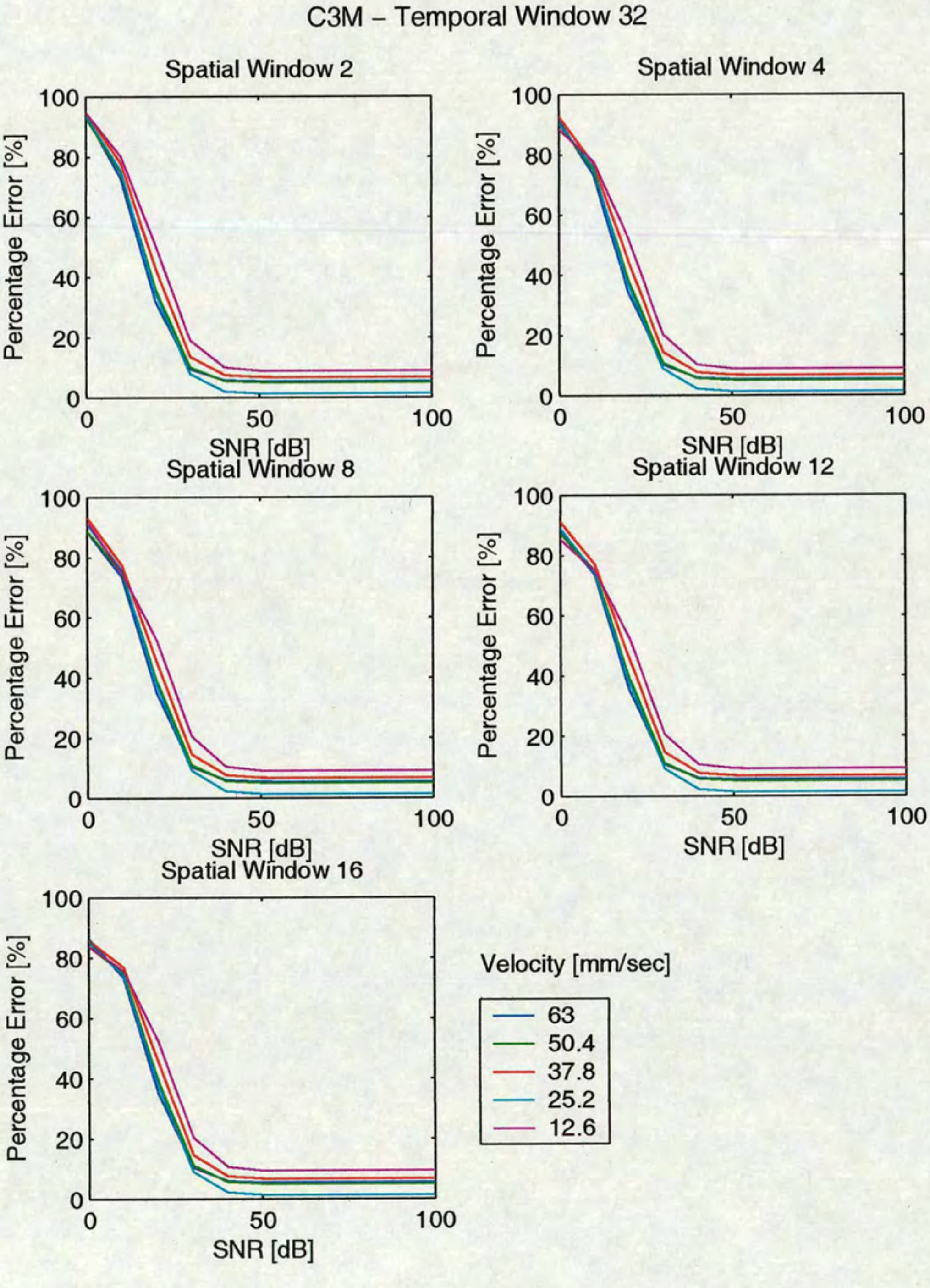

**Figure 4.36:** *Noise performance of C3M estimator with 32 temporal samples.*

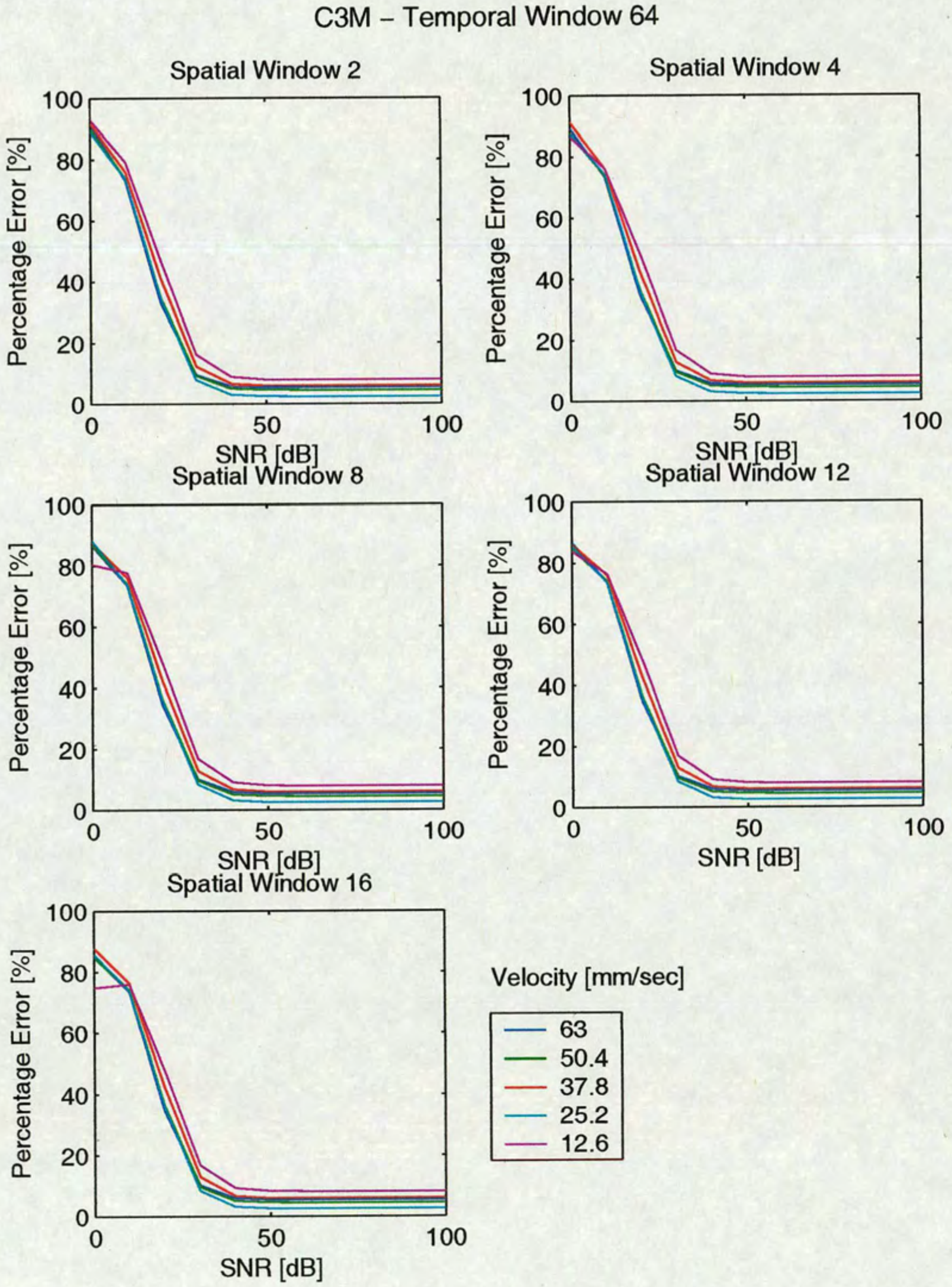

**Figure 4.37:** *Noise performance of C3M estimator with 64 temporal samples.*

nearly an order of magnitude improvement in the accuracy.

In terms of noise, all three of the techniques had a very definite threshold SNR below which their performance decreased significantly. Overall, the C3M estimator was shown to be the least sensitive to noise, but in all cases it was observed that if the SNR was greater than 40 dB then the estimator would give maximum performance.

Doppler tissue imaging is usually used to give two dimensional images showing the variation in velocity over entire regions of the heart. When using this technique, it is very important to have a sufficiently high frame rate, otherwise the motion of rapidly moving structures such as the valves and some of the more subtle motions of the myocardium will be missed. This imposes severe limitations on the time available to make the velocity estimation. If a frame rate of 25 frames per second is assumed (a reasonable minimum) and there are, say, 64 lines in the region of interest, then there could only be a maximum of 0.625 ms for each line. If two lines are to be captured for each of the 64 velocity lines, then this equates to a minimum pulse repetition frequency of around 1.57 kHz. The problem with this is that the minimum velocity which may be measured is related to the pulse repetition frequency by equation (4.25).

$$V_{\text{min}} = \frac{c f_{\text{prf}}}{2 f_s} \tag{4.25}$$

Therefore, if $f_{\text{prf}} = 1.57 \times 10^3$ Hz and assuming $c = 1480$ m/s and $f_s = 50 \times 10^6$ Hz then this implies a minimum velocity of 23.25 mm/s, which is clearly too large for most DTI applications. It is, therefore, desirable to have as low a PRF as possible. Of course, this can be achieved by reducing the number of velocity lines, however it would not be possible to reduce this number sufficiently to enable more lines to be captured per velocity line while still maintaining a useful image. In practice, the minimum measurable velocity would be less than this because some form of interpolation of the cross-correlation function would be used, but the results for the cross-correlation estimator (which did use interpolation) clearly show that the accuracy decreases for the lower velocities.

It has been shown that the C3M estimator is able to offer significant performance benefits in terms of accuracy compared to the conventional cross-correlation approach. The results also demonstrate that it would be possible to achieve a significantly higher spatial resolution using this method, since it requires only 2 spatial domain samples to operate. However, this improvement in accuracy and spatial resolution comes at the cost of requiring more temporal lines per velocity line. To get the best performance, it was necessary to use at least 32 temporal lines, though increasing this to 64 gave a further improvement.

Initially, Doppler tissue imaging was intended for use as a qualitative tool to enable the variation in velocity over regions of the heart to be observed. When used in this manner the required accuracy of the velocity estimations is fairly low since the operator is unlikely to be able to detect subtle variations in the velocity.

The current trend is towards quantification of the velocities to enable more accurate diagnosis to be made and to make it easier to interpret the results. It seems that most of the research into quantification of DTI is focused on the use of velocity gradients from which it is possible to derive variables such as the strain or the strain rate. Much research has been published describing evidence of the clinical usefulness of this technique, however the velocity measurements required to calculate the velocity gradients come from DTI and very little attention to the accuracy of these initial estimations appears to have been made. Kowalski et al. [52] studied the potential value of such 'deformation' measurements and clearly demonstrated the potential clinical relevance. However, their study also showed that the reproducibility of the results obtained using the technique was relatively poor. This was caused in part by the fact that they were scanning a wide image sector and hence had a relatively low frame rate, but also by the lower SNR obtained when the difference between the two velocities used to form the velocity gradient was small compared to the accuracy of the initial estimations.

Given the evidence of clinical relevance of the results obtained using strain and strain rate imaging, the technique is likely to gain rapid acceptance within the medical environment, but for this to occur the problem of reproducibility needs to be resolved. The problem is largely down to the accuracy of the underlying DTI velocity measurements, so an improvement in this will have a corresponding impact on the use of strain and strain rate imaging. The results presented in this chapter were felt to indicate that the accuracy which can be obtained at present is limited by the need to produce 2D images. It has been shown that the complex cross-correlation model based velocity estimator is able to offer not only an order of magnitude improvement in accuracy, but also a similar degree of improvement in spatial resolution. However, this comes at the cost of capturing many more lines per velocity line which would make it impractical to use for forming 2D images.

Originally all ultrasound scans were of the M-Mode form, where a single spatial line is plotted over time, which allows any time variation occurring within that line to be clearly observed. Two dimensional images are obviously more appealing than this approach because they make it much easier to understand the spatial geometry of the area being investigated. It is argued that in order to gain suitably accurate and, most importantly reproducible, quantitative measurements of the velocity it is necessary to abandon the idea of producing 2D images and return to the use of colour coded M-Mode scans. These would allow for the use of anything up to 64 lines per velocity line, which would enable the use of the more accurate techniques described. This would lead to a corresponding improvement in the accuracy and reproducibility of any further measurements, such as strain and strain rate.

# Chapter 5
# The Fractional Fourier Transform and Coded Excitation

## 5.1 Introduction

The problem of velocity estimation is intimately related to the problem of measuring position, since velocity is simply the rate of change of position. The accuracy with which positions can be estimated can be improved by using signals which consist of shorter pulses and hence have wider bandwidths. However, making the transmitted signal shorter will decrease the average energy, unless the transmit power is increased correspondingly. This reduction in energy leads to a decrease in the available imaging depth that could be obtained. It would be possible to counter this by simply increasing the peak power of the signal, however this has serious safety implications, as described by Barnett et al. [53] who detail the possibilities of tissue lesions occurring due to thermal or cavitation effects and also talk about possible genetic implications. Barnett, Ter Haar et al also published a paper detailing the current status of research into the biophysical effects of ultrasound [54] and a further paper outlining various guidelines for the safe use of diagnostic ultrasound [55]. According to [55] the current WFUMB recommendations for the safe use of Doppler ultrasound state that provided tissue / gas interfaces or contrast agents are not present then there would be no reason to withhold the use of Doppler equipment. However, in situations where these conditions might be present, ultrasound exposure levels and duration should be reduced to the minimum necessary to obtain the required diagnostic information. It would therefore be better if ultrasound systems were able to offer the very best imaging so that the time required to obtain the relevant diagnostic information is minimised and that they achieve this using the lowest possible energy signals.

There are two principle measures which are generally used in discussions related to the safety of medical ultrasound equipment; the Mechanical Index (MI) and the Thermal Index (TI). The first of these is defined as peak rarefactional pressure of an ultrasound longitudinal wave propagating in a uniform medium, divided by the square root of the centre frequency of the transmitted ultrasound pulse. The thermal index (TI) is defined as the ratio of the power being emitted to

| | *Single Transmit* | *Multiple Transmit* |
|---|---|---|
| *Phase Coding* | Barker, M-sequence | Golay |
| *Frequency Coding* | Chirp | |

**Table 5.1:** *Different coding techniques used in medical ultrasound [2]*

the power required to raise the temperature one degree Celsius in a uniform medium assumed to have an attenuation of 0.3 dB/cm/MHz.

The imaging resolution can be enhanced through the use of higher frequency signals which result in an increase in both the axial and lateral resolutions and hence the accuracy with which positions can be estimated. However, once again, this is limited because attenuation in media such as water and muscle tissue increases with frequency and so the maximum imaging depth which can be achieved is decreased. A possible solution to both of these problems is to use coded excitation, which as described in the remainder of this chapter, allows the link between axial resolution and signal length to be broken. This makes it possible to use longer signals, which naturally have a higher average energy content and therefore are able to offer improvements in the available imaging depth. Given the definitions of the MI and TI above, it is clear that the use of longer pulses will have benefits in terms of the MI, since the peak rarefactional pressures will be lower.

## 5.2 Coded Excitation in Ultrasound

The technique of coded excitation has been used in SONAR and RADAR applications for some time, where it has been shown to offer significant improvements in the available signal-to-noise ratio at modest peak power levels compared to conventional pulsed techniques [56]. However, the bandwidth of the transducers used in medical ultrasound systems is relatively low compared to that found in RADAR or SONAR applications. This has the effect of smoothing out any high frequencies caused by rapid changes in the code and places limits on the degree of improvement which could be obtained.

A number of different pulse coding techniques have been tried for medical ultrasound systems, the results of which are summarised by Chiao et al. [2]. They categorised the codes according to whether they used single or multiple transmits and whether they used phase coding or frequency coding. Table 5.1 shows the codes which they considered [2].

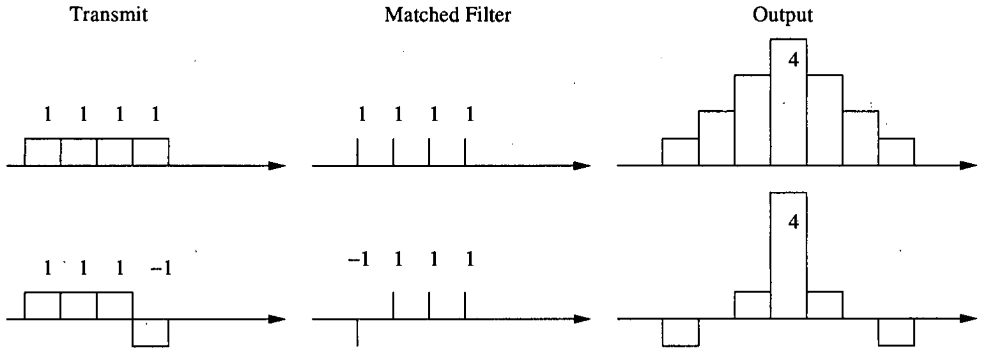

**Figure 5.1:** *Illustration of uncoded (top) and Barker coded (bottom) signals and processing with appropriate matched filters.*

The single transmit codes only require the transmission of one code sequence to achieve the desired pulse compression, whereas the multiple transmit codes require the transmission of two or more sequences. For the phase based techniques the code symbols (known as chips) are generally drawn from the discrete set $\phi_m = 2\pi m/M, m = 1, 2, ..., M$, such that the signal would be given by; $s(t) = \exp(j\phi_m t)$, where $M$ is the order of the code. In frequency coding, the carrier frequency of the signal is modulated to form the code. The most common phase codes are the bi-phase Barker and Golay codes with code symbols $\pm 1$, while the most common frequency code is the linear swept-frequency chirp. Generally, a matched filter will be used in the receive stage to optimise the signal-to-noise ratio by compressing the code into a short time interval. The matched filter will achieve the optimum results regardless of the form of the transmitted signal, so the coding serves only to decrease the level of the range side-lobes which affect the contrast resolution of the resultant ultrasound image. An example of a 4-chip uncoded signal and a Barker coded signal is shown in Figure 5.1.

This clearly illustrates how the use of the Barker code and an appropriately designed matched filter would result in significantly reduced range-lobes.

It is possible to remove the range side-lobes by using a multiple transmit code, such as the Golay code. These are designed so that the range lobes resulting from each transmit will cancel out, leaving only the desired main lobe. This is illustrated in Figure 5.2.

The disadvantage of this technique is that it requires two transmissions for each image line which will reduce the maximum frame rate achievable and that this approach only works perfectly for stationary scatterers. Any motion of the scattering / reflecting objects will introduce an error in the decoding, the severity of which will depend on the magnitude of the velocity.

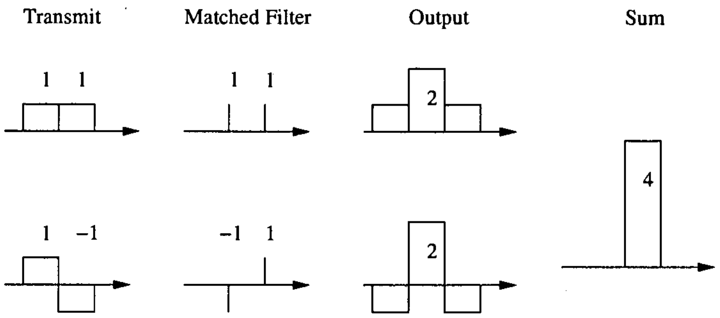

**Figure 5.2:** *Illustration of Golay code.*

Chirp coding differs from the previous two techniques in that it is based on modulating the frequency of the transmitted signal. Generally, this modulation will take the form of a linear ramp, giving a signal which could be expressed as:

$$s(t) = w_0(t) \exp\left[2j\pi(at^2 + bt)\right] \tag{5.1}$$

Where $w_0(t)$ is the window function, $a$ is the rate of change of frequency and $b$ is the centre frequency. The matched filter output for this signal would be:

$$y(t) = \int_{-T/2}^{T/2} s(t-\tau)s^*(\tau)\mathrm{d}\tau \tag{5.2}$$

Which becomes:

$$y(t) = \exp\left[2\pi j(at^2 + bt)\right] \int w_0(t-\tau)w_0^*(\tau)\exp\left[-2\pi jat\tau\right]\mathrm{d}\tau \tag{5.3}$$

Which is essentially the Fourier transform of the autocorrelation function of the window function, which leads to the conclusion that the choice of window function is critical for the control of the range side-lobes and the main lobe width. Given the importance of the window function, it is not surprising that literally hundreds of different window designs have been described in the literature, see for example Harris [57], Nuttal [58] and Geckinili and Yavuz [59].

According to Chiao et al. [2], using a square window ($w_0(t) = 1$) results in the smallest -3 dB mainlobe width, but the range side lobes are then only 13 dB below the mainlobe. They also quote the other extreme when the window function takes the form of a Gaussian or cosine square window in which case the range side lobes are 100 dB below the mainlobe, although the mainlobe width is significantly increased. Takeuchi et al. [60] state that the range side-lobe amplitude should be at least 60 dB below the mainlobe to produce clinically acceptable images. It is therefore evident that the choice of window function is extremely important in the area of medical ultrasound imaging.

There have been a number of publications describing the use of coded excitation in the context of medical ultrasound systems. M. O'Donnell [56] describes a system based on the transmission of 'pseudo-chirp' codes and presents theoretical and practical results which shows that using such a form of coded excitation is able to offer a 15 - 20 dB improvement in signal-to-noise ratio along with a corresponding improvement in imaging depth of 40 - 50 mm. Rao et al. [61] state that the fact that ultrasonic attenuation in soft tissue increases with frequency places an upper limit of the frequency which can be used of about 7 MHz, with corresponding limits on the imaging resolution obtainable. Although this would depend very much on the application, for example, intra-vascular transducers operate at 20 MHz, but they only require a very short range. Rao et al. [61] go on to describe a system which allows the use of linear swept frequency modulated pulses with a 6 dB bandwidth of 1 MHz and demonstrate that this is able to improve the SNR by a factor of 20 and offered similar resolution to a conventional short-pulse system despite have a pulse length of $20\mu s$. Y. Takeuchi [60] describe a two term apodization function which is able to offer time / range side-lobes which are more than 100 dB down from the mainlobe when used with a 100 wavelength duration, linear chirp. They compare this to conventional cosine-square apodization which can reduce the side-lobes to be about 60 dB down from the mainlobe. Misaridis et al. [62] review the potential of coded excitation in medical ultrasound imaging and describe a coded excitation system based on a modified commercial scanner. They also described the use of pre-distorted linear FM chirp signals, where the distortion introduced was designed to reduce the effects of time / range side lobes, in a similar manner to the work described in [60]. They also demonstrated that this system was able to offer improvements in the imaging depth while preserving both axial resolution and contrast. Two years later, Pedersen et al. [63] published the results of a clinical comparison between conventional pulse excitation and chirped excitation. This study was based on a modified clinical scanner which allowed rapid toggling between chirp and pulse excitation to simultaneously produce identical image sequences with both techniques. Nine healthy, male volunteers were scanned and the results were analysed by three skilled medical doctors who were blinded to which technique was being used. They were asked to assess the depth at which the image quality decreased and the depth at which the image would be insufficient for clinical diagnosis. The results showed that an average increase in imaging depth of nearly 20 mm was obtained through the use of the coded excitation technique and side-by-side comparison shows that the coded image quality was consistently rated better. The authors concluded from this that the use of coded excitation with linear FM chirps was able to improve the imaging depth and the image quality in a clinical environment. The technique of coded excitation has recently been adopted by a number of clinical ultrasound manufacturers, see for example G.E. Medical Systems [64] (G.E. Health Care, Chalfont St. Giles, UK).

It is therefore apparent that the technique of coded excitation and in particular, linear FM chirp coding, has the potential to offer many benefits to the field of medical ultrasound imaging. However, one of the complications is the need to design an appropriate apodization window to limit the formation of range / time side-lobes which occur as a result of using a matched filter processing technique. The fractional Fourier transform offers an alternative way of processing linear FM chirp signals which has the potential to offer similar levels of pulse compression to the matched filtering technique, but can operate without a-priori knowledge of the transmitted signal and, as is shown below, is able to produce results which demonstrate significantly lower range / time side-lobes than the matched filtering technique even when a square apodization window was used. The fractional Fourier transform is introduced in more detail in the next section.

## 5.3 The Fractional Fourier Transform

The fractional Fourier transform represents a generalisation of the conventional Fourier transform with an additional *order* parameter, $a$. The $a$th order fractional Fourier transform is mathematically equivalent to the $a$th power of the conventional Fourier transform operator $\mathcal{F}$. For integer values of $a$, the concept of $\mathcal{F}^a$ is readily understood; $\mathcal{F}^0 = \mathcal{I}$ is simply the identity operator, while $\mathcal{F}^1$ is the conventional Fourier transform. It can be seen that any integer power of the Fourier transform can be obtained by repeating the transform, i.e. $\mathcal{F}^1\mathcal{F}^1 = \mathcal{F}^2$. Applying this to a signal, $\mathcal{F}^2 x(t)$ would result in the time reversed signal, while $\mathcal{F}^3 x(t)$ gives the reversed Fourier transform and $\mathcal{F}^4 x(t)$ gives the original signal.

The conventional Fourier transform is a form of the standard integral transform defined by:

$$X(f) = \int B(f,t)x(t)\mathrm{d}t \tag{5.4}$$

In equation 5.4, $B(f,t)$ is the kernel of the transform which in the specific case of the conventional Fourier transform is defined as:

$$B(f,t) = \exp\left(-j2\pi f t\right) \tag{5.5}$$

For the fractional Fourier transform, the kernel $B(f,t)$ becomes [65]:

$$B_\alpha(t_\alpha, t) = A_\phi \exp\left[j\pi\left(t_\alpha^2 \cot\phi - 2t_\alpha t \csc\phi + t^2 \cot\phi\right)\right] \tag{5.6}$$

Where,

$$A_\phi = \sqrt{1 - j\cot\alpha} \tag{5.7}$$

And,

$$\phi = \frac{\alpha\pi}{2} \tag{5.8}$$

The equivalence of this with the conventional Fourier transform kernel may be seen by setting $\alpha = 1$, in which case $\cot\phi = 0$ and $\csc\phi = 1$ which leaves $B(t_\alpha, t) = A_\phi \exp\left[-j2\pi t_\alpha t\right]$.

The change in variables from $f$ to $t_\alpha$ is required because we are no longer dealing with frequency. At a transform order of $\alpha = 1$, then the fractional Fourier transform is equivalent to the conventional Fourier transform and it is only in this case that it would be valid to refer to 'frequency'. The true meaning of the $t_\alpha$ variable is best illustrated through an alternative interpretation of the fractional Fourier transform, which is related to the concept of time-frequency analysis.

The conventional Fourier transform can be used to analyse the frequencies which are present in a particular signal, but it will give no information about *when* those frequency components occurred. Time-frequency analysis techniques allow the frequency content to be analysed at any given time within the signal, there-by allowing the frequency content to be analysed over time. This can be likened to a musical score, where the notes described the frequency to be played at each given time instant. Further explanation of time-frequency analysis is beyond the scope of this work, but the reader is pointed to Loen Cohen's book [66] which provides a very thorough introduction to the subject.

As described in [66], there are numerous different time-frequency analysis techniques, such as the short-time Fourier transform and wavelets, but one which is of particular relevance is the

Wigner distribution, which can be defined as:

$$W(f,t) = \int f\left(t - (\tau/2)\right) f^{*}\left(t + (\tau/2)\right) \exp\left[j2\pi f\right] \mathrm{d}\tau \tag{5.9}$$

Now consider a linear FM chirp signal, defined by:

$$x(t) = \exp\left[j2\pi(at^2 + bt + c)\right] \tag{5.10}$$

where $a$ determines the rate of change of frequency and $b$ controls the centre frequency. The frequency of a signal may be defined as the rate of change of phase, which for the signal expressed by equation (5.10) results in:

$$\phi'(t) = 2at + b \tag{5.11}$$

Equation (5.10) was used in Matlab to create a model chirp signal with $a = -1 \times 10^{12}$,$b = 1 \times 10^{6}$ and $c = 0$. The resulting time and frequency domains for this signal may be seen in Figure 5.3. In this case, the signal was also windowed using a Hanning window to reduce the effects of ringing. Note that only the real part of the signal was considered.

However, much more information about the spread of energy over frequency and time can be obtained through the use of the Wigner distribution, as shown in Figure 5.4, which was calculated using the full analytic signal resulting from equation (5.10). This clearly shows how the energy of the signal is distributed, not only in frequency, but also in time. As would be expected for a linear FM chirp signal, the frequency increases over the duration of the chirp and the centre frequency is at around 3 MHz, which agrees with the frequency domain signal shown in Figure 5.3.

Projecting the Wigner distribution of a signal onto the time axis gives the time-domain envelope of the signal, while projecting onto the frequency axis gives the frequency domain envelope, or the PSD. This idea can be extended through the use of the Radon transform [66], which allows a two-dimensional function to be projected onto an arbitrary axis. In this case, it would be possible to project the Wigner distribution of a signal onto an axis making an angle $\phi$ to the time axis. Simple observation of the situation illustrated in Figure 5.4 reveals that at a certain angle, $\phi_{\text{opt}}$, this projection will be maximally compressed. This is the basis for an alternative interpretation of the fractional Fourier transform, as a Radon transform of the Wigner

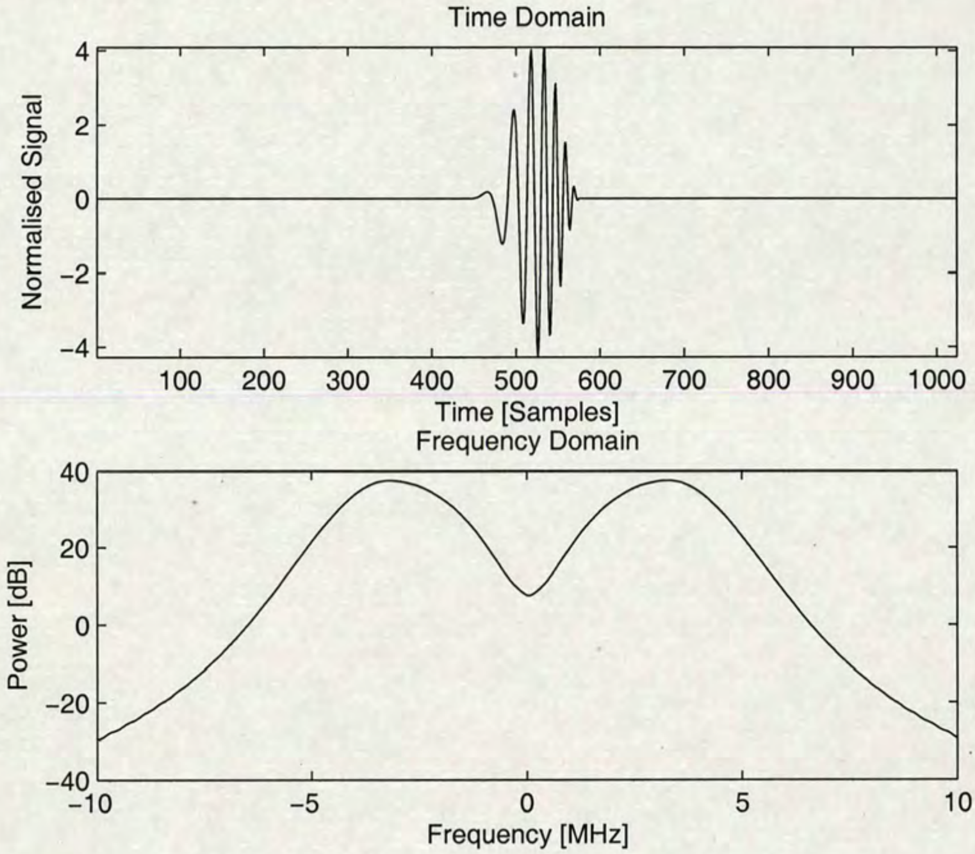

**Figure 5.3:** *Illustration of synthetic chirp signal in time and frequency domains. The frequency domain plot was obtained using the Fast Fourier Transform (FFT) algorithm with the real part of the signal defined by equation 5.10.*

distribution. The angle, $\phi$ corresponds to the fractional transform order, therefore there will be an optimum transform order at which maximum pulse compression will be achieved.

It should be noted from the above interpretation that, unlike the conventional Fourier transform, the fractional Fourier transform will not be shift invariant. Inspection of the geometry of the rotated Wigner distribution reveals that if the chirp signal is shifted in time, then the position of its projection onto the transform axis will also be shifted. The reason the fractional Fourier transform is not shift invariant can be seen by inspecting the transform kernel as expressed in equation 5.6. In the case of the conventional Fourier transform, the kernel takes the form of a series of sines and cosines, but it is clear from equation 5.6 that in the fractional case the kernel will be of the form of a series of chirps. Firstly, the $-2t_\alpha t \csc\phi$ term causes the center frequency of each of these chirps to be dependent on $t_\alpha$, whilst the $t_\alpha^2 \cot\phi$ term defines a similar relationship for the phase. It is therefore clear that the value of $t_\alpha$ which results in the

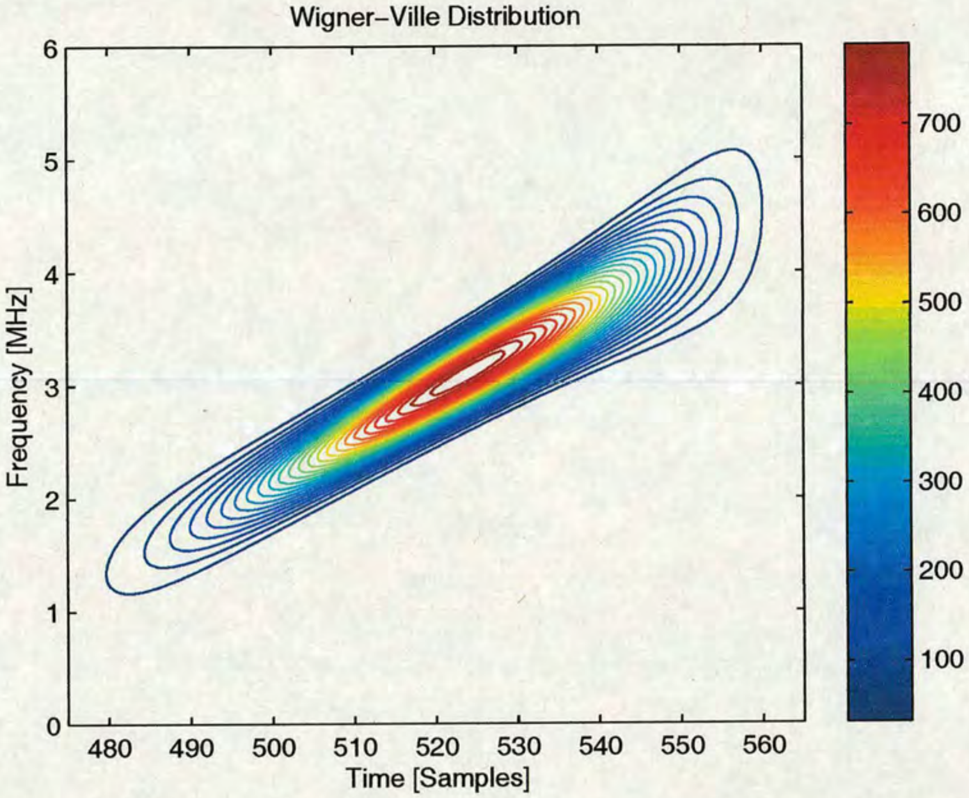

**Figure 5.4:** *Wigner-Ville distribution of synthetic chirp signal showing distribution of signal energy over time and frequency.*

peak response for a particular chirp will depend on the position of that chirp with respect to the chirp defined by the transform kernel. It is also clear that it would be possible to implement the fractional Fourier transform as a bank of matched filters, each with different center frequencies and phases.

### 5.3.1 Optimum Transform Order Determination

As has been illustrated above, the optimum transform order is defined as the transform order which is equivalent to the angle of the projection axis which would result in the greatest degree of pulse compression. In other words, it is the transform order that minimises the width of the projection of the signal. It is also possible to define the optimum transform order in terms of the second order central fractional Fourier transform moments, as demonstrated by Stanković et al. [67], who use the work published by Alieva et al. [68] on fractional Fourier transform moments to extend the well known concept of estimating signal width in either time or frequency domains using second order moments.

The optimum transform order is, therefore, related to the properties of the signal, such as the chirp rate or bandwidth, the sampling frequency and the number of samples in the signal. Capus et al. [69] provide a geometrical derivation of the optimum transform order as:

$$\phi_{\text{opt}} = \tan^{-1}\left(\frac{f_s^2/N_{\text{sig}}}{2a}\right) \tag{5.12}$$

Where $f_s$ is the sampling frequency, $N_{\text{sig}}$ is the length of the signal in samples, $a$ is the chirp rate parameter used in equation (5.10) and $\phi$ is the transform order as defined in equation (5.6). This method allows the optimum transform order to be determined if the parameters of the transmitted chirp are already known, but more interestingly, it also allows the chirp rate to be determined if the optimum transform order could be obtained by some other method.

It has been shown that at the optimum transform order, the projection of the support of the signal will be maximally compressed. This means that the transform domain signal formed at the optimum transform order will contain the highest peak energy, therefore it will be possible to determine this transform order by maximising the peak energy. It is possible to achieve this by evaluating the fractional Fourier transform of a signal over a range of transform orders yielding a two dimensional data set, from which the regions of local maxima may be determined. Evaluating the fractional Fourier transform for the synthetic chirp signal described above over transform orders between $\phi = 0$ and $\phi = \pi$ gave the results shown in Figure 5.5.

Inspection of the resulting data reveals that the top and bottom lines, corresponding to $\alpha = 0$ and $\alpha = 2$, are equivalent to the time-domain and reversed time-domain signals respectively. The centre line, corresponding to $\alpha = 1$ is equivalent to the conventional Fourier transform of the signal and therefore the width of the signal in this transform domain is determined by the bandwidth of the time-domain signal.

It is also apparent that there is one clear region of global maximum, which occurs at $\alpha \approx 0.5$. Zooming in on only this region of the data gives the results shown in Figure 5.6. This would appear to indicate the optimum transform order, $\alpha_{\text{opt}} = 0.55$. Substituting $a = 1 \times 10^{12}$, $N_{\text{sig}} = 1024$ and $f_s = 50 \times 10^6$ into equation (5.12) gives $\phi_{\text{opt}} = 0.8845$, which from equation (5.6) gives $\alpha_{\text{opt}} = 0.5631$, which is in agreement with Figure 5.6.

An automated system for determining the optimum transform order from a signal was developed based on searching the transform domains, as shown in Figure 5.5, for regions of local maxima. This was achieved using a two-dimensional gradient method and searching for areas

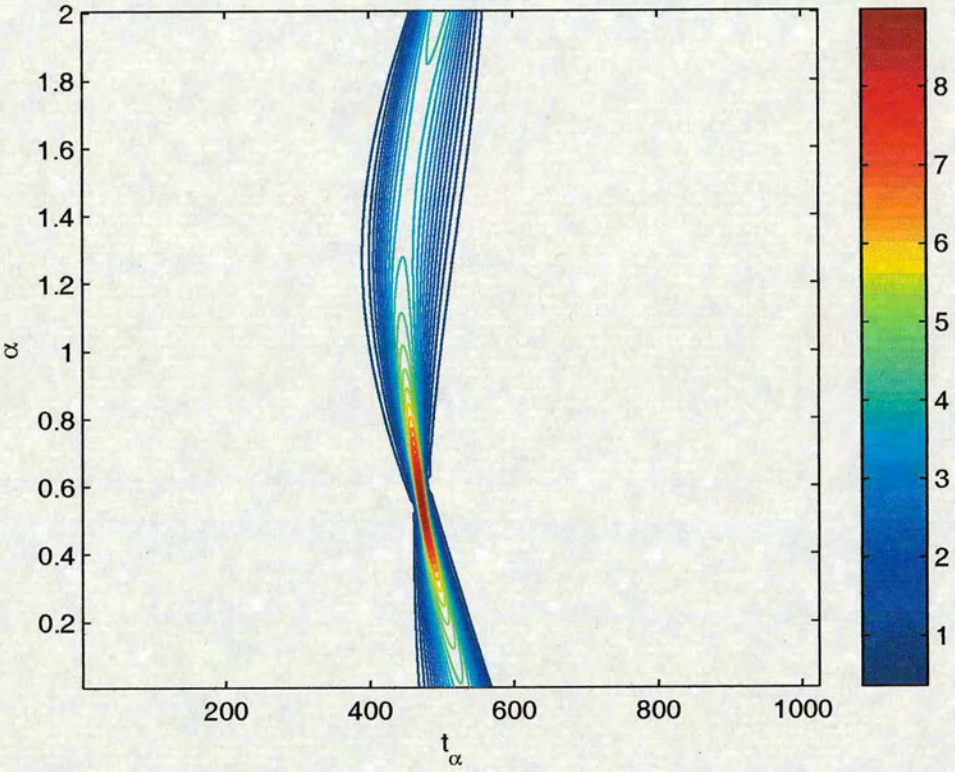

**Figure 5.5:** *Evaluation of the fractional Fourier transform of the synthetic chirp signal over a range of transform orders between* $\phi = 0$ *and* $\phi = \pi$.

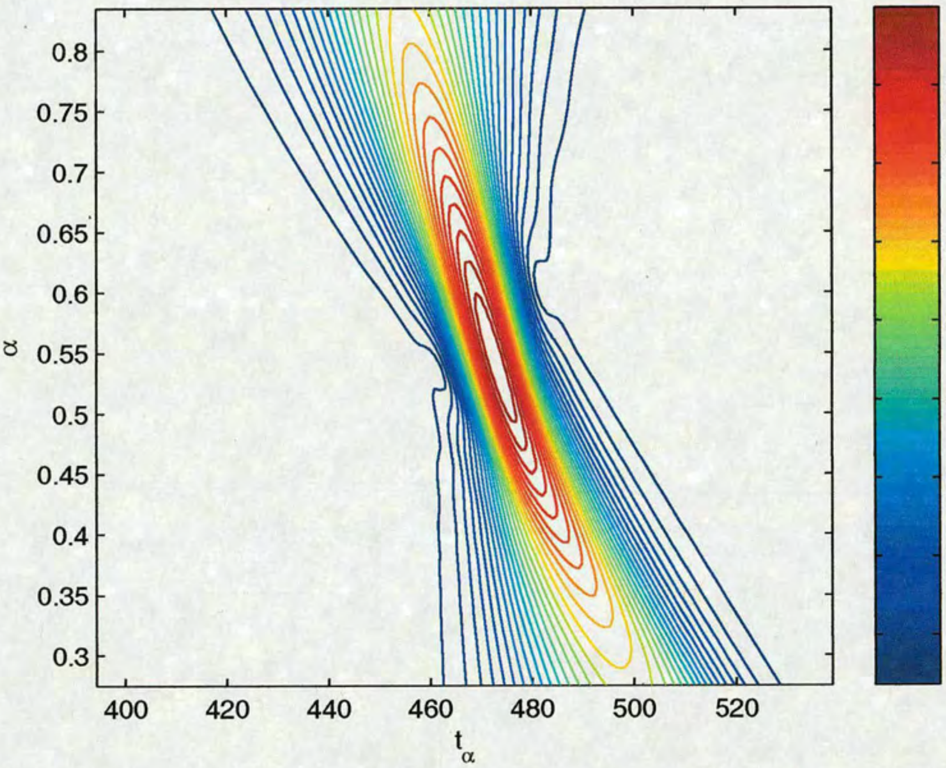

**Figure 5.6:** *Zoomed section of Figure 5.5, showing region of global maximum corresponding to the optimum transform order.*

where the first derivative was close to zero and the second derivative was negative. Since it was not possible to search for points whose first derivative was exactly zero because of the discrete nature of the transform domains, this method would return a number of points around the true local maxima. It was therefore necessary to use some form of thresholding to select only the most significant of these points. This was achieved by considering only those points whose amplitude was greater than the global maximum minus the mean, plus one standard deviation of the whole data set. The use of this value saved the need to manually specify a threshold and was found to give good results in all the cases considered. Once thresholded, the mean ordinate on the $\alpha$ axis of the remaining points was used as the optimum transform order. Applying this method to the fractional Fourier domains shown in Figure 5.5 gave $\phi_{\mathrm{opt}} = 0.8674$ or $\alpha_{\mathrm{opt}} = 0.5522$.

### 5.3.2 Discrete Implementations

The definition of the discrete Fourier transform (DFT) is well known and understood, however there is currently no such formal definition of a discrete implementation of the fractional Fourier transform. The reasons for this are laid out in Ozaktas' book [65], however one of the most fundamental is that there is also no formal definition of the discrete Wigner distribution owing to the difficulty in defining exactly what one sample would represent. There are also difficulties in defining rotations of discrete lattices, such as an approximation of the discrete Wigner distribution. However, there are a number of approximations of the discrete fractional Fourier transform, two of which have been used for the work described.

Firstly, the method developed by Ozaktas et al. [70] was used because of its relatively low computational complexity. With this method, the transform of a signal with a time-bandwidth product of $N_{\mathrm{TB}}$ could be computed in $O(N_{\mathrm{TB}} \log N_{\mathrm{TB}})$ time [70]. This technique was used when a large number of transforms were to be performed, for example, when determining the optimum transform order by searching through the transform domain as described above. This technique will correctly transform the samples of an input signal, $x(t)$ into the samples of the fractional Fourier transform, $X(t_\alpha)$ under the assumption that the representations $X(t_\alpha)$ of the signal $x$ in all fractional Fourier domains are approximately confined to the interval $[-\Delta t/2, \Delta t/2]$. This corresponds to assuming that the Wigner distribution of $x(t)$ is approximately confined to a circle of diameter $\Delta t$. In practice, this condition can be met for any signal by choosing $\Delta t$ to be sufficiently large [65].

The second method was developed by Candan et al. [71]. This technique works by developing a transform matrix, which may then be used to transform a signal in the same manner as for the discrete Fourier transform matrix. This method differs from that described in [70] and others in that it was developed so that its definition would have the following properties:

1. Unitarity
2. Index additivity
3. Reduction to the DFT when the order is equal to unity
4. Approximation of the continuous fractional Fourier transform

Although both of these techniques are approximations of the same thing, it must be noted that they produce slightly different results. It was found that the method described by Ozaktas et al [70] was more suitable for determining the optimum transform order by searching for peaks in the transform domain because it gave more distinct peaks as well as being less computationally complex. It was not, however, possible to use this method in situations where a signal had to be recovered from the transform domain, perhaps after some processing, so in these cases, the method described by Candan et al. [71] was used.

### 5.3.3 Signal Recovery

One of the key advantages of the fractional Fourier transform is its ability to separate signals which overlap in time and / or frequency. Consider the Wigner distribution of two such signals, as shown in Figure 5.7. The two chirp signals were centred in time at 512 samples and 564 samples respectively, as can be observed from Figure 5.7. However, this also illustrates one of the significant problems with the Wigner distribution, which is the generation of the cross-terms which may be seen between the two chirp signals. These are a result of the way the Wigner distribution is calculated and as they are essentially of an oscillatory nature, they can usually be countered by smoothing the distribution, although this will result in a loss of information.

The fractional Fourier transform has been described above in terms of projections of the Wigner distribution onto an arbitrary axis using the Radon transform. Inspection of Figure 5.7 clearly shows that the two chirps overlap in time and in frequency and cannot therefore be separated. However, if this Wigner distribution were to be projected onto an axis whose angle was perpendicular to the chirps, then it may be seen that a degree of separation would be achieved.

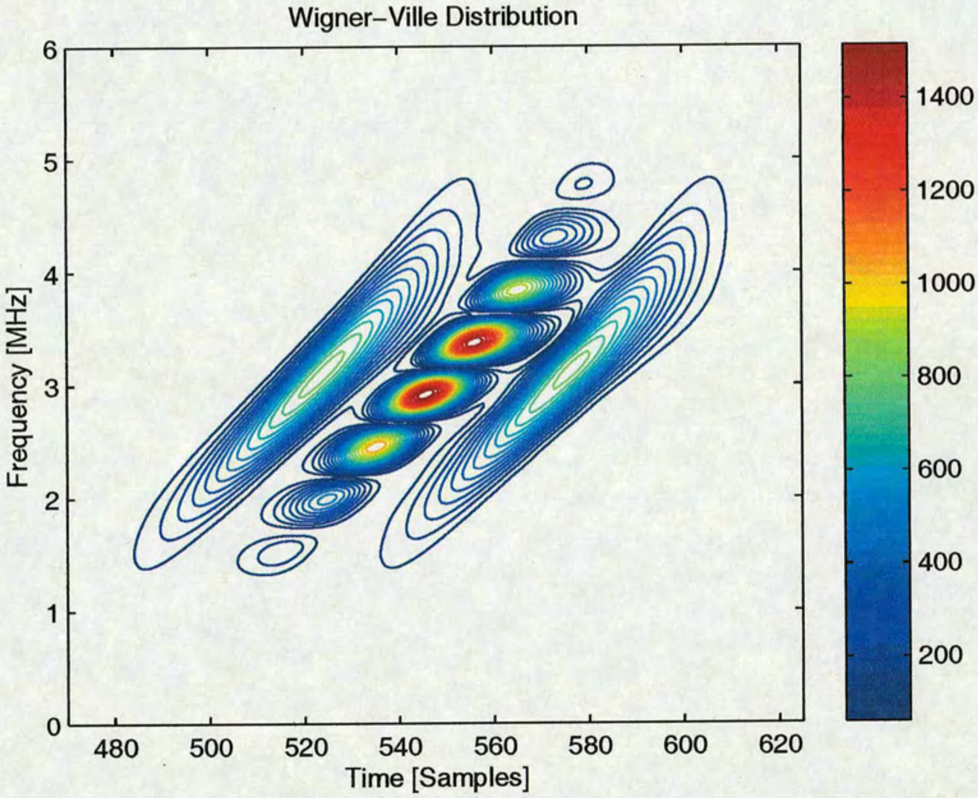

**Figure 5.7:** *Wigner-Ville distribution of a pair of chirped signals which overlap in both time and frequency.*

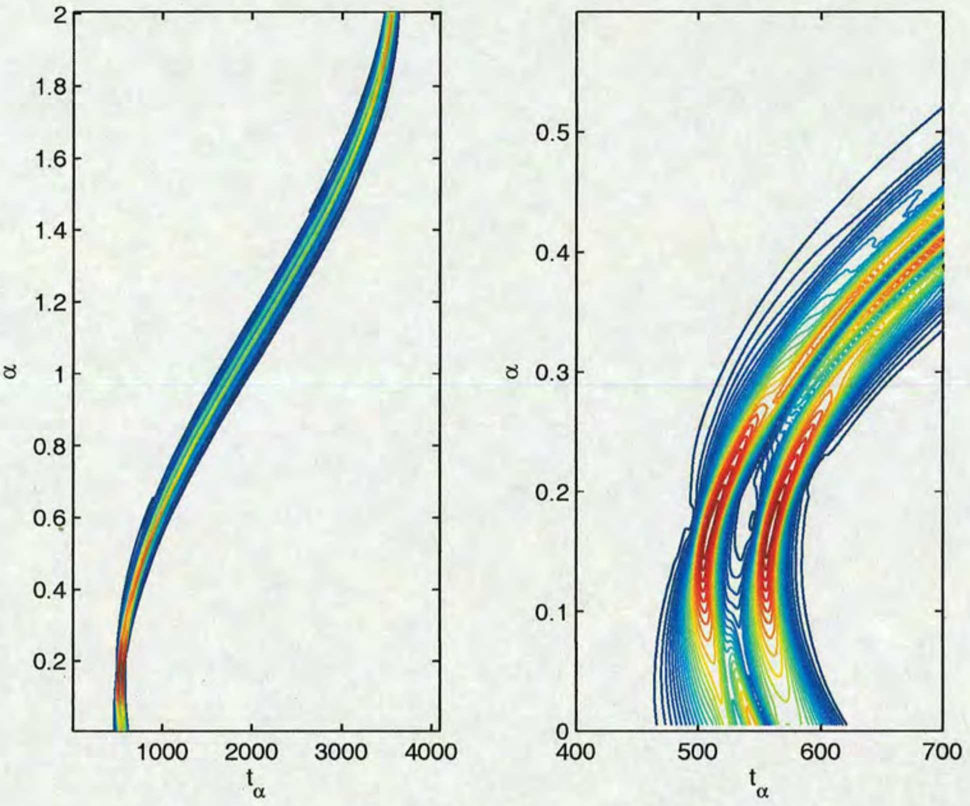

**Figure 5.8:** *Fractional Fourier domains of the two chirp signal, over the whole range of transform orders on the left and zoomed in around the region of interest on the right. Clearly shows separation of the two chirps at* $\phi_{\text{opt}} \approx 0.19$.

Therefore, the fractional Fourier transform should be able to separate the two chirps at the optimum transform order. Evaluating the fractional Fourier transform for this signal over a range of transform orders gave the results shown in Figure 5.8. Given that the chirps were generated using the same parameters as for the single chirp case described above, it would be expected that the optimum transform order would be the same. This was observed to be the case, with the two chirps being well separated when $\alpha \approx 0.55$.

Putting $a = -1 \times 10^{12}$, $N = 4096$ and $f_s = 50 \times 10^6$ into equation (5.12) gave $\phi_{\text{opt}} = 0.3052$, or $\alpha_{\text{opt}} = 0.1943$. Using the automated optimum transform order determining algorithm described above gave $\phi_{\text{opt}} = 0.2657$, which was deemed to be sufficiently accurate. The accuracy could be improved by limiting the range of transform orders which are used during the search for local maxima, however this value was obtained by searching over the entire range. Transforming the signal with a transform order of $\alpha = 0.1943$ gave the results shown in Figure 5.9. These results clearly illustrate the difference between the two implementations of the fractional

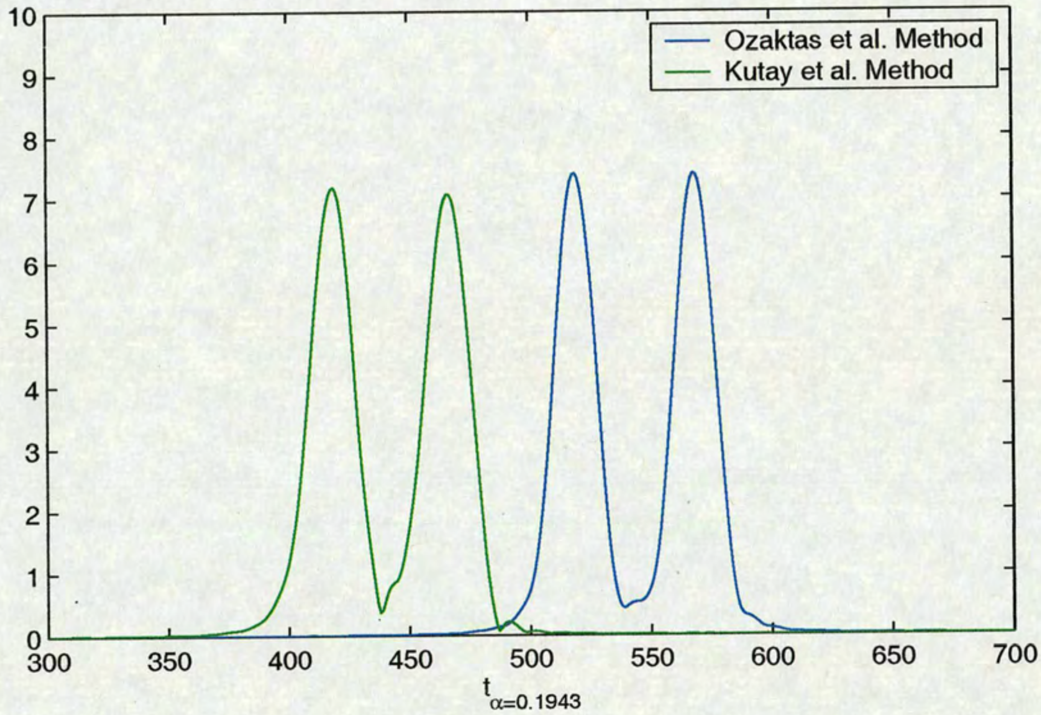

**Figure 5.9:** *Transform domain signal with* $\alpha = 0.1943$*, evaluated with both the Ozaktas et al. method and the Kutay et al. method.*

| Original Position | Candan et al. | Ozaktas et al. |
|---|---|---|
| 512 | 525 | 614 |
| 564 | 577 | 664 |

**Table 5.2:** *Positions of recovered chirps. All in units of samples.*

Fourier transform. Although both of the transformed signals are of similar shape, the peaks occur at different absolute positions in the transform domain although in each case, they are approximately equally separated. The different position has consequences for the recovery of signals. In theory, it is possible to use a simple windowing function to isolate a portion of the transform domain signal and then invert the transform to recover the desired signal component. This is exactly equivalent to conventional Fourier domain filtering, except that the fractional Fourier transform is not time invariant. Therefore, although conventional Fourier filtering will yield the desired frequency components over the whole signal, such filtering in the appropriate fractional Fourier domain will preserve the time information and hence return the desired signal component at the time at which it occurred.

In the case considered here, there are two chirp signals which overlap in both time and frequency domains, however they can be shown to be completely separate in the transform domain corresponding to the optimum transform order. A Hanning window was used to isolate each peak in the transform domain and the result was subjected to the inverse transform. In the case of the Ozaktas et al. method, this was achieved using a transform order $\alpha = -0.1943$, whereas for the Kutay et al. method the transform matrix was inverted using the internal Matlab function for inverting matrices. This gave the results shown in Figure 5.10. The time at which the chirps occurred could be recovered by finding the maximum of the envelope for each one. Table 5.2 shows the positions determined from each of the recovered signals for each method compared with the positions of the original chirps.

### 5.3.4 Direct Recovery of Time Information

It has been shown that it is possible to isolate and extract individual chirps from a signal by windowing around the corresponding feature in the transform domain and inverting the transform [72]. However, once done, the envelope of the result still does not have the level of improvement in axial resolution which could be achieved through the use of matched filters. At the appropriate transform order, the fractional Fourier transform of a signal will be similar to the results obtained using a matched filter in terms of pulse compression.

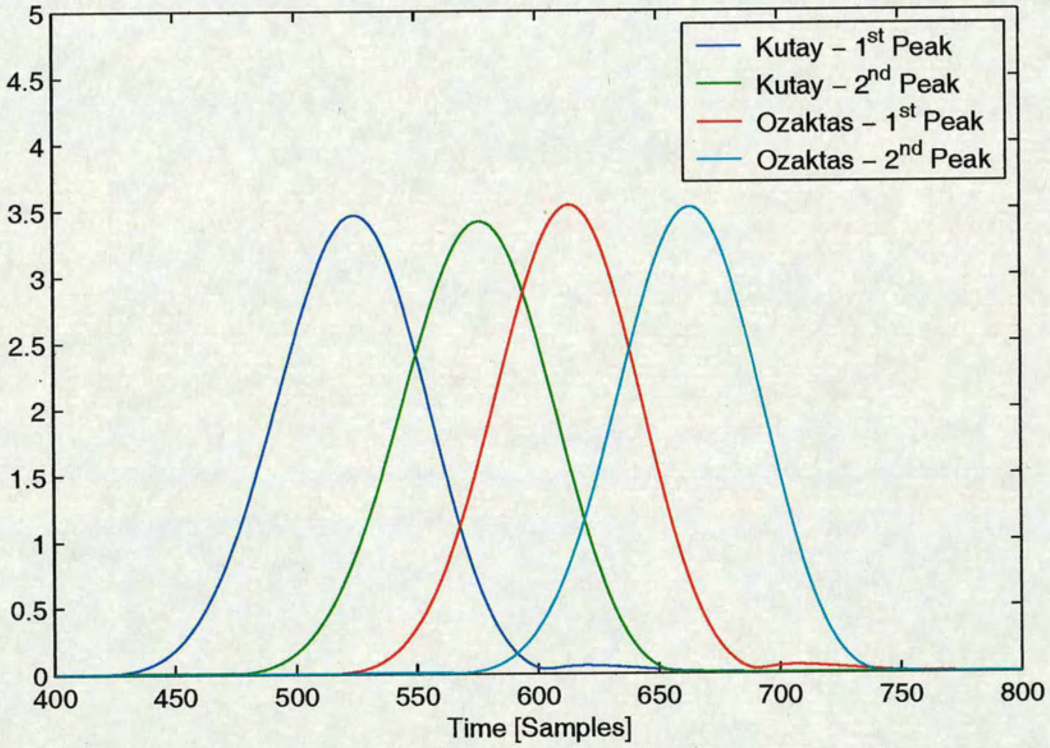

**Figure 5.10:** *Envelopes of recovered chirp signals, showing difference between Ozaktas et al. and Kutay et al. methods.*

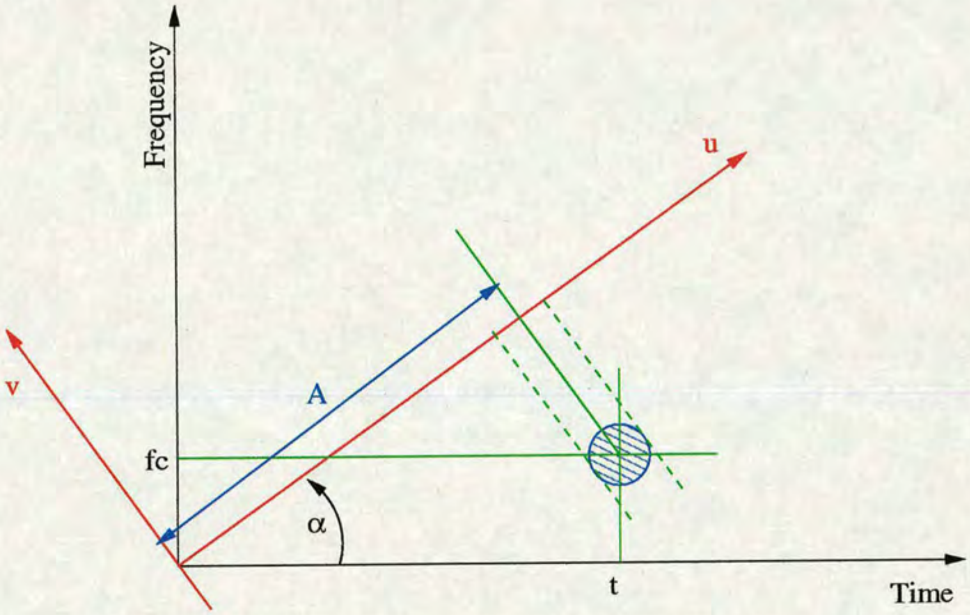

**Figure 5.11:** *Geometry of the time recovery problem*

The fractional Fourier transform is not time invariant in contrast to the conventional Fourier transform, which means that the transformed signal still contains time information. Using the definition of the fractional Fourier transform as a Radon transform of the Wigner distribution, one may arrive at the geometry shown in Figure 5.11. In this Figure, if the circle corresponding to the Wigner distribution of a hypothetical signal were to be moved in time, but not in frequency, then the position of its projection onto the $u$ axis would vary accordingly. Similarly, if time were kept constant but the frequency were varied, then its projection would also move. It may therefore be concluded that the position at which a signal projection occurs is related to both the frequency, or the centre frequency for a chirped signal, and the time at which the signal occurred. Therefore, if one of these two variables were known, it should be possible to extract the other.

Inspection of the geometry shown in Figure 5.11 results in the following expression for the time:

$$t(A) = \frac{\frac{2Nf_c}{f_s} - A\left(\sin\alpha + \cos\alpha\tan\left(\alpha + \pi/2\right)\right)}{\tan\left(\alpha + \pi/2\right)} \tag{5.13}$$

Where, $A$ is the position of the peak in the transform domain, $N$ is the number of samples, $f_c$ is the centre frequency of the transmitted chirp, $f_s$ is the sampling frequency and $\alpha$ the transform order which was used. The geometric relationship between the position of a feature in the fractional Fourier domain and the time at which the chirp that caused that feature existed,

| Original Position | Candan et al. | Ozaktas et al. |
|---|---|---|
| 512 | -433.9244 | -518.9769 |
| 564 | -476.0211 | -561.0736 |

**Table 5.3:** *Time-domain positions of chirp signals recovered directly from the fractional Fourier domain, without inverting the transform.*

as expressed by equation (5.13), may be used to determine relative distances between features. The key advantage of this method is that it is not necessary to invert the transform. This also means that the chirp detection resolution gained through the use of the optimum transform order, isn't lost by transforming the chirp back into the time domain.

Applying this technique to the two chirp problem described above gave the positions shown in Table 5.3. It is not possible to recover the absolute time information with this method, however it can be used to gain relative information about the distance between features in the signal. In the case of the two overlapping chirps considered here, using the direct time-domain position recovery technique on the results of either of the discrete implementations gave a distance between the two chirps of 42.0967 samples. The actual distance was 52 samples, so there is an error of 10 samples. To put this into context, assuming an acoustic wave propagation velocity of 1480 m/s and a sampling frequency of 50 MHz, this would equate to a distance of 0.1480 mm. Bear in mind that the minimum distance between two features to enable them to be completely separated with conventional, un-coded signals is given by the product of the propagation velocity and the period of the wave. Therefore, assuming a centre frequency of 3.5 MHz and a pulse length of one cycle, the minimum separation would be 0.4229 mm. It was therefore concluded that the error in the estimation of the distance between the two chirps was small.

An alternative approach is to recognise that equation (5.13) is simply a linear transform and can therefore be used to directly scale the axis of the transform domain to fit the time-domain. This can be done by setting $A_1 = 1$ and $A_N = N$ (in this case $N = 4096$), then the scaling factor would be given by:

$$s = \frac{N}{|t(A_N) - t(A_1)|} \tag{5.14}$$

Using this to scale the transform domain axis of the two chirp signal results in Figure 5.12, where the results of applying a matched filter have been overlaid for comparison. These results demonstrate that it is possible to directly relate features in the fractional Fourier domain with features in the time-domain. They also show that the fractional Fourier transform is able to

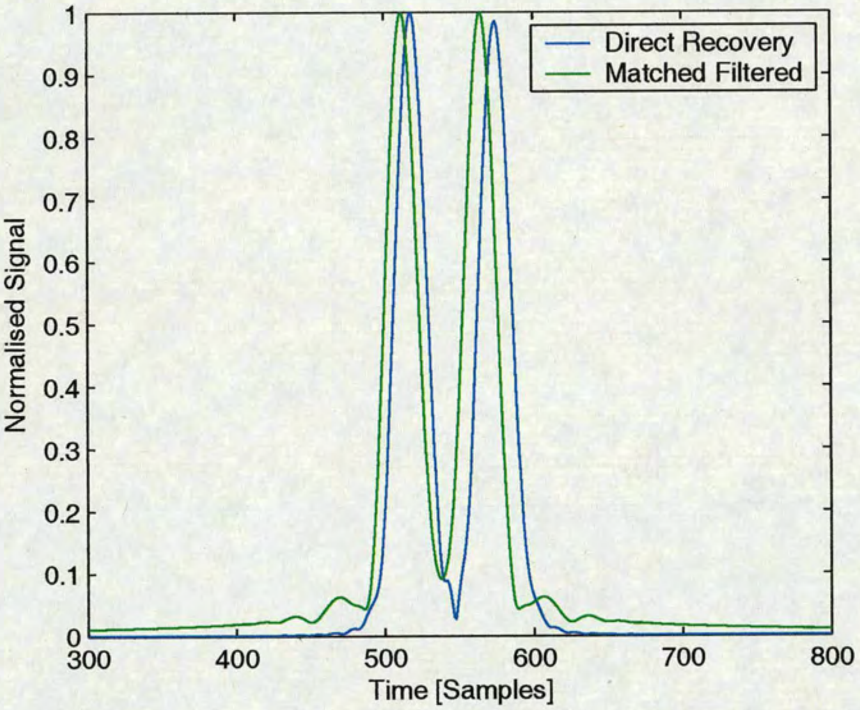

**Figure 5.12:** *Comparison of scaled transform domain signal with the results of applying a matched filter. Illustrates possibility of directly relating the transform domain signals to the time-domain.*

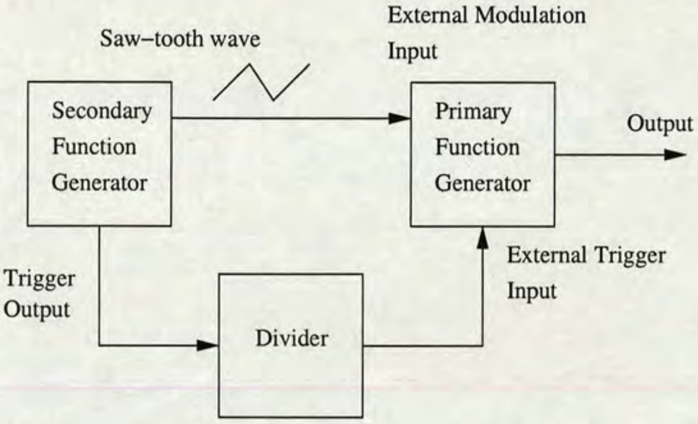

**Figure 5.13:** *Schematic of modified single crystal ultrasound system for the generation of approximately linear FM chirp signals.*

produce results which are very similar to those obtained using a matched filter in terms of resolution and position. It was also observed that the fractional Fourier method appeared to give a greater degree of separation between the two chirps. The matched filter results clearly show the presence of corruption due to side-lobes, which would be expected since the chirp generating system used did not allow for anything other than rectangular windowing of the transmit pulses. However, the results obtained with the fractional Fourier method are clearly less affected by the side-lobe problem. It was therefore concluded that the fractional Fourier method described above was less sensitive to the shape of the transmitted pulse.

## 5.4 Modified Single Crystal System

The single crystal ultrasound system described earlier was modified to allow the generation of approximately linear frequency modulated signals. This was achieved using a secondary function generator providing a signal to the frequency-modulation input of the original function generator. The secondary function generator was setup to produce a saw-tooth wave with a periodic time of twice the required pulse length. In this manner, the required chirp signal could be generated only for the rising portion of the modulating signal, thus creating an ‘up-chirp’. This is illustrated in Figure 5.13. The divider was based around a 74LS161 counter device and was designed to produce one trigger pulse at the output after every set of 16 trigger pulses at the input. This would give a pulse repetition frequency of 1/16th the trigger frequency from the secondary function generator. The trigger output of the secondary function generator went ‘high’ for the duration of the rising portion of the saw-tooth wave and could therefore be used to gate the output of the primary function generator. In this way, it was possible to only produce output signals corresponding to the rising portion of the modulating signal, thus creating up-chirps. However, it was found that the output of the primary function generator did not go completely to zero when the gate input was 'low'. The error was very small, but after passing through the RF power amplifier it became significant. It was therefore necessary to use an analogue switch circuit between the output of the primary function generator and the input to the RF power amplifier to ensure that there were no corrupting signals. With this system, it was possible to control the length of the transmitted signals by varying the frequency of the modulating saw-tooth wave. For the experiments described here, a frequency of 140.6 kHz was used, which gave a pulse length of 14 cycles. The chirp rate, or bandwidth could be controlled by varying the amplitude of the modulating signal. It was not possible to specify the exact bandwidth, so all of the experiments were performed using three 'standard' settings, referred to as 'low', 'medium' and 'high' chirp rate respectively. These corresponded to the first three graduation markers on the amplitude control knob of the secondary function generator.

Figures 5.14 and 5.15 show the transmitted signals and their corresponding Wigner-Ville time-frequency distributions respectively. This clearly illustrates two weaknesses of the chirp generating system. Firstly, it was not possible to implement any kind of windowing of the signals other than square, which will degrade the quality of the results obtained through the use of matched filters, as discussed above. Also, the chirps produced are not completely linear, which will have an impact on the degree of pulse compression which can be obtained using the fractional Fourier transform. However, it was observed that a large region of the transmitted signals was subject to a linear frequency modulation and that the non-linearity occurred mostly at the lower frequency end of the signal. Unfortunately, there was insufficient time to investigate possible methods for improving the signals in either of these respects.

## 5.5 Results of Matched Filtering & Fractional Fourier Transform

### 5.5.1 Phantom Setup

All of the results described below were obtained using a phantom consisting of a cylindrical block of tissue mimicking material immersed in a tank of water. The cylinder had three slits cut out of it of widths 1 mm, 2 mm and 3 mm, as illustrated in Figure 5.16. The 3.5 MHz, 100% bandwidth Panametrics transducer was used, arranged such that one slit in the phantom would

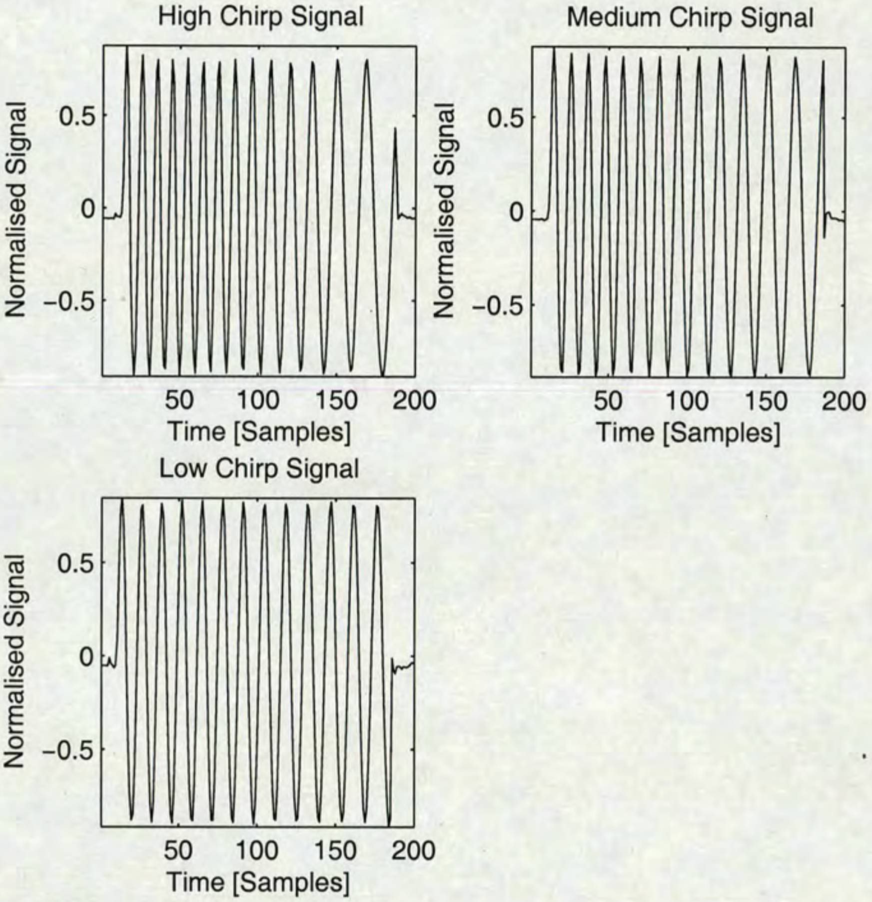

**Figure 5.14:** *Transmitted chirp signals captured prior to RF power amplifier stage.*

be within the focal region. Due to the relatively low sensitivity of this transducer (a consequence of making it with such a wide bandwidth), it was not possible to obtain signals from more than one slit at a time because the maximum available imaging depth was only around 70mm. Therefore, the phantom was rotated after each experiment to present the appropriate slit.

In order to confirm the geometry of the setup, the transducer was first driven with a single-cycle pulse, yielding the signal shown in Figure 5.17. For the case of the 3 mm wide slit, the 'focus' of the system was adjusting by moving the transducer closer to the phantom. This was necessary to ensure that the largest possible signal was received from the top and bottom edges of the slit.

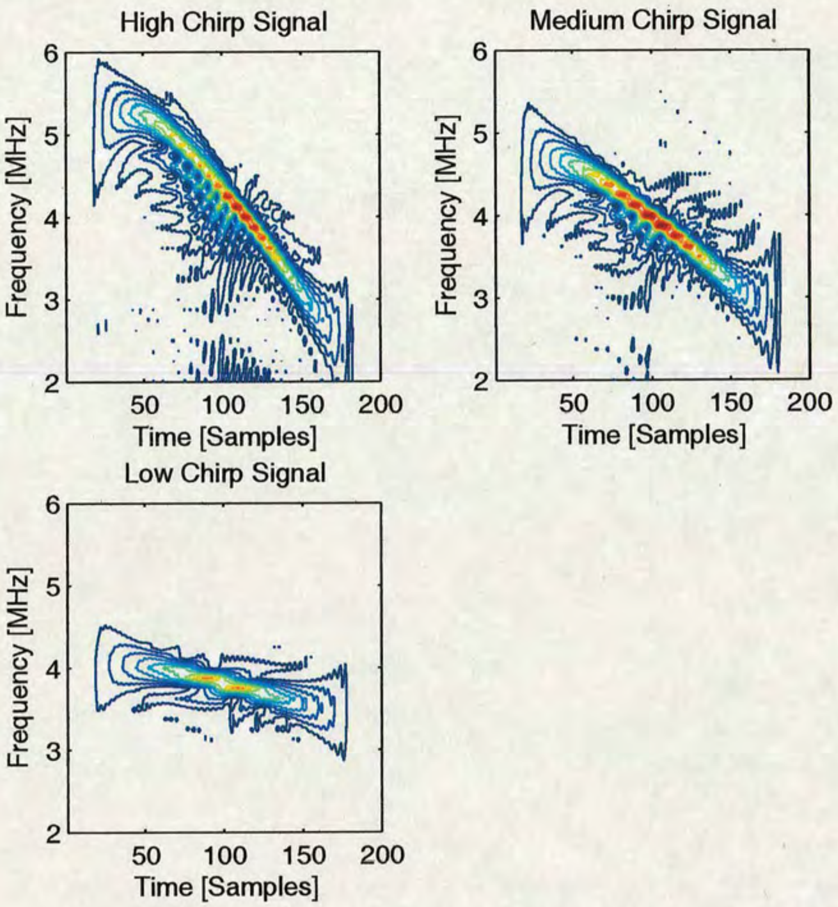

**Figure 5.15:** *Wigner distributions of the transmitted signals.*

### 5.5.2 Matched Filtering

The equipment was setup so that it would be possible to capture the transmitted signal prior to amplification by the RF power amplifier. This could be done in conjunction with the capture of the received echo signals. Matched filtering of the received signals was achieved by time reversing the recorded transmitted signal and convolving this with the received signal in Matlab. The results of doing this with the signals received from the phantom described above are shown in Figure 5.18.

### 5.5.3 Fractional Fourier Transform

The optimum transform orders for the signals were determined using the automated procedure described above, yielding the results shown in Table 5.4. The optimum transform orders for the low chirp rate signals were found to be too close to $\pi/2$ to be determined by the automated

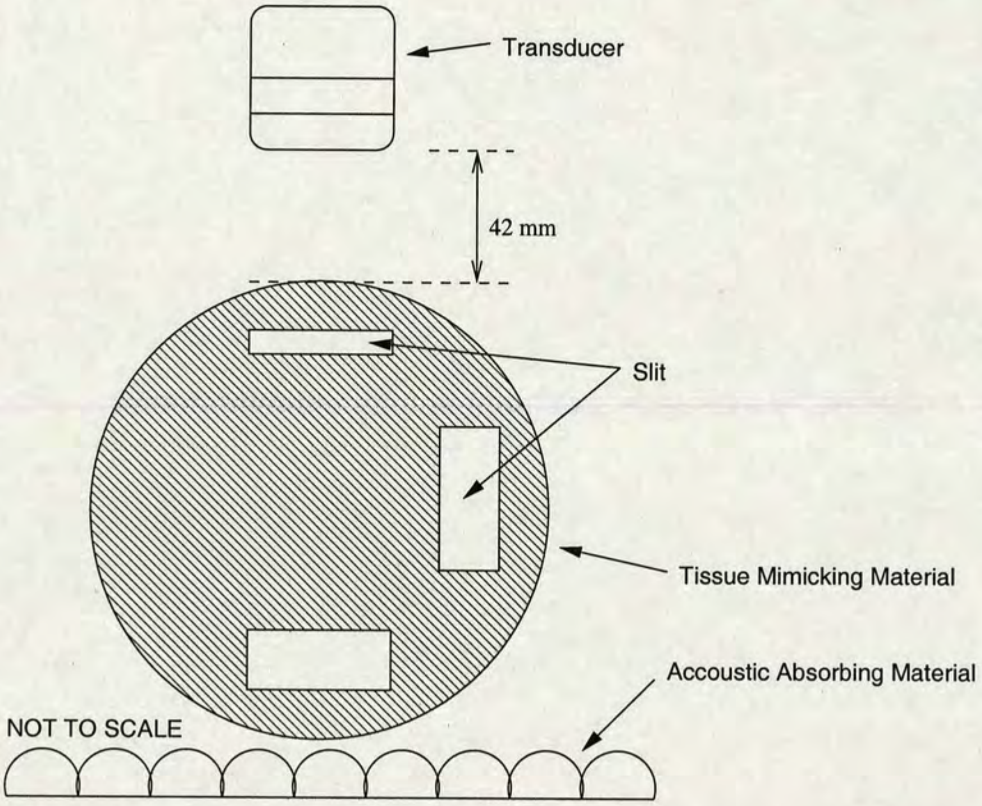

**Figure 5.16:** *Illustration of the phantom setup used for testing the fractional Fourier transform.*

| Chirp Rate | 1 mm | 2 mm | 3 mm |
|---|---|---|---|
| Low | - | - | - |
| Medium | 0.4919 | 0.4156 | 0.4623 |
| High | 0.2838 | 0.2883 | 0.3032 |

**Table 5.4:** *Optimum transform orders ($\alpha_{\text{opt}}$) determined using automated procedure for each of the signals. For the low chirp rate signals, the optimum transform order was very close to $\pi/2$, so they were not used further.*

method. Since a transform order of $\pi/2$ is just the conventional Fourier transform, no further analysis was performed using the low chirp rate signals as there was nothing to be gained. The matched filtering results shown in Figure 5.18 also demonstrate that the low chirp rate signals do not yield a significant improvement in axial resolution compared to the results for either the medium or high chirp rate signals. This is due to the axial resolution after matched filtering being inversely proportional to the bandwidth of the transmitted signal, therefore the lower bandwidth signal shows little improvement compared to the signals of higher bandwidth.

It was found that using an optimum transform order of, for example, $\alpha = 0.2838$ or $\alpha = 0.2883$ did not make a significant difference, therefore all further analysis was performed using the

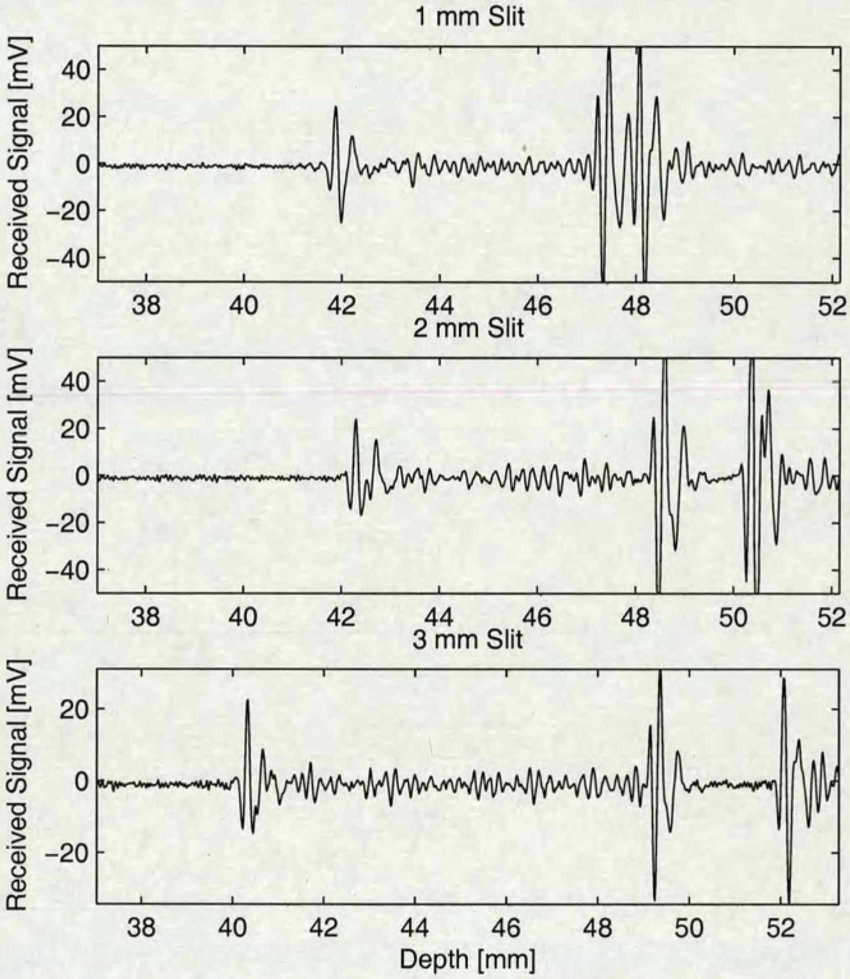

**Figure 5.17:** *Received signal after transmission of a single-cycle pulse. Clearly shows geometry of phantom setup, including distance between transducer and phantom and position and width of the slits.*

mean of the optimum transform orders shown in Table 5.4, for each signal case. Using these transform orders with the fractional Fourier implementation by Ozaktas et al. gave the results shown in Figure 5.19, which clearly demonstrate a similar degree of pulse compression to that shown by the matched filter results. It is also apparent that the results for the high chirp rate signal, which had the highest bandwidth, demonstrated a greater degree of pulse compression compared to those for the medium chirp rate. This was also in keeping with the matched filter results. However, performing the same transforms using the Candan et al. method gave the results shown in Figure 5.20. The transform matrices used to produce these results were generated using the same transform orders that were used for the Ozaktas et al. method and the order of approximation of the 's-matrix' was set to 64, which was found to give the best results.

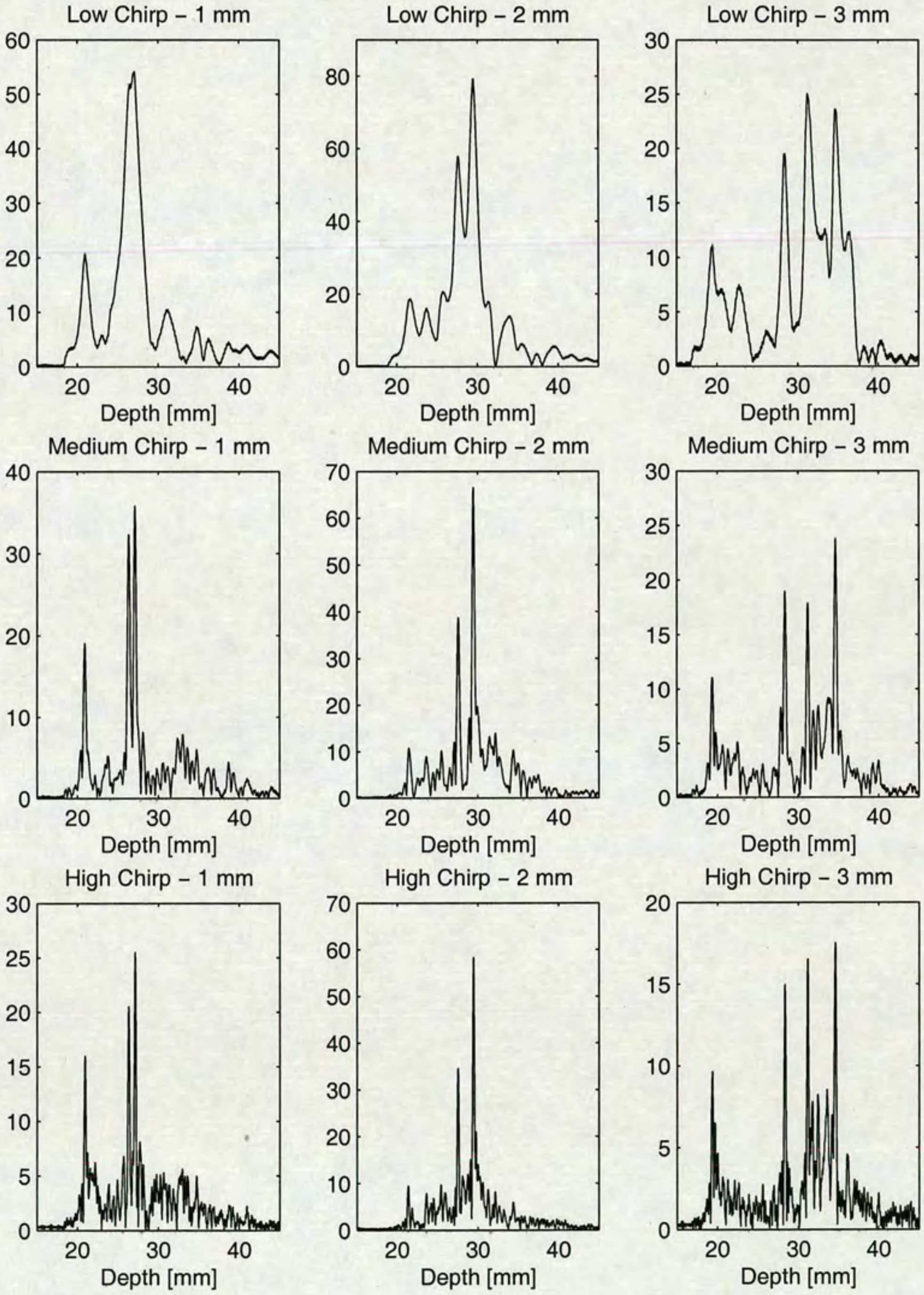

**Figure 5.18:** *Results of matched filtering with high and medium chirp rate signals.*

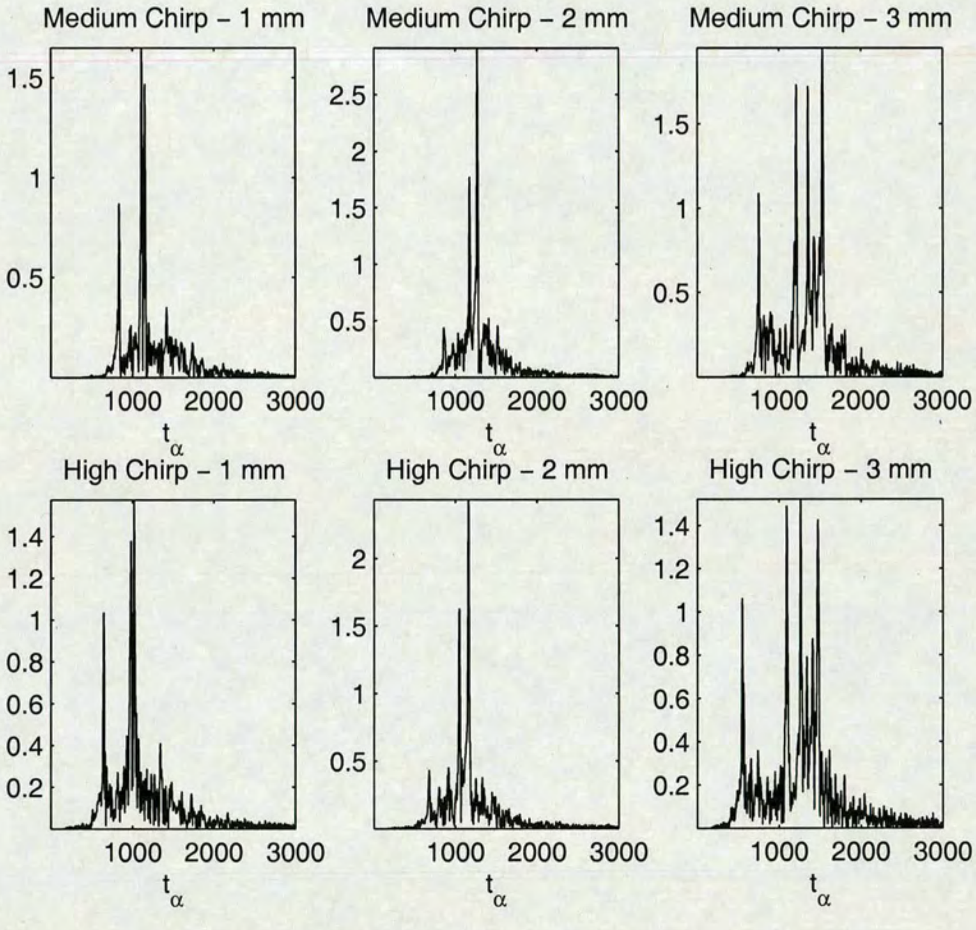

**Figure 5.19:** *Optimum transform order domains of high chirp rate signals, using Ozaktas et al. method.*

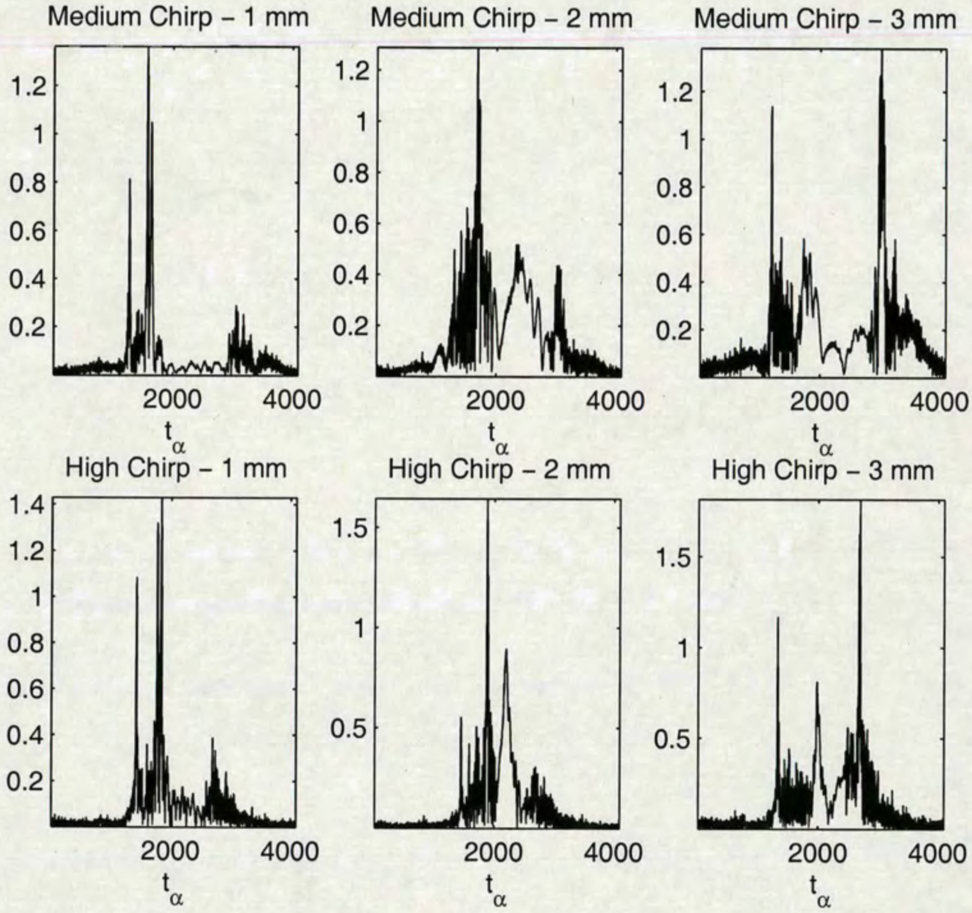

**Figure 5.20:** *Optimum transform order domains of high chirp rate signals, using Candan et al. method.*

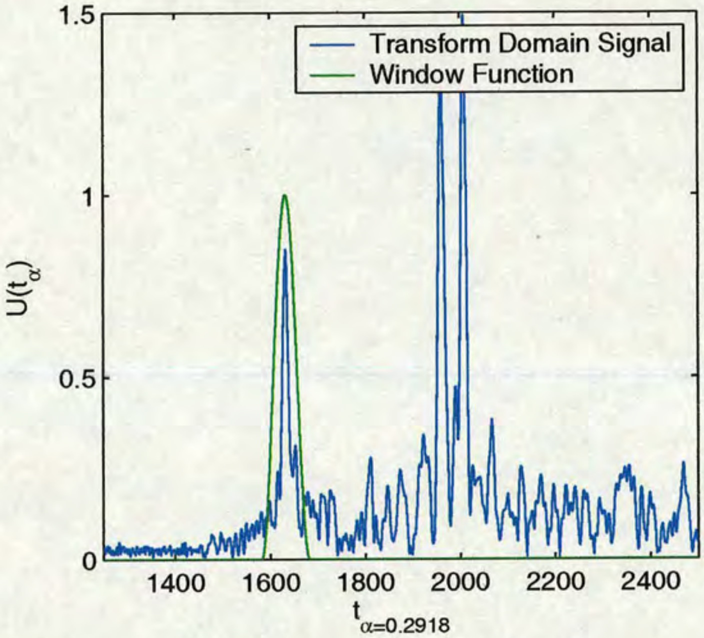

**Figure 5.21:** *Isolation of a key signal component from the transform domain signal using a Hanning window.*

The two methods were observed to give very different results, although both worked very well for the 1 mm slit signals, with both the high and medium chirp rates. However, whilst the Ozaktas method gives results which are clearly similar to those obtained using a matched filter for all signal cases, the Candan et al. method does not. It was not even possible to determine which peaks could be considered to belong to the specific geometry of the phantom, with the exception of the 1 mm slit case.

However, the differences between the two techniques are not limited simply to which produces results most like those obtained through matched filtering. The method by Ozaktas et al. produced what appear to be the 'best' results, however it was not possible to completely recover key signal components in the time domain using this method. Attempting to do so gave signals of approximately the right shape, but did not give the correct location in time. The method by Candan et al., despite producing transform domain signals which do not show any similarity to the matched filter results, was able to correctly recover signal components in the time domain. A Hanning window was used to isolate the signal component which should correspond to the top of the phantom from the transform domain signal generated using the Ozaktas et al. method. This is illustrated in Figure 5.21. The results of isolating the key signal component and transforming it back to the time domain are shown in Figure 5.22 for both methods. These

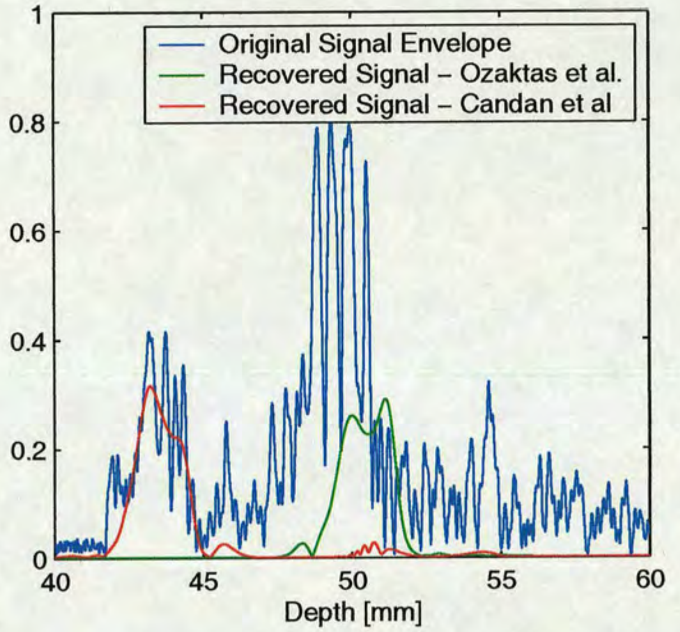

**Figure 5.22:** *Comparison of signal component recovery using the two discrete methods.*

results clearly show that it is possible to isolate a particular signal component, in this case, the signal from the top of the phantom, in the transform domain and to recover only that part of the time domain signal. However, this is only possible with the transform domain signals obtained with the Candan et al. method. The above process was repeated for the other two peaks in the transform domain signal, giving the results shown in Figure 5.23, where the positions of the recovered components are compared to the positions of the corresponding peaks in the matched filtered signal as well as the original chirped signal. The above procedure was repeated for all of what were deemed to be the appropriate peaks for the remaining high chirp rate signals and the medium chirp rate signals. The positions of the recovered signal components are summarised in Table 5.5.

Applying the direct time recovery technique described above to the high chirp rate signal for the 1 mm slit gave the results shown in Figure 5.24. As before, the absolute positions of the features do not agree, however both techniques gave similar results for the distance between the top and bottom edges of the 1 mm wide slit, with the matched filter suggesting a width of 0.7992 mm and the fractional Fourier technique a width of 1.0952 mm. Interestingly it was found that although the discrete implementation by Ozaktas et al. did not work correctly for signal recovery by inverting the transform, it did produce very good results using the direct time recovery method. Figure 5.25 shows the results of applying the direct time recovery technique

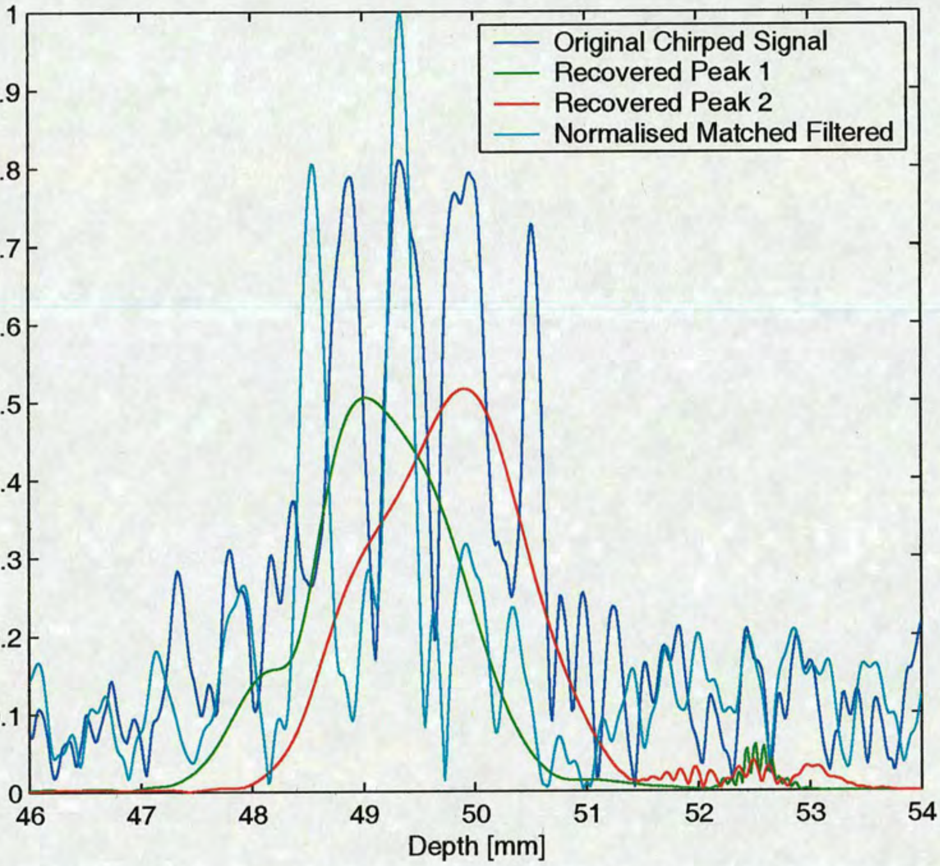

**Figure 5.23:** *Recovered signal components using Canden et al. method, showing accuracy of recovered positions in relation to the matched filtered signals.*

| High Chirp Rate Actual Slit Width [mm] | Top of Phantom [mm] | Top of Slit [mm] | Bottom of Slit [mm] | Slit Width [mm] |
|---|---|---|---|---|
| 1 | 43.23 | 49.03 | 49.91 | 0.880 |
| 2 | 44.12 | 50.25 | 51.73 | 1.480 |
| 3 | 42.59 | 50.66 | 53.56* | 2.900 |
| Medium Chirp Rate Actual Slit Width [mm] | | | | |
| 1 | 43.33 | 48.35 | 49.40 | 1.050 |
| 2 | 44.02 | 49.70 | 50.17 | 0.470 |
| 3 | 41.07 | - | - | - |

**Table 5.5:** *Positions of recovered signal components in high and medium chirp rate signal cases.*

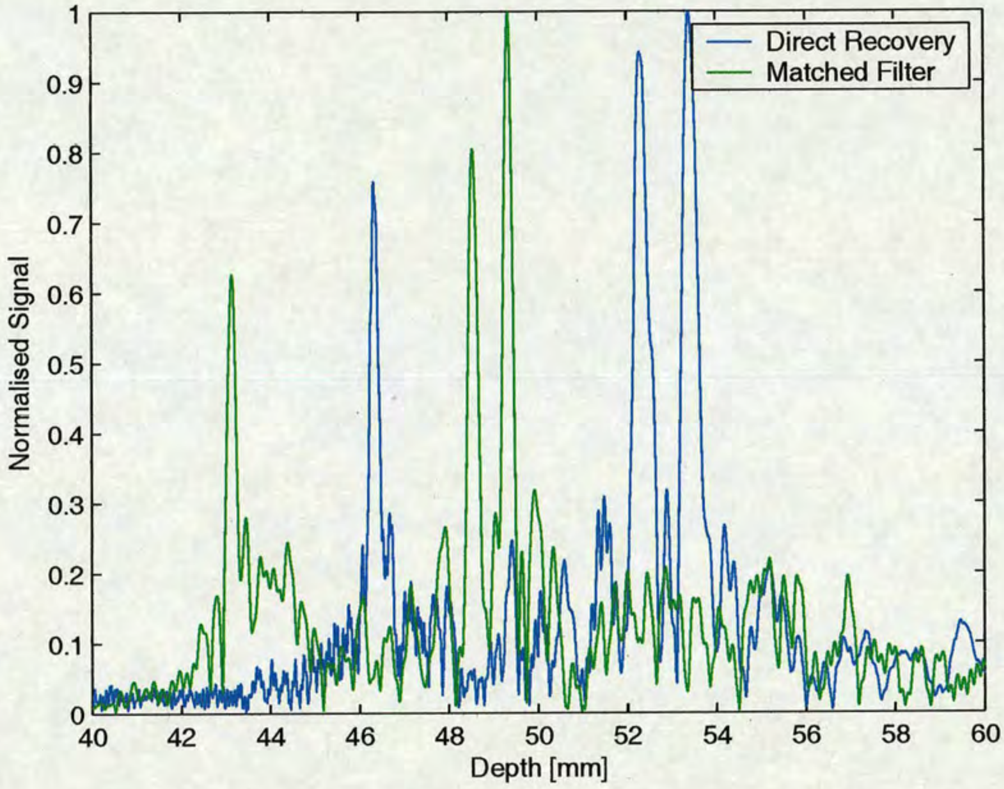

**Figure 5.24:** *Direct recovery vs. matched filtering for the high chirp rate signal and the 1 mm slit*

to the fractional domain signals obtained using the Ozaktas et al. method, for all three of the slits with the high chirp rate signals. This analysis was repeated for the medium chirp rate signals and the positions of the main features and the estimated slit widths are shown in Table 5.6.

## 5.6 Summary and Conclusions

This chapter has briefly described the topic of coded excitation and has highlighted the possible benefits to be gained from using such a technique. The concept of frequency modulated signals of the form of linear chirps has been described and the fractional Fourier transform has been introduced as an efficient technique for processing the resulting received signals. An experimental setup for producing chirped ultrasound signals has been described and signals from this system have been analysed. It has been shown that the fractional Fourier transform can produce results which are very similar to those obtained with matched filtering, although the fractional Fourier technique does not require a-priori knowledge of the transmitted signal since

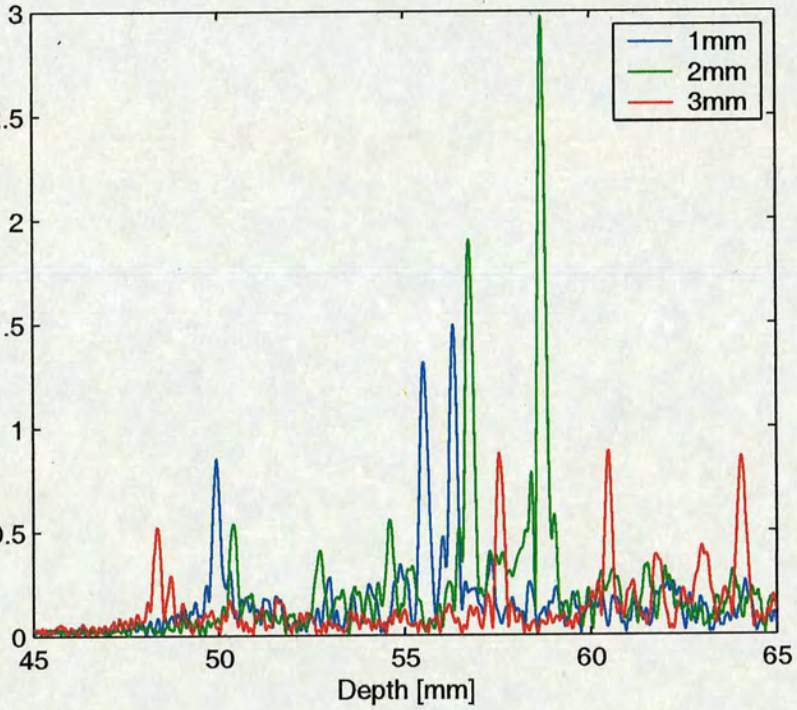

**Figure 5.25:** *Direct recovery of transform domain signals generated with the Ozaktas et al. method, for the high chirp rate case.*

| High Chirp Rate Actual Slit Width [mm] | Top of Phantom [mm] | Top of Slit [mm] | Bottom of Slit [mm] | Slit Width [mm] |
|---|---|---|---|---|
| 1 | 49.943 | 55.515 | 56.314 | 0.7990 |
| 2 | 50.402 | 56.739 | 58.692 | 1.9530 |
| 3 | 58.329 | 57.537 | 60.476 | 2.9390 |
| Medium Chirp Rate Actual Slit Width [mm] | | | | |
| 1 | 60.785 | 66.807 | 67.633 | 0.8260 |
| 2 | 61.503 | 68.176 | 70.242 | 2.0660 |
| 3 | 59.090 | 68.937 | 72.133 | 3.1960 |

**Table 5.6:** *Positions of key phantom features estimated using the direct time recovery technique. All units are in mm.*

it is possible to derive the optimum transform order directly from the received signals.

It has been shown that it is possible to use the fractional Fourier transform to recover specific signal components from the received signal by windowing around the corresponding feature in the transform domain and performing the inverse transform on the result. This approach is very sensitive to the technique used to implement the discrete version of the fractional Fourier transform, while it produces good results with the method by Candan et al., it was found that the transform domain signals derived using the Ozaktas et al. method were not properly invertible. This is due to the technique by which each method is derived since there is currently no formal definition of the discrete fractional Fourier transform. The Candan et al. method is designed to be as close an approximation of the continuous case as is currently possible, whereas the Ozaktas et al. method is designed to have a lower computational complexity and hence higher performance in terms of computing time.

A technique whereby the fractional Fourier transform domain of a signal can be directly related to the time-domain has been presented. This is possible because the fractional Fourier transform is not time-invariant provided that the transform order is not equal to $\pi/2$. In other words, at transform orders other than 0 or $\pi/2$, the resulting transform domain is a mixture of both time and frequency. Therefore, if the centre frequency of the signal is known, then it is possible to recover the time domain information without having to invert the transform. The advantage of this approach is that it is possible to transform the signal and gain similar improvements in axial resolution as would be obtained with a matched filter and then directly derive the corresponding time-domain positions of the key features. Using the alternative technique of isolating a key signal component and the inverting the transform gives the same information, but the resulting signal envelope no longer has the improvement in axial resolution.

It has also been shown that since the operation to directly relate a fractional Fourier transform domain feature to the time domain is essentially a linear transformation, it is possible to simply scale the axis of the transform domain signal so that it corresponds to the time-domain. This has been shown to produce results which are very similar to those obtained with a matched filter and was able to produce good estimates of the width of the slit in all cases considered.

The discrete implementation by Ozaktas et al. is able to operate in $N\log(N)$ time, where $N$ is the number of samples in the signal, however, as has been stated above the transform is not properly invertible. The Candan et al. method is very efficient once the transform matrix has been formed, however for the case of a 4096 sample signal this took about 35 minutes on 2.0 GHz Intel Xeon processor. It is probable that, eventually, a formal definition of the discrete fractional Fourier transform will be found, along with a fast version in the manner of the fast-Fourier transform, then it will be possible to consider real-time applications of the above techniques. However, for the time being that remains out of the question.

# Chapter 6

# Empirical Mode Decomposition for Tissue Harmonic Imaging

## 6.1 Introduction

### 6.1.1 Propagation of finite-amplitude acoustic waves

It is common to describe acoustic wave propagation in terms of a linear system. However, this only applies to waves which have infinitesimal acoustic pressures. In reality, all waves will have finite acoustic pressures, so this linear approximation does not always hold, although it is perfectly adequate for describing the behaviour of relatively low power systems, such as fetal heart monitors. Beams used for therapeutic applications have been shown to give rise to effects which cannot be explained by the linear approximation, such as distortion of the acoustic waveform, the associated generation of harmonics of the fundamental frequency and an increase in acoustic attenuation caused by harmonic generation and acoustic shock formation.

The principle and mechanism by which an acoustic wave travelling through a nonlinear medium becomes distorted has been understood for some 150 years, however over a century later the initial development of medical ultrasound was done without any consideration of these effects. It was Stokes in 1848 who first recognised the true impact of Poisson's earlier work on the exact solution for finite amplitude sound waves and published the first sketches of what the distorted waves might look like.

In order to understand the cause of these effects, it is firstly necessary to differentiate between local and cumulative non-linear effects. Local effects occur due to displacements of vibrating sources, variations in pressure/particle velocity relationships and perhaps most significantly, the pressure/radius relationship of acoustically driven micro-bubbles. Cumulative effects occur due to a variation in the propagation speed of the wave, which causes the distortion to develop with distance [73]. In the case of this work, it is only the effects of the latter which are considered.

The change in shape of the waveform is caused by the variation in the phase speed of the wave over its length. The phase speed will be higher in the compressed regions and lower in the rarefacted regions. The effect of this is to cause the regions of compression and rarefaction to move in opposite directions relative to the zero-crossings and eventually they will coincide. At this point, the phase shift of peak compression will be $\pi/2$ and that of peak rarefaction will be $-\pi/2$, which leads to a pressure discontinuity or acoustic shock. As the wave propagates further, dissipation causes the acoustic shock to diminish in amplitude and eventually return to a low amplitude sinusoidal wave.

Given that the change in the shape of the waveform is progressive and linear with distance, the theoretical distance from the transducer at which the acoustic shock phenomenon will occur is given by [73]:

$$I_d = \left(\frac{\rho c^3}{2\pi}\right) \frac{1}{p_0 f \beta} \tag{6.1}$$

Where $\rho$ is the density of the medium, $c$ is the wave speed, $p_0$ is the acoustic pressure at the source, $f$ the frequency of the waveform and $\beta$ is the coefficient of non-linearity for the medium.

The degree of distortion experienced by the waveform at displacement $z$ from the source, can be expressed by $\sigma = z/I_d$, or in terms of the properties of the medium by [73]:

$$\sigma = \frac{2\pi}{\rho c^3} \left(p_0 f z \beta\right) \tag{6.2}$$

From which it may be observed that the degree of distortion varies linearly with distance from the source $z$ and with the nonlinear properties of the material.

In order to demonstrate the effects described above, an experiment was carried using the transmit section of the single crystal ultrasound system described previously, along with a hydrophone and a long tank of de-gassed water, arranged as illustrated in Figure 6.1. The hydrophone and the transducer were arranged in a linear fashion such that the distance between them could be varied easily. It was necessary to use a hydrophone to received the signals from the transducer because the bandwidth of the transducer would have been too narrow to observe the full effects of the non-linear distortion. The transducer was driven with a 2.25 MHz signal consisting of bursts of 4 cycles, repeated at a pulse repetition frequency of 1 KHz. The drive voltage from the programmable function generator was set to 1 Vp-p, which was the maximum input to the RF power amplifier. Signals were captured using the Signatec PDA12 capture card, with a sampling frequency of 50 MHz. The acoustic absorbing material was placed at the end

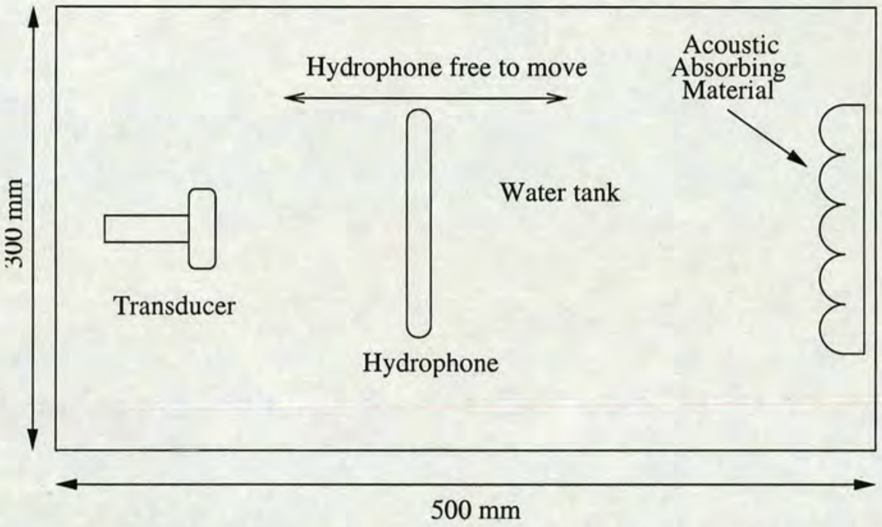

**Figure 6.1:** *Equipment setup used to demonstrate the effects of non-linear propagation on the wave shape.*

of the tank such that it would prevent any stray reflections from the end of the tank. It was not felt that it would be necessary to line the sides of the tank in a similar manner since the beam width from the transducer used was narrow compared to the width of the tank.

This setup was used to capture a series of nine signals with the transducer progressively moved further away from the hydrophone for each one. The first signal was arranged to be approximately 15 mm from the hydrophone, while the last was at a distance of 235 mm. Since none of the received signals occurred at the same time, it was possible to improve the signal-to-noise ratio by summing the nine signals [1]. In this manner, the random noise will cancel itself out to some extent, but the non-random signals will be unchanged. The nine received signals were then isolated from this longer signal and are shown in Figure 6.2. With the experiment setup used, it was not possible to accurately specify or determine the distance between the transducer and the hydrophone. The distances were therefore derived from the received ultrasound signals using the time-of-flight method. The signals were bandpass filtered around 2.25 MHz using a 128 element FIR filter in Matlab and the envelope of the results was found using the Hilbert transform. This envelope was then thresholded to leave only the significant peaks, the locations of which were then found by searching for the local maxima. Table 6.1 gives the resulting distances between the transducer and the hydrophone.

---

[1] The receive process was triggered at the time of transmission, therefore each of the received signals contained the detected echo at a different time. It was thus concluded that adding these signals together would improve the SNR because the random noise would be cancelled out to some extent.

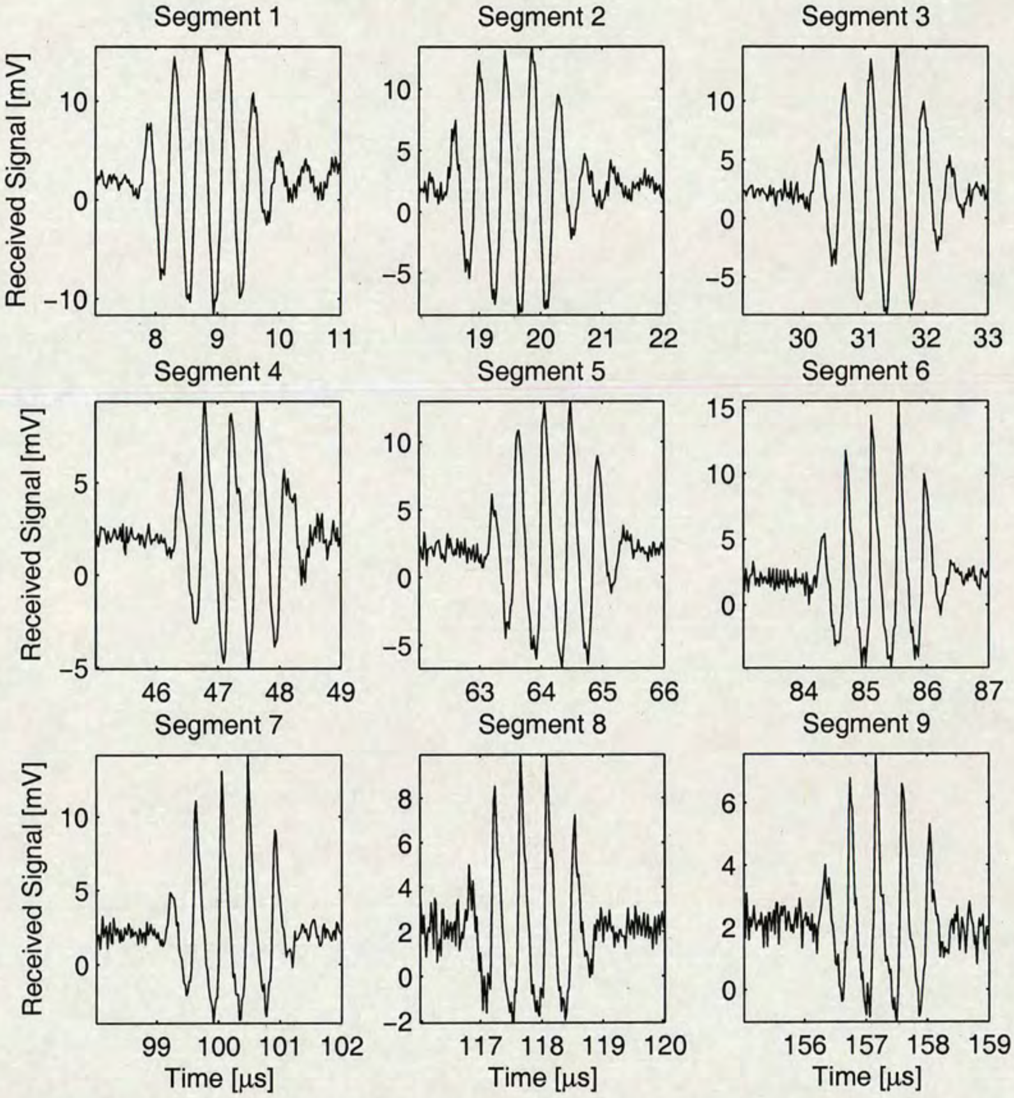

**Figure 6.2:** *Signals received by hydrophone with transducer at nine different displacements, clearly showing increasing distortion with depth (Segment 1 was the closest, while segment 9 was the furthest away).*

| Segment Number | Distance [mm] |
|---|---|
| 1 | 13.02 |
| 2 | 29.01 |
| 3 | 46.32 |
| 4 | 69.97 |
| 5 | 94.99 |
| 6 | 126.19 |
| 7 | 148.27 |
| 8 | 174.34 |
| 9 | 232.72 |

**Table 6.1:** *Distance between the transducer and the hydrophone for each segment.*

These results clearly show how the shape of the wave changes with increasing distance, segment 1 at a distance of only 13 mm from the transducer is clearly sinusoidal, but this changes rapidly and by segment 4 at a depth of 70 mm, the distortion is clearly visible. It is interesting to note that the peak positive amplitude of the signals doesn't change much until the 8th and 9th segments at depths of 174 mm and 233 mm respectively. However, the peak negative pressure decreases much more rapidly. The Fourier spectra of these signals give a more complete picture of what is happening as seen in Figure 6.3. From these, it is obvious that as the distance and hence the degree of distortion increases, the corresponding Fourier spectra shows an increase in the proportion of signal energy which exists at the harmonic frequencies of the fundamental. In the case of the first segment, nearly all of the energy is concentrated at the fundamental frequency of 2.25 MHz, as would be expected. However, the second segment shows a significant increase in the energy at the second harmonic (4.5 MHz), which continues to increase up to the fourth segment at a depth of 70 mm. Signal energy can be observed at the third harmonic (6.75 MHz) from the third segment onwards, while there is clearly energy at the fourth harmonic from segment 5 onwards and so on. Segment 7, corresponding to a depth of 148 mm shows the most signal energy, taking into account all of the harmonics, while segments 8 and 9 shows progressively less signal energy. The reason for the sudden decrease in signal energy after the seventh segment is due to increased attenuation. From this, it was concluded that the depth at which acoustic shock formation occurs must be around 148 mm, because after this point, the total amount of energy in the signals appears to decrease.

Putting the appropriate values into equation (6.1), ($\rho = 0.99707\text{gml}^{-1}$, $\beta = 3.5$ (for water), $c = 1480\text{ms}^{-1}$,$p_0 = 0.44\text{MPa}$ (estimated from peak pressure of first segment) and $f = 2.25\text{MHz}$), gave $l_d = 148.47\text{mm}$ which matched almost perfectly with the experimental observations.

It was not until 1980 that two companion papers published by Carstensen et al [74] and Muir and Carstensen [75] highlighted the fact that the nonlinear propagation of finite amplitude acoustic waves might have an impact in biomedical ultrasound fields. The second of these two papers ([75]) gives an excellent theoretical introduction to the nonlinear effects which could be expected to occur at biomedical frequencies and intensities. The much later review paper by Duck [73] summarises much of the work in the Muir and Carstensen paper, but only mentions the concept of harmonic generation very briefly. Of particular interest is that Muir and Carstensen realised that the technique of Fourier analysis seemed to be perfect for analysing

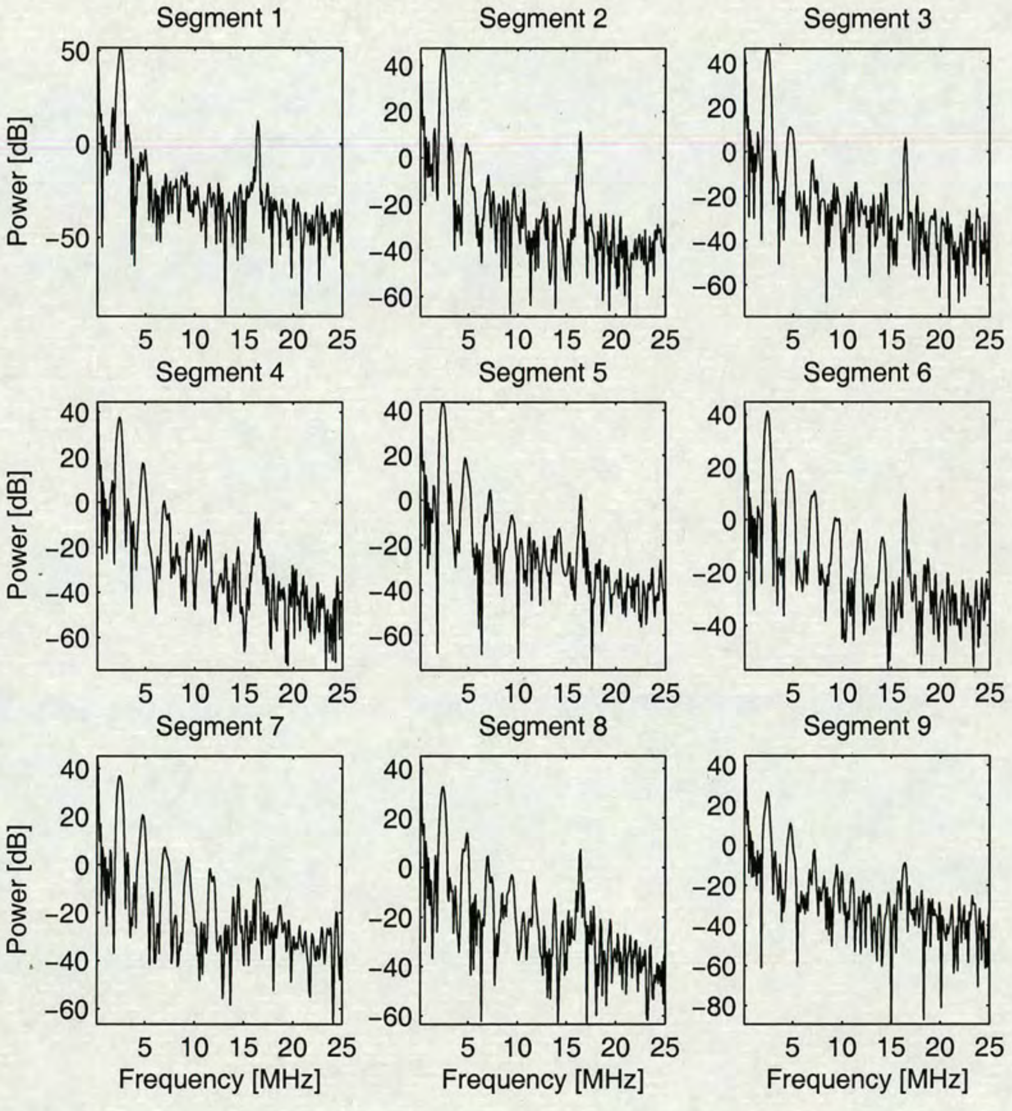

**Figure 6.3:** *Fourier spectra of signal segments, clearly showing increasing energy in the harmonic frequencies with increasing depth.*

the nonlinear and periodic waveforms under consideration. They state that the distorted, finite-amplitude pressure wave as might be measured by a broadband hydrophone can be expressed as:

$$p = p_0 \left(\frac{r_0}{r}\right)^a \sum_{n=1}^{\infty} B_n(r,\sigma) \sin\left(n\left[\omega t - k(r - r_0)\right]\right) \tag{6.3}$$

Where $a = 1$ for spherical waves, or $a = 0$ for plane waves. In the plane wave case, $r_0 = 0$ and $r = z$. The authors go on to quote Blackstock's result for the Fourier coefficients:

$$B_n = \left(\frac{2}{n\pi}\right) W_b + \left(\frac{2}{n\pi\sigma}\right) \int_{\phi_{\min}}^{\pi} \cos\left(n\left[\phi - \sigma \sin\phi\right]\right) \mathrm{d}\phi \tag{6.4}$$

Where:

$$W_b = \frac{1}{\sigma}\left[j_0^{-1}\left(\frac{1}{\sigma}\right)\right] H(\sigma - 1) \tag{6.5}$$

Where $H()$ is the Heavyside step function and $j_0^{-1}(1/\sigma)$ is a quantity whose zero order Bessel function is $1/\sigma$. $\phi_{\min} = \sigma W_b$ is an intermediate variable. Once the Fourier coefficients have been obtained, Muir and Carstensen state that the intensity of each component can be calculated from:

$$I_n = I_0 \left(\frac{r_0}{r}\right)^{2a} B_n^2(r,\sigma) \tag{6.6}$$

They go on to use these results to demonstrate that the harmonic components grow cumulatively with distance at the expense of the fundamental. As appeared to be the case with the signals considered above, the growth of the harmonic components was shown to taper off after the initial shock formation.

### 6.1.2 Tissue Harmonic Imaging

Two independent groups simultaneously arrived at the idea of using the distortion of the waveform propagating through a nonlinear medium to improve the performance of medical ultrasound systems. One group was led by T. Christopher [76],[77] based in the USA and the other was led by V. Humphrey at the University of Bath in the UK [78]. Ward et al. [78] used an experiment setup consisting of a 2.25 MHz circular transducer and a membrane hydrophone of identical diameter (38 mm). They arranged these axially with a polymer lens to give an imaging geometry similar to that found in many B-mode clinical scanners. A hydrophone was used for the received stage because it would have sufficient bandwidth to capture the first four harmonics of the signals, whereas an ultrasound transducer would be much more limited. Using this setup with a wire phantom, they were able to demonstrate a large improvement in lateral resolution and signal-to-clutter ratio for the higher harmonics. The group led by T.Christopher [76] looked at the problem of lateral and contrast resolution degradation caused by the defocusing effects of inhomogeneities in body tissues. They state that in homogeneous media the side-lobes of the nonlinearly generated higher harmonics are much lower than their linear counterparts. They go on to describe computations performed which suggest that this relationship holds for the case of beam propagation through abdominal wall and breast wall tissue. Their results also suggested that the lateral resolution limits imposed by these tissues are slightly smaller in the case of the nonlinearly generated harmonics and they investigate the potential of these harmonics to improve image resolution.

The work of these groups is based on the idea that the second and higher harmonics of a signal are able to offer improved lateral resolution because the beam width is reduced by the nature of the higher frequency signal. The signal-to-clutter ratio may be improved because the returned signal from clutter will be relatively small compared to that from tissue, or scatterers of interest. It can be shown that when the amplitude of the fundamental is increased by a factor of two (by doubling the transmitted amplitude), then the amplitude of the second harmonic increases by a factor of four [79]. This occurs because the process of nonlinear distortion is highly sensitive to the amplitude of the wave. Therefore, when looking at the second or higher harmonics, the difference in power between the clutter signal and the desired signal will be proportionally greater than when looking at the fundamental frequency.

At around the same time that these two groups were investigating the potential benefits of using the higher harmonics, the manufacturers of ultrasound scanners were interested in the higher harmonic signals returned from micro-bubbles, a technique now commonly referred to as Contrast Harmonic Imaging (CHI) [80]. The interaction of micro-bubbles with an acoustic field is a highly complex phenomenon which would be beyond the scope of this work to describe in detail. Lord Rayleigh was the first to describe the nonlinear radial motion of a gas bubble in an acoustic field and his theory, suitable elaborated by a series of further investigations led to the notion that a bubble, driven into nonlinear resonant oscillation by an incident sound field, would give rise to a scattered signal which would contain higher harmonics of the original signal [81]. It was in part thanks to this work that tissue harmonic imaging was developed. Originally, it was thought that thermo-viscous absorption in tissue would prevent the higher harmonics developing, since even though most tissues have similar coefficients of nonlinearity to water, they have significantly higher absorption. Averkiou et al. [82] based at ATL in the USA, demonstrated that the wide dynamic range, digital architecture and signal processing capabilities of modern scanners made it possible to utilise the harmonic energy generated by propagation through tissue. It would appear that Averkiou et al. were the first to use the term *tissue harmonic imaging* and they describe how they used the Khokhlov-Zabolotskaya-Kuznetsov (KZK) equation to form a model which could be used to estimate the degree of harmonic generation that would take place in body tissues. Using this model, they were able to determine that it should be possible to detect the second or higher harmonics resulting from the propagation through tissue. Experiments were performed using a sample of beef tissue to confirm their theoretical results and were found to be in agreement. Averkiou also holds a patent for an implementation of this technology [83], which was filed in December, 2002.

Of the many developments that have occurred in the field of medical ultrasound imaging in recent years, most have been very effective when applied to patient groups who are easy to image [84]. However, the effect of these developments for the group of 'technically difficult' patients, or those who are more difficult to image due, for example due to excess weight, has been much less significant. The general solution in these cases is to use lower frequency transducers which thus give a greater imaging depth, but at the expense of axial resolution The introduction of *tissue harmonic imaging*, however, has had a great impact on the imaging of technically difficult patients since it allows greater imaging depths with significantly less compromise to the image quality than would have to be tolerated when using lower frequencies.

Since the technique of tissue harmonic imaging produces more visually appealing images, the technique has become increasingly prevalent and is now the default mode on most, if not all, clinical scanners [85]. Certainly, a number of studies have shown the technique to be useful, for example Mele et al. [86] assert that tissue harmonic imaging improved the accuracy and reproducibility of echocardiographic evaluation of left ventricular ejection fraction. However, the effects of using tissue harmonic imaging techniques for the assessment of rheumatic mitral valve stenosis were studied by Prior et al. [85] and it was pointed out that the structures may appear thicker and brighter when imaged by this modality than when imaged by fundamental 2-dimensional imaging. They go on to conclude that the use of tissue harmonic imaging changes the values used for the quantitative assessment of mitral valve stenosis, the very least effect of which is to render invalid the comparison of results obtained using tissue harmonic imaging with those obtained using fundamental imaging. They also claim that the use of tissue harmonic imaging results in an increased splitability score that may result in the exclusion of patients otherwise suitable for percutaneous balloon valvuloplasty. It is also well known that using tissue harmonic mode involves a certain trade-off between lateral and axial resolution, namely that the lateral resolution will improve due to increased receive frequency and the axial resolution will worsen due to the reduced receive bandwidth [87]. Clearly the technique is not without its disadvantages and further work is needed before its true impact on echocardiography can be determined.

Up until now, all of the analysis of signals resulting from distortion due to propagation through a non-linear medium have been performed using Fourier based techniques, either in the form of the conventional Fourier transform or a short-time variant such as the short-time Fourier transform or wavelets. However, the Fourier transform is only valid for signals which are stationary and have propagated through a linear system, that is, signals which result from a system which can be modelled by the linear superposition of a series of simpler signals. However, it has clearly been shown that these assumptions are not strictly valid for acoustic waves of the type used for medical ultrasound. The basis of tissue harmonic imaging is that the signal energy is spread into the harmonic frequencies by the non-linear distortion of the wave, therefore different information can be obtained by looking at the second or higher harmonics compared to the fundamental. It can be argued that these harmonic frequencies are only the result of the use of Fourier based analysis techniques and do not necessarily relate to the actual physical process. This will be discussed in more detail later in this chapter, but it leads to the question of whether a different signal analysis technique might lead to a different understanding of the process underlying tissue harmonic imaging.

### 6.1.3 Empirical Mode Decomposition

The concept of instantaneous amplitude is readily understood and is well accepted, however, the notion of instantaneous frequency is somewhat more vague. One of the issues is that from Fourier analysis, the frequency is defined for a sine or cosine wave spanning the whole dataset, therefore, if one extends this definition to the idea on instantaneous frequency, then this too must correspond to the frequency of a sine or cosine function. Therefore, it would be necessary to have at least one complete period of oscillation to be able to define the frequency. In the case of non-stationary signals, it would be possible for the frequency to vary within the time for one period, so this definition is unsuitable.

The instantaneous frequency of a signal may be defined using the Hilbert transform. For a signal $X(t)$, the Hilbert transform $Y(t)$ will be given by 6.7.

$$Y(t) = \frac{1}{\pi} P \int_{-\infty}^{\infty} \frac{X(t')}{t - t'} \mathrm{d}t' \tag{6.7}$$

From this, the analytic signal $Z(t)$ can be defined as in equation 6.8 below:

$$Z(t) = X(t) + iY(t) = a(t)e^{i\theta(t)} \tag{6.8}$$

where,

$$\begin{aligned} a(t) &= \left[X^2(t) + Y^2(t)\right]^{1/2} \\ \theta(t) &= \arctan\left(\frac{Y(t)}{X(t)}\right) \end{aligned} \tag{6.9}$$

The instantaneous frequency can then be defined as:

$$\omega(t) = \frac{\mathrm{d}\theta(t)}{\mathrm{d}t} \tag{6.10}$$

The problem with this definition is that it only gives a single value at each time instant, but real signals will often consist of multiple frequency components, so the instantaneous frequency will be ambiguous. To avoid this ambiguity, it is necessary to limit the signal to be narrow band, although no precise definition of a suitable bandwidth has yet been found. For the definition of instantaneous frequency to be meaningful, the real part of the Fourier transform of the signal should only consist of positive frequencies. However, this is a global restriction which might not be of use for non-stationary data. Huang et al. [88] state that it is necessary, therefore, to develop a modified version of this restriction which can be applied locally. They go on to define a class of functions, called *Intrinsic Mode Functions* (IMFs) for which the instantaneous frequency can be defined anywhere. They also propose a technique called *Empirical Mode Decomposition* which breaks a signal down into a set of intrinsic mode functions, each corresponding to a single oscillatory mode of the original data. Since each IMF is formed from only one oscillatory mode, the requirement for the signal to be narrow band is achieved.

The technique proposed by Huang et al. is based on the principle of identifying the intrinsic oscillatory modes according to their characteristic time scales. There are two ways of doing this, firstly from the time between alternations of local maxima and minima and secondly from the time between the zero crossings. EMD is based on the first of these two, since measuring the time between the zero crossings would require the data to be of zero mean.

The IMFs are extracted using a sifting process, the first step of which is to define envelopes from the local maxima and minima. This is achieved using cubic splines to connect all the local maxima together to define one envelope and all of the local minima to define the second envelope. These two envelopes should then encompass all of the data. The first component, $h_1(t)$ is then found from the difference between the mean of the two envelopes, $m_1(t)$ and the original signal, $x(t)$. This is illustrated in Figure 6.4. This process is repeated until the standard deviation of two consecutive sifting results falls below a specified threshold, at which point the result, $h_{1n}(t)$ is regarded as the first IMF, $c_1(t)$. This is then subtracted from the data and the process is repeated, as illustrated in Figure 6.5, until there are is no longer a sufficient number of local maxima or minima in the remaining signal to continue. This results in a set of intrinsic mode functions, the number of which depends on the nature of the original signal. The remainder of the process is the general trend of the signal.

### 6.1.4 The Hilbert Spectrum

Once the data have been separated into IMFs, the Hilbert transform can be applied to each one without any difficulty. This done, it is possible to calculate the instantaneous frequencies using equation (6.10). Once each component has been transformed using the Hilbert transform, the original signal could be reconstructed using [88]:

$$X(t) = \sum_{j=1}^{n} a_j(t)\exp\left(i\int \omega_j(t)\mathrm{d}t\right) \tag{6.11}$$

Equation (6.11) shows how the instantaneous amplitude and frequencies could be represented as functions of time on a three dimensional plot, where the amplitude can be shown as contours on the time-frequency plane [88]. This is called the Hilbert amplitude spectrum, $H(\omega, t)$, or simply the Hilbert spectrum.

Using the Fourier method, the signal would be reconstructed using equation (6.12):

$$X(t) = \sum_{j=1}^{\infty} a_j\exp\left(i\omega_j t\right) \tag{6.12}$$

Comparing equations (6.11) and (6.12) clearly illustrates the difference between these two tech-

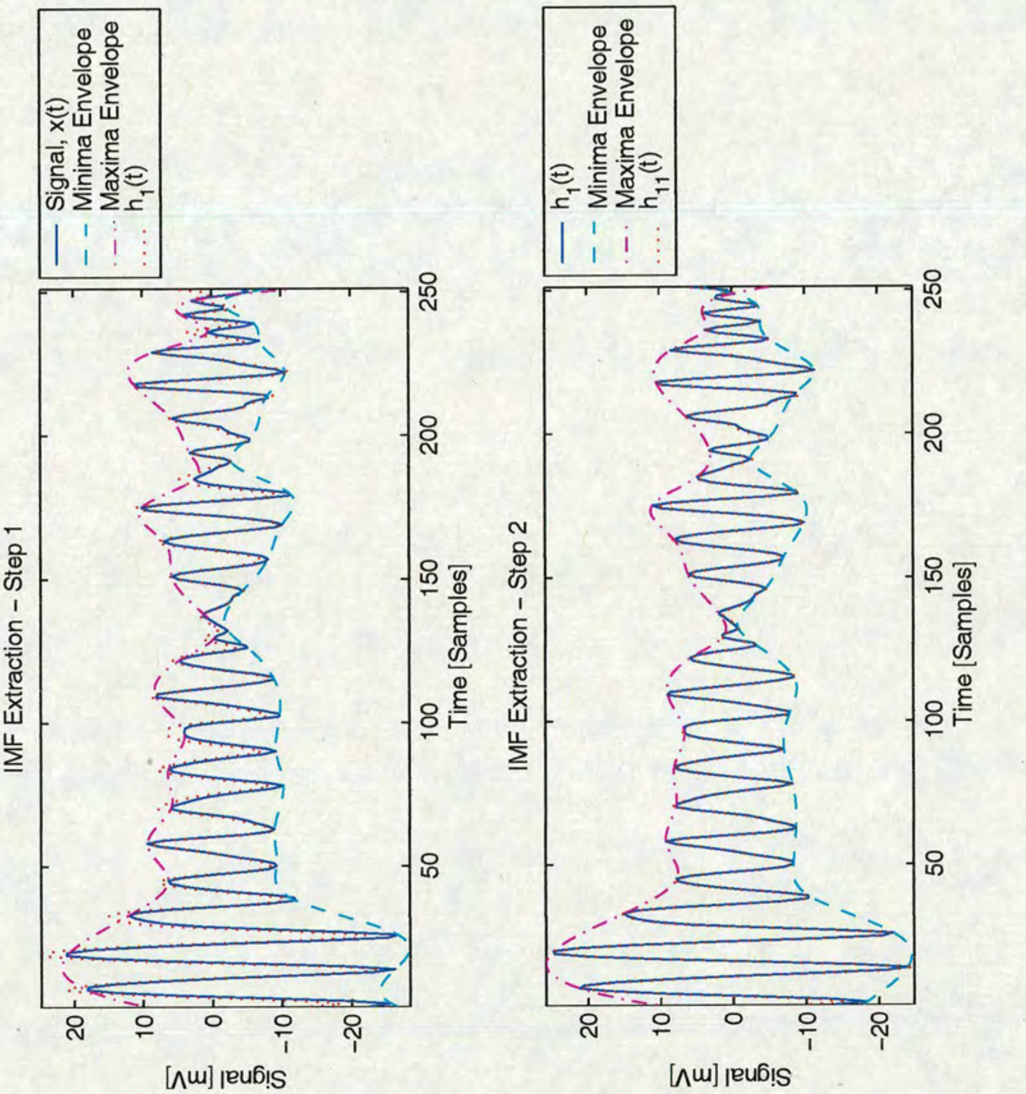

**Figure 6.4:** *Extraction of the first IMF. The mean of the maxima and minima envelopes is subtracted from the original signal to give $h_1(t)$ [top]. The minima and maxima envelopes of $h_1(t)$ are then found and their mean is subtracted from $h_1(t)$ to give $h_{11}(t)$ [bottom]. The difference between $h_{11}(t)$ and $x(t)$ is now small, so $h_{11}(t)$ is taken to be the first IMF. In general, the process is repeated until the difference is sufficiently small.*

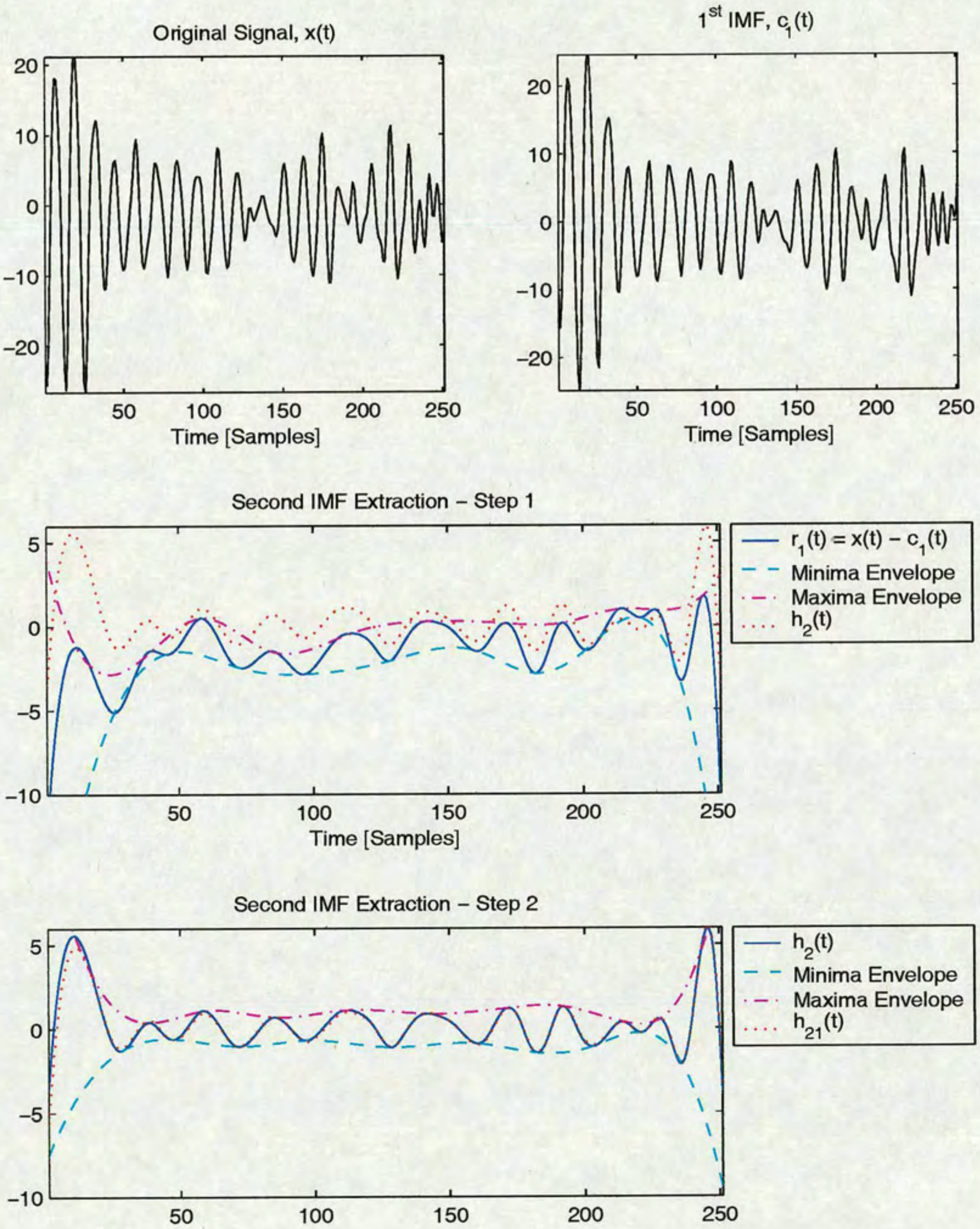

**Figure 6.5:** *Extraction of the second IMF. The* $1^{st}$ *IMF is subtracted from the original signal to give* $r_1(t)$ *and the process is repeated with* $r_1(t)$ *as the signal.*

niques. In the Fourier method given by equation (6.12), each of the amplitude and frequency terms are fixed for the entire signal, whereas the Hilbert method given by equation (6.11) allows them to be functions of time. Therefore, to model a non-stationary signal, the Fourier method must contain many additional components, whereas the Hilbert method does not need any, since the non-stationary nature of the signal can be included in the instantaneous amplitude and frequency terms.

### 6.1.5 Nonlinear, Non-stationary Signals and the Hilbert Spectrum

The combined techniques of Empirical Mode Decomposition and the Hilbert spectrum are able to offer an alternative view of signals which are neither stationary, or result from a linear system. Although the Fourier transform is valid under varied conditions, Fourier spectral analysis is restricted to linear systems and signals which are strictly periodic or stationary, otherwise the resulting spectrum will make little physical sense [88]. This is illustrated by two simple examples, the first of which looks at the issue of non-stationary signals. Consider the signal shown in the middle of Figure 6.6, which consists of a single cycle of a 50 Hz sine wave, sampled at a rate of 1 kHz. Since the Fourier spectrum defines uniform harmonics globally, it needs to introduce additional harmonics to be able to account for the non-stationary signal which is non-uniform globally. This is demonstrated by the short-time Fourier transform shown at the top of Figure 6.6, where although the bulk of the signal energy is centred on a frequency of 50 Hz, the energy is spread into additional harmonic components. It is also important to note that the signal is not well localised in time, even by the short-time Fourier transform. With a technique such as this, there is always an inevitable trade-off between time resolution and frequency resolution; owing to the uncertainty principle, it is not possible to increase one without decreasing the other. The bottom part of Figure 6.6 shows the Hilbert spectrum of the non-stationary signal, which was formed by using the EMD method described above. The significant differences between the Hilbert spectrum and the short-time Fourier transform are that the former offers very good time and frequency localisation when compared to the latter and the Hilbert spectrum does not need to introduce additional harmonic components.

In the case of a nonlinear signal, as shown in Figure 6.7, the Hilbert spectrum offers a completely different picture to that normally given by Fourier analysis. Here, the nonlinear signal in question was defined by:

$$s(t) = \cos\left(\omega t + \epsilon \sin(\omega t)\right) \tag{6.13}$$

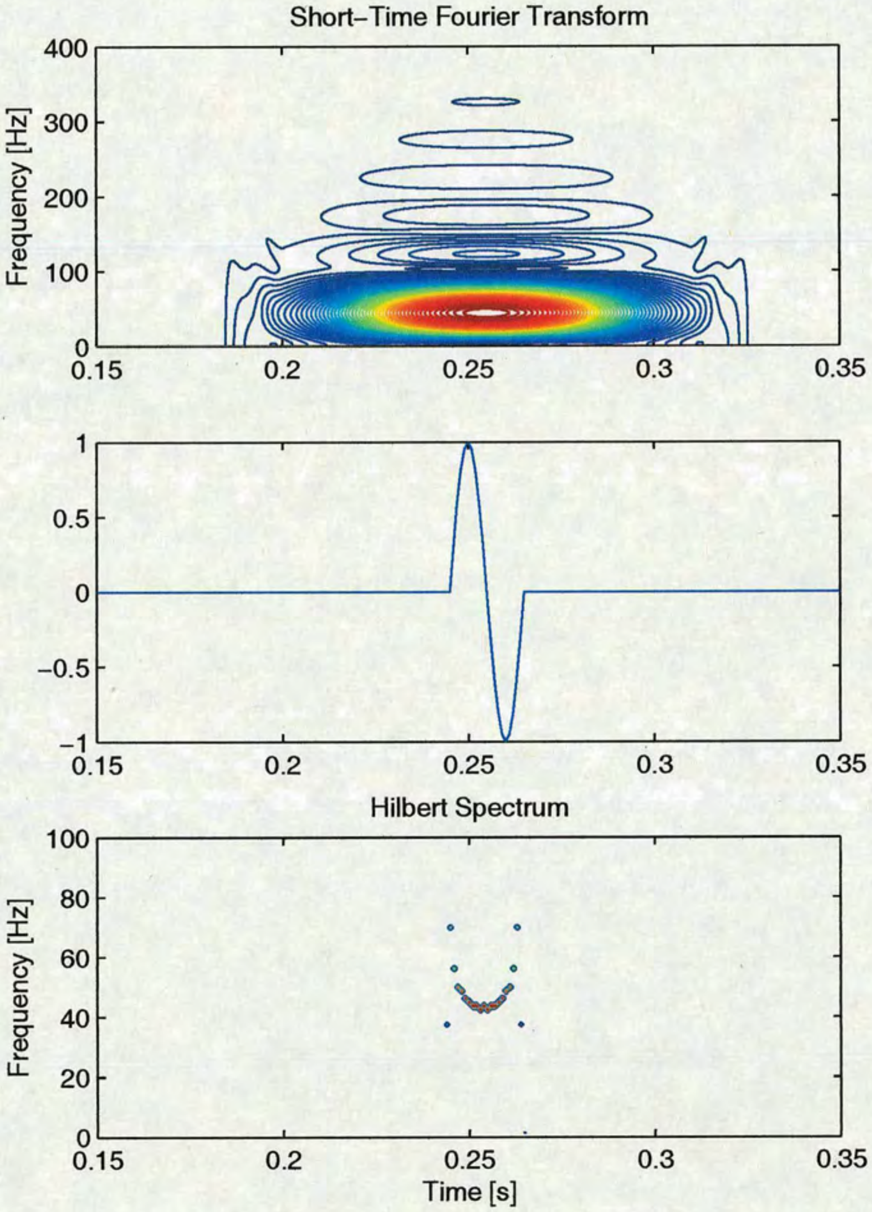
Short–Time Fourier Transform

Hilbert Spectrum

**Figure 6.6:** *Illustration of non-stationary signal which demonstrates how the Fourier transform will introduce additional harmonic components which it needs to be able to model the more complex signal. Note that the Hilbert spectrum contains no such additional harmonic frequencies and instead introduces an intra-wave frequency modulation which is centred on the main frequency of the signal, 50 Hz.*

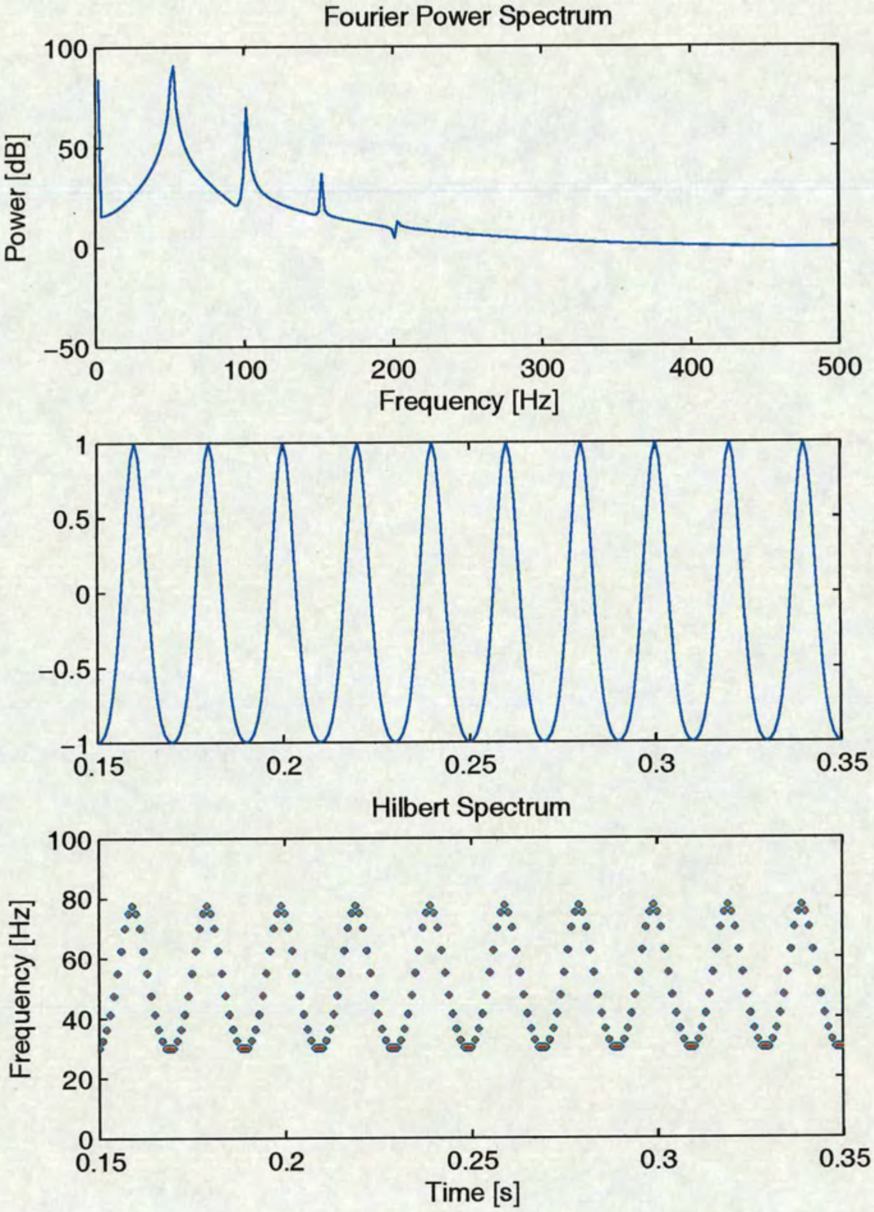

**Figure 6.7:** *Illustration of non-linear signal demonstrating how the Fourier transform has to introduce spurious harmonics to represent the non-linearity.*

In this case, $\epsilon = 0.5$ and the signal was defined to have a frequency of 50 Hz with a sampling frequency of 1 kHz. The top part of Figure 6.7 shows the Fourier power spectrum of the signal, which clearly shows the introduction of harmonic frequency components, but the Hilbert spectrum shown at the bottom of the Figure again gives a different picture. Here, the signal energy is concentrated around 50 Hz, as would be expected given the signal definition, but instead of having additional harmonic components, the frequency oscillates around the centre frequency. This gives rise to the concept of an intra-wave frequency modulation, where the frequency of a signal can change within the time required for a single period at the centre frequency. Equation (6.10) defined the instantaneous frequency of a signal as the rate of change of phase. For the signal represent by equation (6.13), this would be given by:

$$f(t) = \omega\left(1 + \epsilon\cos(\omega t)\right) \tag{6.14}$$

This clearly demonstrates where the intra-wave frequency modulation comes from and shows that the period of oscillation of the frequency should be equal to that of the original signal. It also shows that increasing the degree of nonlinearity by increasing the value of $\epsilon$ would increase the amplitude of the intra-wave frequency modulation. Huang et al. [88] go on to provide numerous further examples to verify the Hilbert spectrum and the physical reality of the intra-wave frequency modulation, but for this work it was felt that the above example was sufficient to theorise that any nonlinearly distorted signal could be interpreted as having an intra-wave frequency modulation, the amplitude of which depended on the degree of distortion.

## 6.2 Experiment Setup

The experiments described above, used to demonstrate the effects of nonlinear propagation, were performed using a 2.25 MHz centre frequency, circular transducer with a diameter of 13mm. This was arranged in a tank of water and aligned axially to a wide bandwidth PVDF membrane hydrophone such that the distance between the transducer and the hydrophone could be varied easily. Signals were captured over a range of distances.

Further experiments were carried out using a Panametrics wide-band transducer with a centre frequency of 6 MHz and 100 % bandwidth. In this case, the transducer was arranged above the same phantom described in the previous section, such that it would be possible to insonify one of the slits at a time.

In all cases, the signals were captured using the Signatec PDA12 capture card, with the sampling frequency set to 50 MHz.

## 6.3 Results

### 6.3.1 Hydrophone Signals

The Fourier spectra of the signals captured with the hydrophone have already been shown and described as they provide a good example of the effect of the nonlinear distortion and how the effects increase with depth. However, since these signals are non-stationary in nature, the Fourier spectrum can only give part of the picture since it conveys nothing about how the frequency content varies over time. Therefore, looking at the signals using some form of joint time-frequency analysis will reveal more information. In this case, the Wigner-Ville distribution was chosen because it has good time and frequency resolution. Since each of the signals consists of only a single burst, the cross-terms will not be a problem. Figure 6.8 shows the results obtained for four of the signal segments. These four were chosen so as to include the first one, with the least amount of distortion, one before shock formation (segment 4), one as close to the point of shock formation as possible (segment 7) and one beyond the point of shock formation (segment 9). From these results it was observed that as the distance between the transducer and the hydrophone was increased, the amount of energy being spread into the harmonic frequencies increased, up to the point of shock formation after which the overall signal energy begins to decrease due to increased attenuation. This is exactly as would be expected and matches with the Fourier spectra shown earlier in Figure 6.3.

However, although time-frequency techniques such as the Wigner-Ville distribution allow for some non-stationarity in the signal by operating on a short-time basis, they are still fundamentally based on the Fourier transform. This can be seen by inspecting the equation for the Wigner distribution given in equation (5.9). The Hilbert spectrum, as described above, is not subject to the same limitations as Fourier based analysis because it is based on obtaining the instantaneous frequency directly from the rate of change of phase of a series of narrow band signals, rather than comparing the global signal to a series of infinite sines and cosines. Therefore it should be able to offer results which give a different physical interpretation of the effects of the nonlinear distortion.

The empirical mode decomposition algorithm was applied to each of the signals, yielding be-

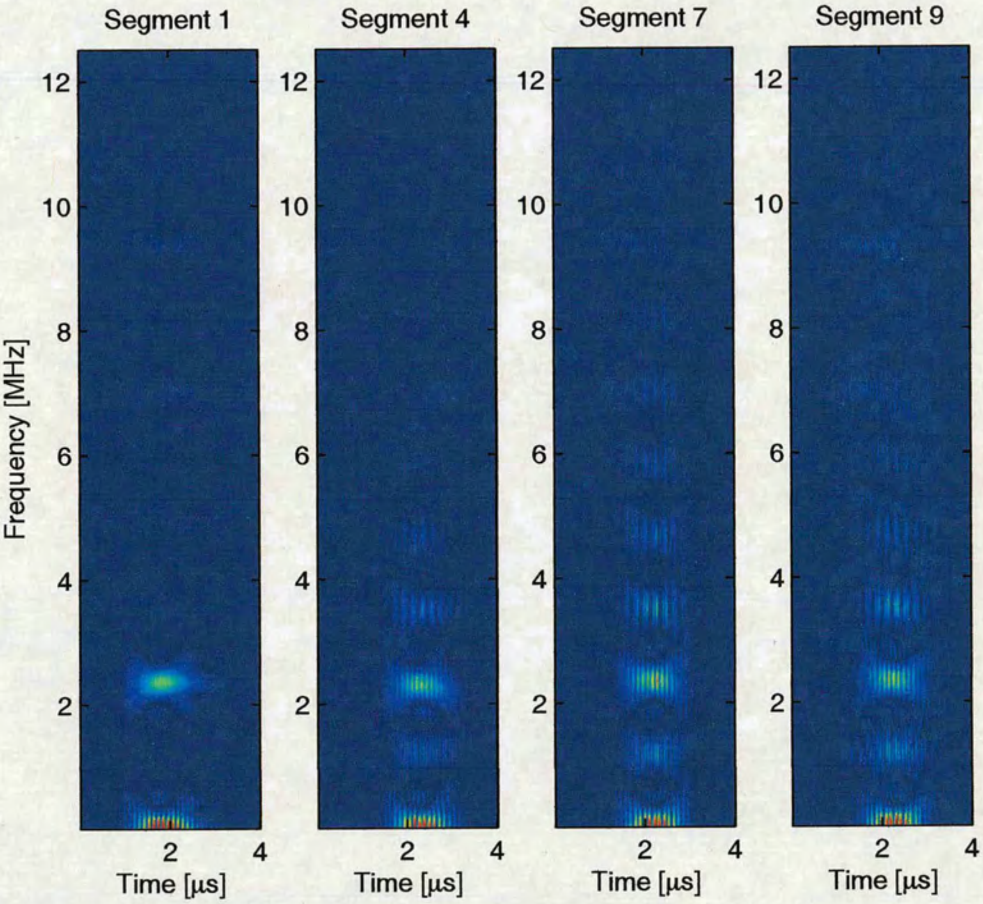

**Figure 6.8:** *Wigner-Ville distributions of three of the signals captured with the hydrophone, clearly showing increasing energy at the harmonic frequencies with increasing depth, until after the point of shock formation when the overall energy starts to diminish. Red colours indicate higher energy, while blue corresponds to lower energy.*

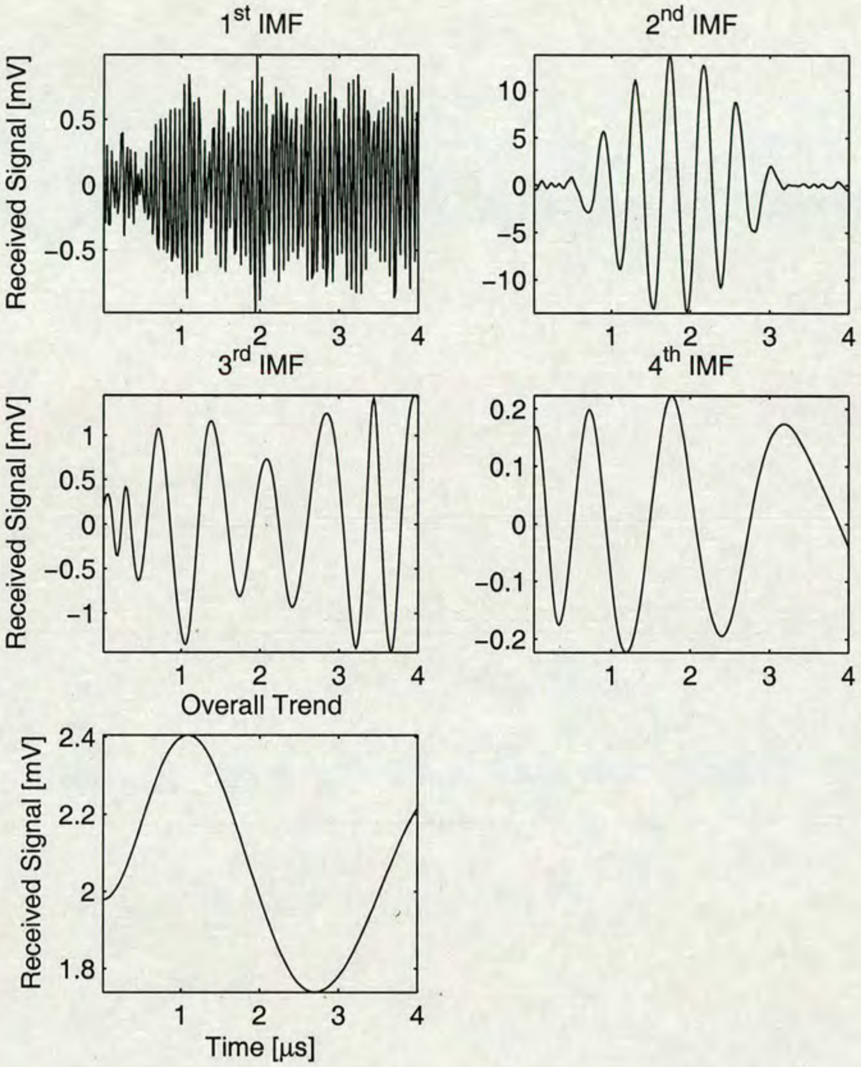

**Figure 6.9:** *The four resulting intrinsic mode functions and the remaining overall trend, for the first segment.*

tween 5 and 7 intrinsic mode functions for each one. Figure 6.9 shows the four resulting IMFs and the overall trend for the first segment, which had the least distortion. These results clearly indicated that the second IMF contained most of the signal energy, while the first IMF was caused by high-frequency noise in the signal. It was not clear if there was any physical meaning behind the third and fourth IMFs, but the overall trend is mostly due to the data capture card not being quite biased correctly leading to a non-zero signal mean. According to equation (6.11), it should be possible to reconstruct the original signal without the noise simply by adding together the second, third and fourth intrinsic mode functions. The results of doing this, along with the original signal for comparison, may be seen in Figure 6.10. The resulting

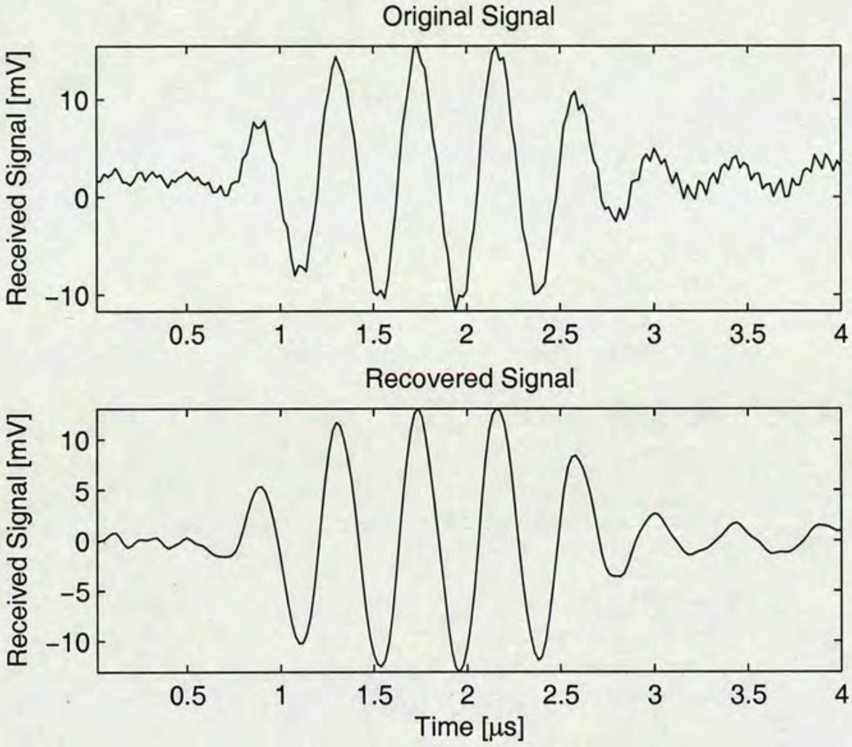

**Figure 6.10:** *Example of reconstructing a signal from the intrinsic mode functions, leaving out the high frequency noise.*

Hilbert spectrum for the first segment may be seen in Figure 6.11. The Hilbert spectrum has been coloured according to energy in such a way such that blue corresponds to low energy, while red and black correspond to progressively higher energy. Although slightly unusual, presenting the colours this way was found to give the clearest picture of what was happening. It was immediately apparent that according to the Hilbert spectrum, there was no signal energy at the second harmonic as would be expected since this segment had not been distorted to any significant degree. Figure 6.12 shows the results for the seventh segment, which corresponded to the distance at which shock formation should occur and would therefore have the maximum level of distortion. In contrast with the results obtained with the Fourier based methods, these results do not show any energy at the second harmonic frequency. Instead, it would appear that the distortion of the waveform has been caused by an intra-wave frequency modulation.

Figure 6.13 shows the Hilbert spectra obtained for the first eight of the signal segments captured with the hydrophone, as described above. These results show that as the nonlinear distortion increases, there is a corresponding increase in the amplitude of the intra-wave frequency modulation, in keeping with the theory outlined previously. It was interesting to note that up to the

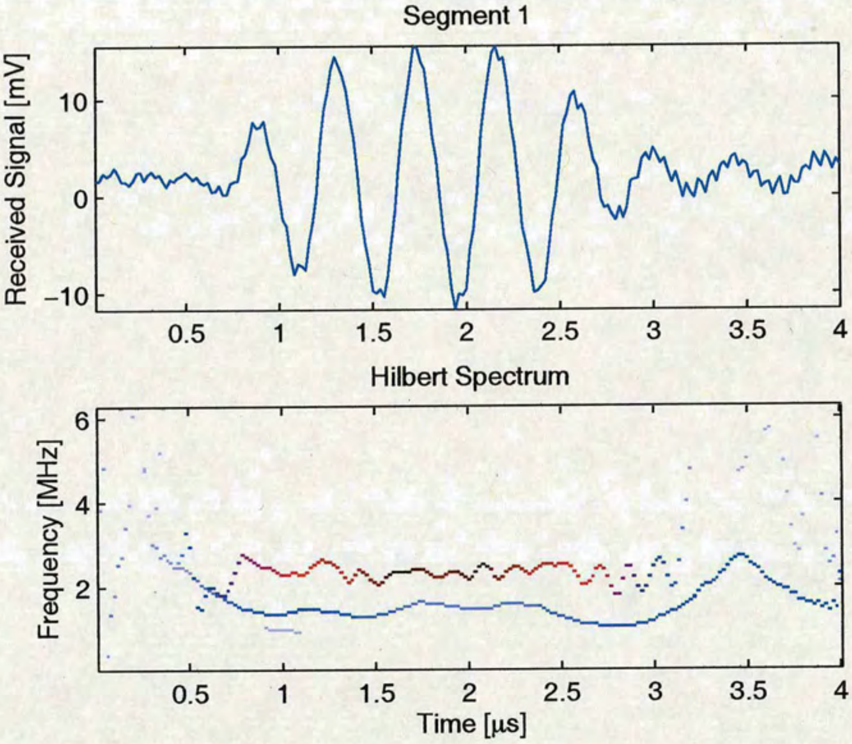

**Figure 6.11:** *Hilbert spectrum for the first segment, clearly showing bulk of signal energy at 2.25 MHz and no signal energy at the second harmonic. Note that the Hilbert spectrum has been coloured such that blue represents low energy, while red through to black represents increasingly higher energy levels.*

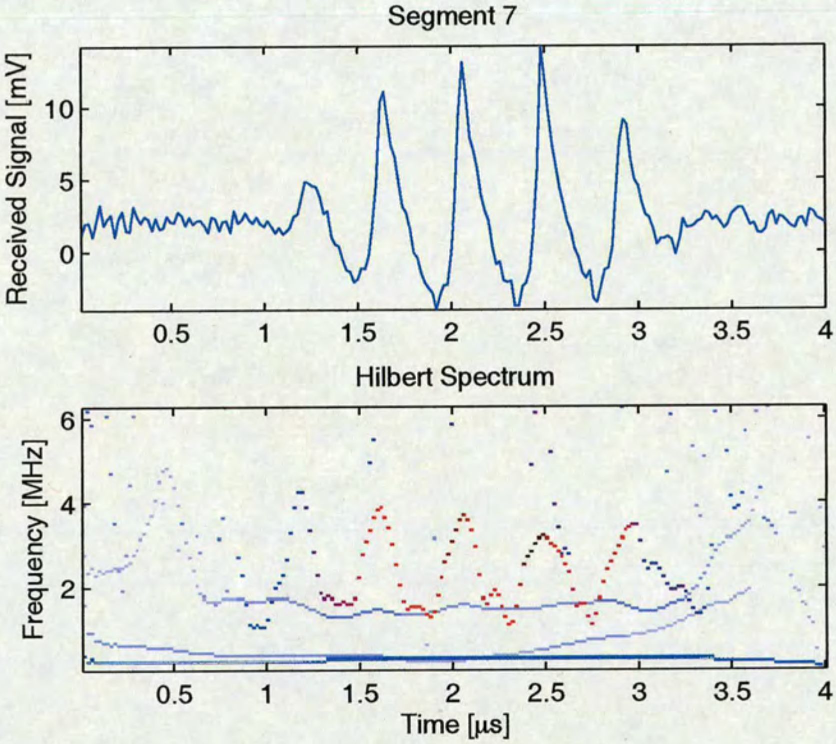

**Figure 6.12:** *Hilbert spectrum for the seventh, maximally distorted segment. This clearly shows the bulk of the signal energy oscillating around 2.25 MHz, corresponding to an intra-wave frequency modulation. There is still no energy at the second harmonic. Note that the Hilbert spectrum has been coloured such that blue represents low energy, while red through to black represents increasingly higher energy levels.*

point of shock formation, which occurred at a position roughly corresponding to the seventh segment, the intra-wave frequency modulation was fairly well defined, but it appears that after this point, the situation becomes more disordered.

### 6.3.2 Scattered TMM Signals

The tissue-mimicking material phantom, described previously in Chapter 5, was used to investigate if the alternative interpretation offered by the process of empirical mode decomposition and the Hilbert spectrum could offer any advantages compared to conventional tissue harmonic imaging. In order to achieve this, the Panametrics 6 MHz, 100 % bandwidth transducer was used, which would allow signals in the range of 3 MHz to 9 MHz to be used. As for the work described in Chapter 5 which was based on the 3.5 MHz centre frequency transducer, the sensitivity was rather low, which severely limited the imaging depth which was obtainable. The focal depth of the transducer was 50 mm and it was possible to obtain useful signals to a depth of around 70 mm. Apart from the different transducer, the experiment setup was exactly as illustrated in Figure 5.16.

Initially, the transducer was driven with a 4 cycle duration pulse with a centre frequency of 4 MHz, repeated at a pulse repetition frequency of 1 kHz. The centre frequency was chosen such that the second harmonic would be within the bandwidth of the transducer and the phantom was arranged such that the 3 mm wide slit would be visible. Figure 6.14 shows the time and frequency content of the received signal. The short-time Fourier transform portion of Figure 6.14 clearly shows that the bulk of the signal energy is concentrated around 4 MHz, as would be expected. There is also a smaller, but still significant amount of energy distributed into the second harmonic, with a smaller portion remaining into the third harmonic. The contour plot of the short-time Fourier transform was produced without log scaling of the values, so the plot of the PSD gives a better idea of the relative signal power at each frequency. The short-time Fourier transform also demonstrates relatively poor localisation in both the time and frequency domains.

However, attempting to apply the technique of tissue harmonic imaging by filtering around the second harmonic of this signal failed to give any improvement compared to simply using the fundamental frequency. It should have been possible to observe an increase in the available 'imaging' depth, or the depth to which the signal contained useful information, though in practice this was not the case. It was known that the SNR of the single crystal ultrasound system

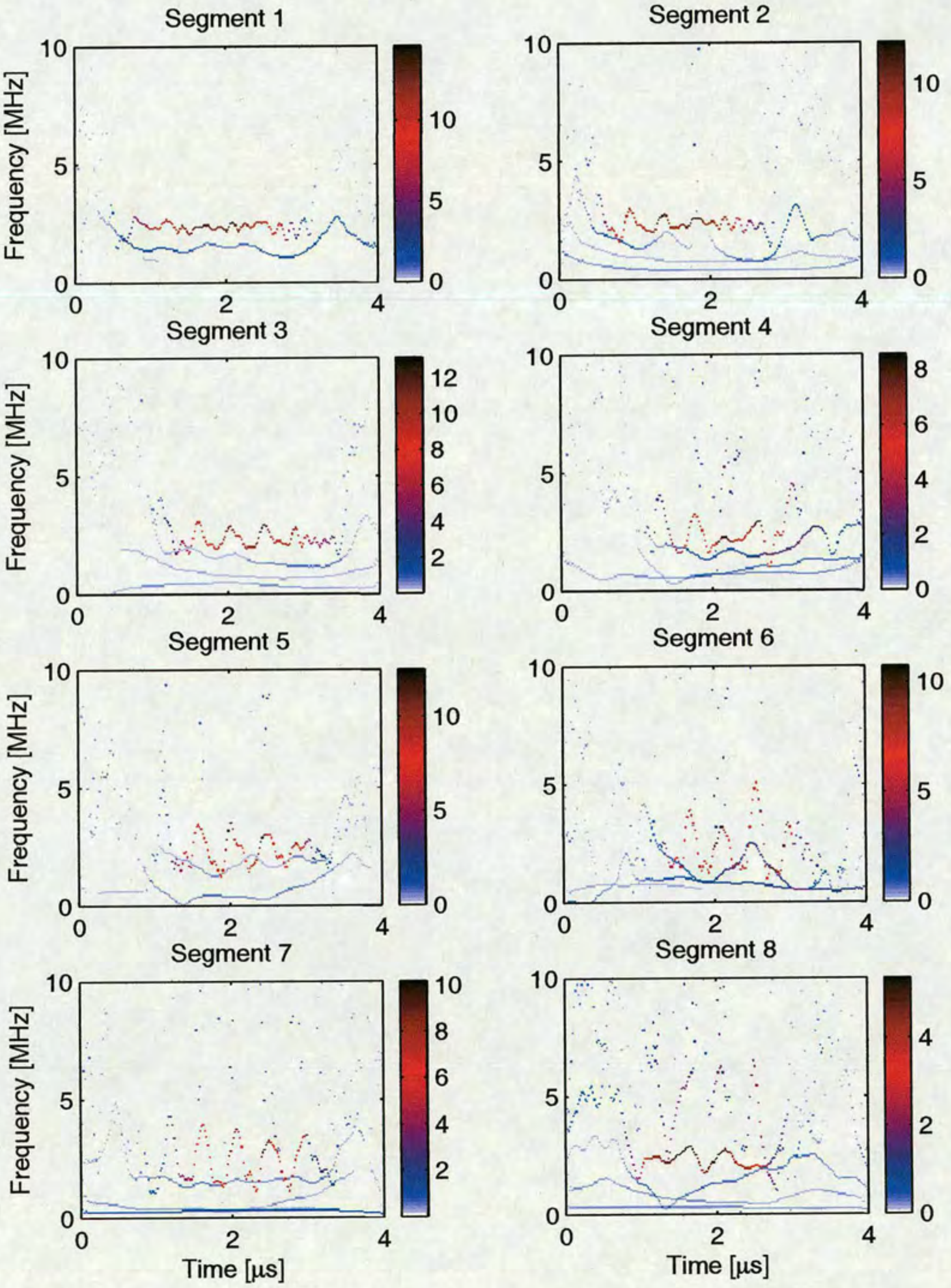

**Figure 6.13:** *Hilbert spectra of the first eight signal segments captured with the hydrophone at progressive distances from the transducer, illustrating that the increase in distortion causes a corresponding increase in the amplitude of the intra-wave frequency modulation, rather than spreading signal energy into harmonics of the centre frequency.*

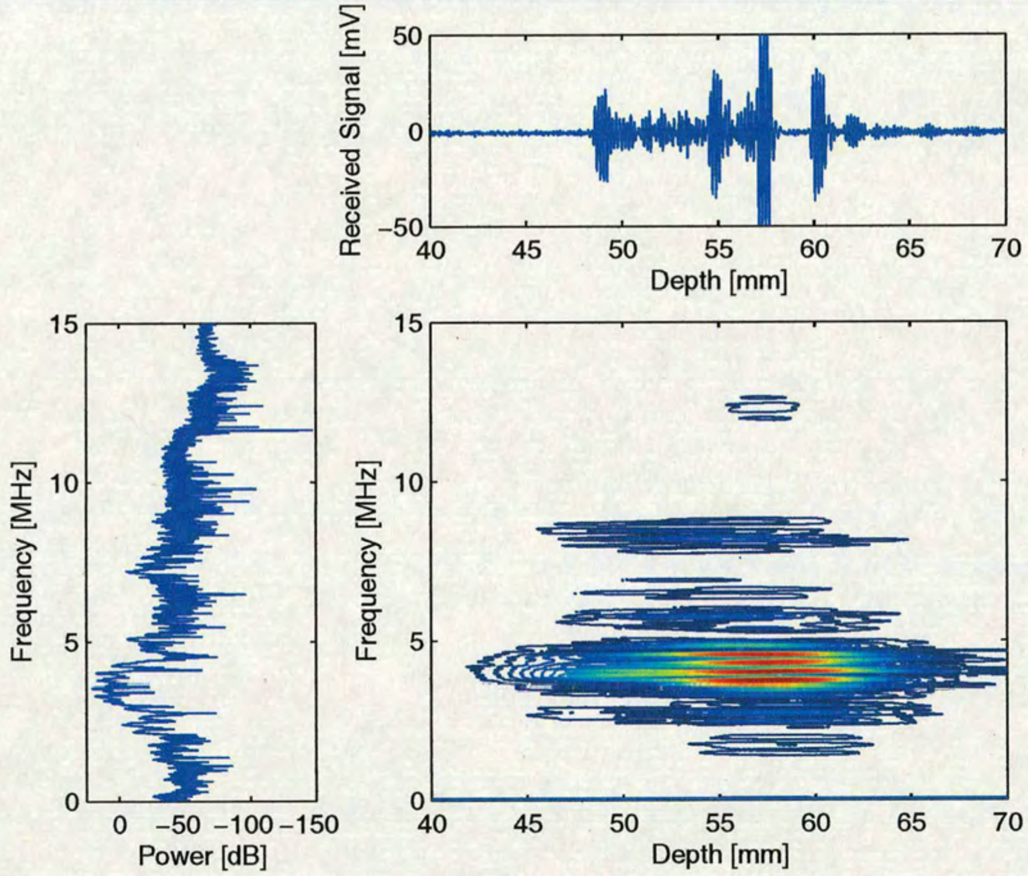

**Figure 6.14:** *Time and frequency analysis of 4 MHz signal.*

was substantially lower than that of a clinical scanner and it was therefore felt that this was the likely cause of the 'failure' of tissue harmonic imaging applied to signals captured with this system. The amplitudes of the signal received at the second harmonic are very low, therefore a high SNR is required to be able to detect them.

It has been shown that the combined techniques of Empirical Mode Decomposition and the Hilbert spectrum are able to offer significantly better localisation in time and frequency and that they offer an alternative view of the nonlinear distortion in terms of an intra-wave frequency modulation. Applying the EMD process to the signal being considered here gave 11 Intrinsic Mode Functions, which may be seen in Figure 6.15, along with the overall trend. The Hilbert spectrum for a small portion of this 4 MHz signal may be seen in Figure 6.16. These results clearly demonstrate the presence of an intra-wave frequency modulation and in contrast to the short-time Fourier transform results, do not show any signal energy at the harmonics of the fundamental. Only a short portion of the signal was analysed at a time for the sake of clarity of the figures. In this case, the portion chosen was from the top of the phantom, so the first 0.5 mm corresponds to just water following which the signal is due to backscatter from the TMM. Figure 6.17 shows similar results for a different portion of the signal covering the 3 mm slit. These results were taken to indicate that it was possible to observe an intra-wave frequency modulation occurring in signals which are the result of back-scatter from tissue mimicking material. Since the Hilbert spectra are obtained essentially by plotting the instantaneous frequencies of the intrinsic mode functions and given that the intra-wave frequency modulation has been shown to be a result of the nonlinear propagation, then this leads to the conclusion that it should be possible to achieve similar results to tissue harmonic imaging using the empirical mode decomposition technique. As has been stated above, tissue harmonic imaging is concerned with extracting the information from a signal which is due to the way the nonlinear properties of the medium through which it has propagated have changed the shape of the waveform. Empirical mode decomposition appears to offer an alternative way of obtaining this information.

Close inspection of the signal IMFs, shown in Figure 6.15, revealed that the second IMF appeared to contain information to a greater depth than either the first IMF or the original signal. This is shown more clearly in Figure 6.18. In this case, it is important to note that the amplitudes of the signal envelopes have been normalised to aid comparison and that in reality, the magnitude of the second IMF was significantly smaller than that of the original signal envelope.

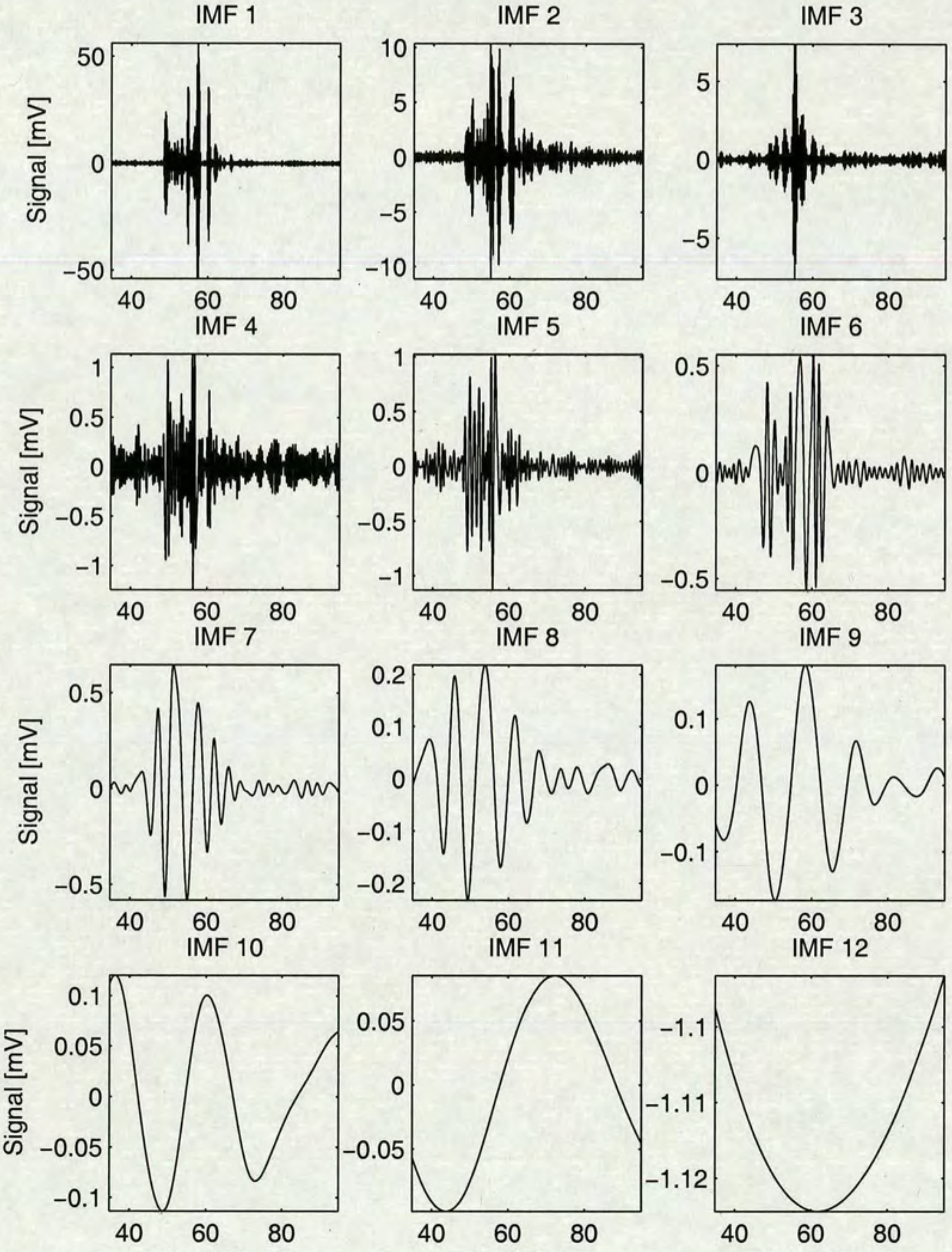

**Figure 6.15:** *Intrinsic mode functions resulting from using the EMD algorithm with the 4 MHz TMM signal.*

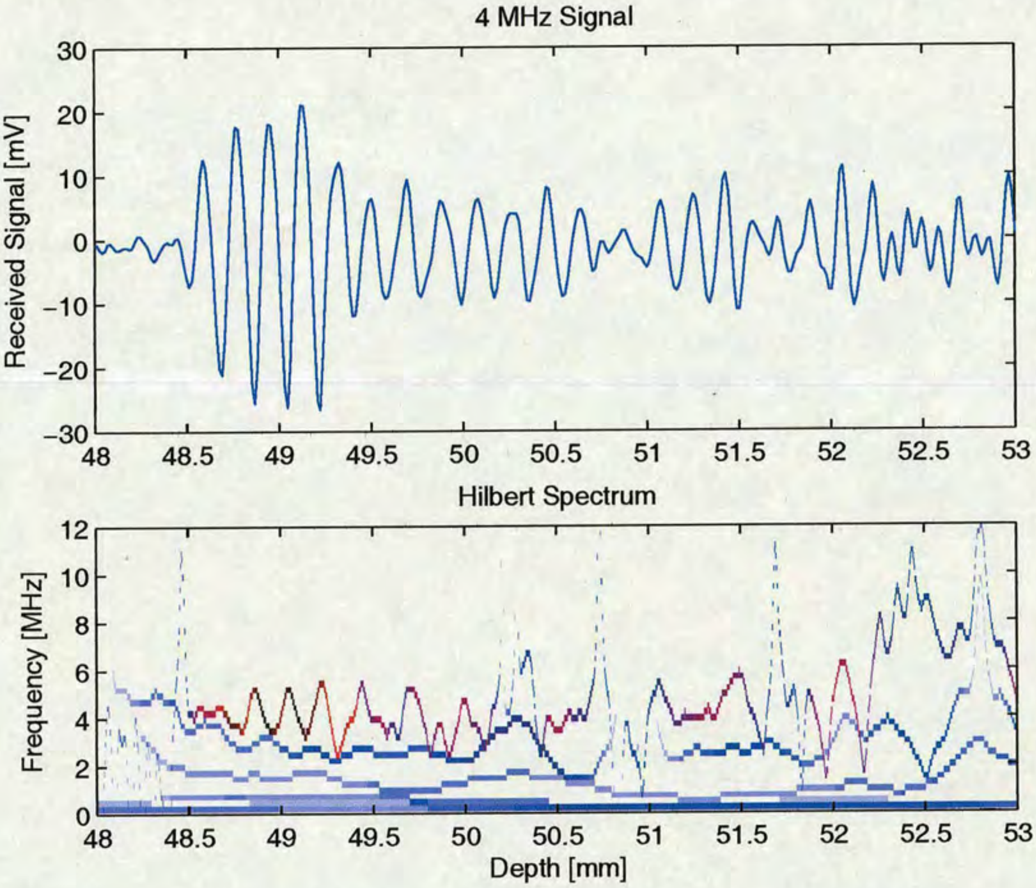

**Figure 6.16:** *Hilbert spectrum for short portion of 4 MHz signal.*

The apparent increase in depth at which useful information can be obtained was confirmed by plotting the SNR against depth, as shown in Figure 6.19. The SNRs were calculated by finding the mean noise amplitude over a 1000 sample region prior to the backscattered signals being received and plotting the ratio between the current amplitude and this figure against depth. From these results, it was observed that at a depth of 80 mm, the peak SNR of the second IMF was around 4 dB higher than that of the original signal. However, it was found that this apparent improvement was approximately the same as would be gained using a 100 % bandwidth, bandpass filter centred on the fundamental. It was therefore concluded that the intrinsic mode function did not extend the available imaging depth.

Figures 6.20 and 6.21 show the results obtained when the setup used above was driven with a 6 MHz signal and a 9 MHz signal respectively. In both of these cases, the second harmonic of the signal would be beyond the bandwidth of the transducer, so that the results from filtering around the second harmonic are just random noise. However, the results from extracting the second

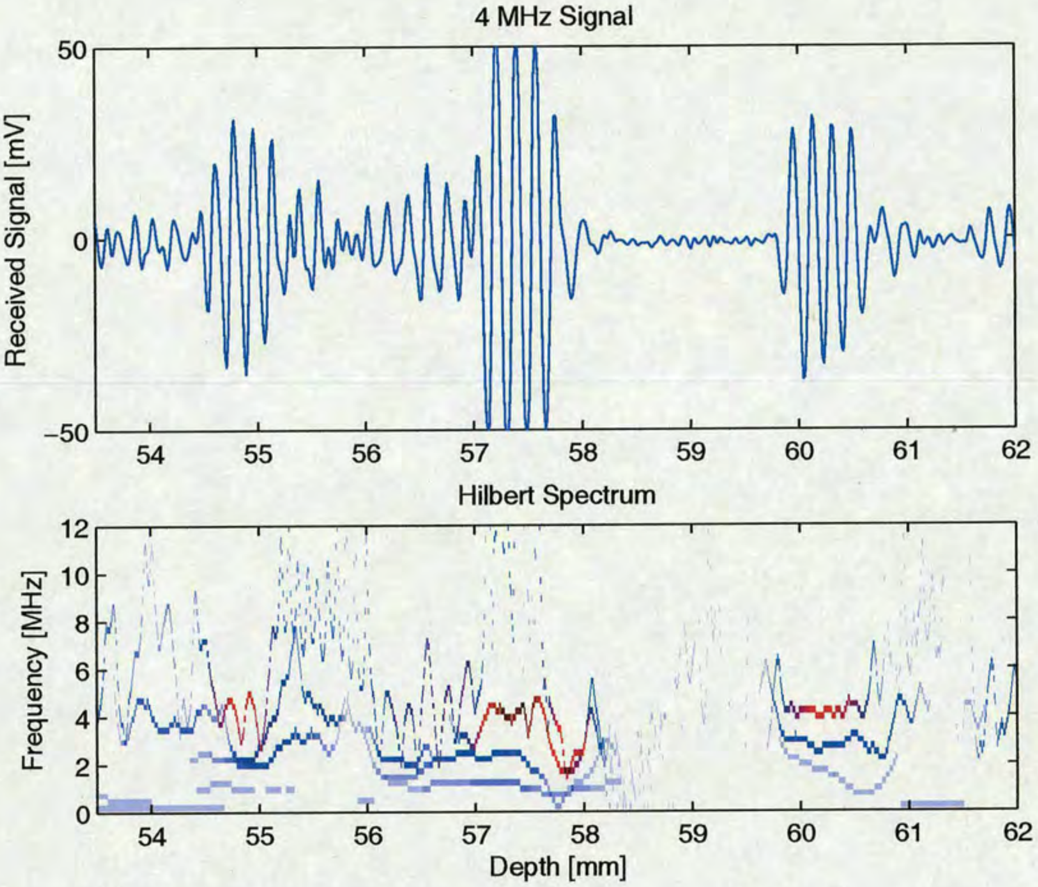

**Figure 6.17:** *Hilbert spectrum for short portion of 4 MHz signal.*

intrinsic mode function, as described above, demonstrate that this technique still produced good results despite the bandwidth limitations.

The above experiments were repeated using the 3.5 MHz centre frequency transducer, firstly using a transmit frequency of 1.75 MHz which would allow the second harmonic frequency (3.5 MHz) to be within the transducer bandwidth, followed by signals at the centre frequency (3.5 MHz fundamental, 7 MHz second harmonic) and at 5.25 MHz, with a second harmonic at 10.5 MHz. Looking initially at the 1.75 MHz signals, as shown in Figure 6.22 and their corresponding short-time Fourier transforms shown in Figure 6.23 demonstrated two interesting results. Firstly, it was observed that with a pulse length of 4 cycles, the bandwidth of the resulting signal was too high and it was not possible to observe any second harmonic energy. An attempt was made to improve this situation by increasing the pulse length to 8 cycles, which has the expected effect of reducing the bandwidth. However, the second interesting observation was that neither of these two short-time Fourier transforms showed any significant energy at

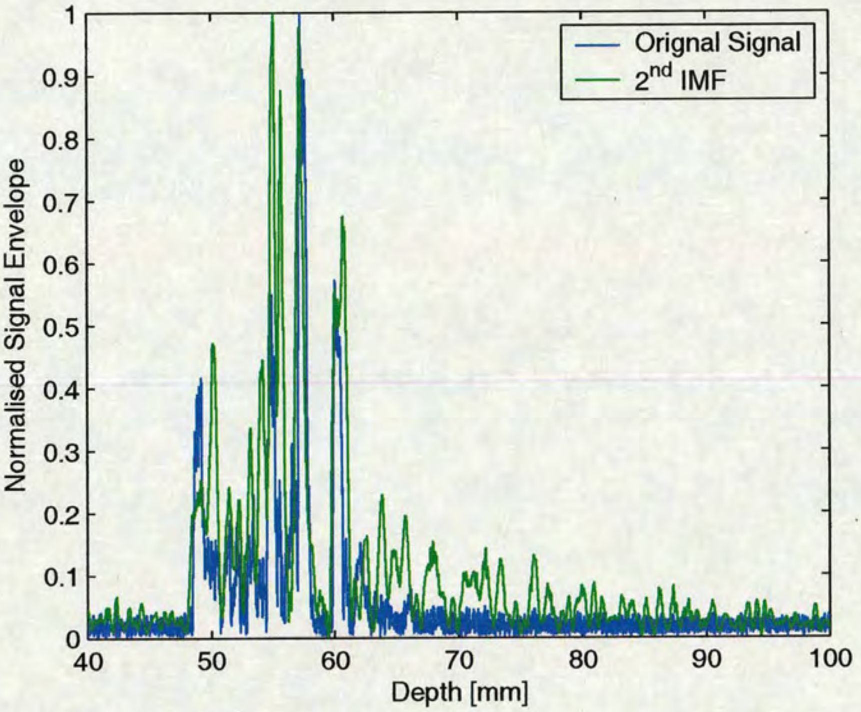

**Figure 6.18:** *Comparison of original, unfiltered signal with the second IMF. Demonstrates that the second IMF contains information to a depth of around 90 mm, compared to only around 65 mm for the unfiltered signal.*

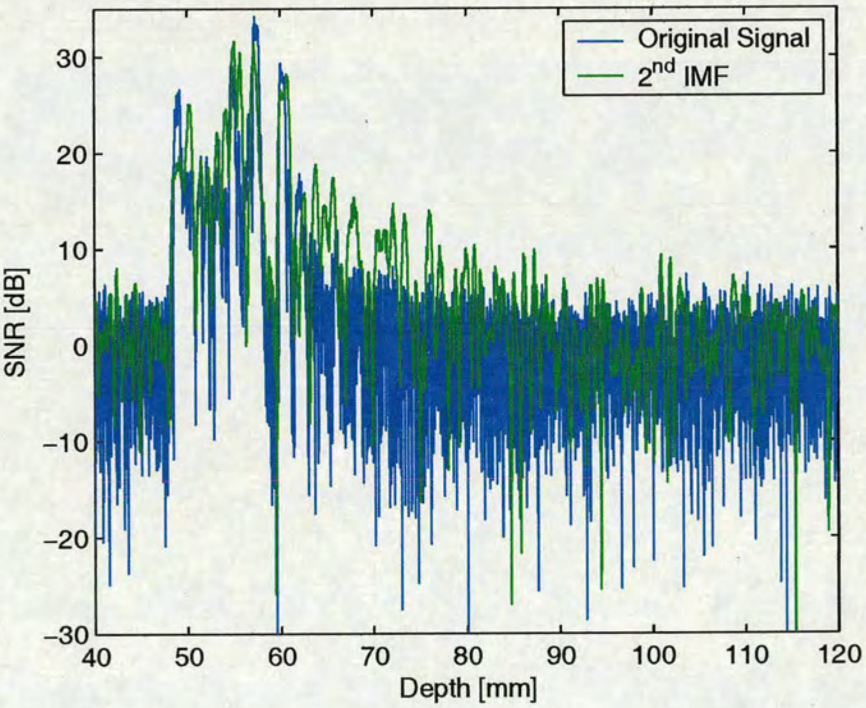

**Figure 6.19:** *Comparison of the SNRs of the original signal and of the second IMF, clearly showing that the SNR for the latter falls off more slowly with depth.*

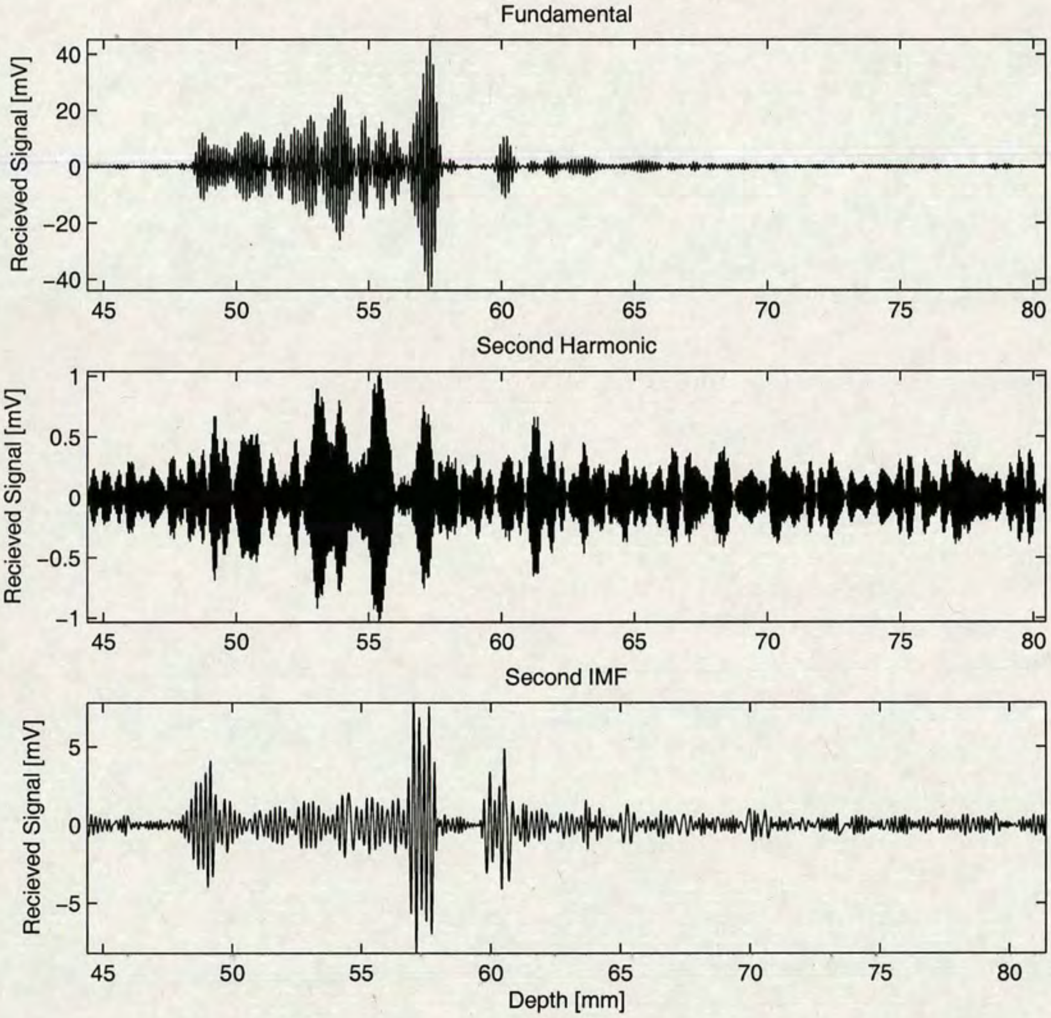

**Figure 6.20:** *Comparison of fundamental and second harmonic filtering of the 6 MHz signal with the second IMF. The second harmonic frequency of 12 MHz was beyond the bandwidth of the transducer and so was greatly suppressed, however, the second IMF clearly shows improvement over the fundamental signal in terms of delineating the slit and available imaging depth.*

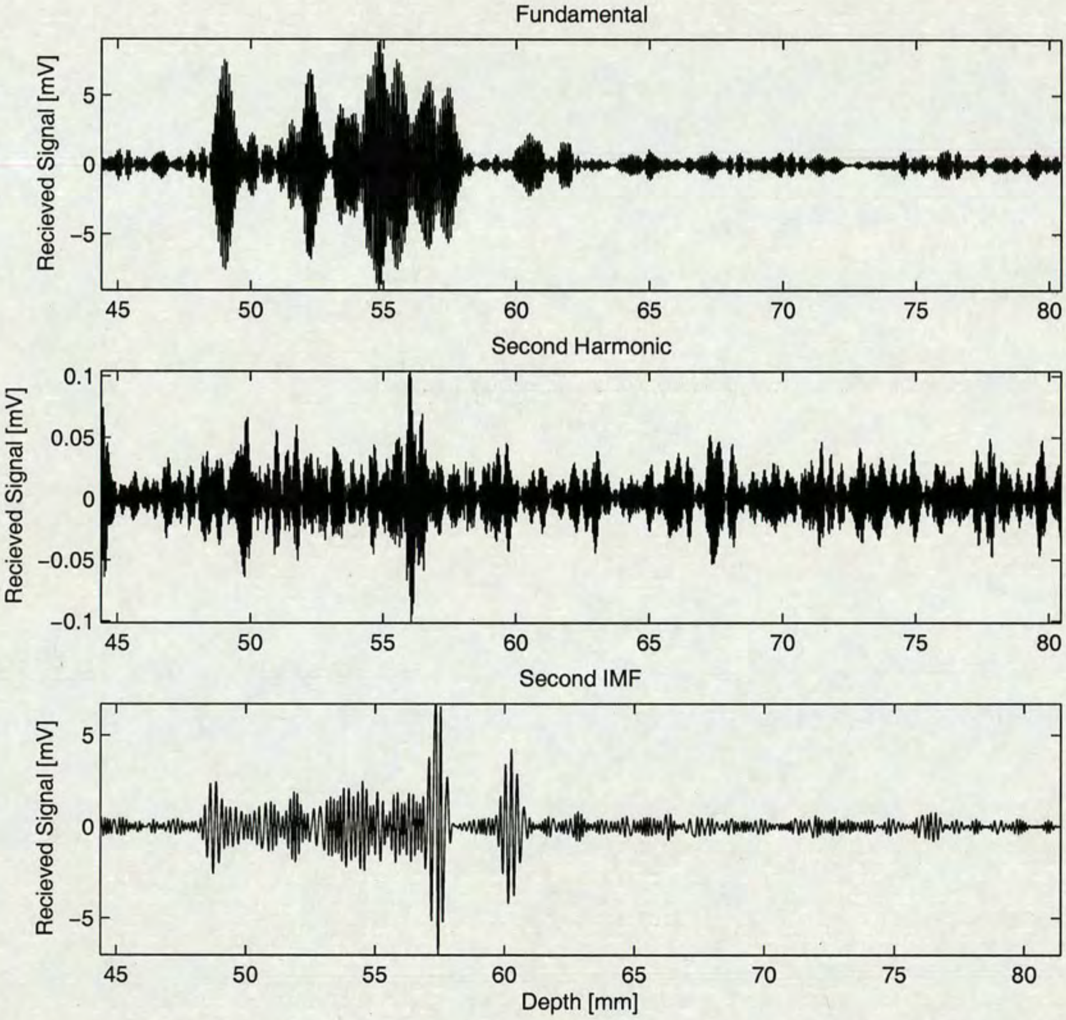

**Figure 6.21:** *Comparison of fundamental and second harmonic filtering of the 9 MHz signal with the second IMF. In this case the second harmonic frequency was 18 MHz, which was well beyond the maximum frequency of the transducer (9 MHz), hence the extremely low magnitude of the second harmonic signal. However, the second IMF still shows significant improvement.*

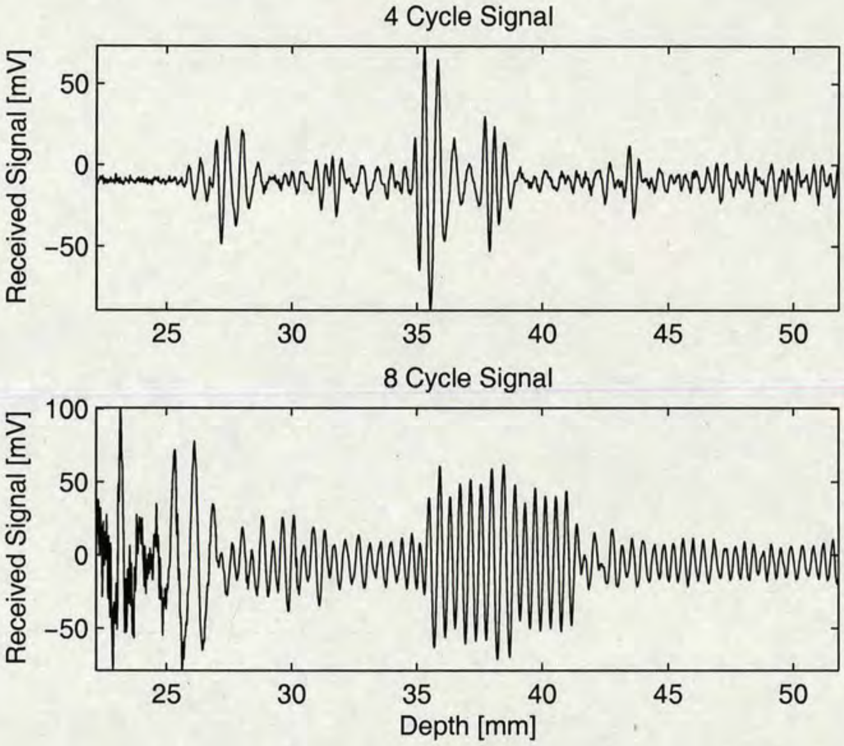

**Figure 6.22:** *Plot of a section of two of the 1.75 MHz signals, with pulse lengths of 4 cycles (top) and 8 cycles (bottom).*

the second harmonic, in contrast to the results obtained for the 4 MHz signal and show in Figure 6.14 above. The reason for this may be seen by looking back at Figure 3.6, which shows the frequency response of the receiver amplifier, which peaks between 1 MHz and 2 MHz, corresponding exactly to the frequency of the transmit signal. The difference between the amplifier response at 1.75 MHz and 3.5 MHz was approximately 5 dB, whereas the difference between 4 MHz and 8 MHz was only around 3 dB. Therefore, the difference in received signal energy between the fundamental frequency of 1.75 MHz and the second harmonic of 3.5 MHz was much greater than between 4 MHz and 8 MHz.

The mechanical scanner described in Chapter 3 was used to collect signals over the whole width of the phantom. The scan speed and pulse repetition frequency were set such that 128 lines would be captured. Figure 6.24 shows the results obtained and compares the effectiveness of filtering around the fundamental and the second harmonic for each of the transmit frequencies described above. As would be expected given the frequency response of the amplifier, filtering around the second harmonic frequency does not appear to offer any advantage. Similar results were obtained for the 8 cycle pulse length signals, as shown in figure 6.25.

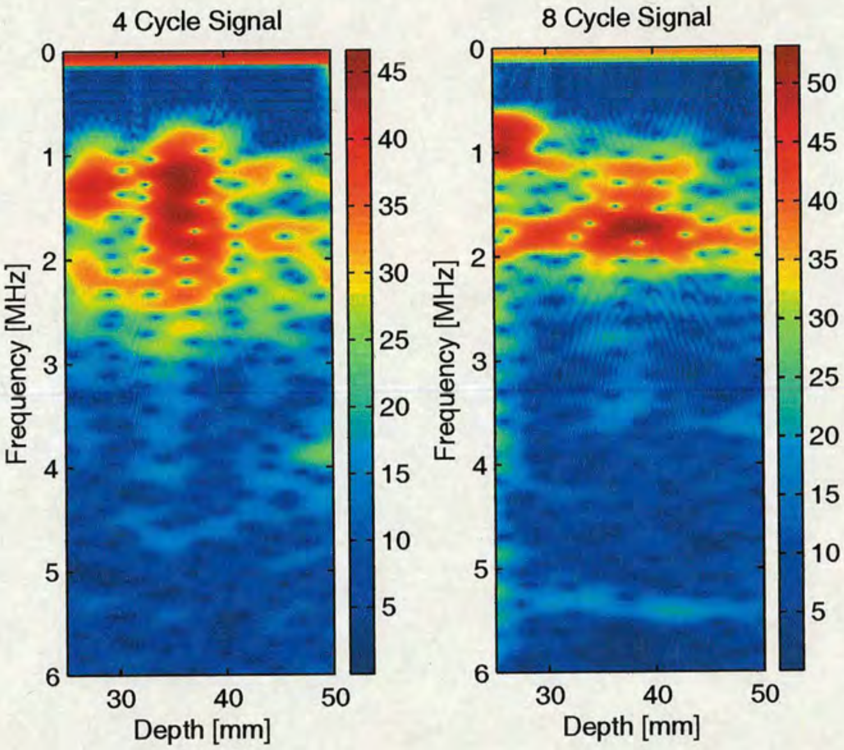

**Figure 6.23:** *Short-time Fourier transforms of the two low frequency signals shown in Figure 6.22.*

The combined techniques of Empirical Mode Decomposition and the Hilbert spectrum have already been shown to be able to offer an alternative time-frequency view of a signal, therefore using these techniques with the signals from the lower frequency transducer gave the results shown in Figures 6.26 to 6.28. These results appear to demonstrate that the bulk of the signal energy is concentrated at around 1.8 MHz in all cases, even when the transmit frequency was higher. This was thought to reflect the frequency response of the amplifier and it was found that increasing the signal energy by increasing the length of the transmitted pulses from 4 cycles to 8 cycles gave much better results. These results may be seen in Figures 6.29 to 6.31. In all cases, these results clearly indicate the presence of signal energy at the transmit frequency. Figure 6.29 clearly show the presence of an intra-wave frequency modulation, particularly in the region between 35 mm and 40 mm, which corresponded to the higher energy reflected signals from the edges of the slit. It was not possible to observe such an intra-wave frequency modulation with the higher frequency signals when the Hilbert spectra are plotted in this way because they become too broken up.

The results obtained with the 6 MHz centre frequency transducer, for transmit frequencies up to

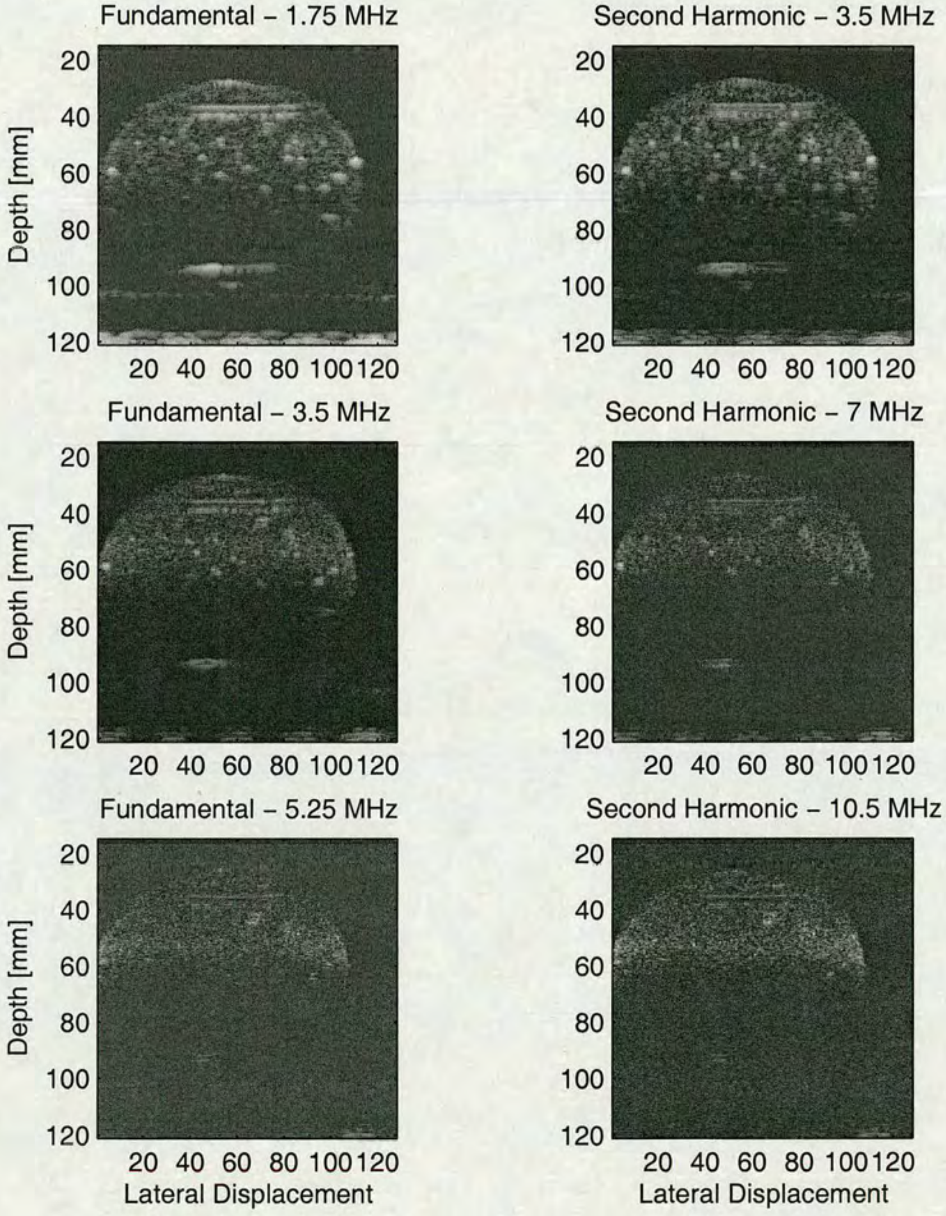

**Figure 6.24:** *Fundamental and second harmonic images produced with the low frequency transducer and the mechanical scanner, with a pulse length of 4 cycles.*

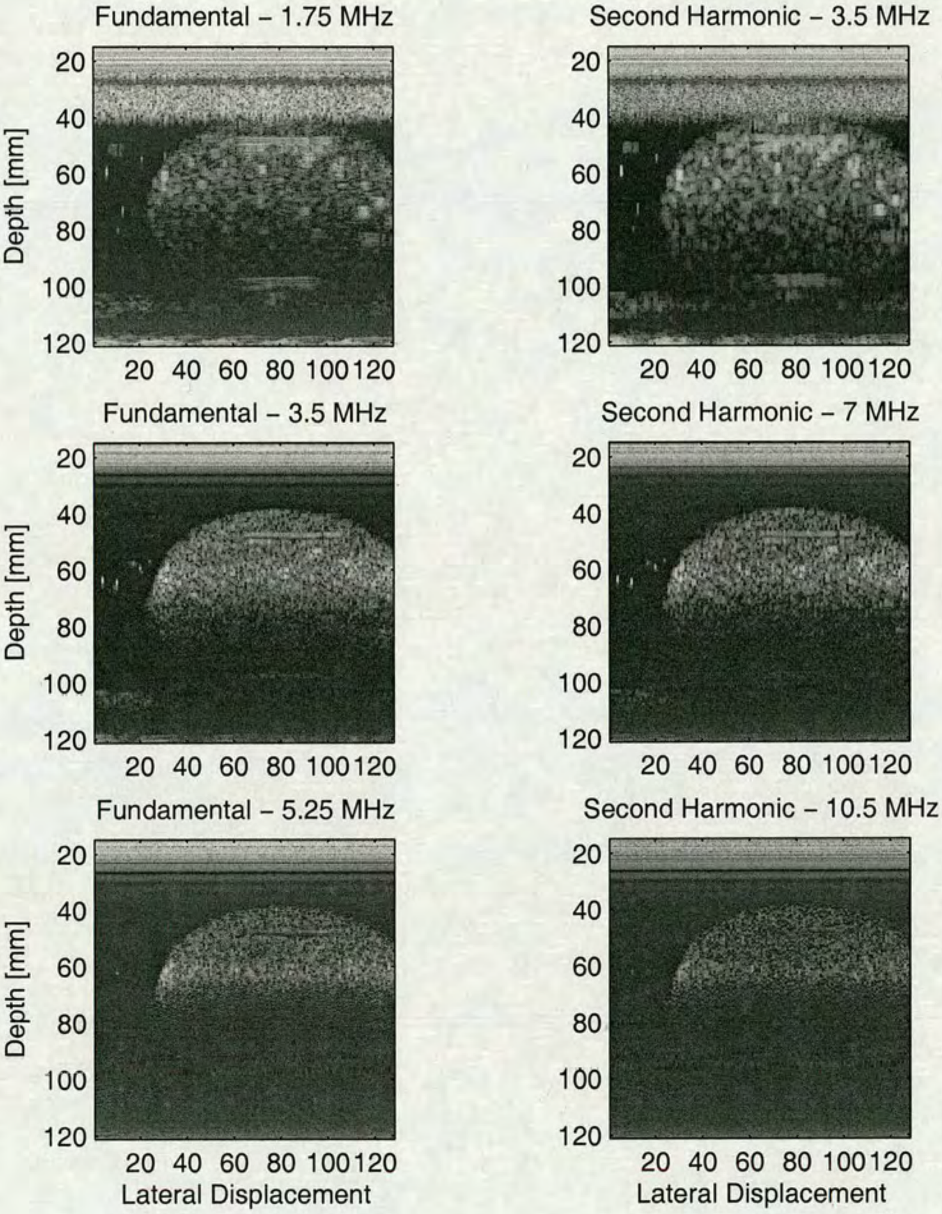

**Figure 6.25:** *Fundamental and second harmonic images produced with the low frequency transducer and the mechanical scanner, with a pulse length of 8 cycles.*

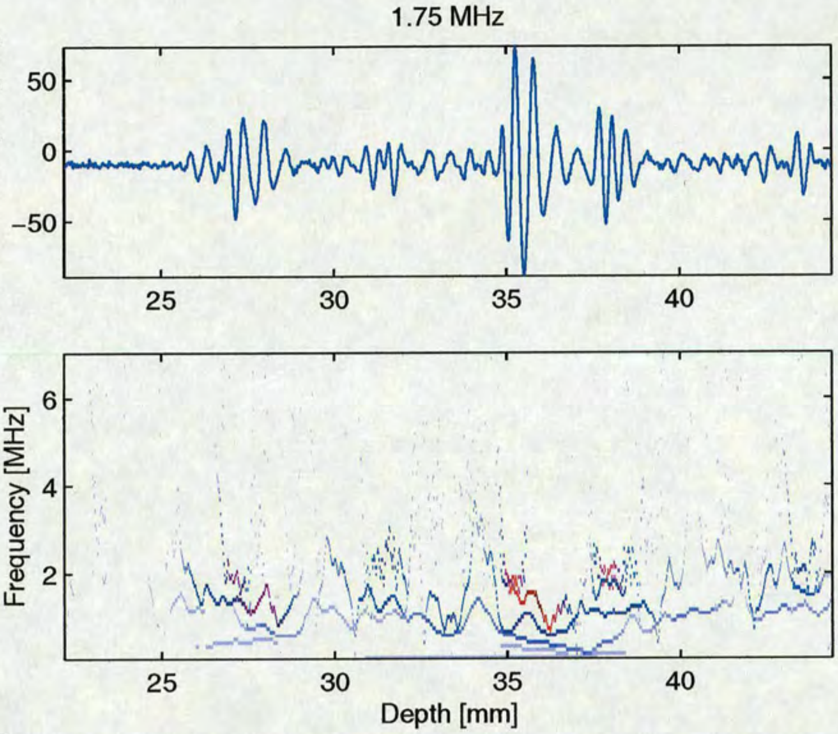

**Figure 6.26:** *Hilbert spectra of 1.75 MHz signals, with a pulse length of 4 cycles.*

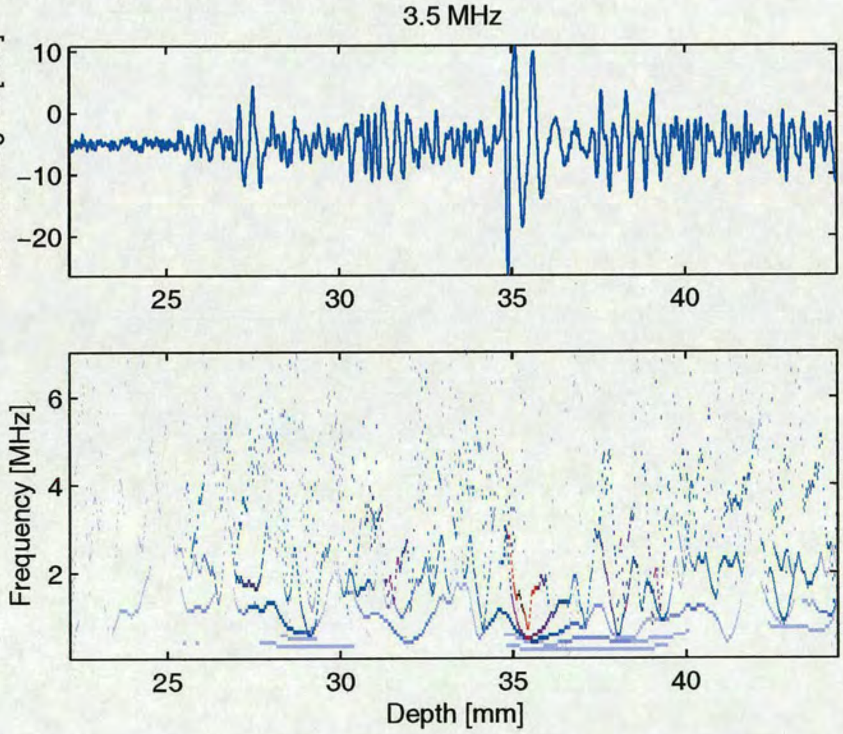

**Figure 6.27:** *Hilbert spectra of 3.5 MHz signals, with a pulse length of 4 cycles.*

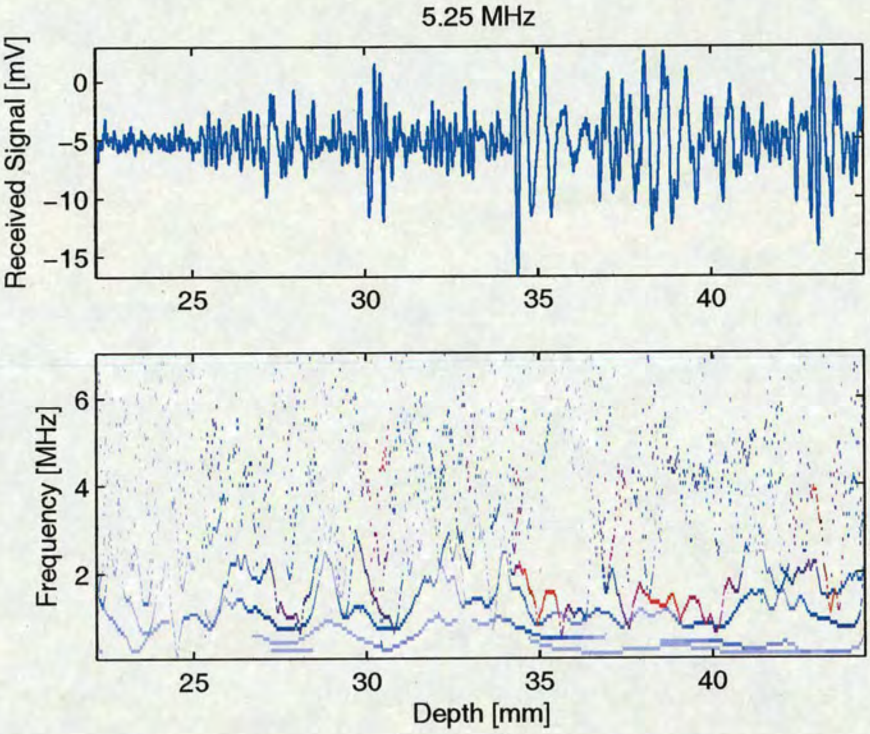

**Figure 6.28:** *Hilbert spectra of 5.25 MHz signals, with a pulse length of 4 cycles.*

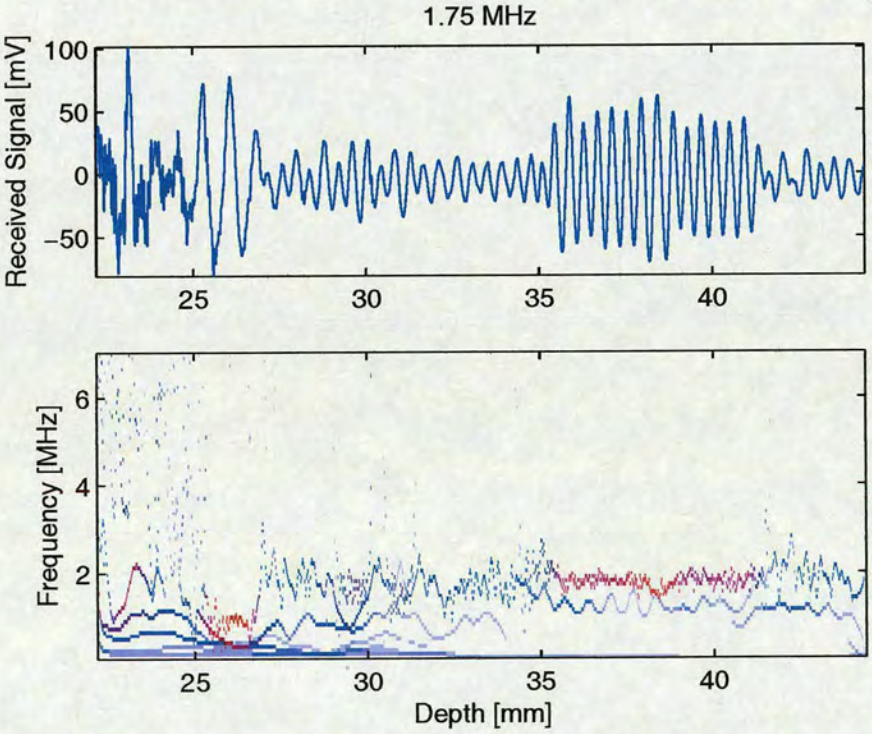

**Figure 6.29:** *Hilbert spectra of 1.75 MHz signals, with a pulse length of 8 cycles.*

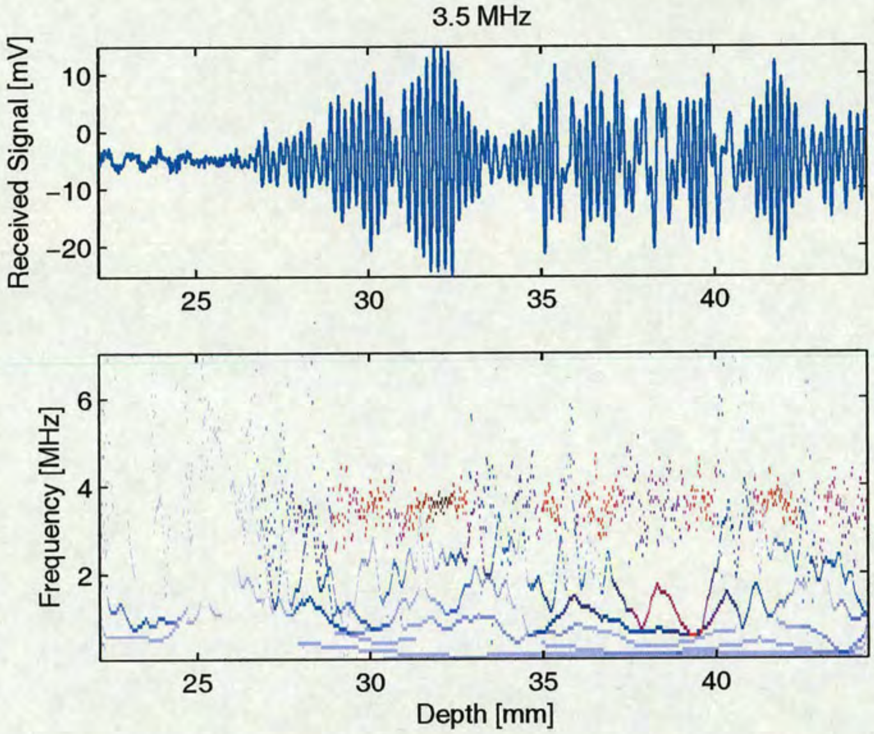

**Figure 6.30:** *Hilbert spectra of 3.5 MHz signals, with a pulse length of 8 cycles.*

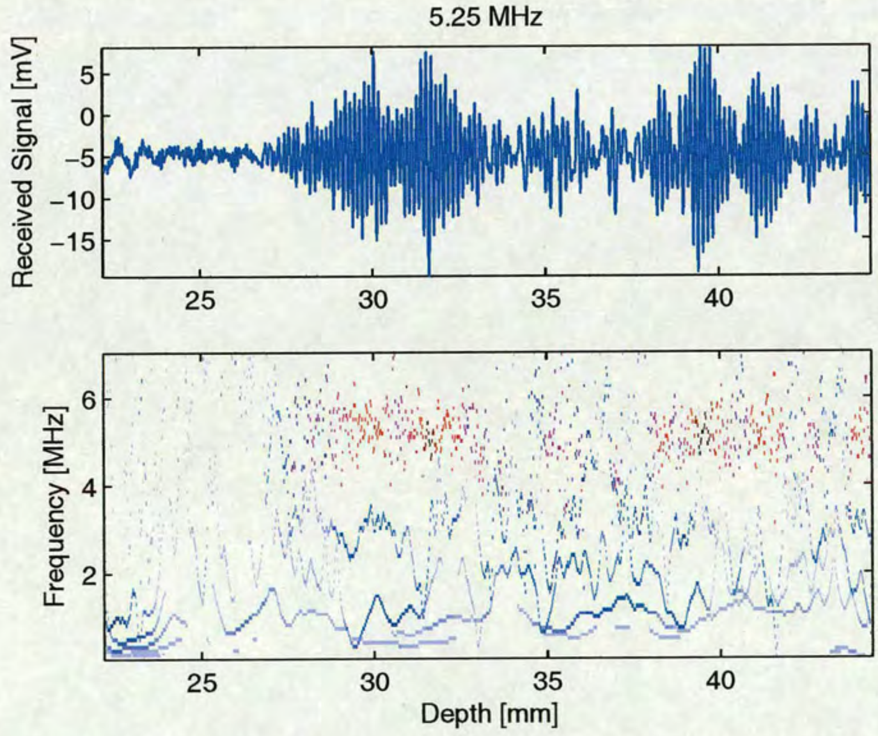

**Figure 6.31:** *Hilbert spectra of 5.25 MHz signals, with a pulse length of 8 cycles.*

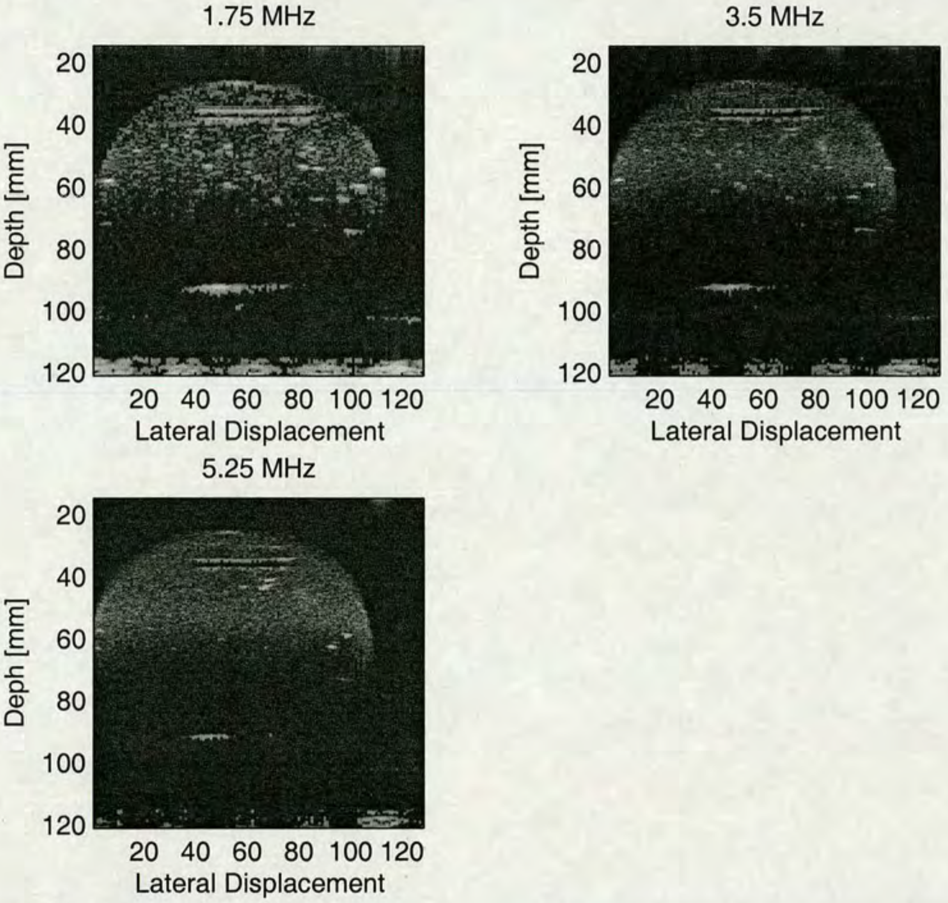

**Figure 6.32:** *Images produced by summing the first two intrinsic mode function images for each of the transmit frequencies, for the 4 cycle pulse length signals.*

9 MHz, clearly showed that the intrinsic mode functions could continue to contain significant useful information, even when the transmit frequency was increased right up to the transducer limit. This was also observed to be the case with the signals from the lower frequency transducer, although in this case it was found that forming images from the sum of the first two intrinsic mode functions appear to give very good results, with clearer definition of the slit than fundamental imaging in all cases. These results are shown in Figures 6.32 and 6.33 for the 4 and 8 cycle pulse lengths respectively. As would be expected, the higher frequency signals give greater resolution of the slit, while increasing the pulse length degrades this somewhat compared to the equivalent frequency shorter pulse length case.

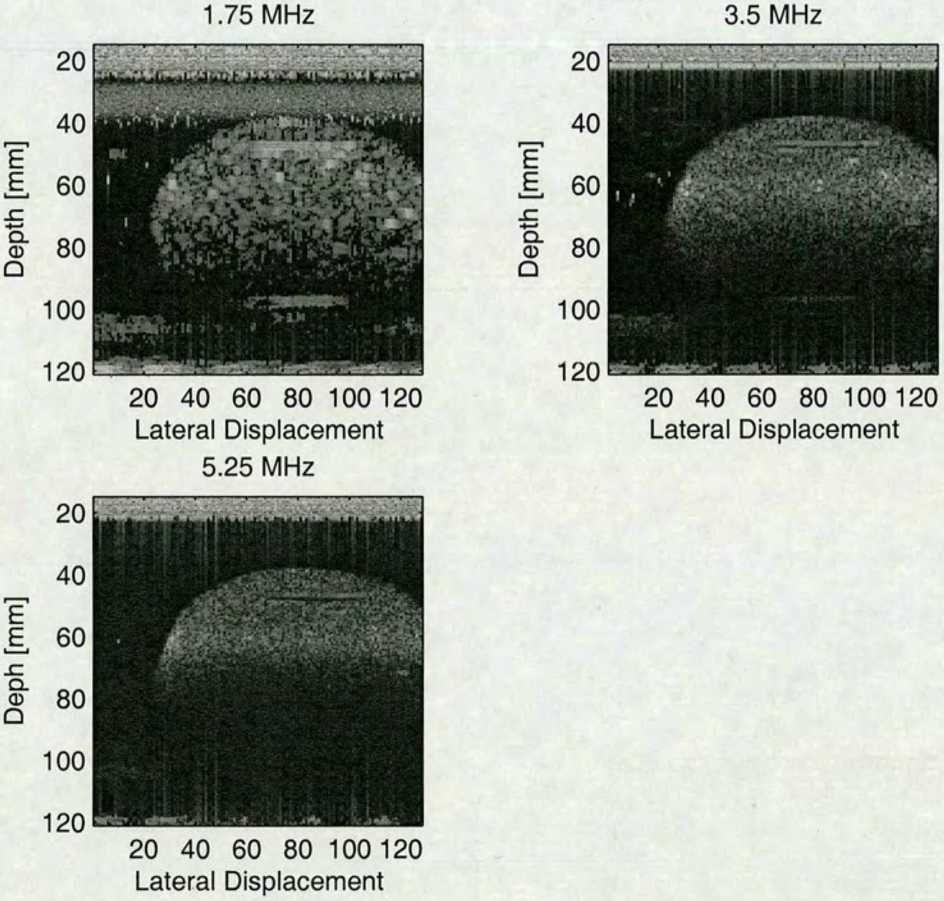

**Figure 6.33:** *Images produced by summing the first two intrinsic mode function images for each of the transmit frequencies, for the 8 cycle pulse length signals.*

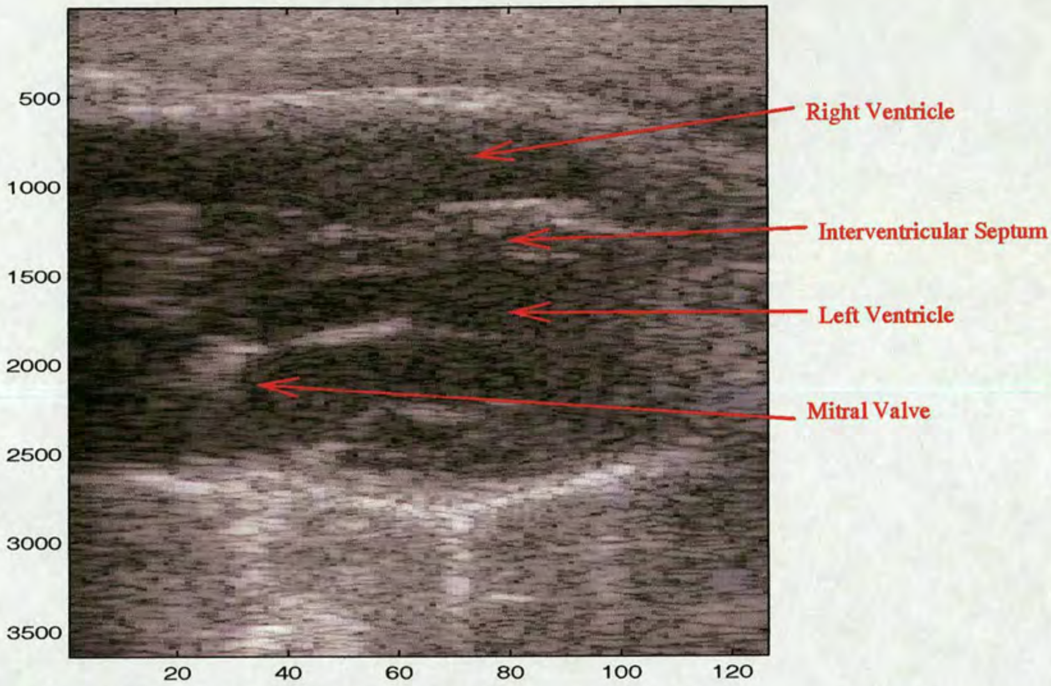

**Figure 6.34:** *Example in-vivo data presented in rectilinear format.*

### 6.3.3 Clinical Scanner Data

The Philips SONOS 5500 clinical scanner was used to collect in-vivo data from a healthy volunteer. The transducer used was of the form of a 128 element phased array, with a transmit frequency of 1.9 MHz. The volunteer was arranged in a seated position and the scans were performed via the parasternal long-axis view. An example of the results obtained may be seen in Figure 6.34, which has been annotated to highlight the key features. The techniques described above were applied to this data and images produced from the first three intrinsic mode functions may be seen in Figure 6.35. It was felt that the image produced from the second IMF was clearer and had higher contrast than the image produced from the raw, original data. The two images may be seen side-by-side in Figure 6.36. Inspecting the IMFs of a single line from this data set revealed that the first two IMFs contained nearly all of the signal information, therefore, summing these two did not yield any significant improvement compared to the original, unprocessed data. Figure 6.37 shows the result from summing the first two IMFs.

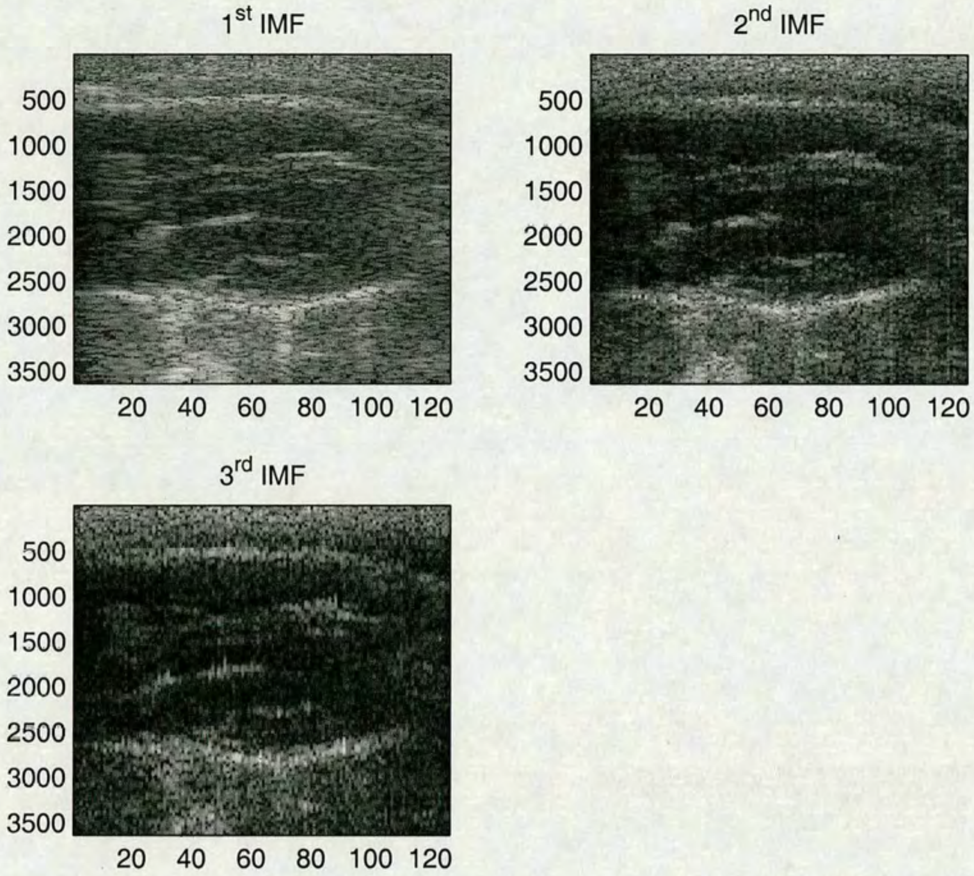

**Figure 6.35:** *Images produced from the first three IMFs of the in-vivo data.*

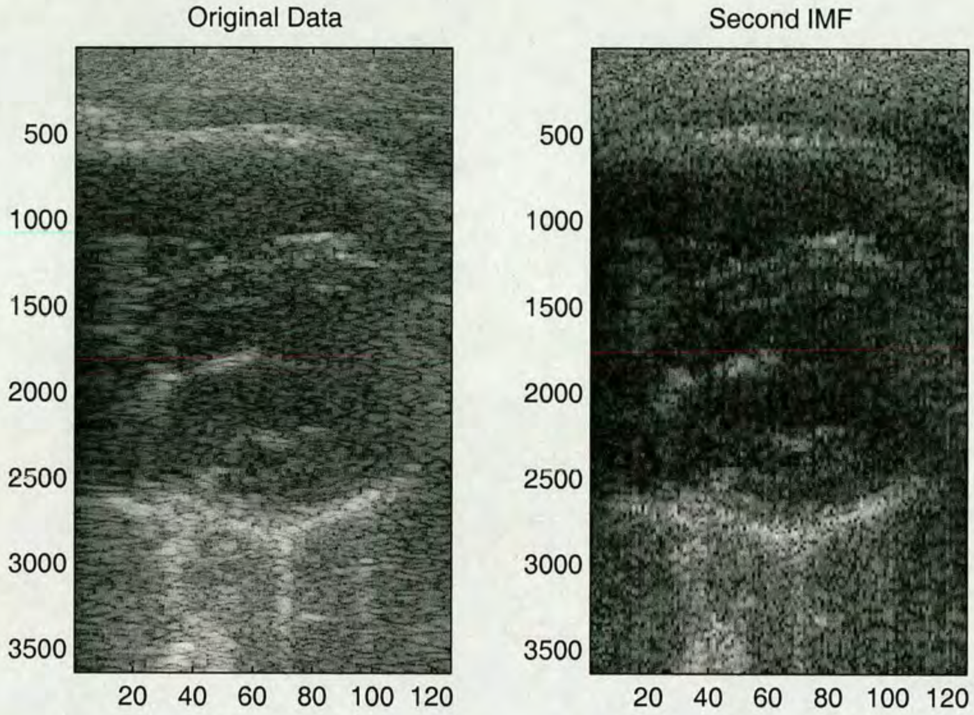

**Figure 6.36:** *Comparison of image produced from raw, original data (left) and second IMF (right). The image on the right is clearer with higher contrast.*

## 6.4 Summary and Conclusions

The phenomenon of non-linear distortion leading to a change in the shape of an initially sinusoidal waveform has been known for some time. Results have been presented which clearly show this process occurring in a water tank and demonstrate the general explanation that the distortion causes energy to be spread over to harmonics of the fundamental frequency.

The Fourier transform and Fourier analysis techniques have traditionally been used to analyse such effects. It has been shown that the harmonic components which appear to result from the nonlinear distortion are in reality due to the use of these techniques to look at signals which are non-stationary and non-linear, two conditions for which they are not valid. It is argued that while the harmonic components clearly represent a good mathematical model of the signal, they do not necessarily reflect an underlying physical process.

The concept of instantaneous frequency has been introduced, along with the idea of intrinsic mode functions for which the instantaneous frequency can be defined at any point without ambiguity. The technique of Empirical Mode Decomposition for the generation of such intrinsic mode functions has been introduced. These techniques, coupled with the Hilbert spectrum

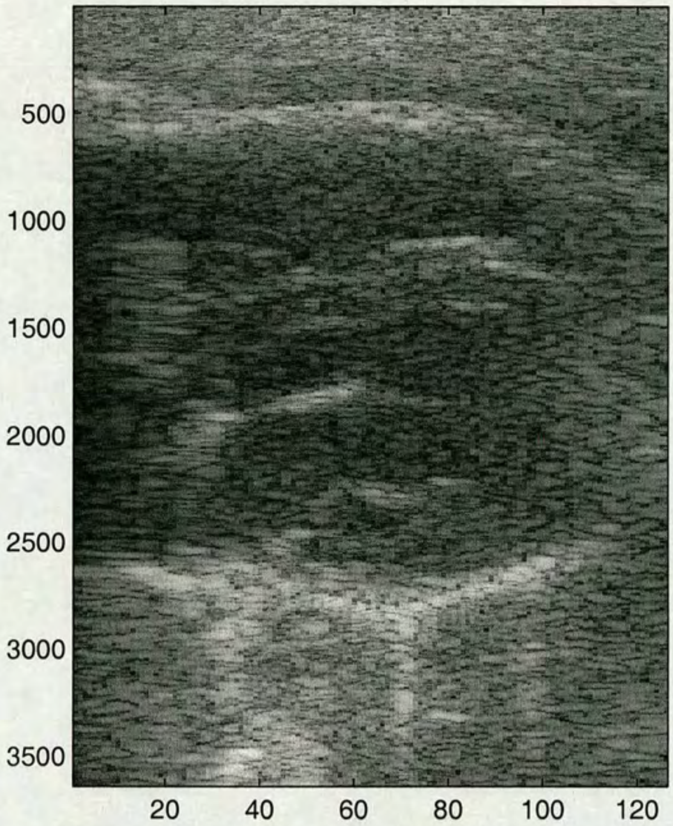

**Figure 6.37:** *Image produced by summing the first two IMFs. These were found to contain nearly all the signal information, therefore there is little improvement from the original, un-processed data.*

have been shown to be able to offer an alternative interpretation of the non-linear distortion of a waveform based on the introduction of an intra-wave frequency modulation, rather than the spreading of energy into the harmonic frequencies.

Results have been presented which clearly demonstrate the validity of this argument, both in a simple water tank arrangement with the signals being received by a wide-band hydrophone and in the case of back-scattered signals from a phantom constructed of tissue-mimicking material received using a 100 % bandwidth ultrasound transducer.

As well as giving information about the intra-wave frequency modulation and hence the non-linear distortion which is taking place, the EMD method has been shown to be able to extract useful signal information, even in the case where the transmit frequency was such that the second harmonic would be well beyond the bandwidth limitations of the transducer.

The results obtained with the 3.5 MHz centre frequency transducer were not as good as those for the 6 MHz transducer. This was felt to be due to the frequency response of the amplifier having a sharp peak in the region of 1.8 MHz, which meant that the difference between the fundamental frequency and the second harmonic frequency was much greater than in the case of the signals which were of higher frequency to start with.

Basically, ultrasound imaging in general is based on the idea that the medium through which the wave is passing will modulate the amplitude of that wave. Images can therefore be built up by displaying this amplitude modulation. However, the idea of the intra-wave frequency modulation leads to an extension of this whereby the medium not only modulates the amplitude, but also the frequency of the original signal. Currently, ultrasound systems seem to ignore this additional information. Even tissue harmonic imaging doesn't really make use of it directly, since it is based around producing images from the intensity of a few of the components of the Fourier transform of the signal. The phase-inversion method of tissue harmonic imaging, of course, is different, but this technique also fails to make use of this additional frequency information.

# Chapter 7
# Conclusions

## 7.1 Introduction

The current trend in echocardiography appears to be one of greater quantification of the results obtained, however for any significant improvements to be made it will be necessary for the current technology to be improved significantly. In the light of this, the principle aim of this thesis was to investigate the use of more modern signal processing techniques and to determine if these would enable any improvement in the degree of quantification achievable. According to the literature, there has been a significant amount of work done in the area of quantifying the results obtained using this technique of Doppler tissue imaging. Much of this research has focused on using the estimated velocities to calculate velocity gradients, which are inherently immune to a number of factors, such as Doppler angle and global motion, which would otherwise corrupt the result and decrease the accuracy of the quantification. However, it was felt that the accuracy of the velocity estimation techniques used might be insufficient for any form of reliable quantification and there appears to be some evidence in the literature to back this up, see Kowalski et al. [52] who demonstrate that the technique of estimating the strain from the velocity gradient suffers from poor reproducibility. They go on to conclude that this could be, in part, due to problems caused when the difference between the two velocities used to estimate the gradient is small compared to the accuracy of the initial velocity measurements. Therefore, any technique which could improve the accuracy of these estimations would be of significant benefit.

## 7.2 Doppler Tissue Imaging

Chapter 4 focused on the accuracy of the existing velocity estimation techniques and introduced the concept of using correlation-model based methods in the form of the cross-correlation model and the complex cross-correlation model estimators. Although neither of these estimators are new in any way, it is believed that the work in this thesis forms the first proper analysis of their performance with a view to using the estimations for further analysis, such as strain or strain-rate imaging.

One of the significant problems for Doppler tissue imaging is that it is necessary to capture multiple lines for each velocity line of the resulting image. This is because the velocity estimation is usually performed using the cross-correlation over two or more signals to determine the extent to which the scatterers have shifted in the time between each line. There is an ever greater demand for higher imaging frame rates and this effectively limits the number of lines which can be used for each image (velocity) line to two. Therefore, it is only possible to use cross-correlation of these two signals to estimate the velocity. The results presented in Chapter 4 clearly demonstrate that this method is able to measure the velocity with errors of the order of 10 % to 20 %, which confirms the figures quoted in the literature.

The correlation-model based techniques are based on forming a two dimensional model of the cross-spectrum of a series of signals and then using the Weiner-Khinchin relation to transform this into a model for the cross-correlation. Given that the actual cross-correlations can be estimated from a set of received signals, it is possible to use these to work backwards to calculate the model parameters, which includes a term for the temporal frequency. This frequency is equivalent to the Doppler shift that would be caused by the motion of the scatterers and so it is possible to arrive at an estimation for the velocity.

Results have been presented for both of these techniques which clearly demonstrate that the cross-correlation model estimator gives an accuracy which is similar to simply using the cross-correlation of two signals, but the complex cross-correlation estimator gave a near order of magnitude improvement, with errors of the order or 1 % to 2 % in the best case. Using velocity measurements which are this much more accurate would clearly have an impact on the reproducibility of any further estimations derived from them and it would be very interesting to carry out further work to investigate what the actual impact would be.

Simulations based on the Field II ultrasound simulation engine were used to test the noise performance of all of the techniques and it was observed that they were all fairly similar. In all cases, there was a threshold signal-to-noise ratio of around 30 dB to 40 dB, above which they all achieved maximum performance. In the case of the correlation model based estimators it was observed that the estimated velocity rapidly fell to zero when the SNR fell below the threshold between 30 dB and 40 dB, which caused the percentage error to settle in the region of

100 %. However, the time domain cross correlation estimator displayed a more gradual decline in accuracy with falling SNR.

The degree in improvement in accuracy of the complex cross correlation model based estimator comes at the expense that the estimator requires the use of more temporal domain samples. Indeed, the best results were obtained when the complex cross-correlation model estimator was used with 64 temporal domain samples. Since the velocities encountered in Doppler tissue imaging contexts are fairly low there is a limit on the maximum pulse repetition frequency which can be used. All of the results presented in Chapter 4 were obtained using a PRF of 1 kHz, which for the case of 64 temporal domain samples, would equate to 64 ms to capture enough data to produce a single line. Obviously this would render producing two dimensional images at an acceptable frame rate (25 f.p.s. or higher) impossible.

Originally, echocardiography was of the form of a single scan line on an oscilloscope, called A-mode (amplitude mode). The requirement to be able to visualise changes over time caused this to be developed into M-mode (motion mode). This was later developed into the 2D imaging form that is used today because of a requirement to get a better understanding of the spatial geometries involved. However, the M-mode scans have the advantage that it is only plotting a single spatial line over time, therefore enabling the technique to get much higher frame rates then would be possible for 2D images. Because of this, M-mode scanning allows much more time per line, so the use of this imaging technique would make it possible to make use of up to 64 temporal domain samples to perform the velocity estimations.

Although the use of M-mode scans may seem like a step backwards, it was felt that the degree of improvement in the accuracy of the velocity estimations would more then make up for the lack of 2D geometric information. Even the most modern clinical scanners still support M-mode scanning since it is still the only way to reliably visualise the motion of the heart tissue with a sufficiently high temporal resolution to be able to analyse the motion of some of the faster moving parts.

The overall conclusion from the results presented in Chapter 4 was that for the new techniques designed to improve the quantification of Doppler tissue imaging, such as strain imaging, to be reliable it would be necessary to significantly improve the accuracy of the original velocity estimations. This could be achieved by using the complex cross-correlation model based estimator, although this requires many more temporal domain samples to work effectively. This would render it unable to produce 2D images, but it would work very well with colour M-mode. It was therefore argued that for truly quantitative and above all, reproducible results, it will be necessary to move away from 2D imaging and return to the older imaging technique of M-mode.

## 7.3 The Fractional Fourier Transform and Coded Excitation

The inspiration behind Chapter 5 was the idea that further performance improvements might be obtained by changing the form of the transmitted signal. The results in Chapter 4 clearly indicated that there was an optimum pulse length of 2 cycles and pulses which were shorter or longer then this did not yield as accurate velocity estimates. This is clearly at odds with the requirements for producing high resolution images because the longer pulse will lead to a reduction in the axial resolution. For the best images, a pulse length of only 1 cycle is generally used. As a result of this, it is believed that clinical scanners generally use longer pulses for the velocity estimation part of the process (it is not possible to determine this because the manufacturers do not reveal such details easily). This means that they have to transmit separate signals for producing the image and for producing the velocity estimations, or accept a degradation in the quality of the gray-scale image when using DTI.

Chapter 5 introduced the idea of coded excitation, which is a technique that has been used in the fields of RADAR and SONAR for many years because it allows longer signals to be used without sacrificing the axial resolution. However, up take of the technique for medical ultrasound imaging has been slow because the bandwidths of most ultrasound transducers are too narrow and this limits the effectiveness of any coding scheme. However, G.E. [89] now manufacture ultrasound scanners which use coding schemes similar to the Golay codes described in Chapter 5.

An alternative to this form of coding is to use linear, frequency modulated chirps. Signals such as this are used extensively in SONAR and are also used by some species of bats and dolphins for echo location. When the received signal is processed using a matched filter, the axial resolution of the result is inversely proportional to the bandwidth of the transmitted signal and is no longer dependent on the length of the signal. This makes it possible to use longer signals without sacrificing axial imaging resolution. These longer signals have a higher average energy which enables images to be formed of features deeper inside the body, without having to increase the peak energy which is known to have potentially damaging consequences.

Chapter 5 introduced the fractional Fourier transform and demonstrated the effectiveness of using this technique to process signals received after the transmission of approximately linear FM chirps. Results were presented which clearly demonstrate that this technique is able to produce levels of pulse compression similar to those obtained by matched filtering, but without the need to a-priori knowledge of the transmitted signal. This is possible because the chirp parameters may be derived from the received signal by evaluating a series of fractional Fourier transforms over a number of different transform orders and searching the resulting two-dimensional data set for local maxima, which would indicate significant peaks. Although this process is computationally very expensive, it would only be necessary to perform it once for each set of received signals where the parameters of the transmitted signals were not changed. To obtain optimum performance, a matched filter should be designed to match the signal which actually leaves the transducer and enters the body. The impulse response of the transducer used will alter the shape of the signal as it is transmitted, which means that an optimum matched filter should be designed with knowledge of the transducer impulse response. Although the nature of the transmitted signal will always be known at 'design time' in the medical ultrasound context, there is some potential advantage in a technique which could automatically adapt to a different signal / transducer arrangement. The fractional Fourier transform method demonstrated in Chapter 5 would be able to adapt in such a way.

Results were also presented which demonstrate that it is possible to isolate key signal components in the transform domain by windowing around significant peaks and then inverting the transform to recover the time-domain signals which caused those peaks. Signals from a test phantom consisting of a cylinder of tissue mimicking material with three different size slits cut into it were used to demonstrate that the positions of the recovered time-domain signals gave very accurate measurements of the positions and relative dimensions of the phantom.

Given that the fractional Fourier transform is not time invariant, it was possible to derive a method for directly relating the positions of features in the transform domain to their corresponding positions in the time domain without having to invert the transform. Using this method, it was clearly demonstrated that the fractional Fourier transform was able to give results which not only had a similar degree of pulse compression to a matched filter, but which also had significantly reduced range lobes. It is believed that this is the first time such a relationship between the transform domain and the time domain has been demonstrated to offer a reduction in the range side lobes. It was, however, noted that there was an error in the resulting positions, the reason for which was not known at the time of writing. It would be interesting to conduct further work to investigate the cause of this error.

One significant caveat with the fractional Fourier transform is that is currently no formal definition of the discrete transform. Two different implementations have been used in the work described in this thesis and the results clearly show that there is a significant difference between them. Work is currently underway to derive a formal discrete transform [65], but until then it is necessary to use approximations.

The fact that coded excitation allows longer signals to be used without sacrificing the imaging performance may have benefits in terms of producing velocity images, however there wasn't time to study this. Results have been presented which clearly demonstrate the possibility of using the fractional Fourier transform based approach for producing images, but it would be very interesting to conduct further investigation in to the possibility of estimating the velocity from these signals.

In order to truly quantify the benefits of the fractional Fourier technique in terms of resolution enhancement and range side lobes, it would be necessary to perform experiments using a wire phantom. Such a phantom consists of a thin wire suspended in water such that it intersects with the ultrasound beam from the transducer. The transducer can the be moved to a series of different positions with respect to the wire and measurements of the received echo made. This would give a quantitative measure of the range and beam side lobes obtained. Further wires could be introduced with various spacings in order to give a measure of the resolution of the system. It is intended to carry out further work to implement just such an experiment with the fractional Fourier transform processing method.

## 7.4 Empirical Mode Decomposition and Tissue Harmonic Imaging

The work described in Chapter 6 resulted formed an investigation into alternative ways of looking at the received signals which focused on the use of the relatively new technique of empirical mode decomposition. This technique was first described by Huang et al. [88] in 1998 and is designed to break a single down into a series of intrinsic mode functions, each of which has a clearly defined instantaneous frequency at each sample.

The concept of instantaneous frequency defined as the rate of change of phase of a signal was introduced and it was explained that for this to be valid a signal has to be 'narrow band', although no precise definition of what would constitute 'narrow' in this context has been put forward [88]. Empirical mode decomposition was designed to over come this problem.

It has been known for some time that the propagation of finite-amplitude acoustic waves in water is a highly non-linear process, however it was only relatively recently that it was demonstrated that non-linear effects occur in tissue with waves of the frequencies and intensities used in medical ultrasound imaging. Previously, all interpretations of this process were based on analysis of the signals using Fourier based methods. This lead to the idea that the non-linear distortion was causing a progressive shift of signal energy from the fundamental frequency of the transmitted signal to the harmonics. This lead to the 'invention' of tissue harmonic imaging in the early 1990s which makes use of the signal energy which is shifted to the second harmonic of the transmitted signal and it has been shown that this offers clear advantages in terms of clutter rejection and imaging depth.

The results presented in the first section of Chapter 6 illustrate the process of non-linear distortion occurring for a simple 4 cycle sine wave transmitted using part of the single crystal ultrasound system. This clearly shows that as the distance between the source transducer and the hydrophone was increased, so the degree of distortion increased until shock formation occurred. At this point, it is not possible for the wave to distort any further, so the amplitude diminishes quickly.

The same signals were analysed using the combined techniques of empirical mode decomposition and the Hilbert spectrum and the results clearly demonstrated a difference to the results obtained using the Fourier transform. Instead of showing signal energy being shifted into the harmonic frequencies, the Hilbert spectrum demonstrated the occurrence of an intra-wave frequency modulation. The physical significance of an intra-wave frequency modulation was briefly discussed in Chapter 6, but a much more thorough analysis is given by Huang et al. [88].

Prior to this work, all the analysis performed on waveforms which have been distorted as a result of propagation through non-linear media has been based on Fourier analysis. It was argued in Chapter 6 that the apparent spreading of energy into the second and higher harmonic frequencies is a result of the use of Fourier based techniques and does not represent the physical situation. The results presented in Chapter 6 are the first to show that the non-linear distortion of the waveform causes an intra-wave frequency modulation.

Signals were captured from a tissue mimicking material phantom using the single crystal ultrasound system with wide-band transducers with center frequencies of 3.5 MHz and 6 MHz. Analysis of these signals using empirical mode decomposition and Hilbert spectrum clearly demonstrated that it was possible to detect the occurrence of the intra-wave frequency modulation even with a comparatively narrow band transducer (compared to the hydrophone) in signals resulting from scattering within a phantom.

As well as producing the Hilbert spectra, the technique of empirical mode decomposition lead to the generation of a series of intrinsic mode functions. Each signal which was analysed generally resulted in around 8 to 10 IMFs and it was observed that the second of these appeared to contain significant signal information which was different to that observed in the original signal. Results were presented clearly showing that the second IMF continued to contain useful signal information when the frequency of the transmitted signal was increased right up to the limit of the bandwidth of the transducer, while bandpass filtering around the fundamental or second harmonic frequencies obscured most of the information about the phantom.

The mechanical scanner was used with the 3.5 MHz transducer to acquire pseudo 2D images of the phantom and the resulting images for pulse lengths of 4 and 8 cycles and both fundamental and second harmonic filtering were presented. It was observed that in these cases, good results could be obtained by summing the first two IMFs resulting from each signal. Images produced using this technique were presented and compared to those resulting from fundamental and harmonic filtering. The results clearly demonstrated that the images resulting from summing the first two IMFs were of higher contrast compared to 'conventional' imaging and the 1 mm wide slit was more clearly defined. This was particularly noticeable in the case of the 8 cycle pulse length signals where the slit was more or less completely obscured with both fundamental and second harmonic filtering. Also, in both of the conventional filtering cases, the signal from the 3 mm wide slit at the bottom of the phantom was very weak, but it is clearly visible in the IMF images.

The clinical scanner was used to capture signals from a healthy volunteer and the resultant image after filtering around the second harmonic was presented. The signals were then broken down into IMFs using the empirical mode decomposition technique and images were produced from the first three IMFs. These results clearly showed that the second IMF appeared to contain useful signal information. The image produced using the second IMFs was compared to the original and it was observed that this method was able to give higher contrast and more clearly defined features. Producing an image from the sum of the first two IMFs was observed to give a result which was very similar to the original, unfiltered data.

## 7.5 Summary

Although the technique of echocardiography is well suited to the task of studying the motion of cardiac structures, improvements in the B-mode contrast and spatial resolutions, as well as DTI velocity resolutions will be required if truly quantitative results are to be obtained. The work described in this thesis has clearly shown that such improvements are possible and has looked at three different techniques by which this might be achieved. Results have been presented which clearly demonstrate the the use of the complex cross correlation model velocity estimation technique can lead to a near order of magnitude improvement in the accuracy of DTI, while the fractional Fourier transform has been shown to be an effective technique for processing the echo signals resulting from the transmission of linear FM chirp signals. The combined techniques of empirical mode decomposition and the Hilbert spectrum were used to demonstrate an alternative interpretation of the phenomenon of non-linear wave propagation, which was based on the generation of an intra-wave frequency modulation. Results were presented which demonstrated that it was possible to use the EMD technique to significantly improve the contrast resolution obtainable with 2D B-mode images.

## 7.6 Future Work

The work presented has highlighted several interesting avenues for further exploration. Firstly, further work should be done to investigate the accuracy of strain estimations made using the velocity estimation techniques described in Chapter 4. Ultimately this would lead to performing in-vivo studies to determine the clinical effects of the choice of velocity estimation technique.

The fractional Fourier transform work described in Chapter 5 could be extended by using a wire phantom to measure the resulting point-spread functions, which would give a definite measure of the improvement in imaging resolution which could be obtained. It would be beneficial to develop an open ultrasound system which would offer better 2D imaging facilities, while allowing complete control over the transmitted signal. With such a system, it would be easier to assess the degree of improvement in imaging offered by this technique.

The combined techniques of empirical mode decomposition and the Hilbert spectrum have demonstrated the presence of an intra-wave frequency modulation in non-linearly propagated signals. However, further investigations should be carried out into the exact nature of the intra-wave frequency modulation, specifically looking at what extra information about the propagating medium might be extracted.

# References

[1] Yale Center for Advanced Instructional Media, Yale University School of Medicine, "Introduction to cardiothoracic imaging." Internet Website. http://info.med.yale.edu/intmed/cardio/imaging/.

[2] R. Chiao and X. Hao, "Coded excitation for diagnostic ultrasound: A system developer's perspective," in *IEEE Ultrasonics Symposium*, vol. 1, pp. 437 – 448, IEEE, October 2003.

[3] A. Guyton, *Textbook of medical physiology*. W.B.Saunders Company, 8 ed., 1991.

[4] H. Feigenbaum, *Echocardiography*. Lea & Febiger, 1976.

[5] C. Doppler, "Ueber das farbige licht der doppelsterne und einiger anderer gestirne des himmels," *Abhandl. d. Konigl. Bohmischen Gesellschaft der Wissenschaften Sers.*, vol. 2, pp. 465 – 482, 1843.

[6] S. Satomura, "Study of the flow patterns in peripheral arteries by ultrasonics," *J Acoust Soc Jap*, vol. 15, pp. 151 – 158, 1959.

[7] D. Franklin, W. Schlegel, and R. Rushmer, "Blood flow measured by doppler frequency shift of back-scattered ultrasound," *Science*, vol. 134, no. 3478, pp. 564 – 465, 1961.

[8] J. Griffith, "Resolution performance of doppler ultrasounds flowmeters," *Journal of the Acoustical Society of America*, vol. 60, no. 3, pp. 607 – 610, 1976.

[9] V. Newhouse, "Analysis of transit time effects on doppler flow measurement," *IEEE Transactions on Biomedical Engineering*, vol. 23, pp. 381 – 387, 1976.

[10] V. Newhouse, "Geometrical spectrum broadening in ultrasonic doppler systems," *IEEE Transactions on Biomedical Engineering*, vol. 24, pp. 478 – 481, 1977.

[11] V. Newhouse, "The dependence of ultrasound doppler bandwidth on beam geometry," *IEEE Transactions on Sonics and Ultrasonics*, vol. 27, pp. 50 – 59, 1980.

[12] A. Fleming, W. McDicken, G. Sutherland, and P. Hoskins, "Assessment of colour doppler tissue imaging using test phantoms," *Ultrasound Med Biol*, vol. 20, no. 9, pp. 937 – 951, 1994.

[13] I. Zuna, M. Fein, S. Reinert, S. Delorme, G. V. Kaick, and W. Lorenz, "Pc-based system for quantification of medical color doppler images," in *Acoustic Sensing and Imaging*, no. 369, pp. 50 – 55, IEE, 1993.

[14] A. Criton, T. Loupas, H. Routh, and P. Pesque, "Automated quantification in tissue doppler imaging," *Computers in Cardiology*, vol. 25, pp. 93 – 95, 1998.

[15] W. McDicken, G. Sutherland, C. Moran, and L. Gordon, "Colour doppler velocity imaging of the myocardium," *Ultrasound Med Biol*, vol. 18, no. 6/7, pp. 661 – 654, 1992.

[16] C. Kasai, K. Namekawa, A. Koyano, and R. Omoto, "Real-time two-dimensional blood flow imaging using an autocorrelation technique," *IEEE Trans Sonics Ultrasonics*, pp. 458 – 463, 1985.

[17] E. O. Ofili and N. C. Nanda, "Color doppler imaging of the myocardium: Current status and potential clinical applications," *Ultrasound Med Biol*, vol. 24, no. 2, pp. 177 – 185, 1998.

[18] G. Sutherland, M. Stewart, and K. Grounstroem, "Colour doppler myocardial imaging: a new technique for the assessment of myocardial function," *J Am Soc Echo*, vol. 7, pp. 441 – 458, 1994.

[19] K. Miyatake, M. Yamagishi, N. Tanaka, M. Uematus, N. Yamazaki, Y. Mine, A. Sano, and M. Hirama, "New method for evaluating left ventricular wall motion by color-coded tissue doppler imaging: in-vitro and in-vivo studies," *J Am Coll Cardiol*, vol. 25, no. 3, pp. 717 – 724, 1995.

[20] D. S. Bach and W. F. Armstrong, "Management and technology updates: Doppler tissue imaging," tech. rep., Americal College of Cardiology, 1996.

[21] L. Kapusta, J. Thussen, M. Cuypers, P. Peer, and O. Daniels, "Assessment of myocardial velocities in healthy children using tissue doppler imaging," *Ultrasound Med Biol*, vol. 26, no. 2, pp. 229 – 237, 2000.

[22] L. Kapusta, J. Thijssen, J. Groot-Loonen, J. V. Druten, and O. Daniëls, "Disctiminative ability of conventional echocardiography and tissue doppler imaging techniques for the detection of subclinical cardiotoxic effects of treatment with anthracyclines," *Ultrasound Med Biol*, vol. 27, no. 12, pp. 1605 – 1614, 2001.

[23] P. Frommelt, J. Ballweg, B. Whitstone, and M. Frommelt, "Usefulness of doppler tissue imaging analysis of tricuspid annular motion for determination of right ventricular function in normal infants and children," *The American Journal of Echocardiography*, vol. 89, pp. 610 – 613, 2002.

[24] D. Fyfe, W. Mahle, K. Kanter, G. Wu, R. Vincent, and D. Ketchum, "Reduction of tricuspid annular doppler tissue velocities in pediatric heart transplant patients," *The Journal of Heart and Lung Transplantation*, vol. 22, no. 5, pp. 553 – 559, 2003.

[25] A. Lange, P. Palka, P. Caso, L. Fenn, R. Olszewski, M. P. Ramo, T. Shaw, A. Nowicki, K. Fox, and G. Sutherland, "Doppler myocardial imaging vs. b-mode grey-scale imaging: a comparative in vitro and in vivo study into their relative efficacy in edocardial boundary detection," *Ultrasound Med Biol*, vol. 23, no. 1, pp. 69 – 75, 1997.

[26] A. Fraser, N. Payne, C. Mädler, B. Janerot-Sjøberg, B. Lind, R. Grocott-Mason, A. Lonescu, N. Florescu, U. Wilkenshoff, P. Lacellotti, M. Wütte, and L.-Å. Brodin, "Feasibility and reproducibility of off-line tissue doppler measurement of regional myocardial function during dobutamine stress echocardiography," *Eur J Echocardiography*, vol. 4, pp. 43 – 53, 2003.

[27] A. Fleming, X. Xia, W. McDicken, G. Sutherland, and L. Fenn, "Myocardial velocity gradients detected by doppler imaging," *British Journal of Radiology*, vol. 67, no. 799, pp. 679 – 688, 1994.

[28] M. Uematsu, S. Nakatani, M. Yamagishi, H. Matsuda, and K. Miyatake, "Usefulness of myocardial velocity gradient derived from two-dimensional tissue doppler imaging as an indicator of regional myocardial contraction independent of translational motion assessed in atrial septal defect," *American Journal of Cardiology*, vol. 79, pp. 237 – 241, 1997.

[29] K. Miyatake, N. Tanaka, A. Sano, N. Yamazaki, M. Hirama, and M. Yamagishi, "Myocardial velocity gradient as a new indicator of regional left ventricular contraction: Detection by a two-dimensional tissue doppler imaging technique," *Journal of the American College of Cardiology*, vol. 26, no. 1, pp. 217 – 223, 1995.

[30] H. Tsutsui, M. Uematsu, H. Shimizu, M. Yamagishi, N. Tanaka, H. Matsuda, and K. Miyatake, "Comparative usefulness of myocardial velocity gradient in detecting ischemic myocardium by a dobutamine challenge," *J Am Coll Cardiol*, vol. 31, no. 1, pp. 89 – 93, 1998.

[31] R. Hoffmann, E. Altiok, B. Nowak, N. Heussen, H. Kühl, H. Kaiser, U. Büll, and P. Hanrath, "Strain rate measurment by doppler echocardiography allows improved assessment of myocardial viability in patients with depressed left ventricular function," *J Am Coll Cardiol*, vol. 39, no. 3, p. 52, 2002.

[32] C. Pislaru, P. Anagnostopoulos, J. Seward, J. Greenleaf, and M. Belohlavek, "Higher myocardial strain rates during isovolumic relaxation phase than during ejection characterise acutely ischemic myocardium," *Journal of the American College of Cardiology*, vol. 40, no. 8, pp. 1487 – 1494, 2002.

[33] P. Kiraly, L. Kapusta, J. Thijssen, and O. Daniëls, "Left ventricular myocardial function in congenital valvar aortic stenosis assessed by ultrasound tissue velocity and strain rate techniques," *Ultrasound Med Biol*, vol. 29, no. 4, pp. 615 – 620, 2003.

[34] D. Phillips, J. Hossack, K. Beach, and D. S. Jr., "Testing ultrasonic pulsed doppler instruments with a physiologic string phantom," *J Ultrasound Med*, vol. 9, pp. 429 – 436, 1990.

[35] S. Russell, D. McHugh, and B. Moreman, "A programmable doppler string test object," *Phys Med Biol*, vol. 38, pp. 1623 – 1630, 1993.

[36] S. Stewart, "Effects of transducer, velocity, doppler angle and instrument settings on the accuracy of colour doppler ultrasound," *Ultrasound Med Biol*, vol. 27, no. 4, pp. 551 – 564, 2001.

[37] P. Embree and W. O'Brian, "Volumetric blood flow via time-domain correlation: Experimental verification," *IEEE Trans UFFC*, vol. 37, no. 2, pp. 176 – 189, 1990.

[38] C. Veyrat, D. Pellerin, F. Larrazet, L. Cohen, and S. Witchitz, "Dynamic myocardial velocity changes between phases of the cardiac cycle," *Ultrasound in Medicine and Biology*, vol. 29, no. 8, pp. 1077 – 1084, 2003.

[39] B. Lind, J. Nowak, P. Cain, M. Quintana, and L. å. Brodin, "Left ventricular isovolumic velocity and duration variables calculated from colour-coded myocardial velocity images in normal individuals," *European Journal of Echocardiography*, vol. 5, pp. 284 – 293, 2004.

[40] J. A. Jensen and N. B. Svendsen, "Calculation of pressure fields from arbitrarily shaped, apodized and excited ultrasound transducers," *IEEE transactions on UFFC*, vol. 39, no. 2, pp. 262 – 267, 1992.

[41] J. Jensen, "Field: A program for simulating ultrasound systems," in *Medical & Biological Engineering and Computing*, vol. 34, pp. 351 – 353, 1996.

[42] J. Jensen, "Field ii ultrasound simulation program." http://www.es.oersted.dtu.dk/staff/jaj/field/index.html.

[43] D. Evans and W. McDicken, *Doppler Ultrasound - Physics, Instrumentation and Signal Processing*. John Wiley and Sons, LTD, 2000.

[44] "http://www.gehealthcare.com/inen/rad/us/technology/msudigit.html." Internet web site, 2005.

[45] P. Pesque and J. Souguet, "Digital ultrasound: from beamforming to pacs." http://www.medical.philips.com/main/news/assets/docs/medicamundi/mm_vol43_no3/mm_vol43_no3_article_digital_ultasound.pdf, September 1999.

[46] D. Dotti, E. Gaiit, V. Svelto, A. Uggé, and P. Vidali, "Blood flow measurements by ultrasound correlation techniques," *Energia Nucleare*, vol. 23, no. 11, pp. 571 – 575, 1976.

[47] O. Bonnefous and P. Pesqué, "Time domain formulation of pulse-doppler ultrasound and blood velocity estimation by cross correlation," *Ultrasonic Imaging*, vol. 8, no. 2, pp. 73 – 85, 1986.

[48] S. Foster, P. Embree, and W. O'Brian, "Flow velocity profile via time-domain correlation: error analysis and computer simulation," *IEEE Transactions on Ultrasonics, Ferroelectrics and Frequency Control*, vol. 37, no. 2, pp. 164 – 175, 1990.

[49] P. de Jong, T. Arts, A. Hoeks, and R. Reneman, "Determination of tissue motion velocity by correlation interpolation of pulsed ultrasonic echo signals," *Ultrasonic Imaging*, vol. 12, pp. 84 – 98, 1990.

[50] P. de Jong, T. Arts, A. Hoeks, and R. Reneman, "Experimental evaluation of the correlation interpolation technique to measure regional tissue velocity," *Ultrasonic Imaging*, vol. 13, pp. 145 – 161, 1991.

[51] P. Brands, A. Hoeks, L. Ledoux, and R. Reneman, "A radio frequency domain complex cross-correlation model to estimate blood flow velocity and tissue motion by means of ultrasound," *Ultrasound Med Biol*, vol. 23, no. 6, pp. 911 – 920, 1997.

[52] M. Kowalski, M. Herregods, and L. Herbots, "The feasibility of ultrasonic regional strain rate imaging in quantifying dobutamine stress echocardiography," *Eur J Echocardiography*, vol. 4, pp. 81 – 91, 2003.

[53] S. Barnett, H. Rott, G. Ter Haar, M. Ziskin, and K. Maeda, "The sensitivity of biological tissue to ultrasound," *Ultrasound Med Biol.*, vol. 23, no. 6, pp. 805 – 812, 1997.

[54] S. Barnett, G. Ter Haar, M. Ziskin, W. Nyborg, K. Meada, and J. Bang, "Current status of research on biophysical effects of ultrasound," *Ultrasound Med Biol.*, vol. 20, no. 3, pp. 205 – 218, 1994.

[55] S. Barnett, G. Ter Haar, M. Ziskin, H. Rott, F. Duck, and K. Maeda, "International recommendations and guidelines for the safe use of diagnostic ultrasound in medicine," *Ultrasound Med Biol*, vol. 26, no. 3, pp. 355 – 366, 2000.

[56] M. O'Donnell, "Coded excitation system for improving the penetration of real-time phased-array imaging systems," *IEEE Transactions on Ultrasonics, Ferroelectrics, and Frequency Control*, vol. 39, pp. 341 – 351, May 1992.

[57] F. Harris, "On the use of windows for harmonic analysis with the discrete fourier transform," *Proc. IEEE*, vol. 66, pp. 51 – 83, 1978.

[58] A. Nuttal, "Some windows with very good sidelobe behaviour," *IEEE Trans. Acoust. Speech, Signal Processing*, vol. ASSP-29, pp. 84 – 91, 1981.

[59] N. Geckinili and D. Yavuz, "Some novel windows and a concise tutorial comparison of window families," *IEEE Trans. Acoust. Speech, Signal Processing*, vol. ASSP-26, pp. 501 – 507, 1978.

[60] Y. Takeuchi, "Chirped excitation for ¡-100db time sidelobe echo sounding," in *IEEE Ultrasonics Symposium*, vol. 2, pp. 1309 – 1314, IEEE, Novemeber 1995.

[61] N. Rao and S. Mehra, "Medical ultrasound imaging using pulse compression," *Electronics Letters*, vol. 29, no. 8, pp. 649 – 651, 1993.

[62] T. Misaridis, K. Gammelmark, C. Jørgensen, N. Lindberg, A. Thomsen, M. Pedersen, and J. Jensen, "Potential of coded excitation in medical ultrasound imaging," *Ultrasonics*, vol. 38, pp. 183 – 189, 2000.

[63] M. Pedersen, T. Misaridis, and J. Jensen, "Clinical comparison of pulse and chirp excitation," *IEEE Ultrasonics Symposium*, pp. 1673 – 1676, 2002.

[64] "http://www.gemedicalsystemseurope.com/euen/rad/us/products/logiq_7/msulog7.html."

[65] H. Ozaktas, Z. Zalevsky, and M. Kutay, *The fractional Fourier transform and applications in optics and signal processing*, ch. 6, p. 298. Wiley, 2000.

[66] L. Cohen, *Time-Frequency Analysis*. Prentice Hall Signal Processing Series, 1995.

[67] L.Stanković, T. Alieva, and M. Bastiaans, "Time-frequency signal analysis based on the windowed fractional fourier transform," *Signal Processing*, vol. 82, pp. 2459 – 2468, 2003.

[68] T. Alieva and M. Bastiaans, "On fractional fourier transform moments," *IEEE Signal Processing Letters*, vol. 7, no. 11, pp. 320 – 323, 2000.

[69] C. Capus and K. Brown, "Short-time fractional fourier methods for the time-frequency representation of chirp signals," vol. 113, pp. 3253 – 3263, Acoustical Society of America, 2003.

[70] H. Ozaktas, Z. Zalevsky, and M. Kutay, "Digital computation of the fractional fourier transform," *IEEE Transactions on Signal Processing*, vol. 44, pp. 2141 – 2150, 1996.

[71] C. Candan, M. Kutay, and H. Ozaktas, "The discrete fractional fourier transform," *IEEE Transactions on Signal Processing*, vol. 48, no. 5, pp. 1329 – 1337, 2000.

[72] M. Kutay, H. Ozaktas, O. Arikan, and L. Onural, "Optimal filtering in fractional fourier domains," *IEEE Transactions on Signal Processing*, vol. 45, no. 5, pp. 937 – 940, 1997.

[73] F. A. Duck, "Nonlinear acoustics in diagnostic ultrasound," *Ultrasound Med Biol*, vol. 28, no. 1, pp. 1 – 18, 2002.

[74] E. Carstensen, W. Law, and N. McKay, "Demonstration of nonlinear acoustical effects at biomedical frequencies and intensities," *Ultrasound Med Biol*, vol. 6, pp. 359 – 368, 1980.

[75] T. Muir and E. Carstensen, "Prediction of nonlinear acoustic effects at biomedical frequencies and intensities," *Ultrasound Med Biol*, vol. 6, pp. 345 – 357, 1980.

[76] T. Christopher, "Finite amplitude distortion-based inhomogenious pulse echo ultrasonic imaging," *IEEE Trans. UFFC*, vol. 44, no. 1, pp. 125 – 139, 1997.

[77] T. Christopher, "Experimental investigation of finite amplitude distortion-based, second harmonic pulse echo ultrasonic imaging," *IEEE Trans. UFFC*, vol. 45, no. 1, pp. 158 – 162, 1998.

[78] B. Ward, A. Baker, and V. Humphrey, "Nonlinear propagation applied to the improvement of resolution in diagnostic medical ultrasound," *J. Accoust. Soc. Am.*, vol. 101, pp. 143 – 154, 1997.

[79] J. Thomas and D. Rubin, "Tissue harmonic imaging: why does it work?," *Journal of the American Society of Echocardiography*, pp. 803 – 808, 1998.

[80] B. Ward and T. Whittingham, "Tissue harmonic imaging: what is it and how does it work?," *BMUS Bulletin*, 1999.

[81] P. Burns, D. Simpson, and M. Averkiou, "Nonlinear imaging," *Ultrasound in Med. & Biol.*, vol. 26, no. Supplement 1, pp. S19 – S22, 2000.

[82] M. Averkiou, D. Roundhill, and J. Powers, "A new imaging technique based on the nonlinear properties of tissues," *IEEE Ultrasonics Symposium*, pp. 1561 – 1566, 1997.

[83] M. Averkiou, "Ultrasonic diagnostic imaging system transmitter for sum and difference frequency imaging." United States Patent, December 2002. Patent Number: US 6,494,839 B1.

[84] F. Tranquart, N. Grenier, V. Eder, and L. Pourcelot, "Clinical use of ultrasound tissue harmonic imaging," *Ultrasound Med Biol*, vol. 25, no. 6, pp. 889 – 894, 1999.

[85] D. Prior, W. Jaber, D. Homa, J. Thomas, and E. Sabik, "Impact of tissue harmonic imaging on the assessment of rheumatic mitral stenosis," *Am J Cardiol*, vol. 86, pp. 573 – 576, 2000.

[86] D. Mele, M. Campana, M. Sclavo, G. Seveso, D. Aschieri, F. Nesta, I. D'Aiello, R. Ferrari, and R. Levine, "Impact of tissue harmonic imaging in patients with distorted left ventricles: Improvement in accuracy and reproducibility of visual, manual and automated echocardiographic assessment of left ventricular ejection fraction," *Eur J Echocardiogr*, vol. 4, pp. 59 – 67, 2003.

[87] M. Wijk and J. Thijssen, "Performance testing of medical ultrasound equipment: fundamental vs. harmonic mode," *Ultrasonics*, vol. 40, pp. 585 – 591, 2002.

[88] N. Huang, Z. Shen, S. Long, M. Wu, H. Shih, Q. Zheng, N. Yen, C. Tung, and H. Liu, "The empirical mode decomposition and the hilbert spectrum for nonlinear and non-stationary time series analysis," *Proceedings of the Royal Society of London*, no. 454, pp. 903 – 995, 1998.

[89] "http://www.gemedicalsystemseurope.com/euen/rad/us/products/logiq_9/19_codescan.html." Internet web site, 2004.

# Appendix A
# List of Publications

*Filtering of Ultrasound Echo Signals with the Fractional Fourier Transform.* Michael Bennett, Steve McLaughlin, Tom Anderson and Norman McDicken. Engineering in Medicine and Biology Society, 2003. Proceedings of the 25th Annual International Conference of the IEEE EMBS, Volume 1, 17-21, Sept. 2003.

*Filtering of Chirped Ultrasound Echo Signals with the Fractional Fourier Transform.* Michael Bennett, Steve McLaughlin, Tom Anderson and Norman McDicken. IEEE Ultrasonics, Ferroelectrics and Frequency Control Joint Conference. Pages 2036-2040. August 2004.

*Empirical Mode Decomposition and Tissue Harmonic Imaging.* Michael Bennett, Steve McLaughlin, Tom Anderson and Norman McDicken. Ultrasound in Medicine and Biology. Vol. 31, No. 8, Pages 1051-1061, August 2005.

*The use of the Fractional Fourier Transform with Coded Excitation in Ultrasound Imaging.* IEEE Transactions on Biomedical Engineering. In press.

*An Analysis of the Accuracy of Velocity Estimtion Techniques With a View to Further Quantification through Strain and Strain-Rate Imaging.* Michael J. Bennett, Steve McLaughlin, Tom Anderson and W. Norman McDicken. Ultrasound in Medicine and Biology. Under review.